Enhancing Near-Infrared Down-Shifting Luminescence in Core–Shell Nanostructures via Controlled Intermixing for Short-Wavelength Infrared Imaging

Zur Erlangung des akademischen Grades eines

DOKTORS DER INGENIEURWISSENSCHAFTEN (Dr.-Ing.)

von der KIT-Fakultät für Elektrotechnik und Informationstechnik des Karlsruher Instituts für Technologie (KIT)

angenommene

DISSERTATION

von

Fernando Arteaga-Cardona, M.Sc.

Tag der mündlichen Prüfung: 17.09.2026

Hauptreferent: Prof. Dr. Bryce S. Richards

Korreferent: Prof. Dr. Jonathan de Roo

Zusammenfassung

Die Entwicklung heller und biokompatibler Nanopartikel auf Basis seltener Erden hat in den letzten Jahren zunehmendes Interesse geweckt, insbesondere im Hinblick auf die Verbesserung ihrer Photolumineszenz-Effizienz. Unter den verschiedenen untersuchten Strategien haben sich Core–Shell-Architekturen als besonders vielversprechend erwiesen. Trotz erheblicher Fortschritte bei der Effizienzsteigerung wurde jedoch der räumlichen Verteilung der optisch aktiven Ionen in diesen Nanostrukturen, insbesondere nach dem Wachstum der Schale, bislang wenig Aufmerksamkeit geschenkt. Eine weit verbreitete Annahme in diesem Forschungsfeld besagt, dass der Kern während des Schalenwachstums strukturell und chemisch unverändert bleibt. Diese Vorstellung wurde jedoch weitgehend ohne direkte experimentelle Bestätigung akzeptiert und könnte subtile, aber entscheidende strukturelle Phänomene an der Kern-Schale-Grenzfläche übersehen. Diese Arbeit hinterfragt diese Annahme und zeigt, dass es möglich ist, eine klar segregierte Kern- und Schalenregion zu erzeugen – jedoch nur unter sehr spezifischen Bedingungen. Untersucht wurde dies durch die Analyse der räumlichen Verteilung der optisch aktiven Ionen, die ursprünglich ausschließlich im Kern verbleiben sollten, und wie sich diese Verteilung nach dem Schalenwachstum verändert. Durch die Untersuchung der Ionenverteilung lässt sich ein Zusammenhang zwischen bestimmten Synthesebedingungen und dem Kationen-Migrationsverhalten herstellen, was eine gezieltere Gestaltung von Nanostrukturen für spezifische Anwendungen ermöglicht.

Eine besonders vielversprechende Anwendung ist die Fluoreszenzbildgebung im kurzwelligen Infrarotbereich (SWIR). Diese bietet im Vergleich zu herkömmlichen optischen Verfahren entscheidende Vorteile, darunter geringere Gewebestreuung, minimale Autofluoreszenz und größere Eindringtiefe. Ihre breite Anwendung wird jedoch durch die geringe Quantenausbeute (PLQY) derzeit verfügbarer Nanopartikel eingeschränkt. Zur Lösung dieses Problems untersucht diese Arbeit systematisch die strukturellen, chemischen und synthetischen Einflussfaktoren auf die Kationenintermischung und die optische Leistungsfähigkeit seltenerdhaltiger Core–Shell-Nanokristalle.

Im ersten Teil dieser Arbeit wird gezeigt, dass die Verwendung einer konventionellen α-$NaYF_4$-Schale auf einem α-$NaYF_4$:Yb,Er(Ce)-Kern zu starker Kationenintermischung führt, wobei optisch aktive Ionen aus dem Kern in die Schale migrieren. Im Gegensatz dazu konnte durch den Einsatz von CaF_2 als Schalenmaterial auf demselben Kern eine klare Phasensegregation erzielt werden. Dies führte zur Bildung einer wohlstrukturierten α-$NaYF_4$:Yb,Er(Ce)/CaF_2-Heterostruktur, in der die Kationenintermischung effektiv unterdrückt wurde. Die resultierende chemisch reine und strukturell definierte Schale reduzierte Oberflächenabschreckungseffekte und führte zu einer PLQY von 50 % – einem der höchsten bisher berichteten Werte für Nanokristalle unter 15 nm mit Emission im SWIR-Bereich. Diese Nanokristalle wurden anschließend erfolgreich für *in vivo*-Bildgebung über 1450 nm eingesetzt, was ihr praktisches Potenzial für biomedizinische Anwendungen unterstreicht.

Aufbauend auf diesen Ergebnissen untersucht der zweite Teil der Arbeit verschiedene Materialkombinationen basierend auf α-$NaTmF_4$- und $LiTmF_4$-Kernen, kombiniert mit α-$NaYF_4$-, CaF_2- und $LiYF_4$-Schalen. Die strukturelle Analyse ergab, dass nur bestimmte Kombinationen zu gut definierten Core–Shell-Architekturen führten. Eine Phasensegregation konnte nicht nur in der heterogenen Kombination α-$NaYF_4$:Yb,Er(Ce)/CaF_2, sondern auch in der homogenen Kombination $LiTmF_4$/$LiYF_4$ beobachtet werden – trotz moderater Intermischung. Im Gegensatz zu α-$NaYF_4$ konnten jedoch keine der heterogenen Kombinationen mit $LiTmF_4$-Kernen die optisch aktiven Ionen vollständig im Kernbereich halten. Es zeigte sich jedoch, dass bereits eine reine Schale mit einer Dicke von mindestens 3 nm ausreicht, um eine hohe PLQY zu erzielen, wie am Beispiel des $LiTmF_4$/$LiYF_4$-Systems mit einer PLQY von 39 % oberhalb von 1600 nm demonstriert wurde. Diese Ergebnisse deuten darauf hin, dass zwar scharfe Grenzflächen vorteilhaft sind, jedoch die Fähigkeit der Schale, die optisch aktiven Ionen räumlich zu begrenzen, eine entscheidendere Rolle für eine effiziente Energieumwandlung spielt.

Im dritten und letzten Teil dieser Arbeit wird der Einfluss intrinsischer (Kristallstruktur, Materialzusammensetzung) und extrinsischer (Schalendicke, Synthesetemperatur, Wachstumsmethodik) Parameter auf das Ausmaß der Intermischung und die

Emissionseffizienz systematisch untersucht. Eine anhaltende Intermischung wurde bei homogenen Core–Shell-Systemen aus α-$NaTmF_4$ und β-$NaGdTmF_4$ beobachtet, während die heterogene Kombination α-$NaTmF_4/CaF_2$ sowie die homogene Kombination $LiTmF_4/LiYF_4$ – durch gezielte Kontrolle extrinsischer Parameter – eine starke räumliche Trennung der Aktivatorenionen und hohe PLQYs aufwiesen. Diese Ergebnisse zeigen einen klaren Zusammenhang zwischen intrinsischen und extrinsischen Eigenschaften sowie deren Einfluss auf Grenzflächenorganisation, Ionenverteilung und Energieumwandlungseffizienz.

Insgesamt bietet diese Arbeit einen umfassenden Rahmen zum Verständnis und zur gezielten Kontrolle der Grenzflächenorganisation in Core–Shell-Nanokristallen auf Fluoridbasis mit Seltenen Erden. Die gewonnenen Erkenntnisse liefern praxisnahe Gestaltungsprinzipien für die Entwicklung hocheffizienter SWIR-Nanopartikel mit Relevanz für eine Vielzahl biomedizinischer Anwendungen.

Abstract

The development of bright and biocompatible rare-earth (RE^{3+})-based nanoprobes has attracted growing interest in recent years, particularly in efforts to enhance their photoluminescence efficiency. Among the various strategies explored, the formation of core–shell architectures has consistently yielded the most promising results. However, despite significant progress in improving emission efficiency, little attention has been paid to understanding the spatial distribution of the optically active ions in these nanostructures, especially after shell growth. A prevailing assumption in the field has been that the core remains structurally and compositionally intact during shell formation; yet, this notion has been accepted without direct experimental validation and may overlook subtle but critical interfacial structural patterns. This thesis challenges that assumption and demonstrates that it is possible to obtain a segregated core and shell area, but only under very specific conditions. This was investigated by tracking the spatial distribution of optically active ions originally intended to remain confined to the core, and by characterizing how that distribution changes after shell growth. By analyzing the ion organization after the shell growth, it becomes possible to correlate specific synthetic conditions with cation migration, enabling more rational design of nanostructures for specific applications. Among these, short-wave infrared (SWIR) fluorescence imaging stands out as a particularly compelling area. SWIR imaging offers key advantages over traditional optical modalities, including reduced tissue scattering, minimal autofluorescence, and increased penetration depth. Nonetheless, its broader implementation is limited by the low photoluminescence quantum yield (PLQY) of current nanoprobes. To address this challenge, this thesis systematically investigates the structural, chemical, and synthetic factors that govern cation intermixing and optical performance in RE-based core–shell nanocrystals (NCs).

The first part of this work demonstrates that using the conventional α-$NaYF_4$ shell on α-$NaYF_4$:Yb,Er(Ce) core NCs led to significant cation intermixing, where the optically active ions migrate from the core into the shell region. In contrast, when CaF_2 was employed as the shell material on the same α-$NaYF_4$:Yb,Er(Ce) core, clear phase

segregation was achieved. This resulted in the formation of a well-defined α-$NaYF_4$:Yb,Er(Ce)/CaF_2 heterostructure, in which cation intermixing was effectively suppressed. The formation of a chemically pure and structurally distinct shell mitigated surface quenching effects and led to a PLQY of 50%, one of the highest values reported for sub-15 nm NCs emitting in the SWIR region. These NCs were further used for SWIR *in vivo* imaging above 1450 nm, highlighting their practical potential for biomedical applications.

Building upon the data, the second part of the thesis explores different material combinations based on α-$NaTmF_4$ and $LiTmF_4$ cores paired with α-$NaYF_4$, CaF_2, and $LiYF_4$ shells. Structural analysis revealed that only select combinations led to well-defined core–shell architectures, and the phase segregation is not only achieved with the heterogeneous combination of α-$NaYF_4$:Yb,Er(Ce)/CaF_2, but also with the homogeneous combination of $LiTmF_4$/$LiYF_4$ (despite a moderate intermixing). In contrast to the α-$NaYF_4$ studied previously, none of the heterogeneous materials combinations using $LiTmF_4$ as seeds managed to confine the optically active ions in the core region. Nevertheless, the results showed that having at least 3 nm of pure shell gives high PLQY results, as $LiTmF_4$/$LiYF_4$ system achieved a PLQY of 39% above 1600 nm. This indicates that while abrupt interfaces are beneficial, the presence of a shell capable of spatially confining the optically active ions is of greater importance for maximizing the energy conversion.

The third and final part of this thesis systematically examines the influence of intrinsic (crystal structure, material composition) and extrinsic (shell thickness, synthesis temperature, and growth methodology) parameters on the degree of intermixing and emission efficiency. Persistent intermixing was observed in homogeneous core–shell systems of α-$NaTmF_4$ and β-$NaGdTmF_4$; whereas the heterogeneous material combination of α-$NaTmF_4$/CaF_2 and the homogeneous combination of $LiTmF_4$/$LiYF_4$ consistently exhibited strong spatial confinement of activator ions and high PLQYs, through the modifications of extrinsic properties. These findings establish a direct correlation between intrinsic-extrinsic properties and interfacial organization, ion distribution, and energy conversion efficiency.

Altogether, this work provides a comprehensive framework for understanding and controlling the interfacial organization of RE-based fluoride core–shell NCs. The insights presented here offer practical design principles for the development of high-efficiency SWIR nanoprobes, with implications for a range of biomedical applications.

Acknowledgements

I would like to express my deepest gratitude to Prof. Dr. Bryce S. Richards for giving me the opportunity to pursue a PhD by welcoming me into the Nanophotonics for Energy research group. His insightful feedback and academic support played a significant role in shaping the direction and quality of my work. His expertise and perspective were instrumental in refining my research and broadening my scientific outlook.

I am also sincerely thankful to my supervisor, Dr. Damien Hudry, for his exceptional guidance, support, and mentorship throughout my PhD journey. His dedication, patience, and willingness to share his knowledge have been invaluable to both my research and personal growth. Under his mentorship, I not only gained technical expertise in my field but also developed a deeper understanding of how to approach scientific challenges with curiosity and resilience.

Special thanks go to the Karlsruhe School of Optics and Photonics for organizing numerous events, including summer schools, symposiums, and seminars, which provided invaluable opportunities to connect with inspiring scientists and continuously expand my knowledge.

All this work wouldn't have been possible without the three years of funding provided by the Mexican government through the Mexican institution Consejo Nacional de Ciencia y Tecnología (CONACyT) y el Consejo Nacional de Ciencia y Tecnología del Estado de Puebla (CONCyTEP).

I am particularly grateful to Dr. Dmitry Busko for his support during the measurements, for teaching me about optical spectroscopy, and for our insightful work conversations. I deeply appreciate the time and effort he dedicated to building the measurement setup, which greatly facilitated the data acquisition process.

I would also like to extend my sincere appreciation to Dr. Radian Popescu from the Laboratory for Electron Microscopy for his support in the characterization and analysis of my samples, as well as for sharing his extensive knowledge in this field. Additionally, I am

grateful to Prof. Dr. Dagmar Gerthsen for granting us access to the instruments at the LEM institute, which were essential for my research.

A heartfelt thank you to my colleagues and friends at the Institute of Microstructure Technology—Dr. Andrey Turshatov, Dr. Dejing Meng, Dr. Anamul Haque, Dr. Eduard Madirov, Dr. Arzu Ergene, Dr. Jan Fischer, and Dr. Kishin Matsumori—for their collaboration, stimulating discussions, and for fostering a supportive and enjoyable research environment. Their camaraderie made this journey both productive and memorable.

The success of my publications was made possible through invaluable collaborations with researchers from various institutes at KIT and other universities. I am particularly grateful to the NANOlab Center of Excellence at the University of Antwerp, Belgium, and extend my special thanks to Dr. Noopur Jain, Dr. Annick De Backer, Prof. Sara Bals, and Prof. Sandra Van Aert for their support and contributions. Additionally, I deeply appreciate the collaboration with the Functional Imaging in Surgical Oncology group at the National Center for Tumor Diseases, and I sincerely thank Dr. Bernardo A. Arús, Dr. Andriy Chmyrov, and Prof. Dr. Oliver Bruns for their valuable input.

I would also like to express my sincere gratitude to Dr. Miguel Méndez and Dr. Ulises Salazar, who guided me during my bachelor's and master's theses, respectively. Their mentorship during those formative years laid the foundation for my scientific career and greatly influenced my development as a researcher.

Beyond the academic sphere, I am profoundly grateful to my friends—Sasha, Tim, Laura, Eduard, Jan, Melina, Dom, Dilara, Saskia, Jonas, Michi, Pascal, Alex, Kristi, Dina, Gabi, and both Flo's—whose friendship and unwavering support have carried me through the most challenging moments and with whom I have celebrated some of the most memorable milestones of my life.

Lastly, none of this would have been possible without the unwavering support of my family. I would also like to thank my sister for her constant support and belief in me, always reminding me of my strengths and pushing me forward. I am especially grateful to my

mother, the strongest person I know and an irreplaceable pillar in my life, whose love, sacrifices, and encouragement have been the foundation of my journey.

List of Publications

During the course of my doctoral research, I have authored three first-author publications. Two of these have been published in peer-reviewed scientific journals, while the third is currently under review. In addition, I contributed as a co-author to two other publications that have already been published.

First-author publications

Arteaga Cardona, F., Jain, N., Popescu, R., Busko, D., Madirov, E., Arús, B. A., Gerthsen, D., De Backer, A., Bals, S., Bruns, O. T., Chmyrov, A., Van Aert, S., Richards, B. S., & Hudry, D. (2023). Preventing cation intermixing enables 50% quantum yield in sub-15 nm short-wave infrared-emitting rare-earth based core–shell nanocrystals. Nature Communications, 14(1), 4462. https://doi.org/10.1038/s41467-023-40031-4

Arteaga Cardona, F., Madirov, E., Popescu, R., Wang, D., Busko, D., Ectors, D., Kübel, C., Eggeler, Y. M., Arús, B. A., Chmyrov, A., Bruns, O. T., Richards, B. S., & Hudry, D. (2024). Dramatic Impact of Materials Combinations on the Chemical Organization of Core–shell Nanocrystals: Boosting the Tm^{3+} Emission above 1600 nm. ACS Nano. https://doi.org/10.1021/acsnano.4c07932

Arteaga Cardona, F., Madirov, E., Mirmajidi, H., Popescu, R., Busko, D., Eggeler, Y. M., Hemmer, E., Richards, B. S., & Hudry, D. Mapping the Influence of Intrinsic and Extrinsic Synthesis Parameters on Cation Intermixing in Tm^{3+}-doped Fluoride Core–Shell Nanocrystals Emitting in the Third Biological Window. *Submitted to Small Journal*.

Co-author publications

Chauhan, A., Kataria, S., Busko, D., **Cardona, F. A.**, Turshatov, A., & Richards, B. S. (2021). Elucidating the role of metal-ion co-doping towards boosting upconversion

luminescence in gadolinium vanadate. Journal of Materials Chemistry C, 9(46), 16709–16720. https://doi.org/10.1039/D1TC03205D

Madirov, E., Busko, D., **Cardona, F. A.**, Hudry, D., Kuznetsov, S. V, Konyushkin, V. A., Nakladov, A. N., Alexandrov, A. A., Howard, I. A., Richards, B. S., & Turshatov, A. (2023). Comparison of Quantum Yield of Upconversion Nanocrystals Determined by Absolute and Relative Methods. Advanced Photonics Research, 4(2), 2200187. https://doi.org/https://doi.org/10.1002/adpr.202200187

International conferences

Fernando Arteaga-Cardona, Radian Popescu, Eduard Madirov, Andrey Turshatov, Dmitry Busko, Ian A. Howard, Bryce S. Richards, Damien Hudry. High quantum yield SWIR heterogeneous core–shell lanthanide-based nanocrystals for biomedical imaging applications. Spectral sHaping For biomedical and energy applicaTions (SHIFT, oral presentation), 10-14th October 2022, Tenerife, Spain.

Fernando Arteaga-Cardona, Eduard Madirov, Dmitry Busko, Radian Popescu, Noopur Jain, Annick De Backer, Sara Bals, Sandra Van Aert, Bernardo A. Arús, Andriy Chmyrov, Oliver T. Bruns, Bryce S. Richards, and Damien Hudry. Imaging into the SWIR region with different lanthanides based nanocrystals. UPCON conference (Poster), 7 – 11th April 2024, Montréal, Canada.

Summer Schools and Symposia

MaTeLiS Materials Day, 16th October, 2024. “Optimizing Light Conversion Efficiency Through Advanced Material Combinations."

KSOP Summer School, 26 – 27th September, 2024, Bad Herrenalb. “Optimizing Light Conversion Efficiency Through Advanced Material Combinations.”

Horizons Symposium: Electronic and Energy Materials, 25 - 26th September 2023, Berlin. “Core–shell phase segregation in Nanocrystals: A pathway for unlocking new internal photoluminescent quantum yield efficiencies.”

9th Karlsruhe Days of Optics and Photonics, 16 – 17th November 2023, Karlsruhe. “Controlled synthesis of photoluminescent fluoride nanoparticles.”

8th Karlsruhe Days of Optics and Photonics, 10 – 12th November 2021, online “Understanding cation distribution and alloying in fluoride nanocrystals.”

List of Abbreviations

B.P.	Boiling Point
$Ca(TFA)_2$	Calcium Trifluoroacetate
DS	Downshifting
EDXS	Energy Dispersive X-ray Spectroscopy
HAADF-STEM	High-Angle Annular Dark Field Scanning Transmission Electron Microscopy
ICG	Indocyanine Green
λem	Emission Wavelength
λexc	Excitation Wavelength
LiTFA	Lithium Trifluoroacetate
Ln	Lanthanide
M	Molarity (mol/L)
NaTFA	Sodium Trifluoroacetate
NCs	Nanocrystals
NIR	Near-Infrared
OA	Oleic acid
OAm	Oleylamine
ODE	1-Octadecene
PLQY	Photoluminescence Quantum Yield
PXRD	Powder X-Ray Diffraction
QDs	Quantum Dots
RE	Rare-earth
$RE(OAc)_3$	Rare-Earth Acetate
$RE(TFA)_3$	Rare-Earth Trifluoroacetate
RT	Room Temperature
STEM	Scanning Transmission Electron Microscopy
SWIR	Short-Wave Infrared
UC	Upconversion
UV	Ultraviolet
VIS	Visible
WPPM	Whole Powder Pattern Modelling

Contents

Zusammenfassung ii
Abstract v
Acknowledgements viii
List of Publications xi
First-author publications xi
Co-author publications xi
International conferences xii
Summer Schools and Symposia xii
List of Abbreviations xiv
Contents xv
1.Introduction 1
1.1 Optical Imaging and the Short-Wave Infrared (SWIR) Window 1
1.2 The $NaREF_4$ Host Material and the Core–Shell Strategy 4
1.3 Ion Migration: The Critical Interface Challenge 7
2. Theoretical Background 13
2.1 Rare-Earth Ions: Electronic Structure and Optical Properties 13
2.1.1 Electronic Configuration and the Shielded 4f Orbitals 13
2.1.2 Laporte Selection Rules and the Nature of f–f Transitions 14
2.1.3 Relevant Energy Levels: Er^{3+}, Tm^{3+}, Yb^{3+}, and Ce^{3+} 15
2.1.4 Downshifting vs. Upconversion 16
2.2 Fluoride Host Materials 17
2.2.1 Why Fluorides? 17
2.2.2 Fluoride Based Host Materials: α-$NaREF_4$ (Cubic Phase), β-$NaREF_4$ (Hexagonal Phase) and $LiREF_4$ 18
2.3 Synthesis of RE-Based NCs 20
2.3.1 Colloidal Synthesis Strategies 20
2.3.2 Role of Ligands: Oleic Acid and Oleylamine 21
2.3.3 Variations of the Thermolysis Synthesis: Heating Up and Hot Injection 22
2.3.4 Core–Shell Synthesis: Seed-Mediated Growth 22
2.4 Photoluminescence Quantum Yield: Definition, Measurement, and Limiting Factors 23
2.4.1 Definition of PLQY 23
2.4.2 Absolute PLQY Measurement: Integrating Sphere 23

2.4.3 Limiting Factors for the PLQY Determination 24
2.4.4 Shell Passivation: The Principle of Surface Protection for Improving the PLQY 25
2.4.5 State-of-the-Art PLQY Values for SWIR-Emitting NCs 25
2.5 SWIR Fluorescence Imaging 27
2.5.1 Advantages of SWIR Imaging over Conventional Fluorescence Imaging 27
2.5.2 Current SWIR Fluorophores 28
2.5.3 Advances in SWIR Imaging Systems 30
3. Materials and Methods 33
3.1 Synthesis of Precursors 33
3.1.1 Synthesis of RE Trifluoroacetates [$RE(OOCCF_3)_3$, RE = Y, Er, Tm, Yb] 33
3.1.2 Synthesis of Ca Trifluoroacetate [$Ca(OOCCF_3)_2$] 34
3.1.3 Synthesis of Gd Acetate [$Gd(OOCCH_3)_3$] 35
3.1.4 Synthesis of Tm Acetate [$Tm(OOCCH_3)_3$] 35
3.2 Synthesis of Core NCs 35
3.2.1 Synthesis of α-$NaREF_4$ Core NCs 36
3.2.2 Synthesis of β-$NaGdTmF_4$ Core NCs 36
3.2.3 Synthesis of $LiTmF_4$ Core NCs 37
3.3 Synthesis of Shell Layer Domains 37
3.3.1 Synthesis of α-$NaREF_4/NaYF_4$ NCs 37
3.3.2 Synthesis of α-$NaREF_4/CaF_2$ NCs 38
3.3.3 Synthesis of α-$NaREF_4/LiYF_4$ NCs 38
3.3.4 Synthesis of β-$NaGdTmF_4/NaYF_4$ NCs 39
3.3.5 Synthesis of β-$NaGdTmF_4/CaF_2$ NCs 39
3.3.6 Synthesis of $LiTmF_4/NaYF_4$ NCs 39
3.3.7 Synthesis of $LiTmF_4/CaF_2$ NCs 39
3.3.8 Synthesis of $LiTmF_4/LiYF_4$ NCs 40
3.4 Water Transfer Procedures 40
3.4.1 Micelles 40
3.4.2 Polyacrylic Acid 40
3.5 Structural Characterizations 41
3.5.1 Powder X-ray Diffraction Pattern Acquisition (PXRD) 41
3.5.2 High-Angle Annular Dark-Field Scanning Transmission Electron Microscopy Imaging (HAADF-STEM) 42

3.5.3 High-Resolution Transmission Electron Microscopy Imaging (HRTEM) 42
3.6 Atomic Organization: Energy-Dispersive X-ray Spectroscopy (EDXS) 42
3.6.1 Chemical Maps 42
3.6.2 Line Scans 43
3.6.3 Integrated Differential Phase Contrast (iDPC)-STEM Imaging 43
3.7 Photoluminescence Characterization 44
3.7.1 Light Absorption Measurements 44
3.7.2 Downshifting PLQY Measurements 44
3.7.3 Macroscopic SWIR Imaging System 45
3.7.4 Brightness Signal Measurements 45
3.7.5 In vivo SWIR Fluorescence Imaging 45
3.7.6 SWIR imaging of NCs Fluorescence in Intralipid Phantoms 46
4. Cation Intermixing in Homogeneous and Heterogeneous RE Core–Shell NCs for SWIR Emission 48
4.1 Motivation 49
4.2 Overview 50
4.3 Results 51
4.3.1 Starting α-$NaYF_4$:Yb,Er Core NCs Characterizations 51
4.3.2 Growth of Homogeneous and Heterogeneous Shells Domains 53
4.3.3 Elemental Distribution after Shell Growth 55
4.3.4 Atomic-Scale Organization of the Core–Shell NCs 56
4.3.5 SWIR Emission Properties 58
4.4 Discussion 60
4.5 Summary 63
5.Influence of Core–Shell Material Combinations for Enhancing Tm^{3+} Emission Beyond 1600 nm 64
5.1 Motivation 64
5.2 Overview 66
5.3 Results 67
5.4 α-$NaTmF_4$ Core Based Material Combinations 69
5.4.1 Starting α-$NaTmF_4$ Core NCs Characterizations 69
5.4.2 Homogeneous and Heterogeneous Material Shell Combinations Derived from α-$NaTmF_4$ 70
5.4.3 Homogeneous and Heterogeneous Material Shell Combinations Derived from α-$NaTmF_4$: Chemical organization 73
5.5 $LiTmF_4$ Core Based Material Combinations 76

5.5.1 Starting $LiTmF_4$ Core NCs Characterizations 76
5.5.2 Homogeneous and Heterogeneous Material Shell Combinations Derived from $LiTmF_4$ 77
5.5.3 Homogeneous and Heterogeneous Material Shell Combinations Derived from $LiTmF_4$: Chemical organization 80
5.6 X-ray Diffraction Analysis of Core–Shell Phase Composition 83
5.7 SWIR Emission of Tm^{3+} Based Material Combinations 89
5.8 Discussion 92
5.9 Summary 95
6. Effect of Intrinsic *vs.* Extrinsic Parameters on Cation Intermixing in RE Core–Shell Fluoride NCs 97
6.1 Motivation 98
6.2 Overview 98
6.3 Results 100
6.3.1 Structural Characterizations. 100
6.3.2 The Influence of Varying Shell Thicknesses on Tm^{3+} Ion Distribution in α-$NaTmF_4$-based Core–shell NCs 102
6.3.3 The Effect of Varying Shell Thicknesses on Tm^{3+} Ion Distribution in β-$NaGdTmF_4$-based Core–shell NCs 105
6.3.4 Different Shell Thicknesses Effect on Tm^{3+} Ion Distribution on $LiTmF_4$-based Core–Shell NCs111
6.3.5 Diffraction Data Analysis from α-$NaTmF_4/CaF_2$ and β-$NaGdTmF_4/CaF_2$ 113
6.3.6 Effect of Shell Growth Temperature on Intermixing 118
6.3.7 Optical Characterization 123
6.4 Summary 125
7. Comparison of SWIR Fluorescence Performance: Nanocrystal Emitters *vs*. Indocyanine Green 127
7.1 Motivation 128
7.2 Overview 128
7.3 Results 129
7.3.1 Intralipid Phantom Test 129
7.3.2 Brightness Test 131
7.3.3 Fluorescent SWIR Imaging 133
7.4 Discussion 134
7.5 Summary 135
8. Conclusions and Outlook 137
8.1 Conclusions 137
8.2 Outlook 139

References.....140

1. Introduction

1.1 Optical Imaging and the Short-Wave Infrared (SWIR) Window

The ability to visualize biological processes in living organisms with high spatial and temporal resolution represents one of the most powerful capabilities in modern biomedical science.[1,2] Non-invasive optical imaging, in particular, has long been valued for its capacity to probe the structure and function of tissues and cells without the ionizing radiation associated with X-ray or nuclear medicine techniques.[3,4] Still, conventional optical imaging performed in the visible (VIS, 400–700 nm) and near-infrared-I (NIR-I, 700–900 nm) spectral windows is fundamentally constrained by the optical properties of biological tissue.[5] Photons traversing tissue at these wavelengths are strongly scattered by cellular structures and absorbed by endogenous chromophores such as hemoglobin and water, resulting in blurred images, shallow penetration depths (typically not exceeding a few millimeters), and elevated background signals arising from tissue autofluorescence.[6] These limitations reduce imaging contrast, restrict the depth at which meaningful signals can be resolved, and ultimately impede the translation of optical imaging into clinical practice. Figure 1.1 shows a scheme of the incident photons getting scattered by the tissue layers.

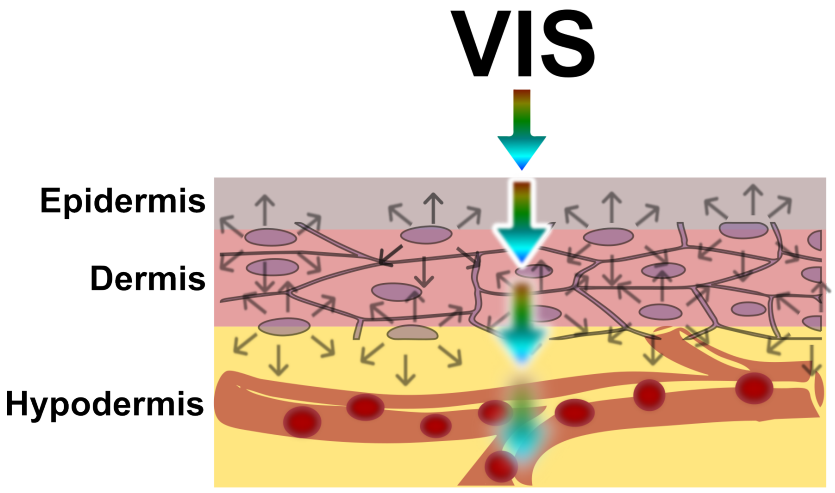


Figure 1.1 *Schematic visualization of visible light propagation in biological tissue. Visible light undergoes stronger scattering and attenuation in superficial tissue layers, which limits imaging depth and reduces spatial contrast.*

The short-wave infrared (SWIR) spectral window, encompassing wavelengths from approximately 1000 to 2000 nm, offers a compelling route to overcome these barriers.[7] In this spectral region, tissue scattering is substantially reduced relative to the visible (400 - 700 nm) and NIR-I (700 - 1000 nm) windows, following an inverse power-law dependence on wavelength (λ^{-a}).[8] Simultaneously, tissue autofluorescence is markedly suppressed, since the endogenous fluorophores responsible for background signal in conventional fluorescence imaging do not emit appreciably in the SWIR range. The combined effect is a dramatic improvement in signal-to-noise ratio and spatial resolution, enabling imaging at depths and with clarity that are unattainable in the VIS or NIR-I regimes.[9] These properties make SWIR fluorescence imaging an attractive modality for applications that demand both resolution and tissue penetration, including the tracking of metabolic processes of cells,[10] the delineation of tumor margins for preoperative planning,[11] and real-time image-guided surgery.[12] As the far end of the SWIR window is approached, scattering decreases further, making the region above 1500 nm particularly attractive for deep-tissue imaging applications.[13] A scheme representing the reduced scattering from changing the incident light into the SWIR region can be seen in Figure 1.2.

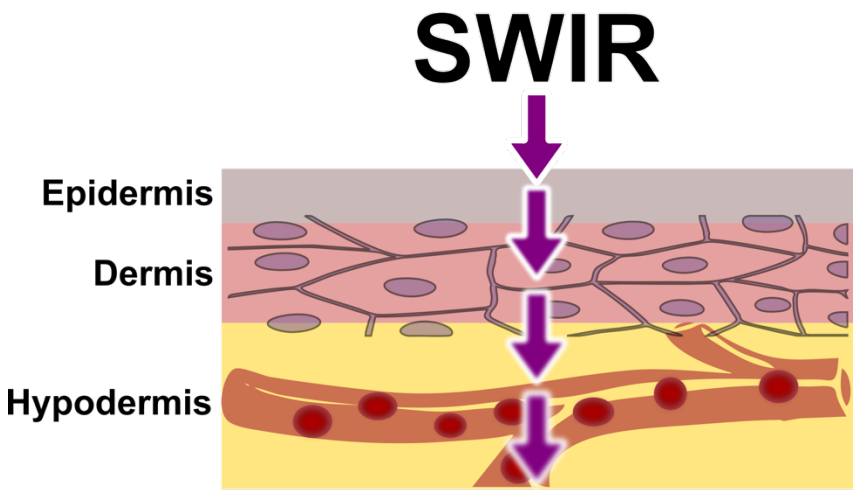


Figure 1.2 *Schematic visualization of SWIR light propagation in biological tissue. SWIR light exhibits reduced scattering and can propagate deeper into tissue, enabling improved contrast for subsurface imaging applications.*

The growing recognition of the SWIR window's imaging potential has driven intense interest in the development of luminescent materials capable of efficient emission in this spectral range. An effective SWIR fluorescent probe must satisfy demanding and often competing requirements: 1) it must absorb light efficiently at a convenient excitation wavelength, 2) convert that absorbed energy to SWIR photons with high efficiency, 3) remain photostable over extended imaging periods, and 4) be sufficiently biocompatible for *in vivo* use.[14] Meeting all these criteria simultaneously has proven to be a substantial materials science challenge, and no single class of SWIR emitter has yet emerged as definitively superior across all dimensions.

Several classes of nanocrystals (NCs) have been explored as SWIR fluorescent probes. Small organic molecules, including some cyanine-based dyes[15] with extended conjugation, can be engineered to emit in the lower portion of the SWIR range, but they generally suffer from rapid photobleaching, modest Stokes shifts, and broad emission spectra that limit their utility in multiplexed imaging applications. Single-walled carbon nanotubes (SWCNTs) offer SWIR emission arising from their chirality-dependent electronic band gaps; however, they suffer from extremely low efficiency of wavelength conversion (< 0.5%),[16] and concerns regarding toxicity remain unresolved.[17] Semiconductor quantum dots (QDs) based on lead sulphide (PbS), indium arsenide (InAs), or related compositions can emit in the SWIR region[18] and have been applied to *in vivo* imaging, but many of the most efficient SWIR-emitting QD compositions contain heavy metals whose toxicity is well-known and documented, representing a significant obstacle to clinical translation.[19] More about the actual probes will be discussed in section 2.5.2.

Rare-earth (RE) ion-doped inorganic NCs have emerged as a distinct and increasingly prominent class of SWIR emitters, offering several intrinsic advantages that partially compensate for their weaker absorption relative to other platforms.[20] The optical properties of RE ions arise from electronic transitions within the partially shielded 4*f* electron shell, which is largely screened from the crystal field environment by the outer 5*s* and 5*p* electrons.[21] RE-doped NCs exhibit large Stokes shifts, which minimize self-absorption and facilitate separation of excitation and emission signals, and they display

exceptionally long luminescence lifetimes (often in the microsecond range) which enable time-gated detection strategies to further reduce background from short-lived autofluorescence.[22] These materials are resistant to photobleaching under continuous illumination, an important advantage over organic fluorophores in long-duration imaging experiments, which is a vitally important aspect for the use in tracking metabolic routes of cells, or surgeries.[23] The cytotoxicity profile of fluoride-based RE NCs has been assessed as favorable relative to heavy-metal-containing QDs and SWCNTs, supporting their potential for biological application.[24]

Despite these attractive properties, two fundamental limitations constrain the practical utility of RE-based NCs as SWIR imaging probes as of now. The first is the inherently weak absorption cross-section of RE ions, which arises because the 4*f*–4*f* transitions responsible for their optical activity are parity-forbidden under Laporte's selection rule.[25] The parity-forbidden transition results in absorption coefficients that are orders of magnitude lower than those of organic dyes or quantum dots, requiring higher concentrations or excitation power densities to generate detectable emission. The second limitation is the relatively modest photoluminescence quantum yield (PLQY) exhibited by many RE-based NC. PLQY quantifies the fraction of absorbed photons that are converted to emitted photons rather than dissipated as heat through non-radiative relaxation pathways. Maximizing the PLQY is therefore essential to achieving bright, detectable SWIR emission at biologically safe excitation intensities. The weak absorption cross-section is an intrinsic property of RE ions that arises from parity-forbidden *f*–*f* transitions and is difficult to overcome without sensitization strategies such as co-doping with Yb^{3+}.[26]

1.2 The $NaREF_4$ Host Material and the Core–Shell Strategy

Among the inorganic host materials investigated for RE-based luminescence, sodium rare-earth fluorides ($NaREF_4$) have established themselves as the dominant host, principally because of their exceptionally low phonon energy of approximately 350 cm^{-1}.[21,27] In the context of RE^{3+} photoluminescence, phonon energy is a critical parameter: non-radiative relaxation of excited RE^{3+} ions proceeds through multiphonon processes, and the rate of this quenching scales strongly with the energy of the host lattice phonons. A low-phonon-energy environment minimizes the probability of non-

radiative decay and thereby increases the fraction of excitation energy that is converted to emission.[28] The sodium rare-earth fluoride ($NaREF_4$) family additionally offers considerable chemical versatility, as a single, or a mixture, of RE^{3+} ions with different electronic configurations can be incorporated at the RE site, enabling systematic tuning of optical properties across a broad spectral range from the ultraviolet to the SWIR. The most widely used optically active ions for SWIR applications include Er^{3+}, which exhibits emission at approximately 1550 nm via the $^4I_{13/2} \rightarrow {}^4I_{15/2}$ transition,[29] and Tm^{3+}, which displays emission above 1600 nm via the $^3F_4 \rightarrow {}^3H_6$ transition.[30] These transitions are shown in Figure 1.3.

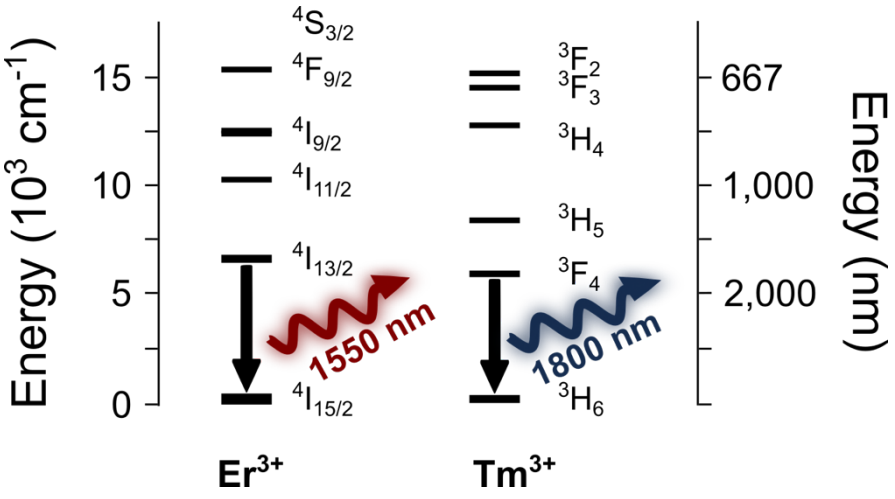


Figure 1.3 *Schematic visualization of the energy levels and radiative transitions of Er^{3+} and Tm^{3+} in the SWIR region.*

$NaREF_4$ can adopt two distinct crystallographic forms: the cubic phase (α, space group $Fm\bar{3}m$) and the hexagonal phase (β, space group $P\bar{6}$).[31] In the α-phase, a single cationic site is shared statistically between Na^+ and RE^{3+} ions. The β-phase in contrast, contains four distinct crystallographic cationic sites; two for Na^+ (Wyckoff positions 1a and 1e) and two for RE^{3+} (positions 1b and 1d), thus this crystallographic phase exhibits a lower crystal symmetry. This lower symmetry is understood to relax the parity-forbidden character of 4*f*–4*f* transitions by mixing states of opposite parity into the RE ion's electronic configuration, thereby improving luminescent efficiency and PLQY.[25] For this reason, the β-phase has historically been regarded as the preferred host for RE-based

upconversion[32] and downshifting[33] applications. The α-phase, while initially considered less efficient, has attracted renewed interest due to heterogeneous core–shell structures (α-$NaREF_4$/CaF_2), where the combination of materials influences the formation and stability of the core–shell interface in ways that are only beginning to be understood.[34] At the moment where this thesis is being written, there is no report of an heterogeneous core–shell structures for the β-phase with an abrupt interface.

When RE-doped NCs are reduced to the nanoscale, a new and substantial challenge emerges that has no counterpart in bulk luminescent materials: surface quenching.[35] NCs possess extremely high surface-to-volume ratios, meaning that a significant fraction of the total RE^{3+} dopant ions reside at or near the particle surface, where they are exposed to quenching species from the surrounding environment.[36] These quenchers include surface defects, dangling bonds, adsorbed solvent molecules (particularly those containing high-frequency O–H and N–H oscillators),[37] and organic ligands used to stabilize the NCs in colloidal suspension (Figure 1.4, right). The high-frequency vibrational modes of these species overlap with the energy gap of the excited RE^{3+} ion, enabling non-radiative relaxation that competes directly with radiative emission and drastically reduces the PLQY. For SWIR emission, where the excited-state energy gaps are comparatively small, this problem is particularly acute, as fewer phonons are required to bridge the gap.

The core–shell architecture has emerged as the most effective and widely adopted strategy for mitigating surface quenching in RE-based NCs.[38,39] In this approach, an optically inert shell is grown to the luminescent core NC, which physically separates the RE^{3+} dopant ions from the quenching species at the outer particle surface and creates a protective barrier that prevents the interaction between surface defects and solvent molecules into the luminescent core NC (Figure 1.4 left).[40] The shell material must be optically inert (i.e., non-absorbing and non-emitting at the wavelengths of interest) so that it does not interfere with excitation or emission processes, and it must be compatible with the core material in terms of crystallographic structure and lattice parameters to enable epitaxial growth without the introduction of interfacial strain or defects.[41] For typical $NaREF_4$ core NCs, the most common shell choice has historically been another $NaREF_4$

material in which the RE site of the shell is occupied by optically inert ions such as Y^{3+} (empty 4*f* shell), Gd^{3+} (half-filled 4*f* shell), or Lu^{3+} (fully filled 4*f* shell).[42] Since these shell materials share similar chemical composition (only exchanging the RE^{3+}) and same crystal structure of the core, they are designated homogeneous shells in the present work.

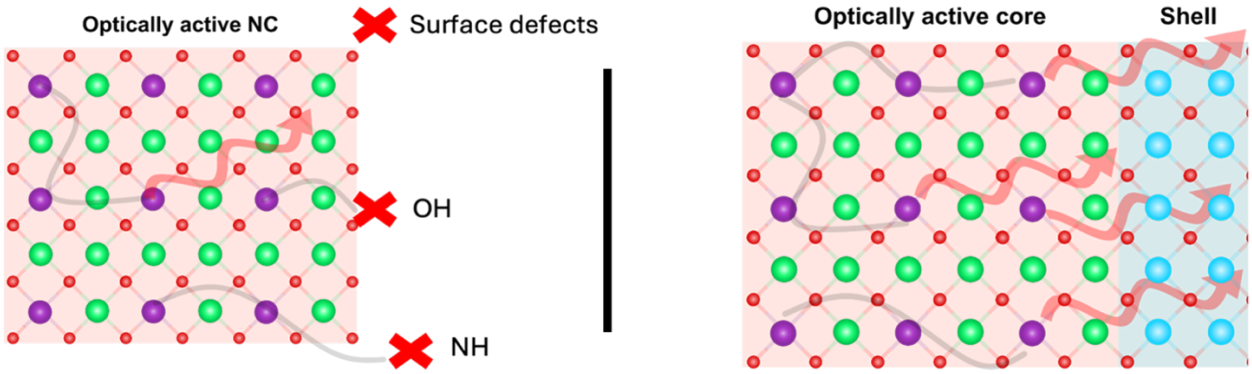


Figure 1.4 *Schematic representation of surface quenching in optically active RE-doped NCs and its mitigation by shell growth. In unshelled RE-doped NCs, the high surface-to-volume ratio places a significant fraction of optically active RE^{3+} ions close to the particle surface, where the absorbed energy can migrate and get transferred to quenchers (surface defects, adsorbed molecules, and high-frequency vibrational groups such as O–H and N–H). Growth of an inert shell spatially separates the optically active core from surface-related quenchers, reducing direct interaction between the emissive RE^{3+} ions and the surrounding environment.*

1.3 Ion Migration: The Critical Interface Challenge

Despite the conceptual simplicity and practical effectiveness of the homogeneous core-shell strategy, experimental evidence accumulated over the past decade has revealed a fundamental complication that undermines its protective function: the phenomenon of ion migration from the core domain to the shell domain.[43–46] It is speculated that because the core and shell materials in a homogeneous $NaREF_4/NaREF_4$ system share the same crystal structure and have closely matched lattice parameters, there is no energetic barrier to impede the migration of ions across this interface; the system is chemically continuous, and ions can be found both the core and shell domains.[47]

The consequences of ion migration for optical performance are severe. When optically active RE^{3+} ions originally confined to the core migrate into the shell domain, several deleterious effects arise. Most critically, migrated ions may approach the outer surface of

the NC, where they become susceptible to the very quenching mechanisms that the shell was designed to prevent; in extreme cases, optically active ions may migrate all the way to the surface and be fully exposed to solvent and ligand quenchers. Additionally, ion migration alters the spatial distribution of the luminescent active RE^{3+} ions within the NC.[45] This change in the interionic distances modify the energy transfer processes and potentially disrupt the energy migration pathways that are essential for efficient emission in the SWIR region. In some material combinations and synthesis parameters (mostly with the homogeneous $NaREF_4$ shell), ion migration is so extreme that the chemical distinction between the core and shell domains is entirely erased, yielding a uniform alloy in which the intended structural benefits of the core–shell architecture is completely absent.[48]

It is possible to identify three distinct interface types between the core and the shell domains: the first type is characterized by a well-defined and abrupt boundary between the core and shell domains, with no detectable redistribution of optically active ions; this configuration maximally preserves the protective function of the shell and is associated with the highest PLQY values. The second type of interface exhibits a degree of intermixing in the boundary region forming a transition area, but the core and shell domains are still identifiable. The third type represent the most extreme case, in which ion migration has proceeded to the point of forming a complete alloy with no distinguishable core or shell; these structures effectively lack the architectural basis for efficient luminescence enhancement (Figure 1.5). Understanding the factors that determine which interface type is formed during synthesis is therefore central to the rational design of high-performance RE-based SWIR NCs.[48–50]

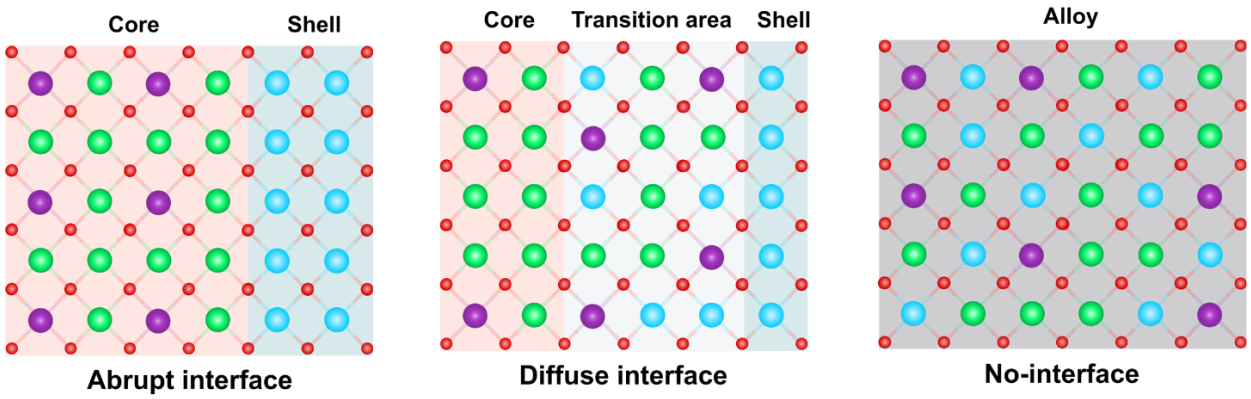


Figure 1.5 Schematic representation of three possible core–shell interface types (abrupt, intermixed and alloyed) in RE-based NCs. These different interface types determine the extent to which the shell can protect the optically active core and are therefore central to the design of efficient RE-based SWIR-emitting NCs.

The realization that ion migration in homogeneous core–shell NCs fundamentally limits achievable PLQY values has motivated the exploration of heterogeneous core–shell structures, in which the shell material differs substantially from the core in chemical composition, crystal structure, or both.[51] The reasoning behind this approach is that a sufficiently distinct shell material may suppress ion migration by introducing a chemical or structural discontinuity at the core–shell interface that raises the energetic barrier for ion redistribution.[52] If the core and shell cations are sufficiently dissimilar in terms of ionic radius, charge, or preferred crystallographic coordination environment, the driving force for cation intermixing may be greatly diminished, promoting the formation of type-I structures with negligible intermixing and abrupt core–shell interfaces.

Among the heterogeneous shell materials explored, calcium fluoride (CaF_2) has emerged as particularly promising when combined with α-$NaREF_4$ cores.[53] CaF_2 adopts a cubic fluorite structure with a lattice parameter that differs from that of α-$NaREF_4$ by less than 1%, enabling epitaxial shell growth without introducing significant lattice strain.[54] Crucially, the Ca^{2+} cations of the shell and the Na^{+}/RE^{3+} cations of the core are chemically distinct, and their different valences are speculated to impede the ion migration that characterizes homogeneous systems.[55]

CaF_2 as the shell domain was the first reported heterogeneous combination with α-$NaYF_4$:Yb,Er, which improved upconversion emission compared to its homogeneous

counterpart.[33] Subsequently, several groups have reported heterogeneous material combinations with CaF_2, primarily for its biocompatibility.[55–58] Experimental studies have confirmed that α-$NaREF_4/CaF_2$ core–shell structures exhibit predominantly abrupt interfaces between the core and the shell and negligible redistribution of optically active RE^{3+} ions.[59,60] As demonstrated in Chapter 4, this approach enables PLQYs approaching 50% in sub-15 nm NCs.

Although the heterogeneous combination of α-$NaREF_4/CaF_2$ NCs has demonstrated the possibility of forming an abrupt core–shell interfaces across a wide range of conditions,[55,60,61] achieving a similar result at the interface using the homogeneous combination of α–$NaREF_4/NaREF_4$ or β-$NaREF_4/NaREF_4$ NCs is obtained in extremely unique and specific cases. By contrast, the chemically related homogeneous $LiREF_4/LiREF_4$ NCs can form interfaces that more closely resemble those observed in heterogeneous α-$NaREF_4/CaF_2$ structures than in homogeneous $NaREF_4/NaREF_4$ NCs.[30,62] This unexpected behavior remains poorly understood and highlights the need for a more systematic investigation of the parameters governing ion migration during shell growth.

This work advances the understanding of the ion migration parameters to be considered for core–shell NCs and how the control of the ion migration is the key to the development of highly efficient luminescent NCs. The full optical potential of RE fluoride NCs remains unrealized, and substantial improvements in PLQY are anticipated through better understanding of interfacial dynamics. The results presented here aim to challenge the assumption that core NCs remain pristine after the shell growth. This assumption remains widespread in the field for many researchers, and it presents major obstacles in the further development of new materials with higher efficiencies. Finally, this work aims to explore the potential of various material combinations for the synthesis of core–shell heterostructures. While research in this area remains limited, investigating additional combinations may reveal design principles that further extend the achievable emission efficiency and spectral range.

The chapters of this thesis focus on the examination of how the materials combination affect the ion migration when producing core–shell NCs and how it influences

downshifting optical performance of RE fluoride core–shell NCs emitting in the SWIR region.

Chapter 1 introduces the idea of improving the bioimaging using the SWIR part of the spectrum while also mentioning why RE-based ($NaREF_4$) NCs are great candidates to be used for SWIR fluorescence bioimaging. Additionally, it also points out the limiting factors for achieving great photoluminescence efficiency, like low absorption cross-section due to parity forbidden transitions and ion migration from the core to the shell domain when growing an optically inert shell onto fluorescent core NCs. The chapter then introduces the distinction between homogeneous and heterogeneous shells and defines ion migration as the central problem of the thesis.

Chapter 2 provides the theoretical background required to understand the materials, mechanisms, and characterization strategies discussed in this thesis. It first introduces the electronic structure and optical properties of RE ions, with particular emphasis on the shielded 4*f* orbitals, the nature of *f*–*f* transitions, and the roles of Er^{3+}, Tm^{3+}, Yb^{3+}, and Ce^{3+} in SWIR-emitting systems. The chapter then discusses fluoride host materials, including α-$NaREF_4$, β-$NaREF_4$, and $LiREF_4$, highlighting how crystal structure, phonon energy, and chemical composition influence luminescence efficiency and ion migration. This is followed by an overview of colloidal synthesis strategies, core–shell growth, shell passivation, and the principles and limitations of PLQY measurements. Finally, the chapter introduces SWIR fluorescence imaging, its advantages over conventional fluorescence imaging, the current state of SWIR fluorophores, and the motivation for developing efficient RE-based NCs for biomedical imaging applications.

Chapter 3 describes the synthesis of precursors, core NCs, and core–shell structures used throughout the thesis. It also details water-transfer methods, structural, chemical, and optical characterization techniques that are utilized throughout the rest of the chapters.

Chapter 4 provides evidence that homogeneous α-$NaYF_4$ shells cause extensive ion migration in α-$NaYF_4$:Yb,Er core–shell NCs, effectively destroying the intended core-shell structure. In contrast, heterogeneous CaF_2 shells preserve a well-defined core–shell

architecture with a >3 nm RE-pure shell. This structural difference leads to major optical improvements, reaching 30% SWIR PLQY and 50% after Ce^{3+} co-doping.

Chapter 5 extends the study to Tm^{3+}-based NCs emitting beyond 1600 nm, and the ion migration dependence to the material combination of the core and shell. In this chapter, two luminescent core NCs (α-$NaTmF_4$ and $LiTmF_4$) were each paired with $NaYF_4$, CaF_2, and $LiYF_4$ shells. The results show that shell performance depends strongly on material compatibility: α-$NaTmF_4$/CaF_2 and $LiTmF_4$/$LiYF_4$ provides the best Tm^{3+} confinement. It also reports a record breaking PLQY value for emission in the far-end region of the SWIR range with an approximately PLQY value of 39%.

Chapter 6 systematically investigates how intrinsic parameters, such as composition and crystal structure, and extrinsic parameters, such as shell thickness, temperature, and synthesis route, influence ion migration. The results show that the appropriate selection of the chemical composition of the core and the shell domains have a stronger influence in the ion migration than the extrinsic parameters.

Chapter 7 compares the best-performing NCs with indocyanine green (ICG), the clinical near-infrared benchmark. Under matched SWIR imaging conditions and tissue-phantom experiments, the RE NCs show good brightness, better signal retention at penetration depths than ICG. Nevertheless, ICG is shown to be an overall brighter probe for SWIR imaging.

Chapter 8 concludes that ion migration is widespread in RE fluoride core–shell NCs and is an important factor controlling PLQY. Suppressing migration through suitable material combinations and synthesis conditions enables highly efficient SWIR emitters. Future work should explore additional shell materials, β-phase systems, multi-shell architectures, lower-temperature routes, and extension to other luminescent probes.

2. Theoretical Background

2.1 Rare-Earth Ions: Electronic Structure and Optical Properties

2.1.1 Electronic Configuration and the Shielded 4f Orbitals

The RE elements comprise the fifteen lanthanide (Ln) elements, from lanthanum (La, Z = 57) to lutetium (Lu, Z = 71), plus scandium (Sc, Z = 21) and yttrium (Y, Z = 39). The Ln subgroup of elements is all characterized by the progressive filling of the 4*f* electron shell. When incorporated into ionic host materials, most of the lanthanides adopt the trivalent oxidation state (Ln^{3+}), with the general electronic configuration [Xe]$4f^{n}$, where n ranges from 0 (La^{3+}) to 14 (Lu^{3+}). The optical behavior of Ln^{3+} ions arises exclusively from intraconfigurational transitions within this 4*f* shell.[63] Figure 2.1 shows the elements on the periodic table that are part of the RE group.

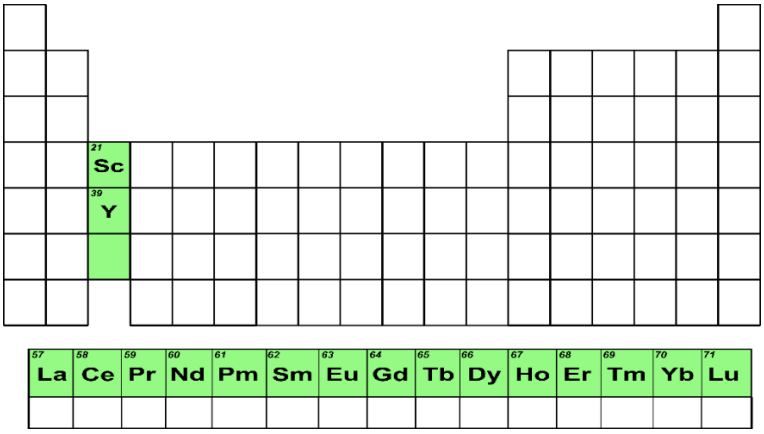


Figure 2.1 *Schematic representation of the periodic table highlighting the position and chemical symbols of the rare-earth (RE^{3+}) elements.*

A defining characteristic of the 4*f* electrons is their shielding by the filled $5s^2$ and $5p^6$ outer orbitals. Although the 4*f* orbitals are energetically inner orbitals, the distribution of the 5*s* and 5*p* wavefunctions extends further from the nucleus than that of 4*f*, effectively shielding the 4*f* electrons from the chemical environment.[63] This shielding has two fundamental consequences. First, the crystal-field splitting of the 4*f* energy levels, is very

small compared to the intrinsic energy of the *f–f* transitions (typically of the order of tens to hundreds of cm^{-1} versus electronic state separations of thousands of cm^{-1}). Second, the spectral positions of the *f–f* emission and absorption bands are largely insensitive to the host matrix and remain quasi-atomic in character, enabling the same ion to be incorporated into different crystalline environments with predictably similar emission wavelengths.[64] The shielding also explains the exceptional photostability of Ln^{3+} emitters which unlike organic fluorophores or quantum dots, Ln^{3+}-based luminescence does not suffer from photobleaching under typical excitation conditions.[65]

2.1.2 Laporte Selection Rules and the Nature of f–f Transitions

From a symmetry perspective, transitions between states of the same parity (such as 4*f* → 4*f*) are formally forbidden by the Laporte selection rule, which requires a change of parity in electric-dipole transitions.[66] In practice, *f–f* transitions of Ln^{3+} ions are weakly allowed through two mechanisms: (i) the mixing of states of opposite parity (e.g., 5*d* character) into the 4*f* wavefunctions through odd-parity crystal-field terms (electric-dipole mechanism) and (ii) magnetic-dipole transitions, which do not require a parity change.[64,66]

The partial lifting of the Laporte selection rule is strongly influenced by the local site symmetry of the Ln^{3+} ion within the host lattice. Hosts with low local symmetry (e.g., lacking an inversion center at the cation site) promote greater mixing of opposite-parity states, thereby intensifying the forced electric-dipole transitions and enhancing radiative rates. This is the primary reason why it is expected that the hexagonal phase β-$NaREF_4$, with its multiple non-centrosymmetric cationic sites, consistently outperforms the cubic phase α-$NaREF_4$ as a luminescent host.[67] The four distinct cationic sites in the hexagonal structure (Wyckoff positions 1a, 1b, 1d, and 1e) include sites that lack inversion symmetry, which is speculated to facilitate the relaxation of the Laporte selection rule and thereby enhance the probability of radiative *f–f* transitions.

2.1.3 Relevant Energy Levels: Er^{3+}, Tm^{3+}, Yb^{3+}, and Ce^{3+}

The specific Ln^{3+} ions investigated in this thesis were Er^{3+}, Tm^{3+}, Yb^{3+}, and Ce^{3+}. Er^{3+} and Tm^{3+} were selected for their roles as emitters within the SWIR spectral range, Yb^{3+} was selected as a sensitizer for Er^{3+} and Ce^{3+} was used to enhance the SWIR performance of Er^{3+}. All these optical properties are based on the energy levels.[68] An energy level diagram of the lanthanides of interest can be seen in Figure 2.2.

Yb^{3+} has the simplest energy level structure among the Ln^{3+}, with only two manifolds: the ground state $^2F_{7/2}$ and a single excited state $^2F_{5/2}$ located approximately 10,200 cm^{-1} above the ground state; this energy gap corresponds to the absorption of 980 nm photons. Additionally, the large absorption cross-section of Yb^{3+} at 980 nm (approximately 10^{-20} cm^2) and the resonance of its excited state with the emitting manifold of Er^{3+} ($^4I_{11/2}$) make it the dominant sensitizer ion used in RE-based luminescent systems.[67]

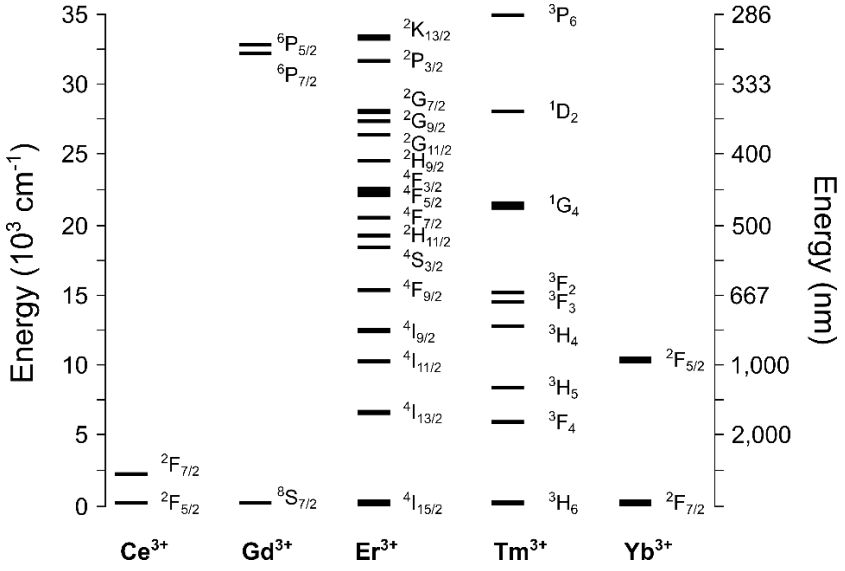


Figure 2.2 *Energy level diagrams of selected RE^{3+} ions relevant to this work, showing their term symbols and corresponding energy in cm^{-1} and nanometers (nm).*

Er^{3+} possesses a ladder-like energy level structure arising from its [Xe]$4f^{11+}$ configuration. In the SWIR context, the most important transition is the $^4I_{13/2} \rightarrow {}^4I_{15/2}$ transition centered at approximately 1550 nm, which falls within the biological imaging window. Efficient

excitation of Er^{3+} proceeds via resonant energy transfer from Yb^{3+} upon absorption of a 980 nm photon by Yb^{3+}, the energy is transferred to the $^4I_{11/2}$ level of Er^{3+}, which then relaxes non-radiatively to $^4I_{13/2}$ before emitting around 1550 nm.[69] Co-doping with Ce^{3+} has been shown to enhance the $^4I_{13/2} \rightarrow {}^4I_{15/2}$ emission of Er^{3+} by promoting rapid non-radiative relaxation of higher excited states of Er^{3+} (via cross-relaxation between Er^{3+} and Ce^{3+}), effectively funneling the excitation population into the $^4I_{13/2}$ emitting state.[70]

Tm^{3+} exhibits emission particularly around 1470 nm ($^3H_4 \rightarrow {}^3F_4$) and beyond 1600 nm ($^3F_4 \rightarrow {}^3H_6$), the latter transition being of primary interest in Chapters 5 and 6 of this thesis. The $^3F_4 \rightarrow {}^3H_6$ transition of Tm^{3+}, centered near 1800 nm, represents one of the longest-wavelength emission bands achievable with lanthanide ions excited at 800 nm, and it falls within a region of very low tissue scattering and moderate water absorption that isn´t being extensively explored for deep-tissue imaging as other regions.[71] An important photophysical process in Tm^{3+} is cross-relaxation between neighboring Tm^{3+} ions: at high Tm^{3+} concentrations, the process $^3H_4 + {}^3H_6 \rightarrow {}^3F_4 + {}^3F_4$ efficiently populates the $^3F_4$ state at the expense of shorter-wavelength emission, making concentration control critical for directing emission toward wavelengths beyond 1600 nm.[30]

Ce^{3+} has a single 4*f* electron and a relatively large energy gap between the $^2F_{5/2}$ ground state and the 5*d* excited states. In the context of Er^{3+}-based SWIR emission, Ce^{3+} acts as a de-excitation mediator. The difference between the $^4I_{11/2} \rightarrow {}^4I_{13/2}$ levels of Er^{3+} are energetically close to the $^2F_{7/2} \rightarrow {}^2F_{5/2}$ levels of Ce^{3+}, enabling rapid non-radiative energy transfer from Er^{3+} ($^4I_{11/2}$) to Ce^{3+} ($^2F_{7/2}$), and avoiding back-energy transfer from the $^4I_{11/2}$ level of Er^{3+} to the $^2F_{5/2}$ level of Yb^{3+}. This depopulates the $^4I_{11/2}$ level faster and enhances population of the $^4I_{13/2}$ emitting level of Er^{3+}. The net effect is a substantial increase in 1550 nm SWIR emission intensity and PLQY.[29,72,73]

2.1.4 Downshifting vs. Upconversion

It is important to distinguish between the two photophysical processes that are both exploited in RE-based optical materials:

Upconversion (UC) refers to the sequential absorption of two or more lower-energy photons to produce emission at a shorter wavelength (higher in energy). For example, excitation of Yb^{3+}/Er^{3+}-co-doped NCs with 980 nm photons yields visible emission at 660, 550 and 530 nm. UC is a non-linear process with a quadratic or higher power dependence on excitation irradiance (Figure 2.3 left).[74]

Downshifting (DS) refers to the absorption of a single higher-energy photon followed by emission of a single lower-energy photon in the infrared (Figure 2.3 right). In the systems studied in this thesis, 980 nm photons are absorbed by Yb^{3+}, and the energy is transferred to Er^{3+}. For the case of Tm^{3+}, it is self-sensitized using an excitation wavelength of 800 nm which emits at longer wavelengths (1450–1650 nm or >1600 nm, respectively). DS is a linear process with emission intensity proportional to the excitation irradiance. The downshifting process is the mechanism in all optical results reported in this thesis.

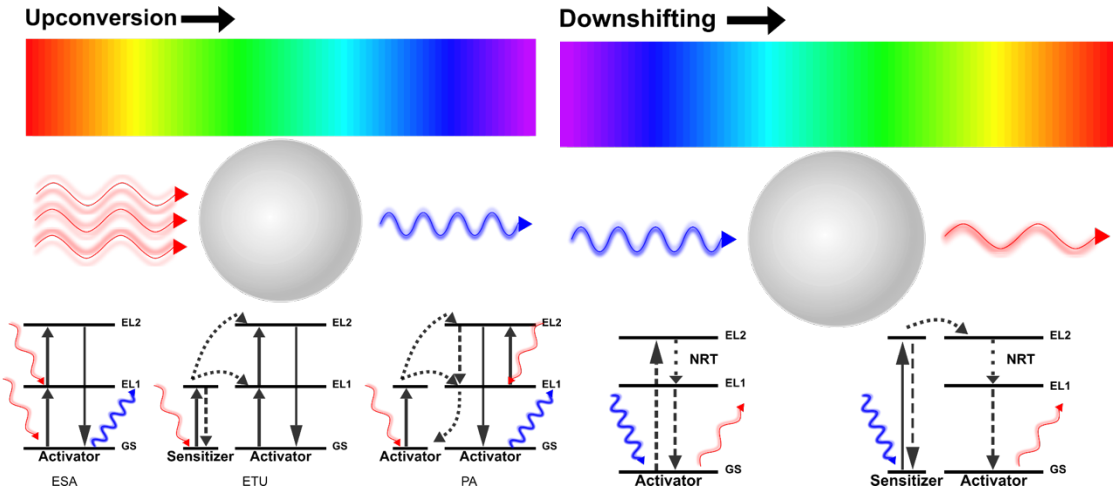


Figure 2.3 *Schematic illustration of the upconversion and downshifting photoluminescence processes, highlighting the principal mechanisms reported in the literature.*

2.2 Fluoride Host Materials

2.2.1 Why Fluorides?

The choice of a fluoride matrix as the host for luminescent lanthanide ions is dictated primarily by the low phonon energy of the fluoride lattice.[21] As established by the energy-gap law, non-radiative multiphonon relaxation is exponentially suppressed in

hosts with low phonon energies. Among several inorganic host families accessible via colloidal synthesis routes, fluorides exhibit some of the lowest phonon energies available: the maximum phonon energy of β-$NaYF_4$, for instance, is approximately 350–360 cm^{-1}, compared to ~800 cm^{-1} for metal oxides[75] and ~1200 cm^{-1} for phosphates.[76] This difference has a dramatic effect on the non-radiative rate of Ln^{3+} excited states that are separated by only a few hundred to a few thousand wavenumbers from the next lower level, around the regime of the SWIR-emitting states relevant to this thesis.

In addition to low phonon energy, fluoride hosts offer chemical stability, optical transparency across the ultraviolet (UV) to mid-infrared spectral range, and the ability to incorporate a wide range of RE^{3+} ions, enabling compositional tunability without considerably perturbing the host lattice.[47]

2.2.2 Fluoride Based Host Materials: α-$NaREF_4$ (Cubic Phase), β-$NaREF_4$ (Hexagonal Phase) and $LiREF_4$

The α phase of $NaREF_4$ adopts the fluorite-type structure (space group $Fm\bar{3}m$, Figure 2.4 right). In this structure, there is only one type of cationic site — an 8-coordinated site (Wyckoff position 4a) — that is statistically shared by both Na^+ and RE^{3+} ions in a mixed manner. The fluoride anions occupy 8c sites in a face-centered cubic arrangement. The random mixing of Na^+ and RE^{3+} on the same lattice site results in a high local symmetry around each cation and therefore a high degree of inversion symmetry at the metal site. As discussed in Section 1.2, high inversion symmetry suppresses the forced electric-dipole *f–f* transitions, leading to lower emission intensities. As a side note, CaF_2 is formally identical in symmetry to the α-$NaREF_4$ cubic phase, and its lattice parameter is close enough to enable near-epitaxial shell growth with small lattice mismatch (typically < 1%).[47] CaF_2 has no optically active transitions in the visible–NIR range (Ca^{2+} has a [Ar]$3d^0$ configuration) and therefore serves as a perfectly inert optical shell material. Critically, the chemical nature of CaF_2 differs fundamentally from $NaREF_4$: it contains Ca^{2+} (divalent) rather than Na^+ (monovalent) and RE^{3+} (trivalent). This chemical incompatibility

imposes a substantial thermodynamic barrier to cation migration across the core–shell interface, because the exchange would require charge-compensating defects.

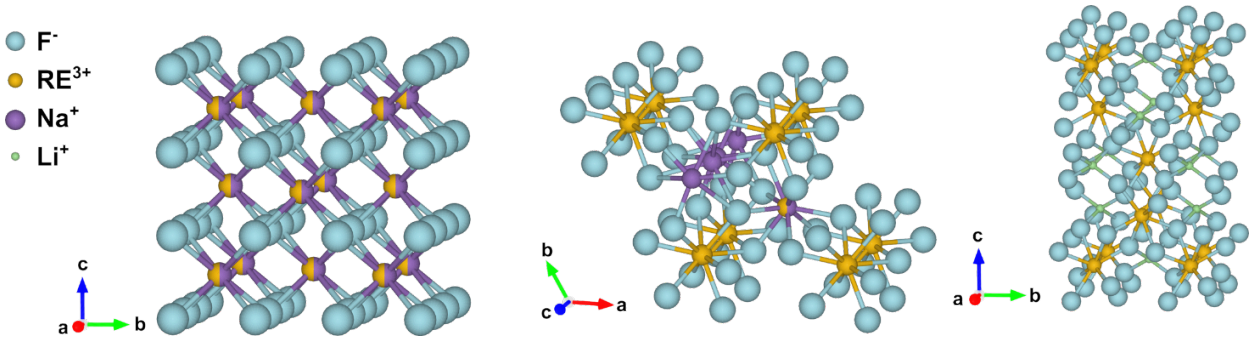


Figure 2.4 *Schematic representations of the crystal structures for the fluoride host lattices investigated in this thesis: (cubic) α-NaREF₄ (left), (hexagonal) β–NaREF₄ (middle), and tetragonal LiREF₄ (right).*

The β phase of $NaREF_4$ (space group $P\bar{6}$, Figure 2.4 middle) contains four distinct cationic sites: two Na^+ sites (Wyckoff positions 1a and 1e) and two RE^{3+} sites (1b and 1d), as well as a mixed Na^+/RE^{3+} site in some descriptions of the structure.[77] The lower crystal symmetry of the hexagonal phase breaks the inversion symmetry at the RE^{3+} sites, promoting the admixture of opposite-parity states into the 4*f* wavefunctions and thereby intensifying the forced electric-dipole *f*–*f* emission.

When lithium replaces sodium as the alkali cation, the crystal structure changes from the cubic or hexagonal $NaREF_4$ structures to a tetragonal scheelite-type structure (space group $I4_1/a$, Figure 2.4 right), analogous to $CaMoO_4$. In $LiREF_4$, the Li^+ ions occupy one fully ordered tetrahedral site (Wyckoff position 4a), and the RE^{3+} ions occupy a separate, fully ordered eight-coordinated site (Wyckoff position 4b). This ordered occupancy contrasts with the partial disorder of $NaREF_4$ structures. The distinct site symmetries of Li^+ and RE^{3+} in $LiREF_4$ might also affect the propensity for ion migration during core–shell synthesis.

2.3 Synthesis of RE-Based NCs

2.3.1 Colloidal Synthesis Strategies

RE^{3+} fluoride NCs are typically synthesized via wet-chemical colloidal routes, of which four main approaches have been developed: (i) hydrothermal/solvothermal synthesis, (ii) sol-gel, (iii) thermolysis of organometallic precursors, and (iv) ion-exchange reactions.[78,79] Among these, the thermolysis route has become the most widely used method for producing monodisperse, phase-pure, and size-controlled RE fluoride NCs,[80] that is why this is the method employed throughout this thesis.

The thermal decomposition synthesis method relies on the breakdown of precursors in high-boiling point (b.p) solvents. Commonly used high-boiling point solvents for this synthesis include trioctylphosphine oxide (TOPO, b.p. 408 ^{o}C), oleic acid (OA, b.p. 360 ^{o}C), 1-octadecene (ODE, b.p. 315 ^{o}C), and squalene (SQL, b.p. 420 ^{o}C).[81] This synthesis procedure allows the precise tuning of NCs characteristics like the size, morphology, and crystal structure by employing surfactants which act as coordination molecules for the RE ions used as precursors. The most frequently used surfactants are oleic acid (OA) and oleylamine (OAm).[82] The chemical structures of the precursors used for the synthesis of the NCs in this thesis are shown in Figure 2.5.

The main RE^{3+} ion precursors are chlorides, acetates, and trifluoroacetates. The combination of these solvents and surfactants, along with careful control of aging time and reaction temperature (usually around 300 °C), enables the preparation of highly monodispersed RE-doped NCs.[83] Defects in the interior of the NCs are less common because the synthesis at 300 °C produces highly crystalline materials; nevertheless, there is still no absolute certainty regarding the complete absence of defects, especially OH^{-} groups, which are known to cause luminescent quenching.[84] Since this work is focused in RE^{3+} fluoride-based NCs, a scheme showing the chemical structure of the most common precursors used for the thermal decomposition synthesis of these materials can be found in the figure below.

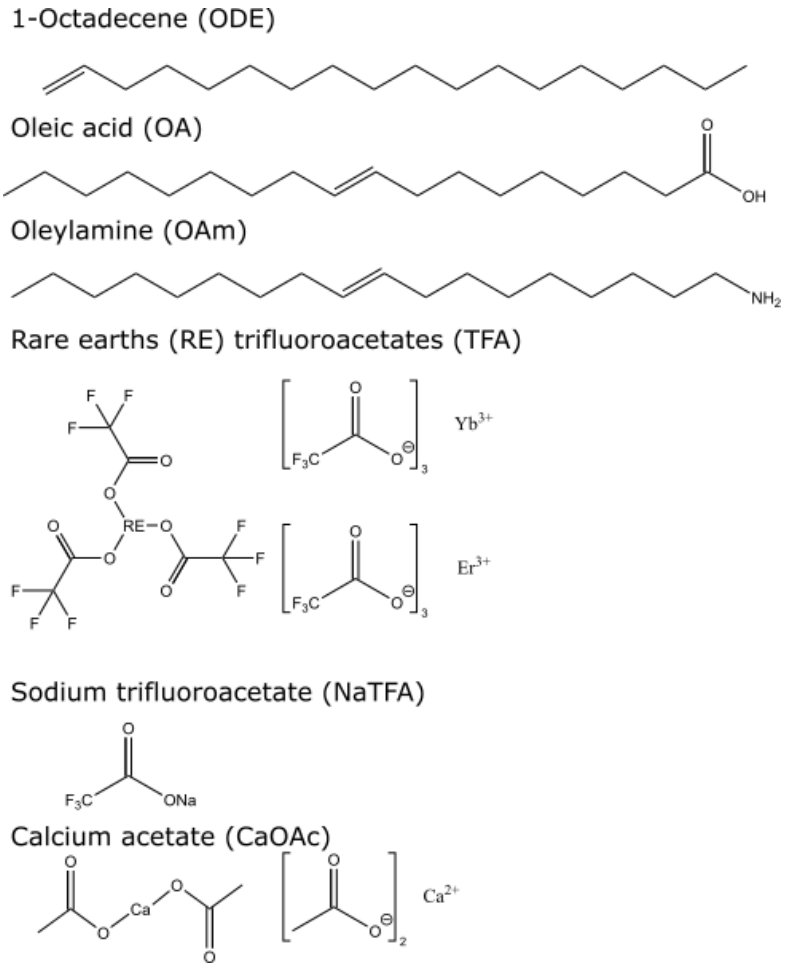


***Figure 2.5**. Chemical structures of the most commonly used precursors for synthesizing RE^{3+} luminescent NCs via the thermal decomposition method.*

2.3.2 Role of Ligands: Oleic Acid and Oleylamine

OA serves as both a coordinating ligand and a particle stabilizer. The carboxylate headgroup coordinates to surface RE^{3+} ions, providing steric stabilization that prevents aggregation and controls growth kinetics. OAm, when present, modulates the surface chemistry by competing with OA for surface sites and can influence phase purity and morphology. The OA/OAm ratio is a key parameter for optimizing the monodispersed size and controlling the final crystal phase of the NCs.[85,86] In the organic solvent environment, the NCs are natively capped with hydrophobic OA ligands, making them dispersible only in nonpolar solvents.

2.3.3 Variations of the Thermolysis Synthesis: Heating Up and Hot Injection

Two variations of this methodology exist (1) is heating up, and (2) hot injection (Figure 2.6). In the thermal decomposition by heating up route, all the precursors are introduced to the flask at room temperature, the flask is then sealed, and the following steps of the methodology are performed (purification – dissolution – heating – aging – cooling down), without the addition of any extra precursor. This is probably the most used thermal decomposition methodology used, as it can produce homogeneous core and/or core-shell NCs, in a relatively rapid and straightforward manner.[83] For the hot injection variation, it is possible that some precursor is added into the flask at room temperature, however the main difference is that additional precursors are introduced to the flask once it reaches a certain temperature, usually the aging temperature.[52,87] The hot injection variation offers the possibility of a more controlled growth of the NC, but at the cost of introducing more variables to the synthesis, like injection temperature and injection rate. Additionally, it requires a more elaborate setup than the heating up variation.

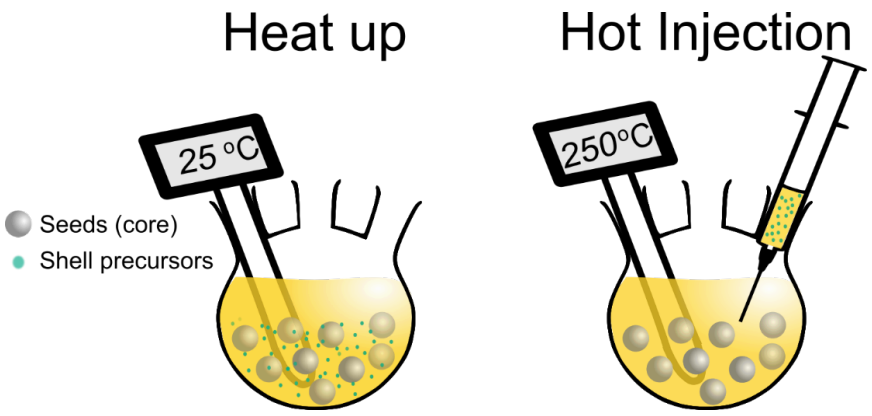


Figure 2.6 *Comparison between the heat-up and hot-injection approaches in thermal decomposition synthesis, illustrating key procedural differences.*

2.3.4 Core–Shell Synthesis: Seed-Mediated Growth

Core–shell NCs are produced by injecting shell precursor solutions onto a colloidal suspension of pre-formed core NCs (seeds). The core–shell NCs can be grown by either

heating up or the hot injection variation. In the thermolysis route, the shell growth proceeds through the controlled decomposition of the injected precursors at the surface of the existing NCs. Under optimal conditions, no new nucleation of separate NCs occurs (secondary nucleation is suppressed), and the shell material grows epitaxially onto the seeds.[39] The thickness of the shell is controlled mainly by the ratio of shell precursor to seed NC mass, although some other synthesis parameters can play also a role in the shell thickness, like aging time and temperature.

2.4 Photoluminescence Quantum Yield: Definition, Measurement, and Limiting Factors

2.4.1 Definition of PLQY

PLQY quantifies the fraction of absorbed photons that are re-emitted as photons.

$$PLQY = \frac{number\ of\ emitted\ photons}{number\ of\ absorbed\ photons}$$

There are two primary methods for measuring PLQY: relative measurement against a standard and absolute measurement. Some of the standards for the relative measurement include quinine sulfate (0.5 M in H_2SO_4) violet (in methanol), $Cs_3[Tb(dpa)_3]$ ($6.5x10^{-5}$ M in 0.1 M HCl), or $[Yb(tta)_3(H_2O)_2]$ (10^{-3} M in toluene).[88,89] The second method is the absolute measurement, while more complex, offers the highest accuracy, as shown in recent works.[90]

2.4.2 Absolute PLQY Measurement: Integrating Sphere

To perform absolute PLQY measurement, an integrating sphere coated with a highly reflective material, with close to 100% reflectance through a wide range of wavelengths. This ensures that the detector receives a proportional number of photons relative to the total emitted photons.[91]

The basic measurements to calculate the absolute PLQY involves measuring the excitation source intensity passing through the sphere with and without the sample. This permits the determination of both the absorbed and emitted photons. While this provides a foundational understanding, it neglects the possibility of reabsorption within the sphere by the sample itself, which can distort the results.[88]

To account for the reabsorption process, the more sophisticated 3M method is employed.[92,93] This approach involves measuring the emission and absorption spectra with the excitation source directly hitting the sample (direct measurement) and then with the sample removed from the excitation path but still inside the integrating sphere (indirect measurement). By performing and analyzing all these combined measurements, a more accurate determination of the sample's real photon conversion efficiency can be achieved.

2.4.3 Limiting Factors for the PLQY Determination

One of the major challenges in measuring the PLQY in RE compounds is the inherently low absorption cross-section of the *f-f* transitions.[64,88] As seen in the PLQY equation, knowing the absorption is an important parameter in determining the efficiency. Low absorption values can introduce substantial uncertainties in the measurement of the PLQY values, with these uncertainties increasing exponentially as the absorption decreases.[90]

Another critical factor involving the accurate PLQY measurement is the state in which the sample is measured, whether the measurement is performed in solid-state or in solution. When measuring solid-state materials, two important considerations must be addressed: powder packing and heat generation. In the first case, it is essential that the material is as tightly packed as possible, minimizing air gaps, as these air gaps can introduce measurement discrepancies. For the case of heat generation, temperature increases can substantially influence non-radiative, phonon-assisted transitions, thereby reducing the material's overall efficiency. This heating effect becomes particularly problematic when measuring PLQY at higher excitation power densities.

For PLQY measurements in solution, careful consideration of the solvent's absorption and potential emission is critical prior to conducting the measurement, any spectral overlap between the solvent and the sample must be known before determining the PLQY of any sample. If the solvent has an absorption band at/or near the excitation wavelength, it can introduce parasitic absorption, affecting the PLQY real value determination. Therefore, selecting a solvent that neither absorbs at the excitation wavelength nor interferes with the emitted photons is vital for obtaining accurate PLQY values. If such an ideal solvent is unavailable, careful characterization of the solvent is required to apply appropriate correction factors, ensuring accurate measurement of the true PLQY.

2.4.4 Shell Passivation: The Principle of Surface Protection for Improving the PLQY

The shell passivation is the most effective strategy to increase the efficiency of the NCs by mitigating surface quenching.[39] The shell serves the primary function of physically shielding the optically active Ln^{3+} ions from the NC surface from environment quenchers. The optically inert shell approach provides a physical barrier that prevents energy transfer from the Ln^{3+} to the solvent molecules and external quenchers. A minimum shell thickness of approximately 1–3 nm has been proposed as necessary to achieve significant suppression of surface quenching.[94] Further shell thicknesses may still improve the efficiency until reaching a saturation point beyond which the core-to-surface distance is large enough that energy migration to the surface becomes negligible.[36] The choice of shell material is guided by three criteria: (i) optical transparency (no absorption or emission in the spectral range of interest); (ii) crystallographic compatibility with the core (to enable epitaxial growth and a coherent interface); and (iii) chemical stability.

2.4.5 State-of-the-Art PLQY Values for SWIR-Emitting NCs

From the wide range of RE-based NCs developed emitting in the SWIR range, unprotected core-only NCs (i.e., without shell protection) typically show moderate to low PLQYs. For example, β-$NaCeF_4$:Yb:Er excited at 980 nm emits at 1525 nm with PLQYs

ranging from 6% to 32%, depending on the overall particle size being the smallest 6 nm and the largest 200 nm; at power density, at 100,000 mW/cm^2.[95] Other core-only structures like β-$NaNdF_4$:Mn^{2+} (emission at 1050 nm) achieved a PLQY of 10% using a relative method,[96] while CaF_2:Nd (1020–1100 nm)[97] and β-$NaLuF_4$:Gd:Yb:Er:Ce[98] (1450-1650 nm) reported PLQYs of 9% and 4%, respectively.[97,98]

Meanwhile core–shell structures with homogeneous core and shell domains have shown variable performance. In β-$NaYF_4$:Yb:Er/$NaLuF_4$ (29 nm overall size), a PLQY of 18% was obtained under 1700 mW/cm^2 power density with 980 nm excitation.[36] The β-$NaYF_4$:Yb:Er system using a β-$NaGdF_4$ shell exhibited emissions at 1000 and 1550 nm with relatively low PLQYs of 13% at an excitation power density of 200 mW/cm^2.[99] Another example, β-$NaYbF_4$:Er,Ce/$NaYF_4$, emitted between 1300 and 1900 nm, reaching 23% PLQY under an excitation power density of 150 mW/cm^2.[29] Similarly, β-$NaErF_4$/$NaLuF_4$ (40 nm) and α-$NaYF_4$:Er:Ce:Zn/$NaYF_4$ (40 nm) yielded 11%[100] and 5%[70] PLQYs respectively.

In β-$NaYF_4$:Nd/$NaYF_4$, emissions at 1064 nm and 1345 nm were observed with PLQYs of 8% and 5%,[101] while β-$NaErF_4$/$NaLuF_4$ rods (30x25 nm) emitted at 1550 nm with 14% PLQY.[102] LiYbF4:Er:Ce/$LiYF_4$ reached 36% PLQY at 1450–1650 nm under a power density of 12,500 mW/cm^2,[73] while α-$NaYF_4$:Yb:Er:Ce/$NaYF_4$ (45 nm) achieved 24% PLQY at 1450–1650 nm.[61] β-$NaYF_4$:Yb:Er/α-$NaYF_4$ in contrast, showed a lower PLQY of 7%.[61]

Finally, the heterogeneous core–shell structures reported so far demonstrated good PLQYs under some conditions. For instance, α-$NaYF_4$:Yb,Nd/CaF_2 (10 nm) emitted at 950–1100 nm with a PLQY of 11% under 1000 mW/cm^2.[69] In α-$NaYbF_4$:Er,Ce,Zn/CaF_2 systems, PLQYs of 22%, 29%, and 40% were reported for particle sizes of 19, 28, and 53 nm, respectively, at 1450–1650 nm and 20,000 mW/cm^2.[72]

Relatively few studies have addressed emission at the far end of the SWIR region.[103] Even when Tm^{3+} is employed, most reports focus on the emission around 1450 nm ($^3H_4$ → $^3F_4$)[99], which does not correspond to a transition to the ground state. Among the limited number of studies reporting PLQY values in this spectral range, one work reported a

PLQY of 1.5% using the highly complex multishell composition of β-$NaGdF_4$:Yb,Tm/$NaYF_4$:Yb/$NaGdF_4$:Yb,Nd/$NaGdF_4$.[104] Chen et al. also reported multishell NCs, β-$NaYbF_4$:Tm/$NaYbF_4$/$NaYF_4$, with a PLQY of 3.9% for the 1800 nm emission.[105] Notably, when the crystal structure was changed to the cubic structure α-$NaYF_4$:Yb,Tm/$NaYbF_4$/$NaYF_4$, the PLQY increased to 14.0%,[106] representing one of the highest previously reported values. The highest PLQY previously reported for the 1800 nm emission of Tm^{3+} was 16% from $LiTmF_4$:Er/$LiYF_4$.[30]

Particularly, in this thesis it is reported α-$NaYF_4$:Yb,Er,Ce/CaF_2 (15 nm) NCs with a PLQY of 50% under an excitation power density 60 mW/cm^2 at 1450–1650 nm emission. Similarly, α-$NaYF_4$:Yb,Er/CaF_2 (15 nm) reached 30% PLQY under the same conditions. These represent some of the highest values reported for sub-15 nm NCs in this emission window.

2.5 SWIR Fluorescence Imaging

2.5.1 Advantages of SWIR Imaging over Conventional Fluorescence Imaging

SWIR imaging, operating in the 1000 to 2000 nm spectral range, has emerged as a valuable tool in biomedical imaging.[107,108] The benefits of SWIR imaging are enhanced deep tissue visualization capability and reduced signal interference. Unlike imaging in the visible (400–700 nm) and near-infrared I (NIR-I; 700–900 nm) spectral range, SWIR imaging markedly benefits from decreased photon scattering and minimal tissue autofluorescence. These advantages contribute to improved spatial resolution, enhanced signal-to-noise ratio (SNR), and greater penetration depth, often reaching several millimeters into biological tissues[109]. Consequently, SWIR imaging is particularly well-suited for capturing high-resolution, real-time functional and structural information *in vivo*.[107]

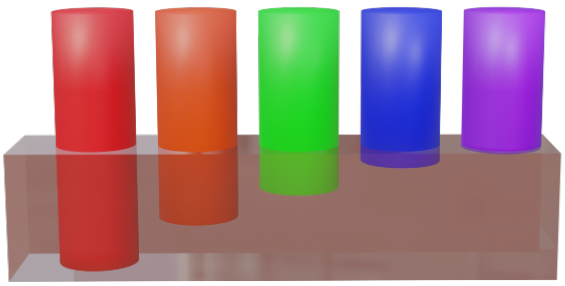


Figure 2.7 *Illustration of the penetration depth of light in human skin, demonstrating that longer wavelengths (e.g., NIR) penetrate deeper than shorter ones.*

To understand its advantages, it is essential to examine how light in the SWIR region interacts with biological tissues. The effectiveness of SWIR imaging is fundamentally based on the interaction of low energy wavelengths with biological tissues. Light scattering in tissues due to Rayleigh mechanism, is greatly reduced at SWIR wavelengths, generally following an inverse power-law relationship with wavelength ($\lambda^{-\alpha}$, where α varies based on tissue characteristics from 0.2 to 0.4). This results in less scattering of SWIR photons compared to visible or NIR-I ranges. Furthermore, biological tissues exhibit minimal autofluorescence in the SWIR region, which enhances imaging contrast and reduces background noise. This spectral window also coincides with reduced water and hemoglobin absorption, which collectively facilitates deeper tissue penetration.[109,110]

2.5.2 Current SWIR Fluorophores

Recent technological progress in the development of fluorophores has further expanded SWIR imaging capabilities. InAs, PbS, and Ag_2S QDs, represent some of the most promising fluorophores, demonstrating improved brightness and biocompatibility that make them appropriate for use in biomedical applications.[14,111] These NCs exhibit narrow, tunable emission spectra throughout the SWIR spectrum, and also exhibit high PLQY values, close to 30%. These fluorophores are noted for their high photostability, uniform size distribution, and ease of surface modification, enhancing their utility in biomedical contexts. Additionally, gold nanoclusters, owing to their ultra-small size, present a promising avenue towards reduced systemic toxicity and efficient renal clearance,

although their fluorescence intensity remains modest.[112] A representation of materials that can emit in the SWIR region are presented in Figure 2.8.

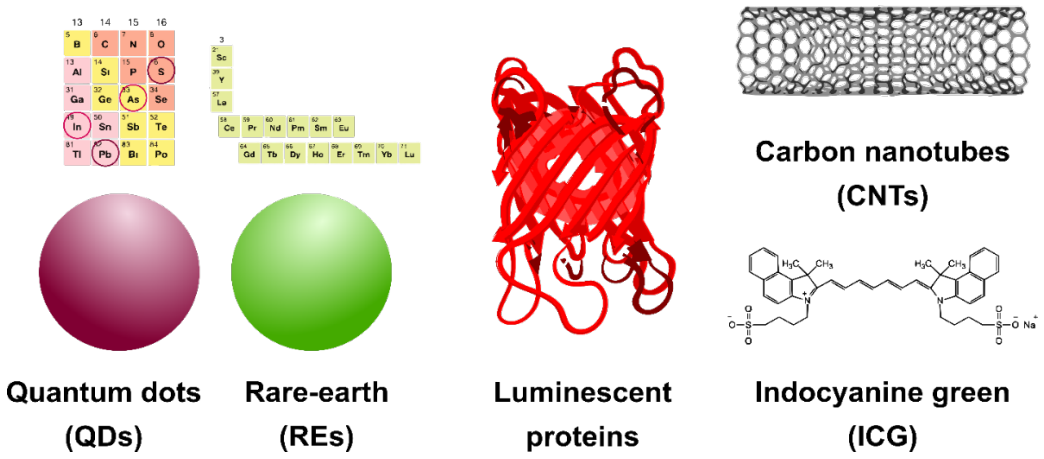


Figure 2.8 *Overview of the most commonly used SWIR emitting materials for imaging and photonic applications.*

From the NCs SWIR probes, InAs QDs offer significantly better properties than the rest. InAs QDs have been successfully functionalized with various coatings to tailor their behavior in biological environments.[19] Phospholipid micelle-coated InAs have enabled applications such as angiography and vital sign monitoring by providing long circulation times in the bloodstream. Nanosomes (nanosized vesicles), formed by incorporating QDs into lipoproteins, facilitate real-time imaging of metabolic activity, such as the uptake of triglyceride-rich particles by brown adipose tissue (BAT). InAs-based composite QDs have also been developed for applications like intravital microscopy and single-particle tracking in brain vasculature, achieving imaging depths up to 300 micrometers with frame rates of 60 fps. These QDs also offer short, excitation-independent photoluminescence lifetimes (~100 ns), essential for high-intensity imaging modalities such as confocal microscopy. These functionalities demonstrate the potential of InAs QDs to serve as versatile platforms for high-speed, high-resolution functional imaging.[19]

The main concern that stops the InAs QDs is the toxicity claim. Although there are studies demonstrating the biocompatibility of InAs and InAs-based QDs, it is better documented the severe toxicity of As. Thus, many concerns arise regarding the overall toxicity of InAs, severely limiting its use for bioapplications, despite their striking properties.

RE NCs present an alternative to the QDs with discrete, narrow emission lines and long lifetimes, suitable for multiplexed imaging applications. RENPs can be doped with specific lanthanides like Tm^{3+} and Er^{3+} to tune emission into different spectral regions of the SWIR, with lifetimes allowing time-domain imaging.[72,113–115] Furthermore, the toxicity concerns regarding RE-based NCs are less than for QDs, making them extremely attractive materials for SWIR imaging.

Moving beyond inorganic materials, researchers have also investigated organic fluorophores and biologically derived systems, like encoded fluorescence proteins, for SWIR applications. Chemically tunable organic molecules, such as polymethine dyes and donor-acceptor systems, offer favorable biocompatibility.[116] They typically exhibit lower PLQY values and poor photostability in aqueous environments. Genetically encoded fluorescent proteins, including variants derived from bacterial phytochromes and cyanobacteriochromes, exhibit emission tails that extend into the SWIR range.[111] These proteins provide the benefit of cell-type-specific expression and capabilities for long-term imaging, although ongoing optimization is needed to improve their brightness and spectral characteristics.

2.5.3 Advances in SWIR Imaging Systems

Alongside fluorophore development, advances in imaging instrumentation have also played a critical role in enabling SWIR imaging. Various imaging modalities have been used to implement SWIR fluorescence imaging, including wide-field, confocal, and light-sheet systems. Wide-field imaging, which uses planar illumination and cooled indium gallium arsenide (InGaAs) cameras, is particularly useful for dynamic, whole-animal imaging. Confocal microscopy is a powerful tool that enables 3-dimensional, high-resolution imaging via raster scanning and sensitive detectors like superconducting nanowire single-photon detectors.[13] Light-sheet microscopy permits rapid volumetric imaging with minimal phototoxicity by simultaneously exciting and imaging a single plane. These systems are further improved by a combination of optical tools like bandpass and long-pass filters to reduce excitation leakage and improve emission collection. Careful

optical design is required to avoid spectral overlaps and to reduce photothermal effects from water absorption bands.[117]

These technological improvements have opened the door to a range of biomedical applications, particularly in vascular and tumor imaging.[11,70,118] One of the main advantages of SWIR imaging in biomedical research is the possibility of imaging the vascular system (the network of blood vessels in the body). Imaging blood vessels is crucial for diagnosis confirmation for several medical complications, it can determine blockages, aneurysms, hemorrhages; additionally, it can improve tumor assessment and surgical planning.[2,16,119] Tumor imaging and image-guided surgery are also substantially enhanced by the deep penetration and high resolution of SWIR fluorescence, enabling precise tumor location. Figure 2.9 shows a scheme illustrating the capabilities of SWIR imaging using contrast agents.

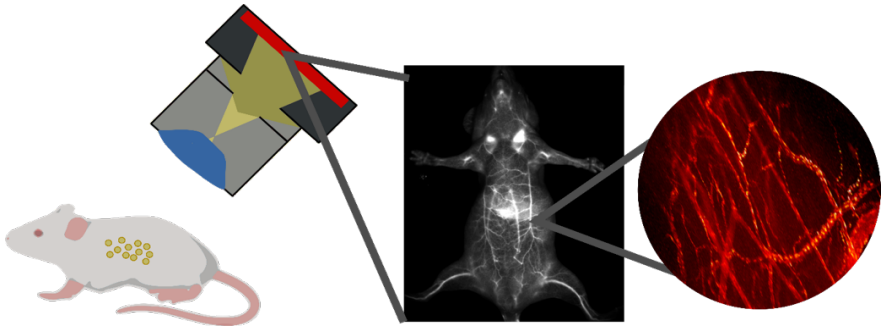


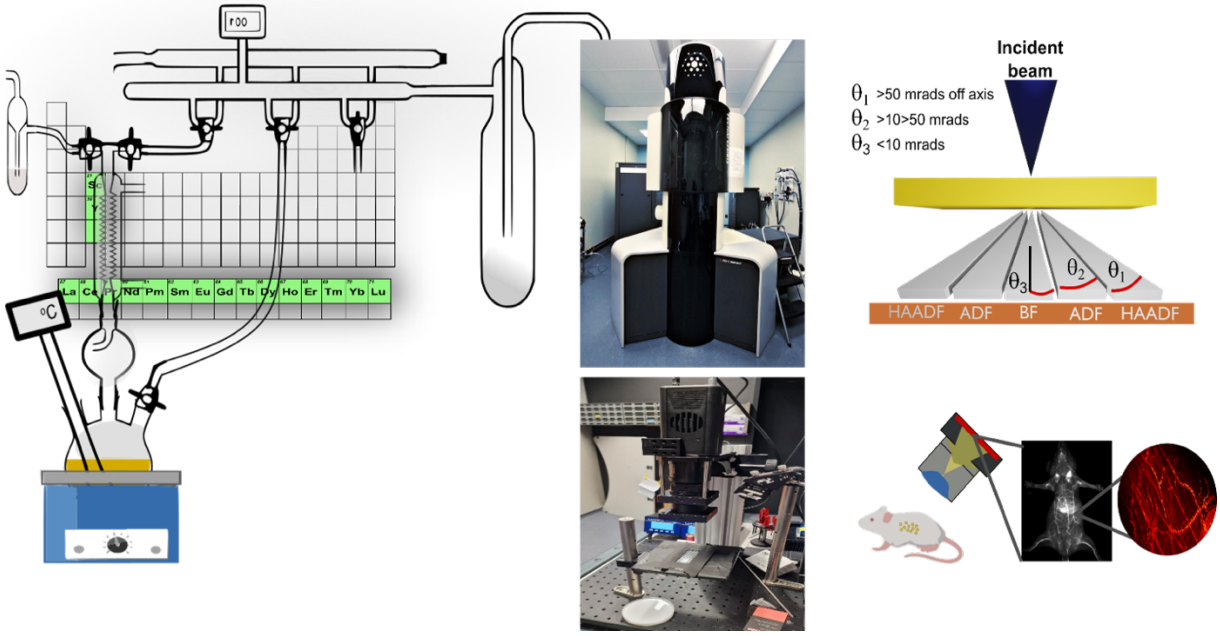
Figure 2.9 *Schematic depiction of potential imaging outputs from SWIR-based visualization of the vascular system.*

Despite its numerous advantages, SWIR imaging faces several challenges. As mentioned before, the most promising probes (InAs, and PbS) present toxicity concerns due to heavy metals, which make the translation to clinical applications more problematic. Additionally, trade-offs between brightness and biocompatibility are often necessary, particularly when choosing between inorganic and organic fluorophores. Careful selection of the excitation source wavelength also limits the development of SWIR imaging, as the excitation wavelength must avoid the water absorption bands to minimize photothermal effects; typical excitation wavelengths used are 800 nm, 980 nm, and 1064 nm.[120–122]

Furthermore, standardization of imaging protocols and fluorophore is needed to guarantee reproducibility and facilitate regulatory approval.[123]

Future directions in SWIR imaging include the development of brighter, safer fluorophores with renal clearance capabilities and the implementation of advanced multiplexing strategies based on spectral and temporal properties. The repurpose of clinically approved agents such as indocyanine green (ICG) for SWIR applications illustrates the potential for rapid translation of this technology into human use.[12] Researchers have proposed dividing the SWIR range into finer segments based on local tissue absorption and scattering characteristics. Although these subdivisions, such as those sometimes referred to as NIR-IIb or NIR-IIc, are not universally established, they are used as practical guides for optimizing imaging contrast and penetration depth. Further integration with multimodal systems (e.g., PET, MRI, optoacoustic) and adaptive optics is anticipated to expand the utility of SWIR imaging in both fundamental research and clinical diagnostics.[8,19] As the field continues to evolve, SWIR imaging is poised to play a transformative role in both preclinical and clinical biomedical imaging.

3. Materials and Methods



This chapter describes the synthesis of precursors and NCs used throughout this thesis, including alkali fluoride ($NaREF_4$, $LiREF_4$) and alkaline-earth fluoride (CaF_2) *NCs. It further describes the synthesis methodologies, structural (X-ray diffraction, electron microscopy) and optical characterization (absorbance, quantum yield, intralipid-phantom analysis, fluorescence imaging) techniques employed. The combination of these synthesis methodologies and the characterization methods enabled a detailed investigation of cation intermixing phenomena and allowed the resulting structural features to be correlated with the optical performance and imaging potential of the NCs.*

3.1 Synthesis of Precursors

An overview of the preparation of the trifluoroacetate precursors is depicted in Figure 3.1.

3.1.1 Synthesis of RE Trifluoroacetates [$RE(OOCCF_3)_3$, RE = Y, Er, Tm, Yb]

RE trifluoroacetates were synthesized by adding 20 mmol of rare-earth oxide (RE_2O_3) to a mixture of 14 mL of trifluoroacetic acid (TFAH) and 36 mL of deionized water in a 100

mL round bottom flask equipped with a reflux condenser. The suspension was stirred and heated to 95 °C in air overnight. After cooling, the solution was filtered, and the solvent was removed using a rotary evaporator at 70 °C for at least 3 h. The resulting wet powder was then dried under vacuum at 150 °C for 22 - 24 h. After drying, the precursor powders were transferred immediately to a glovebox and stored under dry nitrogen to minimize exposure to ambient moisture. Consequently, complete recovery of the powder from the flask was not attempted in order to minimize its exposure to ambient atmosphere. Across repeated syntheses of the different RE trifluoroacetates, isolated gravimetric yields above 90% were consistently obtained. The RE precursors were slightly hydrated, with a water content of less than 3 wt.% as determined by thermogravimetric analysis.

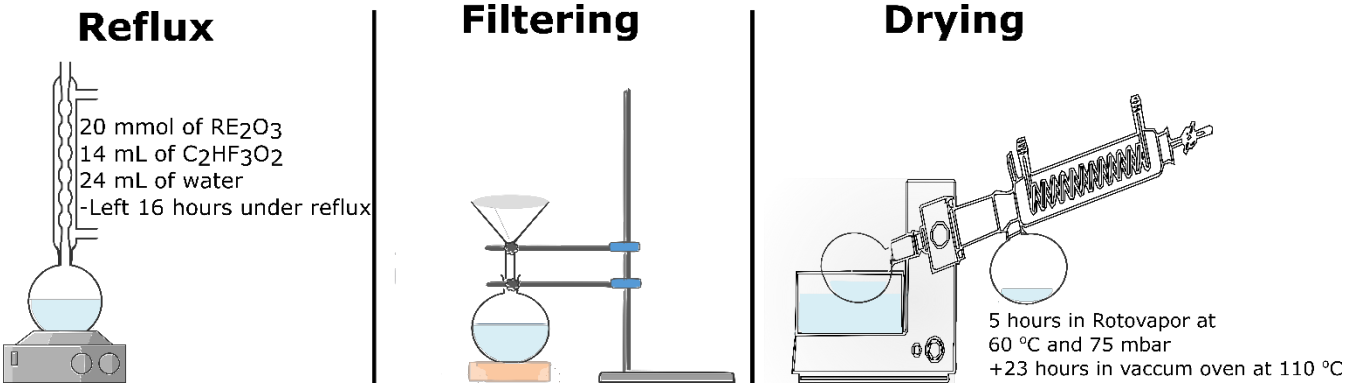


***Figure 3.1**. Overview of the procedure to prepare RE trifluoroacetate or acetate precursors.*

3.1.2 Synthesis of Ca Trifluoroacetate [$Ca(OOCCF_3)_2$]

$Ca(TFA)_2$ was made by mixing 72 mmol of $CaCO_3$ with 16 mL of trifluoroacetic acid and 33 mL of deionized water in a 100 mL round bottom flask with a reflux condenser. The mixture was stirred and heated to 95 °C in air overnight, resulting in a clear, colorless solution. After cooling, the solution was filtered, and the solvent was removed using a rotary evaporator at 70 °C for at least 3 h. The resulting wet powder was then dried under vacuum at 150 °C for 22 - 24 h. After drying, the $Ca(OOCCF_3)_2$ precursor powder was transferred immediately to a glovebox and stored under dry nitrogen to minimize exposure to ambient moisture. Consequently, complete recovery of the powder from the flask was

not attempted in order to minimize its exposure to ambient atmosphere. cross repeated syntheses, isolated gravimetric yields above 90% were consistently obtained for $Ca(OOCCF_3)_2$. The $Ca(OOCCF_3)_2$ precursors obtained were slightly hydrated, with a water content of less than 3 wt.% as determined by thermogravimetric analysis.

3.1.3 Synthesis of Gd Acetate [$Gd(OOCCH_3)_3$]

Gadolinium acetate was synthesized following the same procedure as for the trifluoroacetates, with acetic acid used instead of TFAH.

3.1.4 Synthesis of Tm Acetate [$Tm(OOCCH_3)_3$]

Thulium acetate was synthesized following the same procedure as for the trifluoroacetates, with acetic acid used instead of TFAH.

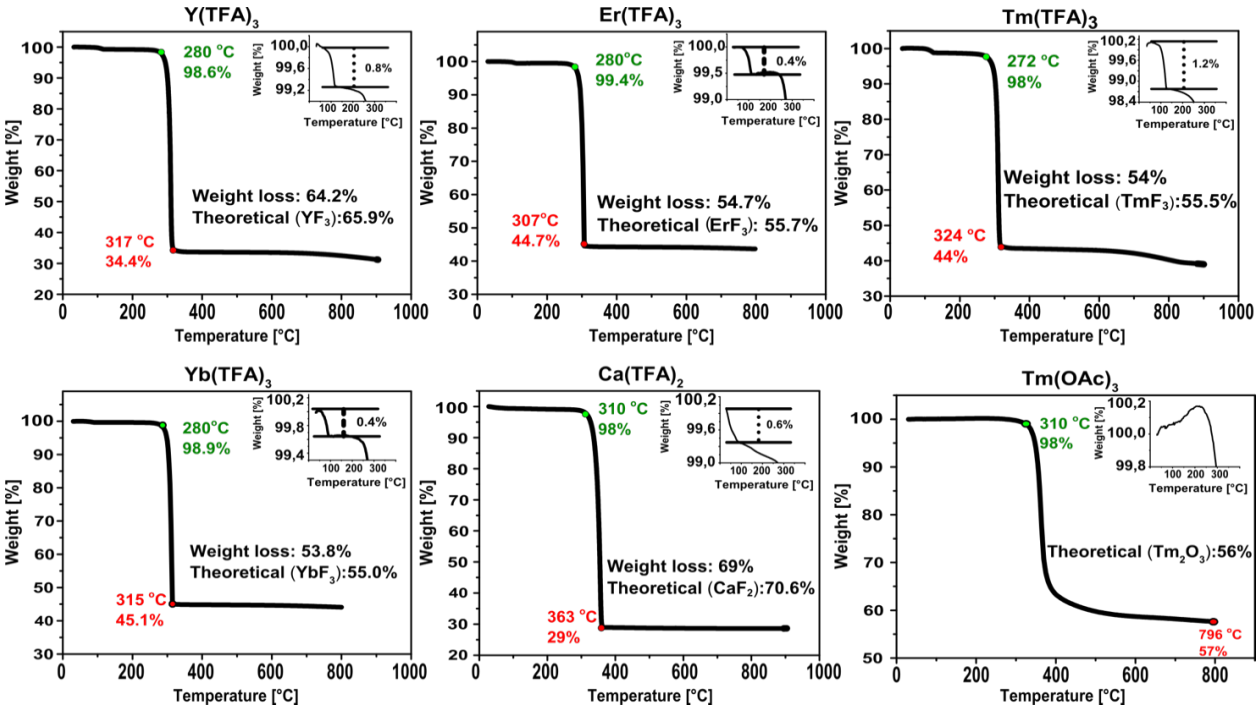


Figure 3.2 *Thermogravimetric analyses (TGA) of the synthesis precursors. TGA graphs of the synthesized precursors to determine the amount of water and the mass loss due to the decomposition at high temperature. The insets in each graph provide a magnified view of the initial mass loss, which is commonly attributed to the release of absorbed water.*

3.2 Synthesis of Core NCs

3.2.1 Synthesis of α-$NaREF_4$ Core NCs

Inside the glovebox, 1 mmol of $NaOOCCF_3$ and 1 mmol of the corresponding $RE(OOCCF_3)_3$ or mixture (Y, Yb, Er or Y, Yb, Er, Ce or Tm) were added to a 50 mL three-neck Schlenk flask, along with 3.2 mL of OA, 3.3 mL of OAm, and 7.5 mL of ODE. The flask was then removed from the glovebox, connected to the Schlenk line, and performed 5 Ar-vacuum cycles at room temperature, each vacuum cycle was performed until a minimum vacuum of $5x10^{-2}$ mbar was reached. Following these cycles, the temperature was raised to 110 °C, and the mixture is left for 30 min to allow the trifluoroacetates to dissolve, forming a clear, slightly yellowish solution. A second set of 5 argon-vacuum cycles, followed by a 10 min dynamic vacuum, was performed to remove as much O_2 and H_2O as possible. Finally, the mixture was heated to 300 °C for 30 min. The flask was then removed from the heating mantle and cooled down using compressed air. The NCs were precipitated from the raw reaction mixture by adding 10 mL of ethanol and 10 mL of acetone for the first extraction, followed by centrifugation at 6,000 rpm (3823 G, 5 min). The supernatant was discarded, and the precipitated NCs were redispersed in 5 mL of toluene. Subsequently, 5 mL of ethanol and 5 mL of acetone were added as antisolvents, followed by centrifugation under the same conditions. This redispersion-precipitation procedure was repeated for a total of at least three purification cycles.

The precipitate was redispersed in 5 mL of toluene, and the purification procedure was repeated at least three times. After purification, the NCs were dispersed in 3 mL of toluene for Yb/Er-based NCs or 3 mL of chloroform for Tm-based NCs. Across repeated 1 mmol syntheses, a typical mass of approximately 65–75 mg was obtained.

3.2.2 Synthesis of β-$NaGdTmF_4$ Core NCs

Inside a glovebox, 2.5 mmol of NaOH and 4 mmol of NH_4F were combined in a vial and 6 mL of methanol were added to solubilize the precursors. The Na and F precursors were left stirring inside the glovebox for approximately 90 minutes. Separately, 0.5 mmol of $Gd(OOCCH_3)_3$ and 0.5 mmol of $Tm(OOCCH_3)_3$ were introduced into a 50 mL three-neck round-bottom Schlenk flask, along with 6 mL of OA and 15 mL of ODE. The flask was

then removed from the glovebox, connected to the Schlenk line, and performed 5 Ar-vacuum cycles at room temperature, each vacuum cycle was performed until a minimum vacuum of $5x10^{-2}$ mbar was reached. Following these cycles, the temperature was raised to 160 °C, and the mixture was left for 30 min to allow the acetates to dissolve, forming a clear, slightly yellowish solution. After heating, the solution was removed from the heating mantle and allow it to cool down. While cooling down, the vial with the Na and F precursor solution was taken out of the glovebox. Once the temperature of the acetate solution drops below 40 °C, a syringe was used to take the NaOH/NH_4F methanol solution from the vial and injected it into the cooled Tm-containing flask. The mixture was heated to 70 °C and maintained this temperature for 30 minutes under Ar flow. Argon-vacuum cycles were carefully performed to remove methanol, keeping the temperature between 60 °C and 76 °C. Finally, the mixture was heated to 300 °C for 60 min. The flask was then removed from the heating mantle and cooled down using compressed air. The NCs were precipitated from the raw reaction mixture by adding 10 mL of ethanol and 10 mL of acetone for the first extraction, followed by centrifugation at 6,000 rpm (3823 G, 5 min). The supernatant was discarded, and the precipitated NCs were redispersed in 5 mL of chloroform. Subsequently, 5 mL of ethanol and 5 mL of acetone were added as antisolvents, followed by centrifugation under the same conditions. This redispersion-precipitation procedure was repeated for a total of at least three purification cycles. After purification, the NCs were dispersed in 3 mL of chloroform. Across repeated 1 mmol syntheses, a typical mass of approximately 70–80 mg was obtained.

3.2.3 Synthesis of $LiTmF_4$ Core NCs

$LiTmF_4$ NCs were synthesized following the same procedure as for β-$NaGdTmF_4$, with LiOH replacing the NaOH, and using 1 mmol of $Tm(OOCCH_3)_3$ as the whole RE ions source.

3.3 Synthesis of Shell Layer Domains

3.3.1 Synthesis of α-$NaREF_4$/$NaYF_4$ NCs

Inside the glovebox, 1 mmol of $NaOOCCF_3$ and 1 mmol of $Y(OOCCF_3)_3$ were added to a 50 mL three-neck Schlenk flask, along with 7 mL of OA and 7 mL of ODE. The flask was then removed from the glovebox, connected to the Schlenk line, and 1 mL of the corresponding α-$NaREF_4$ seeds solution was added. Subsequently, 5 Ar-vacuum cycles were performed at room temperature each vacuum cycle was performed until a minimum vacuum of $5x10^{-2}$ mbar was reached. Following this, the temperature was raised to 120 °C, and the mixture was left for 30 min to allow the trifluoroacetates to dissolve, resulting in a clear yellowish solution. A second set of 5 argon-vacuum cycles followed the dissolution step to remove as much O_2 and H_2O as possible. Finally, the mixture was heated to 300 °C for 45 min. The flask was then removed from the heating mantle and cooled down using compressed air. The NCs were precipitated from the raw reaction mixture by adding 10 mL of ethanol and 10 mL of acetone, followed by centrifugation at 6,000 rpm (3823 G, 5 min). The supernatant was discarded, and the precipitated NCs were redispersed in 5 mL of toluene. Subsequently, 5 mL of ethanol and 5 mL of acetone were added as antisolvents, followed by centrifugation under the same conditions. This redispersion-precipitation procedure was repeated for a total of at least three purification cycles. After the final purification step, the NCs were dispersed in 1 mL of toluene for Yb/Er-based NCs or 1 mL of chloroform for Tm-based NCs. A typical synthesis yielded approximately 130-140 mg of purified core-shell NC material.

3.3.2 Synthesis of α-$NaREF_4$/CaF_2 NCs

This synthesis followed the same procedure as that for α-$NaREF_4$/$NaYF_4$ NCs, except that 2 mmol of $Ca(OOCCF_3)_2$ was used replacing $NaOOCCF_3$ and $Y(OOCCF_3)_3$.

3.3.3 Synthesis of α-$NaREF_4$/$LiYF_4$ NCs

Inside the glovebox, 1 mmol of $LiOOCCF_3$ and 1 mmol of $Y(OOCCF_3)_3$ were added to a 50 mL three-neck Schlenk flask, along with 6 mL of OA and 15 mL of ODE. The flask was then removed from the glovebox, connected to the Schlenk line, and 1 mL of the corresponding α-$NaREF_4$ seeds solution was added. Subsequently, 5 Ar-vacuum cycles were performed at room temperature each vacuum cycle was performed until a minimum

vacuum of $5x10^{-2}$ mbar was reached. Following this, the temperature was raised to 100 °C, and the mixture was left for 30 min to allow the trifluoroacetates to dissolve, resulting in a clear yellowish solution. A second set of 5 argon-vacuum cycles followed the dissolution step to remove as much O_2 and H_2O as possible. Finally, the mixture was heated to 300 °C for 30 min. The flask was then removed from the heating mantle and cooled down using compressed air. The NCs were precipitated from the raw reaction mixture by adding 10 mL of ethanol and 10 mL of acetone, followed by centrifugation at 6,000 rpm (3823 G, 5 min). The supernatant was discarded, and the precipitated NCs were redispersed in 5 mL of toluene. Subsequently, 5 mL of ethanol and 5 mL of acetone were added as antisolvents, followed by centrifugation under the same conditions. This redispersion-precipitation procedure was repeated for a total of at least three purification cycles. After the final purification step, the NCs were dispersed in 1 mL of chloroform. A typical synthesis yielded approximately 130-140 mg of purified core-shell NC material.

3.3.4 Synthesis of β-NaGdTmF₄/NaYF₄ NCs

This synthesis followed the same procedure as that for α-$NaREF_4$/$NaYF_4$ NCs, except that 1 mL of β-$NaGdTmF_4$ seeds was used replacing the α-$NaREF_4$ seeds.

3.3.5 Synthesis of β-NaGdTmF₄/CaF₂ NCs

This synthesis followed the same procedure as that for α-$NaREF_4$/CaF_2 NCs, except that 1 mL of β-$NaGdTmF_4$ seeds was used replacing the α-$NaREF_4$ seeds.

3.3.6 Synthesis of LiTmF₄/NaYF₄ NCs

This synthesis followed the same procedure as that for α-$NaREF_4$/$NaYF_4$ NCs, except that 1 mL of $LiTmF_4$ seeds was used replacing the α-$NaREF_4$ seeds.

3.3.7 Synthesis of LiTmF₄/CaF₂ NCs

This synthesis followed the same procedure as that for α-$NaREF_4/CaF_2$ NCs, except that 1 mL of $LiTmF_4$ seeds was used replacing the α-$NaREF_4$ seeds.

3.3.8 Synthesis of $LiTmF_4/LiYF_4$ NCs

This synthesis followed the same procedure as that for α-$NaREF_4/LiYF_4$ NCs, except that 1 mL of $LiTmF_4$ seeds was used replacing the α-$NaREF_4$ seeds.

3.4 Water Transfer Procedures

3.4.1 Micelles

For the in vivo SWIR imaging experiments, the hydrophobic α-$NaYF_4$:Yb,Er,Ce/CaF_2 NCs were transferred to an aqueous medium through phospholipid micelle formulation. A volume of 100 µL of the NC dispersion (10 mg/mL) was mixed with 400 µL of a 25 mg/mL solution of 18:1 PEG2000 PE [1,2-dioleoyl-sn-glycero-3-phosphoethanolamine-N-[methoxy(polyethylene glycol)-2000], ammonium salt] in NaCl solution diluted in DI water. The resulting mixture was sonicated using a probe sonicator until the appearance of the solution changed from a turbid solution to a perfectly clear solution.

3.4.2 Polyacrylic Acid

A second methodology used to transfer the NCs to water, polyacrylic acid was used to replace the OA in the NCs. Briefly, 300 mg of PAA (M.W. 1,080,000 average M.N. 135,000) was dissolved in 30 mL of DEG at 110 °C in a 100 mL round flask. After 30 min, 700 µL of the hydrophobic NCs solution was added dropwise into the PAA solution and stirred for 1 hr. Subsequently, the NCs-PAA solution was heated to 240 °C for 1.5 hr. The flask was then removed from the heating mantle and cooled down using compressed air. The solution was dispersed in 3 tubes with *ca.* 10 mL of the solution each. The NCs were extracted from the raw solution in each tube via centrifugation at 6,000 rpm (3823 G) for 5 min using equal parts of ethanol and acetone (10 mL each for the first extraction, 5 mL

each for the later extractions). This purification process was repeated at least three times, and the resulting NCs were then dispersed in 1 mL of D_2O.

3.5 Structural Characterizations

3.5.1 Powder X-ray Diffraction Pattern Acquisition (PXRD)

PXRD measurements were conducted at room temperature using a Bruker D8 Discover powder diffractometer in Bragg-Brentano geometry. The diffractometer was equipped with a copper anticathode, a quartz monochromator (Cu $K\alpha_1$ radiation, l = 1.540562 A), and a 1-dimensional detector (LynxEye XE-T). The PXRD patterns were recorded over a 2θ range of 10°−135° with a total duration of 9 h. For PXRD sample preparation, colloidal suspensions of the NCs in either toluene or chloroform were dropped-casted onto low background (911) oriented silicon substrates. Line profile analyses and Rietveld refinements, where corresponding, were carried out using TOPAS software. It must be noted that the silicon substrates contained an impurity peak at $2\theta \approx 80°$, this diffraction peak appeared almost in all the diffraction patterns of the measured NCs, but it does not belong to the NCs (Figure 3.3).

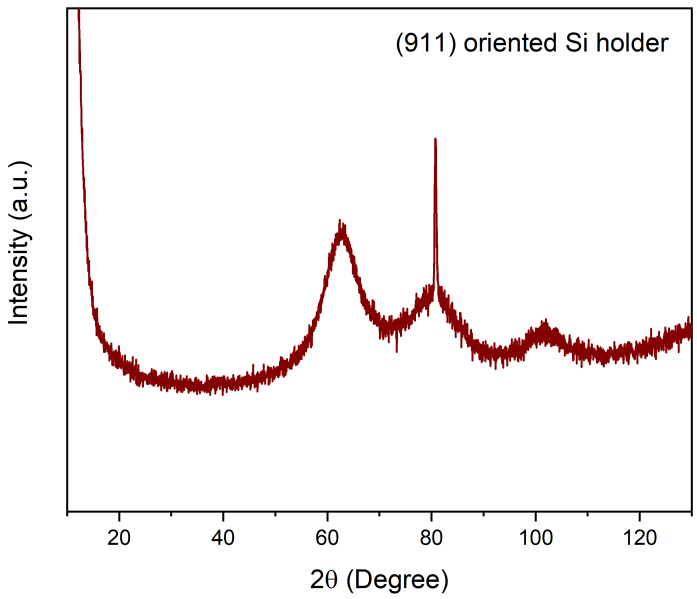


Figure 3.3 *PXRD characterization. XRD pattern of the low background (911)-oriented clean silicon holder, presenting a sharp peak at $2\theta \approx 80°$, which was observed on all experimental X-ray diffraction patterns.*

3.5.2 High-Angle Annular Dark-Field Scanning Transmission Electron Microscopy Imaging (HAADF-STEM)

STEM grids were prepared at room temperature by depositing 10 µL of diluted NCs suspension in toluene or chloroform onto an ultrathin, amorphous 3 nm carbon film supported by a 400 µm mesh Cu grid from Ted Pella Inc. The morphology, size, and elemental composition of the NCs were examined using HAADF-STEM with a FEI Osiris ChemiSTEM microscope, operated at 200 kV. The resulting HAADF-STEM images were used to calculate the average particle size by analyzing size distribution histograms, with measurements taken from over 300 individual particles.

3.5.3 High-Resolution Transmission Electron Microscopy Imaging (HRTEM)

The structure of individual NCs was examined via high-resolution transmission electron microscopy (HRTEM), utilizing an aberration-corrected FEI Titan^3 80-300 microscope operating at 300 kV. The resulting HRTEM images were analyzed by calculating the 2-dimensional Fourier transform (FT), which provided data relating to the crystal structure, i.e. lattice parameters and crystal symmetry of the individual NCs. This analysis involved a comparative assessment of the experimental FT and calculated diffraction patterns, with the latter being generated using Jems software.

3.6 Atomic Organization: Energy-Dispersive X-ray Spectroscopy (EDXS)

3.6.1 Chemical Maps

The chemical composition of the NCs was investigated through EDXS chemical mapping, utilizing a FEI Osiris ChemiSTEM microscope equipped with a Super-X EDXS system that incorporates four silicon drift detectors (Bruker XFlash). Elemental maps of F (F-Kα

line), Na (Na-Kα line), Ca (Ca-Kα line), Y (Y-Lα line), Gd (Gd-Lα line), Er (Er-Lα line), Tm (Tm-Lα line), and Yb (Yb-Lα line) were obtained and subsequently analyzed using Bruker's ESPRIT software. The concentrations of each element were determined based on a refined Kramers' law model, which accounts for corrections related to detector absorption and background subtraction.

3.6.2 Line Scans

The experiments were conducted using an FEI Osiris ChemiSTEM microscope, which features a Super-X EDXS system equipped with four silicon drift detectors. Elemental distributions within individual NCs were analyzed by EDXS line scans acquired using a ChemiSTEM-equipped transmission electron microscope. Quantified EDXS spectra collected across the NC diameter provide position-dependent, path-averaged chemical compositions. To extract the local composition of the core and shell regions, the resulting concentration profiles were further analyzed using a subshell model that accounts for the core–shell geometry. A detailed description of the experimental conditions, data acquisition parameters, and the mathematical framework of the subshell approach can be found in previous published works.[61,62,124]

3.6.3 Integrated Differential Phase Contrast (iDPC)-STEM Imaging

To address the challenge of visualizing the low-intensity fluorine (F) atoms in HAADF-STEM images of both homogeneous and heterogeneous NCs, integrated differential phase contrast-STEM (iDPC-STEM) imaging was utilized to concurrently examine the distribution of light and heavy elements within the crystal lattice. The iDPC-STEM technique generates an image that corresponds to the scalar electrostatic potential field of the sample, effectively providing a direct phase image, contingent upon the sample being sufficiently thin. This approach facilitates the simultaneous visualization of both light and heavy elements.

3.7 Photoluminescence Characterization

3.7.1 Light Absorption Measurements

UV-Vis-NIR absorption spectra were recorded using an Agilent Cary 7000 spectrophotometer, with measurements taken in 2 nm increments across the 600 - 2000 nm range. The spectrophotometer's spectral bandwidth was set to 4 nm, and the integration time was 0.2 s. Standard 1x1 cm quartz cuvettes were used to hold the samples during measurement.

3.7.2 Downshifting PLQY Measurements

The downshifting spectrum and power-dependent PLQY values were determined using a custom-built optical system. A tunable continuous-wave (CW) Ti:Sapphire laser (SolsTiS, M-squared lasers Ltd), pumped by a 532 nm laser (Verdi-V18, Coherent), served as the excitation source, operating at either 770 or 800 nm with an intensity of 600 - 700 mW. For intensity-dependent measurements, the laser beam's power was attenuated using an adjustable, rotatable neutral density filter (NDC-100C-2, Thorlabs) controlled by an Arduino board-driven step motor. Absorption and emission measurements (measurement of the laser at the direct and indirect excitation of the sample and empty sphere) were conducted using one calibrated spectrometer (Thorlabs, CCS200/M) for Y-Er based NCs, or two calibrated spectrometers (Zeiss, PGS NIR 2.2; Thorlabs, CCS200/M) to record the intensities of the Tm-based samples emission and the excitation laser, respectively. The downshifting emission was measured with a longer integration time compared to the excitation light to address potential issues arising from the significant difference in magnitude between the laser and the NCs' emission. Absolute PLQY values were calculated following a modified 3M procedure. This procedure involves acquiring spectra of: i) the empty sphere, ii) the sample directly illuminated by the excitation source within the sphere, iii) the sample indirectly illuminated by the excitation source within the sphere, iv) the excitation source laser through the empty sphere, v) the excitation source transmitted through the sample, and vi) the excitation source indirectly

exciting the sample. To prevent spectrometer saturation caused by scattered laser radiation, a high-quality, ultra-steep long-pass filter was placed between the sphere and the optical fiber. The NCs were measured both in colloidal solution in a non-polar solvent (toluene or chloroform) within a quartz cuvette or in solid state. All detected raw spectra were converted to counts per second using the integration time value. The absorption values typically ranged from 10% to 20%. Given the presence of noise at the spectrometer's end range, all power dependence measurements were repeated at least three times and averaged. The final reported value was also calculated by averaging the power dependency measurements to minimize the impact of noise.

3.7.3 Macroscopic SWIR Imaging System

The macroscopic SWIR imaging system included a liquid nitrogen-cooled InGaAs detector (640 × 512 pixels, Princeton Instruments), SWIR-sensitive 50-mm focal length lens (F2.8, Schneider-Kreuznach), 968-nm diode laser (Lumics) operating in continuous wave mode, and a selection of emission filters. The InGaAs detector was maintained at -190 °C, with an exposure time of 1 second. This camera-lens configuration provided a field of view measuring 8.53 x 6.82 cm. The 968-nm laser was filtered using a 1000 short pass filter. Additionally, a diffuser (20^{o}, Thorlabs) was employed to ensure uniform illumination across the entire field of view; the diffused laser exhibited a mean standard deviation intensity of 99.6 ± 29.3 mW/cm^2 within the mouse area. In the detection pathway, a series of long pass filters were implemented to mitigate laser stray light.

3.7.4 Brightness Signal Measurements

NCs brightness measurements were conducted utilizing the macroscopic SWIR imaging system, with the camera exposure time set to 100 ms and the laser power density maintained at 37 mW/cm^2 in the sample area.

3.7.5 In vivo SWIR Fluorescence Imaging

Animal procedures adhered to institutional guidelines. Mice (Charles River Laboratories, Germany) were housed at 23 °C, 45–65% humidity, with a 12/12 h light/dark cycle. A 5-

6-week-old hairless athymic mouse, with a tail vein catheter implanted, was anesthetized with ketamine (Bremer Pharma GmbH, 100 mg/kg) /xylazine (WDT, 10 mg/kg) solution and positioned within the macroscopic SWIR imaging system, utilizing a 1450 nm long pass filter at 1000 ms. After the start of the image acquisition, the 968-nm laser source was activated and kept for the duration of the experiment. Following an initial series of pre-injection frames, 200 μL of the α-$NaYF_4$:Yb,Er,Ce/CaF_2 micelle formulation were administered via the tail vein catheter, with continuous imaging.

3.7.6 SWIR imaging of NCs Fluorescence in Intralipid Phantoms

The NCs were imaged using a custom-built system featuring an extended InGaAs camera (C-RED 2 ER 1.9 μm, First Light Imaging) and a 35-mm f/1.4 SWIR lens (SWIR35, Navitar). A three-filter slot assembly within a lens tube was implemented to mitigate reflections. Specifically, a 1500-nm long-pass filter (FELH1500, Thorlabs) was positioned in front of the lens, while an LP1150 filter (Edmund Optics) was placed closest to the stage to eliminate off-angle laser reflections.

Excitation of the NCs was achieved using 785 nm and 968 nm laser units (Lumics, LU0785DLU250-S70AN03 and LU0980D350-D30AN, respectively), with their outputs combined via a 4x1 fan-out fiber-optic bundle (Thorlabs BF46LS01). This bundle was connected to an excitation cube (Thorlabs KCB1EC/M), reflected off a mirror (Thorlabs BBE1-E03), and directed through a positive achromat (Thorlabs AC254-050-B), a 1000 nm short-pass filter (FESH1000, Thorlabs), and a diffuser (Thorlabs ED1-S20-MD) designed to ensure uniform illumination across the field of view. The power density was calibrated to approximately 50 mW/cm² at the sample plane. Exposure times ranged from 0.25 to 30 ms. Raw images underwent dark correction, averaging, division by exposure time, and subsequent normalization using a flatfield-based laser power density map to yield images in counts/ms/(mW/cm^2). The full setup is shown in Figure 3.4.

For imaging, the NCs solutions were contained within 10 μL capillary tubes (Minicaps, Hirschmann). Subsequently, a cell culture dish containing 1 vol.% Intralipid (Sigma-

Aldrich), prepared from a 20% stock solution in either D_2O or H_2O, was employed. Varying volumes of this solution were then added to achieve the specified Intralipid thickness.

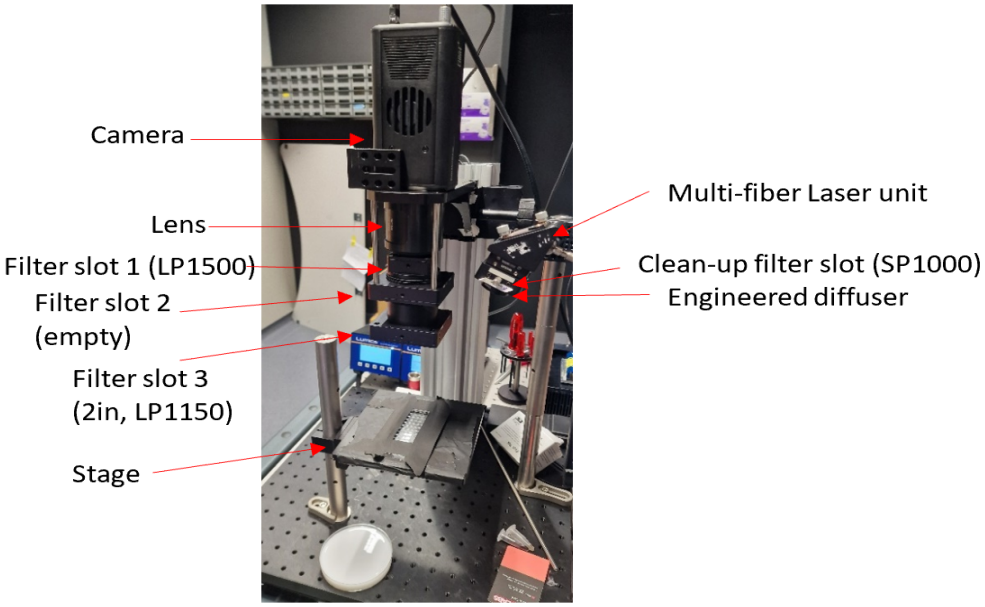
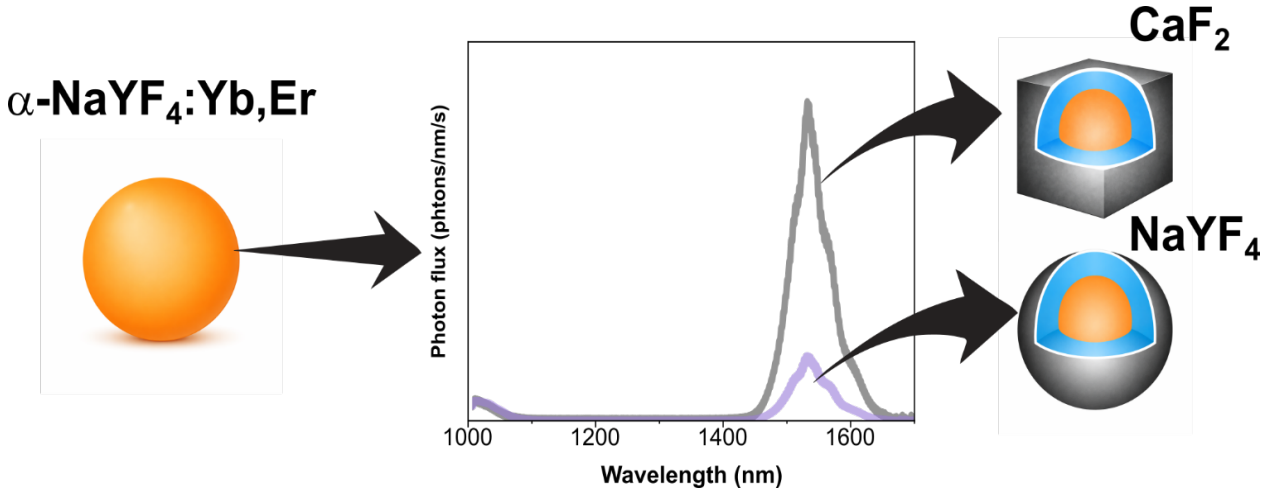


Figure 3.4 *Experimental setup for image acquisition in the long-wavelength end of the SWIR region. Schematic of the optical setup used to capture SWIR images at extended wavelengths. LP: long-pass filter; SP: short-pass filter. Reprinted with permission from ACS Nano 2024, 18, 38, 26233–26250. Copyright 2024 American Chemical Society.*

4. Cation Intermixing in Homogeneous and Heterogeneous RE Core–Shell NCs for SWIR Emission



The content of this chapter has been published in a separate work.

***Arteaga Cardona, F.**, Jain, N., Popescu, R. et al. Preventing cation intermixing enables 50% quantum yield in sub-15 nm short-wave infrared-emitting rare-earth based core–shell nanocrystals. Nat Commun 14, 4462 (2023). https://doi.org/10.1038/s41467-023-40031-4.*

Contributions

The author prepared the samples, performed the XRD measurements and analyzed the results. Noopur Jain, Annick De Backer, Sara Bals, and Sandra Van Aert contributed by obtaining the high-resolution high-angle annular dark-field scanning electron transmission microscope (HR-HAADF-STEM) images and the corresponding analysis of the results. Eduard Madirov and Dmitry Busko measured the optical properties of the prepared samples and calculated the PLQY. Radian Popescu, and Dagmar Gerthsen were in charge of the (electron microscopy) EM characterizations and analysis, including the chemical maps and line scans. Bryce S. Richards supervised the project and provided scientific guidance. Damien Hudry conceived the initial idea, provided guidance during the project, contributed intellectual input, and wrote the final version of the manuscript.

4.1 Motivation

The concept of cation intermixing in RE-based core–shell NCs has gradually gained acceptance within the scientific community. Advances in analytical techniques, particularly high-resolution elemental mapping through EDXS and related methods, have provided strong evidence of non-abrupt interfaces and ion redistribution across core–shell boundaries. Nevertheless, despite these advancements, some degree of skepticism remained, especially concerning the interpretation of chemical maps derived from spherical NCs.

One of the primary limitations in earlier studies stemmed from the geometry of the NCs investigated. In spherical systems, the variation in shell thickness along different crystallographic directions inherently complicates the resolution of the location of an element. This geometric uncertainty made it difficult to unambiguously attribute observed elemental gradients solely to ion redistribution rather than to projection effects or variations in shell morphology. Consequently, even with direct chemical organization evidence, the scientific community in the field remained unconvinced about the extent or even the occurrence of intermixing in these materials.

To address this challenge, shape-related artifacts were minimized by investigating core-shell NCs with well-defined cubic shape. The use of cube-shaped particles markedly simplifies the interpretation of EDXS line scans and elemental maps, as the flat surfaces and uniform thickness minimize the geometrical convolution of signal. Additionally, to further simplify the chemical analysis, materials with simple cubic crystal structures were selected.

Fluorite-type structured materials have a simpler crystallographic structure, consisting of just two atomic columns, one corresponding to the cation and one to the anion (F^-). The chosen materials were α-$NaREF_4$ for the core and CaF_2 as the shell material. α-$NaREF_4$ is an extensively used host material for optically active RE ions, although in the beginning it was supposed to be less efficient for energy conversion, in comparison to the hexagonal structure, this concept has been fading away; meanwhile CaF_2 is a material with low

toxicity concerns, can nucleate in nanocubes, and has a low lattice mismatch comparing to the α-$NaYF_4$ (< 1%). Furthermore, these combinations of materials enable a more straightforward and credible mapping of cation distribution without interference from structural complexity or overlapping atomic columns.

This chapter is therefore motivated by the need to develop a more robust, geometry-independent chemical analysis framework for the study of intermixing in core-shell NCs. By combining controlled particle shape with a chemically simple shell material, the work aims to provide clearer and more convincing evidence of interfacial cation redistribution, thereby contributing to the broader understanding and acceptance of intermixing phenomena in these systems. Additionally, a comparison of the ion distribution and optical properties between the most used homogeneous shell ($NaYF_4$) and heterogeneous shell (CaF_2) is presented, showing striking differences, with the same optically active material.

4.2 Overview

SWIR fluorescence imaging, introduced in the earlier chapters of this thesis, offers a compelling path toward high-contrast biological imaging by exploiting the reduced tissue scattering and autofluorescence in the 1,000–1,700 nm spectral window.[125,126] The practical viability of this imaging modality, however, hinges on the availability of probes that combine strong SWIR emission with photostability and a size compatible with biological delivery. RE-based NCs have long been considered among the most promising candidates for this role, given their sharp emission bands, absence of photobleaching, and tunable photophysics through selection of sensitizer and activator ion pairs.[127–129]

Historically, the optimization of these NCs focused almost exclusively on the chemical composition of the core, *i.e.* the ratio of sensitizer to activator ions, their absolute concentrations, and the choice of host matrix.[130–132] The spatial organization of optically active ions within the particle after shell growth was largely overlooked, and the assumption that the core remains chemically unaltered by subsequent surface reactions persisted without rigorous experimental analysis.[43–45,133,134] The first systematic challenge to this assumption came from studies of cation exchange processes in lanthanide fluoride

systems, which showed that ion migration between crystal domains can proceed at temperatures well below what thermodynamic arguments might suggest.[25,78] That realization opened the broader question of whether shell growth, a process typically carried out at elevated temperatures in the presence of highly reactive precursors and coordination ligands, could itself drive significant ion redistribution.

This chapter addresses that question directly by comparing the structural and optical consequences of growing two chemically distinct shells on the same α-$NaYF_4$:Yb,Er core NCs. The most commonly used homogeneous $NaYF_4$ shell and the less used heterogeneous CaF_2 shell represent two limiting cases: one in which the shell material is chemically similar to the core (same crystal structure, compatible cation sizes, same anion sublattice), and one in which the shell is compositionally distinct (different cation valence, no shared cation species). By holding the core composition constant and varying only the shell chemistry, the contribution of the shell chemical properties to ion organization can be assessed independently of other variables. The results demonstrate that the chemical dissimilarity of the CaF_2 shell effectively suppresses cross-boundary ion migration, preserving the spatial confinement of Yb^{3+} and Er^{3+} within the core domain and enabling a more than fourfold improvement in SWIR emission efficiency relative to the $NaYF_4$-shelled counterpart. The chapter further shows that additional enhancement is achievable through Ce^{3+} co-doping of the core, and that the combination of heterogeneous shelling with Ce^{3+} co-doping yields the highest PLQY reported to date for sub-15 nm SWIR probes.

4.3 Results

4.3.1 Starting α-$NaYF_4$:Yb,Er Core NCs Characterizations

A single batch of α-$NaYF_4$:Yb,Er core NCs was prepared by thermal decomposition to serve as a common starting material for all subsequent shell growth experiments. The nominal cation composition was set to Y = 50 at.%, Yb = 45 at.%, and Er = 5 at.%. Low-magnification HAADF-STEM imaging confirmed the formation of approximately

isotropic sub-10 nm particles (Figure 4.1b), with size distribution analysis identifying two co-existing populations centered at 6.0 ± 1.2 nm and 9.2 ± 1.0 nm (Figure 4.1c).

Phase purity was confirmed by PXRD; the experimental pattern was fully accounted for by Rietveld refinement against the α-$NaYF_4$ structure, with no evidence of residual secondary phases (Figure 4.1d). The refined lattice parameter of 5.484 Å falls between the values for α-$NaYF_4$ (5.507 Å) and α-$NaYbF_4$ (5.452 Å), consistent with the formation of a solid solution at the intended Yb^{3+} loading. The deviation from the ideal 50% mixing value is small and within the expected uncertainty of the refinement (5.480 Å predicted vs. 5.484 Å measured). Crystallite size analysis by the whole powder pattern modelling (WPPM)[135,136] method yielded a mean diameter of 8 nm with a standard deviation of 1.1 nm, in good agreement with the size distributions obtained by the electron microscopy images.

High-angle annular dark-field scanning transmission electron microscopy (HAADF-STEM) results confirmed that individual core NCs are single-crystalline (Figure 4.1e). Integrated differential phase contrast (iDPC)-STEM imaging further resolved both the heavy RE^{3+} cation columns and the comparatively light F^- anion columns within the same image (Figure 4.1f),[137,138] demonstrating the quality and crystallinity of the starting material at the sub-angstrom level.

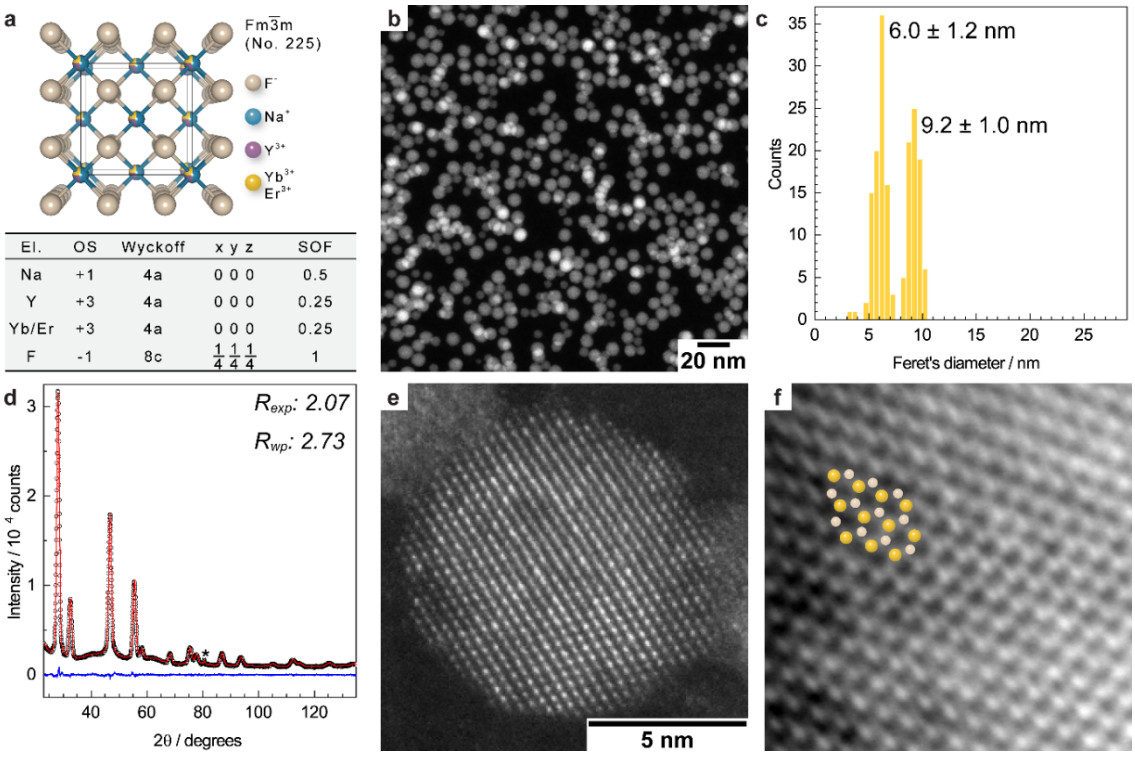


Figure 4.1 *Structural characterization of optically active α-$NaYF_4$:Yb,Er core NCs. (a) Perspective view of the cubic crystal structure of the α-$NaYF_4$:Yb,Er core NCs along the [001] direction, accompanied by crystallographic data including atomic positions (x, y, z) and site occupation frequencies (SOFs). (b) Representative low-magnification HAADF-STEM image of the NCs. (c) Size distribution histogram derived from the image in (b). (d) Experimental (black open symbols) and calculated (red line) PXRD patterns with the corresponding difference curve (blue line). The calculated pattern results from a full Rietveld refinement, with R-factors (R_exp and R_wp) provided to evaluate the fit quality, supported by visual comparison of the difference curve. The peak near 2θ ≈ 80° (marked with *) does not belong to the cubic phase but is accounted for by background modeling, using a scaled signal from the sample holder—a low-background (911) silicon wafer. The XRD pattern of the empty holder is provided in Figure 3.3. (e) High-resolution STEM image of an individual α-$NaYF_4$:Yb,Er NC. (f) iDPC-STEM image of a selected region of an NC, showing atomic columns containing RE^{3+} elements (yellow) and fluorine (beige). Reprinted with permission from Nat. Commun. 2023, 14(1), 4462. Copyright 2023. Springer Nature.*

4.3.2 Growth of Homogeneous and Heterogeneous Shells Domains

Shell growth was carried out using the same thermal decomposition protocol for both shell types, with the only variable being the composition of the cation precursor solution: Na^+/Y^{3+} for the homogeneous $NaYF_4$ shell, and Ca^{2+} for the heterogeneous CaF_2 shell, see Chapter 3, sections 3.3.1, and 3.3.2 for the full details about the methodology. The preservation of the cubic crystal structure after shell growth in both cases was confirmed by PXRD (Figure 4.2a–b). Rietveld refinement was applied for the homogeneous sample,

while Pawley refinement was used for the heterogeneous sample to avoid over-constraining the model in the presence of two closely spaced but distinct phases.

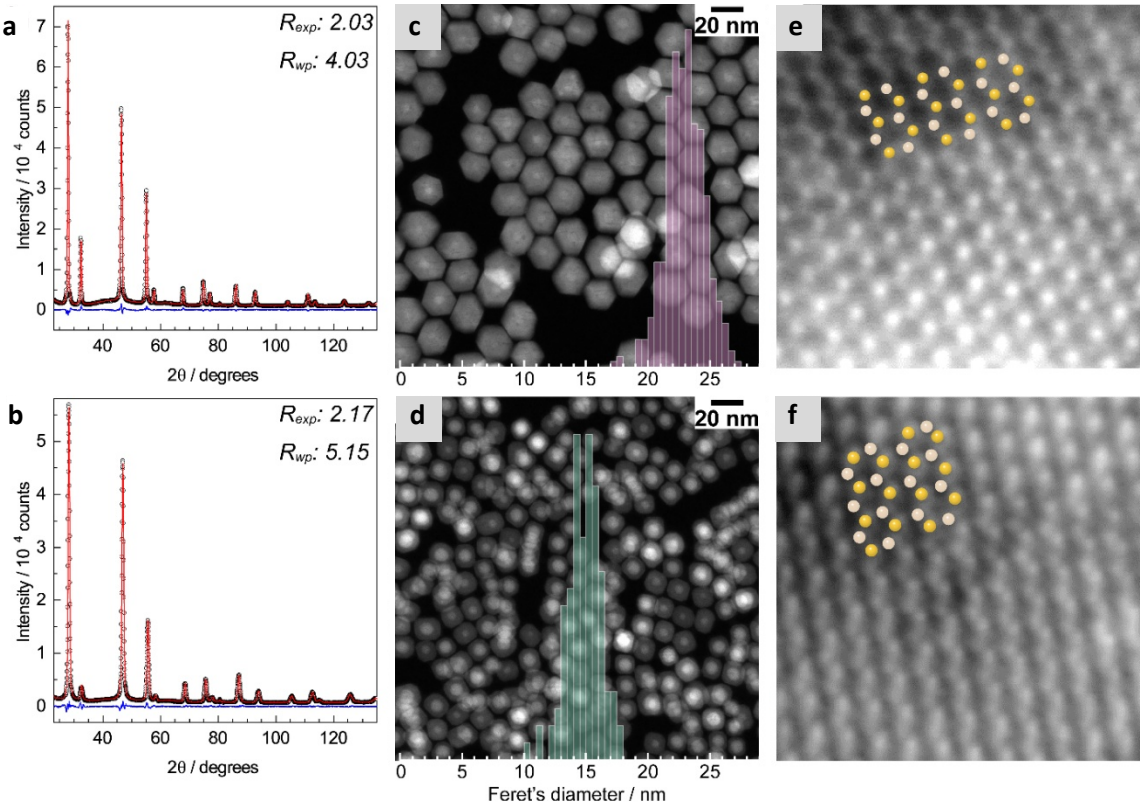


Figure 4.2. *Structural characterization of optically active α-$NaYF_4$:Yb,Er core NCs after growth of homogeneous and heterogeneous shell domains. a,b) Experimental (black open symbols) and calculated (red lines) PXRD patterns, accompanied by the difference curves (blue lines). The calculated patterns are obtained from full Rietveld refinement for the homogeneous sample (a) and Pawley refinement for the heterogeneous sample (b). The expected R factor (R_exp) and the weighted profile R factor (R_wp) are reported to assess the quality of the refinements in conjunction with visual inspection of the difference curves. Representative low-magnification HAADF-STEM images of the resulting homogeneous (c) and heterogeneous (d) core–shell NCs, overlaid with their respective size distribution histograms. (e,f) iDPC-STEM images showing atomic resolution of an individual NC, with RE^{3+} and fluorine atomic columns indicated in yellow and beige, respectively. The same batch of α-$NaYF_4$:Yb,Er core NCs (described in Figure 4.1) and identical experimental conditions were used for both shell growth processes. Reprinted with permission from Nat. Commun. 2023, 14(1), 4462. Copyright 2023. Springer Nature.*

The resulting core–shell NCs differ substantially in their morphology and mean size. The NCs with the homogeneous $NaYF_4$ shell reached 22.9 ± 3.0 nm and displayed well-defined faceted geometries (Figure 4.2c). The NCs with the heterogeneous CaF_2 shell were smaller at 14.8 ± 2.8 nm, than the homogeneous counterparts, and showed rounded-corner cubic shapes (Figure 4.2d). The HAADF-STEM contrast behavior

diverges between the two types: the homogeneous particles display a nearly uniform contrast throughout their volume, whereas the heterogeneous particles exhibit a clear and sharp contrast difference between a bright central region and a darker surrounding shell. This intensity difference in the heterogeneous core–shell reflects the difference in average atomic number (Z-contrast) between the RE-rich core and the Ca-containing shell and provides a visual suggestion of a chemical segregation in the heterogeneous system.

4.3.3 Elemental Distribution after Shell Growth

To map cation distributions at the nanoscale, EDXS was carried out on representative NCs from both sample types. Because the fluoride anion sublattice is shared by all phases involved, only the cation distribution serves as the primary structural indicator for distinguishing core from shell regions. In the homogeneous NCs, the Y^{3+} signal is broadly spread across the entire particle volume as there are Y^{3+} ions in both core and shell domains (Figure 4.3c). The Yb^{3+} distribution follows the same pattern (Figure 4.3e); instead of remaining concentrated in the inner region as it was originally incorporated only to the core, with no identifiable core or shell region. This cation redistribution of Yb^{3+} across a particle that was supposed to consist of a Yb-rich core, and a Y-only shell is direct evidence of extensive ion migration during shell growth.

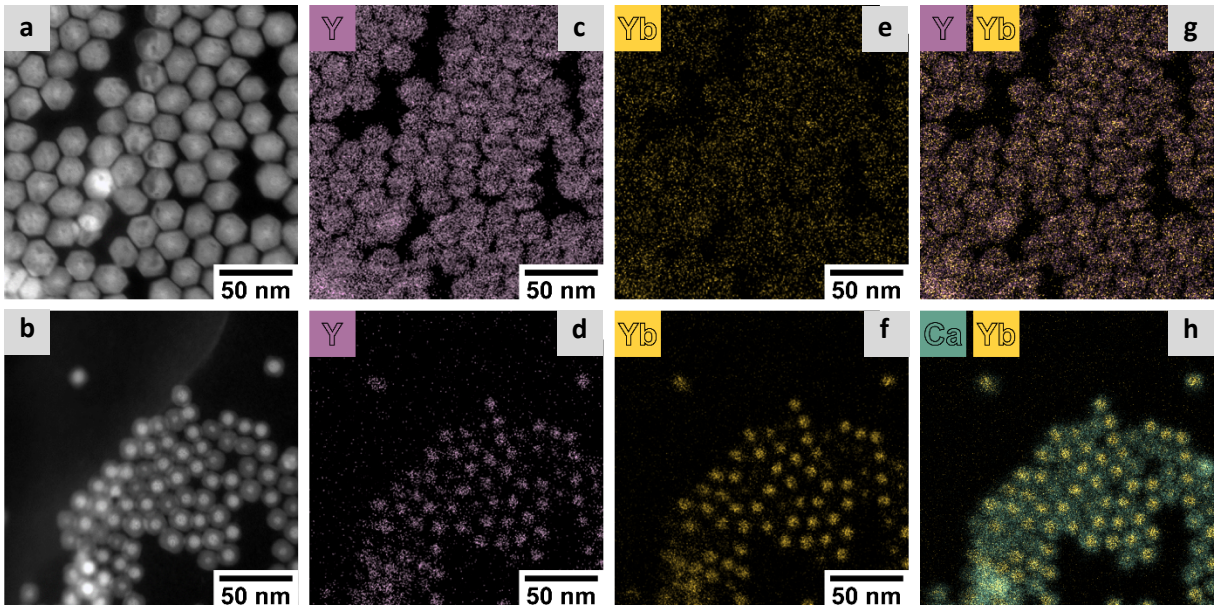


Figure 4.3. *EDXS mapping of Y^{3+} and Yb^{3+} distributions after shell growth on α-$NaYF_4$:Yb,Er core NCs. (a,c,e,g) Homogeneous α-$NaYF_4$ shell and (b,d,f,h) heterogeneous CaF_2 shell grown on optically active α-$NaYF_4$:Yb,Er core NCs. (a,b) Representative low-magnification HAADF-STEM images of the resulting core–shell NCs. (c,d) EDXS chemical maps showing the spatial distribution of yttrium. (e,f) Corresponding chemical maps for ytterbium. (g) Overlay of Yb and Er maps for the homogeneous shell configuration; (h) overlay of Yb and Ca maps for the heterogeneous shell configuration. Reprinted with permission from Nat. Commun. 2023, 14(1), 4462. Copyright 2023. Springer Nature.*

The EDXS results of the heterogeneous NCs stand in contrast. In these NCs, Y^{3+} and Yb^{3+} are localized only in the central region (Figure 4.3d,f). Meanwhile, the Ca^{2+} signal, appears predominantly in the outer shell region, as shown in the Yb^{3+}/Ca^{2+} overlay map (Figure 4.3h). Considering all the EDXS chemical maps from the heterogeneous core-shell structure, these maps confirm that the CaF_2 shell growth preserves the chemical segregation between core and shell.

4.3.4 Atomic-Scale Organization of the Core–Shell NCs

The EDXS chemical maps results were corroborated by a quantitative analysis of high-resolution high-angle annular dark-field scanning transmission electron microscopy (HR-HAADF-STEM) images, which provides chemical information at the level of individual atomic columns. Using the StatSTEM software package,[138] the projected atomic columns in each HR image were modelled as sums of Gaussian functions, and

the volumes of these Gaussians, derived from the scattering cross-sections, were used as a representation for the local average atomic number.[139]

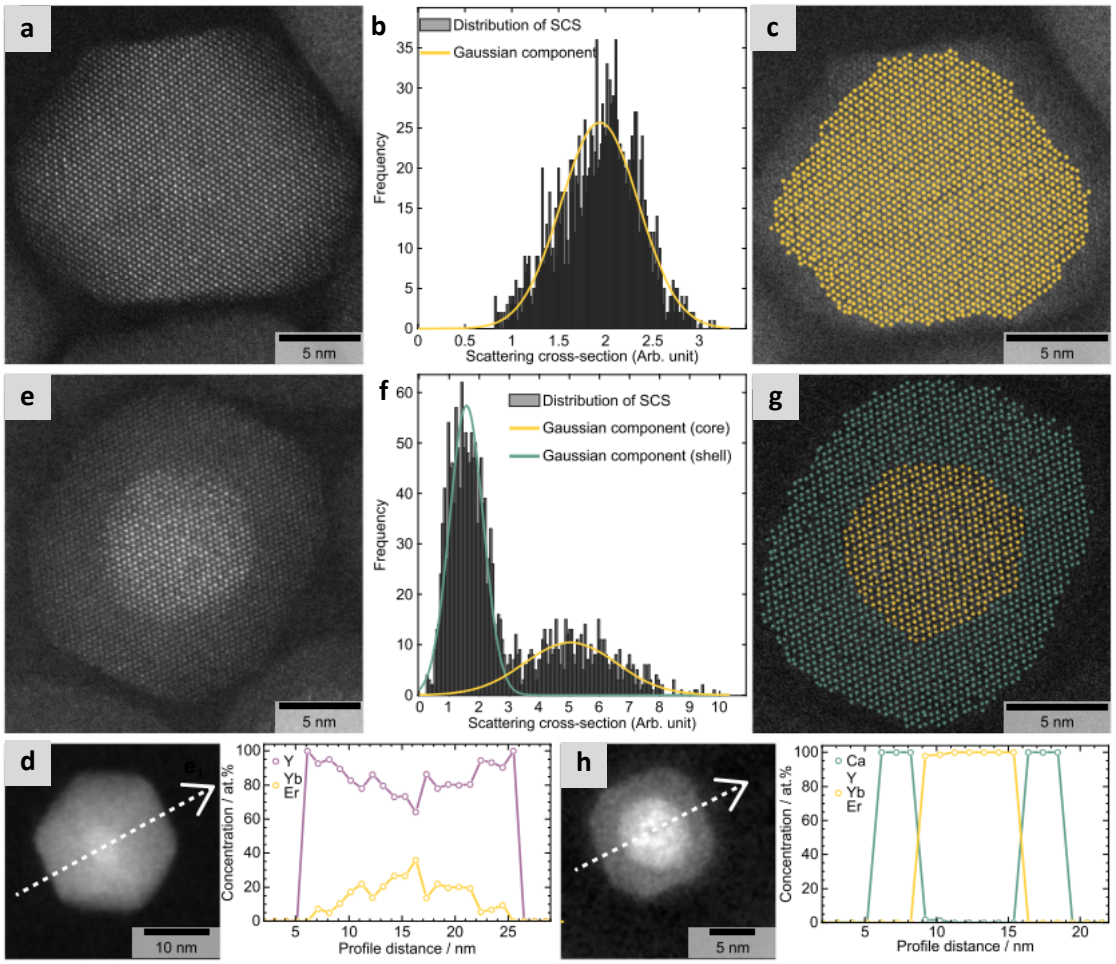


Figure 4.4. *Local chemical composition of α-$NaYF_4$:Yb,Er core NCs after the growth of homogeneous and heterogeneous shell domains. (a–d) Homogeneous α-$NaYF_4$ shell and (e–h) heterogeneous CaF_2 shell grown on optically active α-$NaYF_4$:Yb,Er core NCs. (a, e) High-resolution HAADF-STEM images of individual NCs. (b, f) Scattering cross-section histograms classified using a Gaussian mixture model, identifying distinct atomic column groupings. (c, g) Refined high-resolution HAADF-STEM images (processed using the StatSTEM software) overlaid with probabilistic maps indicating the likelihood of finding at least one Yb atom (orange dots) or one Ca atom (green dots) at each atomic column in the homogeneous (c) and heterogeneous (g) configurations. (d, h) HAADF-STEM images of individual particles paired with their respective chemical concentration profiles. In the homogeneous case (d), concentration profiles of Y and Yb/Er are shown in purple and yellow, respectively, and are representative of measurements from seven randomly selected NCs. In the heterogeneous case (h), Ca and Y/Yb/Er profiles are displayed in green and yellow, respectively, based on data from eight individual NCs. The same α-$NaYF_4$:Yb,Er core NC batch and experimental conditions (as in Figure 4.1) were used for both shell growth processes. Reprinted with permission from Nat. Commun. 2023, 14(1), 4462. Copyright 2023. Springer Nature.*

For the homogeneous NCs, the distribution of scattering cross-sections was best described by a single Gaussian component (Figure 4.4b), indicating that no chemically distinct population of atomic columns can be resolved. This is the signature of an alloyed particle, as the Yb^{3+} ions that were originally doped into the core have distributed throughout the particle to an extent where no clear chemical boundary remains. The corresponding elemental map (Figure 4.4c) shows Yb-containing columns scattered across the full NC volume rather than confined to any specific region.

The analysis of the heterogeneous NCs produces a contrasting result. The scattering cross-section histogram is clearly bimodal, requiring two Gaussian components for an adequate fit (Figure 4.4f). The lower-intensity component corresponds to atomic columns dominated by Ca^{2+} (present in the shell), while the higher-intensity component reflects columns containing at least one Yb^{3+} ion (present in the core). Mapping these two populations back onto the HR-HAADF-STEM image reveals a well-defined spatial separation, where Yb-rich columns cluster in the interior of the NCs, and Ca-rich columns form a surrounding shell domain (Figure 4.4g).

Spatially resolved EDXS line scans provide complementary chemical concentration profiles across individual particles. For the homogeneous NCs, the Y^{3+} and Yb^{3+}/Er^{3+} concentration profiles are largely flat and overlapping, apart from a thin (<1 nm) surface layer that contains only Y^{3+}ions. This pure Y^{3+} shell is too thin to constitute a fully functional passivation shell (Figure 4.4d). For the heterogeneous NCs, the Ca^{2+} and $Y^{3+}/Yb^{3+}/Er^{3+}$ profiles are sharply segregated. Ca^{2+} ions are confined to a shell region exceeding 3 nm in thickness, and the RE-containing core has a diameter of approximately 7.5 nm according to the line scan (Figure 4.4h); this size is in good agreement with the average size of the starting core NCs. The interface between the two domains is narrow and chemically abrupt, consistent with a true core–shell structure.

4.3.5 SWIR Emission Properties

The consequences of these structural differences in the optical properties were evaluated by measuring SWIR emission spectra and absolute PLQY under 980 nm excitation. All samples display the characteristic downshifting emission bands of Yb^{3+} ($^2F_{5/2} \rightarrow {}^2F_{7/2}$,

~1015 nm) and Er^{3+} ($^4I_{13/2} \rightarrow {}^4I_{15/2}$, ~1550 nm) (Figure 4.5a). The ratio of intensities and the overall emission efficiency, however, differ substantially between the two shell types.

For the Er^{3+} SWIR band specifically, the heterogeneous CaF_2 shell raises the absolute PLQY from 7% (obtained from the homogeneous $NaYF_4$ shell) to 30%, representing a more than fourfold enhancement. When the full SWIR window spanning both the Yb^{3+} and Er^{3+} emission ranges is considered, the improvement remains substantial: 17% for the homogeneous versus 41% for the heterogeneous sample. These values were measured across an excitation power range of 50–1000 mW/cm^2, confirming that the advantage of the heterogeneous structure is robust across operationally relevant irradiances.

The effect of Ce^{3+} co-doping was evaluated by preparing a separate core batch with the composition Yb/Er/Ce = 42/5/3 at.% and applying both shell types under the same conditions. Ce^{3+} is known to enhance Er^{3+} SWIR emission through a cross-relaxation process that accelerates the population of the emitting $^4I_{13/2}$ level (see section 2.1.3). As anticipated, Ce^{3+} co-doping increased the PLQY for both shell types. Still, Ce-doped NCs with a homogeneous shell (24%) still fell short of the PLQY achieved by Ce-undoped NCs with a heterogeneous shell (30%), emphasizing that suppression of ion migration through heterogeneous shelling contributes more to the optical performance than Ce^{3+} co-doping alone. The combination of Ce^{3+} co-doping with CaF_2 shell growth yielded a PLQY of approximately 50% at a low excitation power density of 60 mW/cm^2, representing the highest efficiency reported for any SWIR-emitting NC probe smaller than 15 nm.

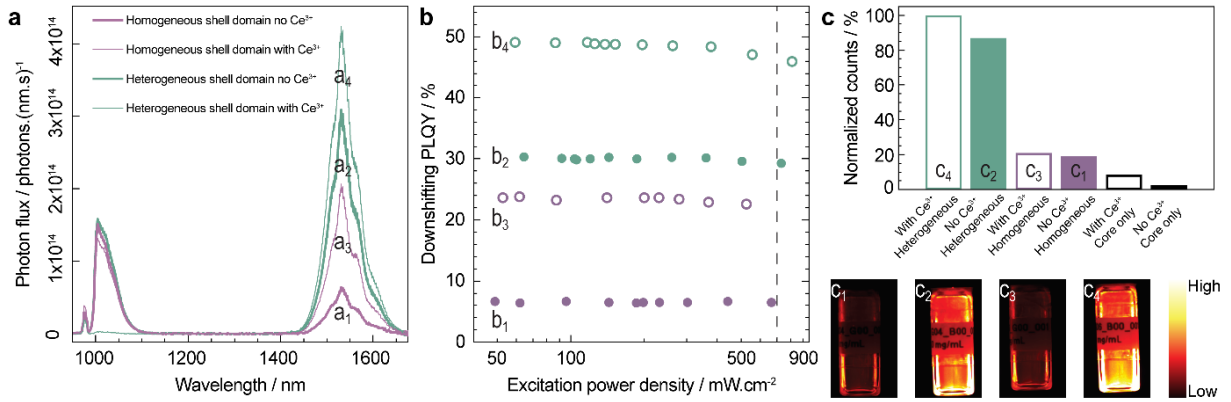


Figure 4.5. *Optical performance of α-NaYF₄:Yb,Er and α-NaYF₄:Yb,Er,Ce core NCs after the growth of homogeneous and heterogeneous shell domains. (a) Absorption-normalized downshifting emission spectra (λ_{ex} = 980 nm, power density = 200 mW/cm²) of α-NaYF₄:Yb,Er and α-NaYF₄:Yb,Er,Ce core NCs after coating with homogeneous (α-NaYF₄) and heterogeneous (CaF₂) shell layers. (b) Power-dependent absolute photoluminescence PLQY measurements for the emission range 1400–1650 nm under 980 nm excitation. Data are shown for α-NaYF₄:Yb,Er (filled symbols) and α-NaYF₄:Yb,Er,Ce (open symbols) core NCs with homogeneous (purple) and heterogeneous (green) shells, across an excitation power range of 50–1000 mW/cm². (c) Brightness measurements (normalized emission counts) under 980 nm excitation at 37 mW/cm² for α-NaYF₄:Yb,Er (solid black bar) and α-NaYF₄:Yb,Er,Ce (open black bar) cores coated with homogeneous (purple bars) and heterogeneous (green bars) shells. Lower panel: Emission images (using a 1300 nm long-pass filter) of individual core–shell NC samples: homogeneous (c1, c3) and heterogeneous (c2, c4) under 980 nm excitation at 37 mW/cm². All brightness measurements were conducted in colloidal toluene dispersions at a concentration of 10 mg/mL. Reprinted with permission from Nat. Commun. 2023, 14(1), 4462. Copyright 2023. Springer Nature.*

4.4 Discussion

To date, the majority of RE-based core–shell structures designed for SWIR downshifting have relied on homogeneous ternary alkali metal fluorides ($NaREF_4$) for both core and shell.[113,140–142] The results described in this chapter establish a clear relationship between ion migration in core–shell NCs and their photoluminescence performance. The central finding is that the outcome of shell growth is not merely determined by reaction conditions or precursor chemistry in isolation, but critically by the chemical compatibility between the core and shell materials. When a homogeneous $NaYF_4$ shell is grown on an α-$NaYF_4$:Yb,Er core, the similar crystal structure and shared cation valence might facilitate cross-boundary ion migration to such an extent that the final particle is better described as an alloyed single-phase NCs than as a core–shell heterostructure.

The effects in the optical properties are severe, the optically active sensitizer (Yb^{3+}) and activator (Er^{3+}) ions, migrated from the core into the surrounding volume, become

exposed to surface-related non-radiative quenching pathways near the NC surface. Additionally, the dilution of these ions across a larger effective volume alters the inter-ion distances and therefore the energy transfer rates of the emitting levels. Both effects contribute to the dramatically lower PLQY measured for the homogeneous samples.

It is speculated that the CaF_2 shell suppresses this redistribution through a combination of factors. The valence mismatch between Ca^{2+} and the RE^{3+}/Na^{+} cation pair that constitutes the core lattice possibly creates a thermodynamic barrier against cation exchange across the interface. Additionally, the distinct cation chemistry might mean that there is no (or reduced) driving force for mutual solubility between the core and shell domains unlike the homogeneous case, where the two phases are essentially the same material with slightly different compositions. The result is a true core–shell architecture in which the RE^{3+} ions in core is spatially isolated from the surface, precisely as intended in the design of passivated luminescent NCs.

Previous work by Wang et al. on upconversion from α-$NaYF_4$:Yb,Er/CaF_2 heterostructures noted superior performance compared to analogous homogeneous core–shell NCs and speculated that suppressed RE^{3+} migration into the shell might be responsible.[33] The data presented here provide direct structural evidence that this is indeed the mechanism. Similar logic applies to reports of enhanced ultraviolet upconversion in α-$NaYbF_4$:Tm/CaF_2 compared to α-$NaYF_4$:Yb,Tm/$NaYF_4$, where the improved performance of the heterogeneous system was attributed to higher shell crystallinity. The atom-scale characterization shown here suggests that preservation of the core integrity through suppressed ion migration is a more fundamental and more universal explanation for the performance advantage of heterogeneous core–shell architectures.

These findings also show that results from composition optimization cannot always be directly transferred from homogeneous to heterogeneous systems. The optimal doping concentrations of sensitizer and activator ions that have been established for homogeneous core–shell NCs (which are the majority of literature reported RE-based NCs) may not apply in heterogeneous systems where the ion spatial distribution is fundamentally different. In an alloyed homogeneous particle, the apparent concentration

of emitting ions in any given volume element is different from what it would be in a true core–shell structure of the same nominal composition due to the ion migration. Similarly, the shell thickness required to suppress surface quenching must be re-evaluated: in a heterogeneous system, the RE^{3+} ions remain confined to the core, so the effective core-to-surface distance is determined by the shell thickness rather than being reduced by ion migration into the shell. Further improvements could be achieved by optimizing doping concentrations and shell thickness in heterogeneous NCs. Similarly, the ideal thickness of the inert outer shell required to prevent luminescence surface quenching should be re-evaluated. This could explain why recent heterostructures designed for SWIR imaging have not achieved similar performance to those reported in this study, despite utilizing heterostructures.[72] However, this is beyond the scope of the current work due to the time-consuming nature of synthesis and atomic-scale characterization. Synthesizing series of core NCs by systematically varying the concentration of one optically active element while maintaining the others constant and then shelling the optically-active NC with varying thicknesses, is a complex task. The emergence of automated synthesis laboratories coupled with artificial intelligence techniques in the field of inorganic NCs may soon address this challenge.[143]

Looking forward, CaF_2 is a single example of what could be a broad class of compatible shell materials that prevent ion redistribution through valence mismatch or structural dissimilarity. Heterogeneous core–shell structures still represent a small minority of reported systems. The results in this chapter make a strong case that this minority deserves far greater attention, and that the deliberate engineering of chemical incompatibility at the core–shell interface is a more powerful strategy for maximizing SWIR emission efficiency than further incremental optimization of doping concentrations within existing homogeneous architectures. The findings presented here make a compelling case that this minority warrants far greater attention, and that the deliberate engineering of chemical incompatibility at the core–shell interface is a more powerful strategy for maximizing SWIR emission efficiency than continued incremental optimization of doping concentrations within existing homogeneous architectures.

4.5 Summary

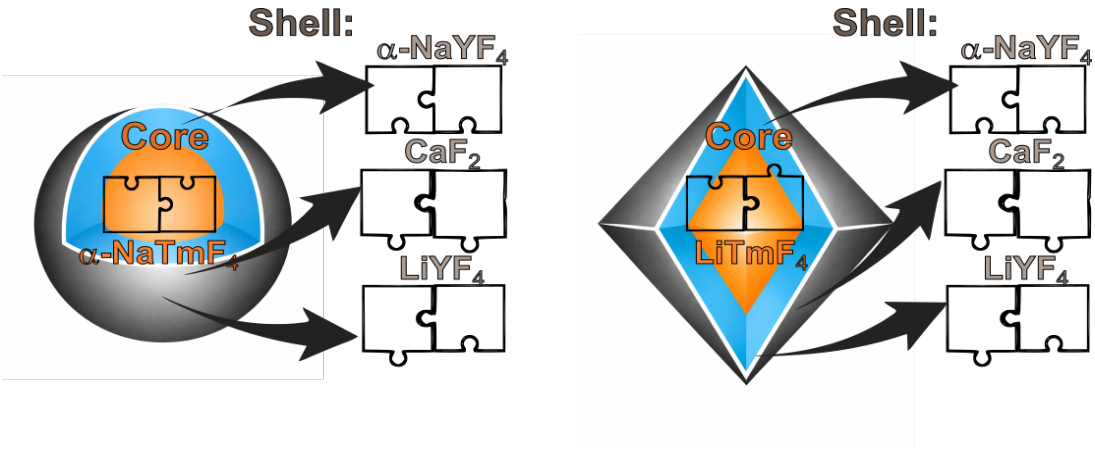
This chapter investigated the structural and optical consequences of cation intermixing in RE-based core–shell NCs by comparing homogeneous ($NaYF_4$) and heterogeneous (CaF_2) shell growth on the same α-$NaYF_4$:Yb,Er(Ce) core NCs.

The key findings of this chapter show that the shell material strongly determines the chemical organization and optical performance of Er^{3+}-based core–shell NCs. Homogeneous $NaYF_4$ shell growth promoted extensive Yb^{3+}/Er^{3+} redistribution, converting the intended core–shell structure into an alloyed NC with no chemically distinct domains. In contrast, heterogeneous CaF_2 shell growth preserved an abrupt core–shell interface, with RE^{3+} ions confined to the core and Ca^{2+} to the shell.

This suppression of intermixing directly improved the SWIR emission efficiency. The use of a CaF_2 shell increased the Er^{3+} SWIR PLQY from 7% to 30%, and its combination with Ce^{3+} co-doping reached approximately 50% PLQY at 60 mW/cm^2. Importantly, the use of heterogeneous shell alone outperformed Ce^{3+} co-doping with a homogeneous shell, demonstrating that preserving the core–shell architecture is more critical for high optical performance than optimizing internal energy-transfer pathways alone.

Collectively, these results establish that cation intermixing during shell growth is not merely a structural curiosity but a decisive factor governing the optical performance of RE-based core–shell NCs. The use of cube-shaped NCs with a simple crystal structure provided the geometrical clarity needed to resolve longstanding ambiguities in the interpretation of chemical maps from spherical particles, and the direct comparison between homogeneous and heterogeneous shells on the same core material isolated the shell chemical composition as the critical variable. The deliberate engineering of the core-shell interface, as demonstrated here through the CaF_2 shell, emerges as a powerful and generalizable strategy (see follow up chapters) for obtaining high-efficiency SWIR emission from fluoride NCs, with direct implications for the development of next-generation biological imaging probes.

5. Influence of Core–Shell Material Combinations for Enhancing Tm^{3+} Emission Beyond 1600 nm



The content of this chapter has been published in a separate work.

***Arteaga Cardona, F.**; Madirov, E.; Popescu, R.; Wang, D.; Busko, D.; Ectors, D.; Kübel, C.; Eggeler, Y. M.; Arús, B. A.; Chmyrov, A.; Bruns, O. T.; Richards, B. S.; Hudry, D. Dramatic Impact of Materials Combinations on the Chemical Organization of Core–shell Nanocrystals: Boosting the Tm^{3+} Emission above 1600 Nm. ACS Nano 2024. https://doi.org/10.1021/acsnano.4c07932.*

Contributions

The author prepared the samples, performed the XRD measurements, designed the figures, and analyzed the results. Eduard Madirov and Dmitry Busko measured and analyzed the optical properties of the prepared samples. Radian Popescu and Yolita M. Eggeler were in charge of the EM characterizations and analysis, including the chemical maps and line scans. Di Wang and Christian Kübel obtained chemical maps for the prepared NCs. Dominique Ectors performed the detailed analysis of the PXRD patterns via Pawley refinement and aided with the calculation of theoretical diffraction patterns. Bryce S. Richards supervised the project and provided scientific guidance. Damien Hudry conceived the initial idea, provided guidance during the project, contributed intellectual input, and wrote the final version of the manuscript.

5.1 Motivation

As discussed in the previous chapter, the heterostructure α-$NaYF_4$:Yb,Er,Ce/CaF_2 successfully achieved a clear core–shell phase segregation, effectively preventing cation intermixing. This led to the formation of a pure shell region of around 3 nanometers thick, which efficiently protected the optically active core from surface quenching and markedly enhanced PLQY. However, this result raised important questions, most notably, whether such phase segregation is an intrinsic consequence of heterostructures and how it would be affected by modifying the chemical and structural mismatch between core and shell materials.

To explore these questions, this chapter investigates the extent to which intermixing is altered when combining core and shell materials with non-matching crystal structures and different chemical compositions. The goal was to determine whether the same level of intermixing suppression observed in α-$NaYF_4$/CaF_2 systems could be retained in more heterogeneous material combinations. The selection of suitable materials was non-trivial as materials with a large lattice mismatch often promote separate nucleation rather than epitaxial shell growth. $LiREF_4$ was ultimately chosen as a good candidate, as it preserved the F^- anionic network, which could potentially support epitaxial growth, despite its lower symmetry. While $LiREF_4$ shares similar a and b lattice parameters with cubic α-$NaREF_4$, it exhibits a significantly different c parameter resulting from the smaller Li^+ ions incorporated into the crystal lattice.

To systematically evaluate structural compatibility and intermixing behavior, combinations of α-$NaREF_4$ and $LiREF_4$ were synthesized in both core–shell configurations: α-$NaREF_4$/$LiREF_4$ and $LiREF_4$/α-$NaREF_4$. In addition, CaF_2 shells were grown on both types of the cores NCs as control systems, due to their previously demonstrated stability and non-intermixing behavior.

Thulium was selected as the optically active RE^{3+} ion in the core NCs. While Tm^{3+} is commonly used for SWIR imaging for its emission around 1400 nm, the deeper Tm^{3+} emission at ~1800 nm is potentially more advantageous for biological imaging, as it benefits from further reduced tissue scattering compared to the widely used 1550 nm emission of Er^{3+}. Moreover, the 800 nm excitation wavelength of Tm^{3+} lies before a strong water absorption band from 900 - 1000 nm, making it favorable for *in-vivo* applications. A

100% Tm^{3+} concentration was employed to exploit self-sensitized excitation, enabled by its relatively strong absorption cross-section at 800 nm. Having 100% of Tm^{3+} ions also benefitted the desired ~1800 nm emission, as that emission results from cross-relaxation processes between Tm^{3+} ions, which are promoted at high dopant concentrations.

Finally, this study also provides insight into whether a lower symmetry crystal field leads to higher emission efficiency than high-symmetry hosts like α-$NaREF_4$, as predicted by Judd–Ofelt theory. Although this hypothesis has been supported in the literature, many of the systems used to validate it may suffer from cation intermixing, casting doubt on the reliability of the conclusions. By ensuring phase-pure systems with minimal intermixing, this study offers a clearer evaluation of symmetry effects on SWIR emission.

5.2 Overview

Over two decades ago, the first reports of RE-based core–shell NCs marked a significant increase in the interest of luminescent nanomaterials.[46,47] The distinctive upconversion, downconversion, and downshifting photoluminescent properties of these materials quickly garnered substantial interest from the scientific community.[104,144,145] The previous chapter demonstrated that the chemical nature of the shell can strongly influence cation intermixing and, consequently, the SWIR emission efficiency of Er^{3+}-based α-$NaYF_4$ core–shell NCs. However, it remained unclear whether the same design principles could be extended to other emitters and host structures, particularly to Tm^{3+}-based materials.

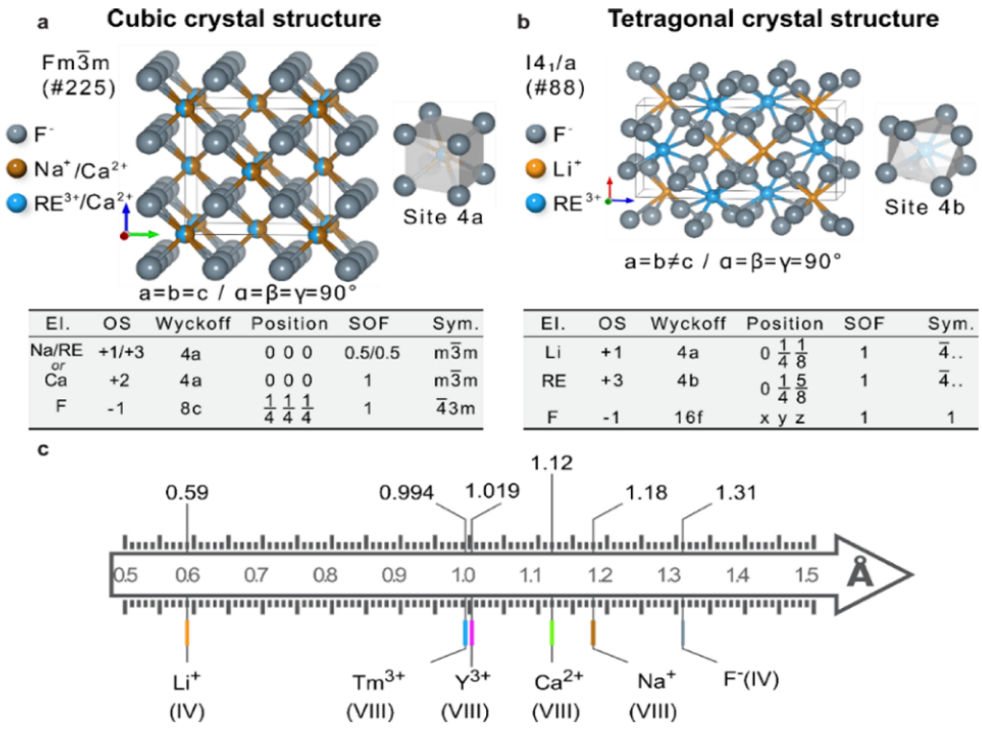
Tm^{3+}-based RE^{3+} NCs are of interest because the $^3F_4 \rightarrow {}^3H_6$ transition produces photons at the far end of the SWIR region. As discussed in chapters 1 and 2, this spectral region is attractive for bioimaging because tissue scattering decreases further at longer wavelengths. Nevertheless, efficient RE-based probes operating in this range remain comparatively limited.[30,105,117,120,122] Therefore, extending the shell-design strategies that limit cation intermixing to Tm^{3+}–based NCs could provide a valuable pathway toward making more efficient luminescent probes operating at the far end of the SWIR region.

This chapter therefore examines how different core–shell material combinations affect the spatial distribution of Tm^{3+} ions and the resulting downshifting emission above 1600 nm.

Cubic α-$NaTmF_4$ and tetragonal $LiTmF_4$ were selected as optically active core materials and combined with $NaYF_4$, CaF_2, and $LiYF_4$ shells. In this context, homogeneous shells refer to shell materials with similar crystal structure and chemical composition to the core, whereas heterogeneous shells differ substantially in crystal structure and/or chemical composition. By comparing these combinations, the chapter evaluates whether phase segregation, partial confinement, or extensive intermixing is favored by specific material combinations. The results reveal that the shell material does not act merely as a passive surface barrier but directly determines the internal chemical organization of the NCs and, in turn, the Tm^{3+} SWIR emission efficiency. These findings are expected to encourage a new era of optimizing the optical properties of homo- and heterostructured RE-based core–shell NCs. This will enable them to meet the challenge of creating highly efficient SWIR-emitting nanoprobes for *in vivo* imaging.

5.3 Results

Figure 5.1 summarizes the two crystal structures used as the basis for the investigated material combination. Additionally, it illustrates the corresponding ionic radii for the elements used in the NCs. α-$NaTmF_4$ and tetragonal $LiTmF_4$ were selected as the optically active core NCs, while α-$NaYF_4$, CaF_2, and $LiYF_4$ were selected as protective optically inert shell materials. The primary goal is to understand how different material combinations affect the chemical organization of the resulting homo- and heterostructured NCs, as well as its effect on the downshifting emission properties of Tm^{3+} above 1600 nm.



El.	OS	Wyckoff	Position	SOF	Sym.
Na/RE or Ca	+1/+3	4a	0 0 0	0.5/0.5	m3̄m
	+2	4a	0 0 0	1	m3̄m
F	-1	8c	1/4 1/4 1/4	1	4̄3m

El.	OS	Wyckoff	Position	SOF	Sym.
Li	+1	4a	0 1/4 1/8	1	4̄..
RE	+3	4b	0 1/4 5/8	1	4̄..
F	-1	16f	x y z	1	1

Figure 5.1 Representative crystal structures illustrating homogeneous and heterogeneous material combinations. *(a) Cubic and (b) tetragonal crystal structures used as the basis for six different material combinations designed for the synthesis of core/shell NCs. These combinations are discussed in detail in the main text. For each structure, the corresponding unit cell is shown along with the symmetry of the metal site (RE = Tm or Y in this study). Tables below the unit cells summarize key crystallographic parameters, including Wyckoff positions, atomic coordinates, site occupation factors (SOFs), and site symmetry. (c) Ionic radii of all investigated cations, based on Shannon's data,*[146] *are provided according to the coordination numbers present in the selected materials. Reprinted with permission from ACS Nano 2024, 18, 38, 26233–26250. Copyright 2024 American Chemical Society.*

Although understanding the detailed mechanism governing shell growth would be highly valuable, they fall outside the scope of this thesis. Instead, only static characterizations performed on the final products are presented. To ensure a fair comparison, all material combinations were synthesized under identical experimental conditions (solvent, surfactant, precursor, aging time, and temperature), as detailed in the chapter 3 *Materials and Methods*.

5.4 α-$NaTmF_4$ Core Based Material Combinations

5.4.1 Starting α-$NaTmF_4$ Core NCs Characterizations

The α-$NaTmF_4$ core NCs were first analyzed by PXRD to confirm their structural characteristics prior to the shell growth. PXRD pattern confirms that the synthesized α-$NaTmF_4$ core NCs exhibits the anticipated cubic structure, and no evidence of secondary phases (Figure 5.2a, black open symbols) were found. Pawley refinement (Figure 5.2, solid line) using a single cubic $Fm\bar{3}m$ phase accurately describes the experimental PXRD pattern, employing the WPPM method with a spherical isotropic model.[135,136] The calculated lattice parameter for α-$NaTmF_4$ was calculated to be 5.4762 Å and reveals an isotropic crystallite size of 9.1 ± 2.4 nm. This result aligns well with the mean size of 8.6 ± 2.0 nm obtained from HAADF-STEM images. These synthesized α-$NaTmF_4$ NCs serve as the initial seeds for creating the following material combinations, with α-$NaYF_4$, CaF_2, and $LiYF_4$.

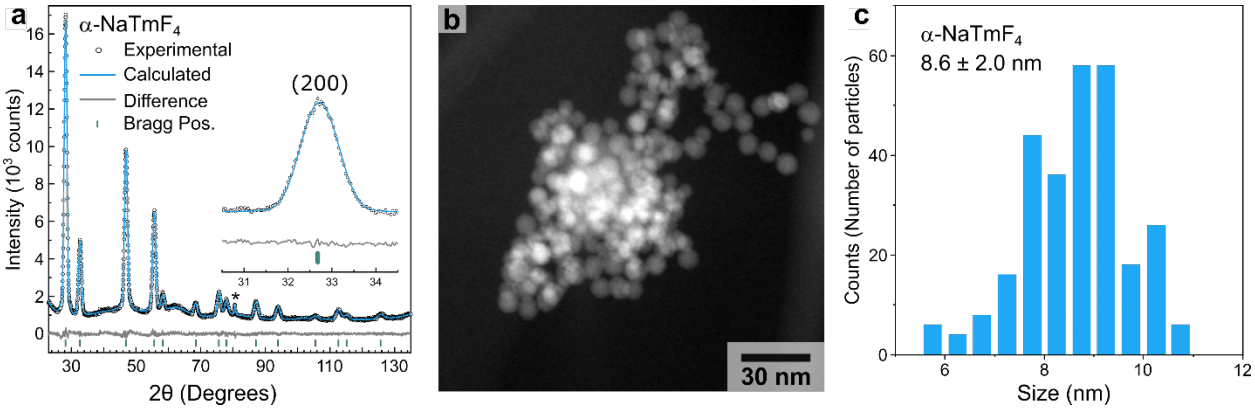


Figure 5.2 *Structural characterization of the α-$NaTmF_4$ core NCs used as seeds for homogeneous and heterogeneous material combinations. (a) Experimental PXRD pattern (black open symbols) and corresponding Pawley refinement (colored solid line). The difference between the experimental and calculated patterns is shown as a gray line, with Bragg peak positions indicated by green vertical bars. The peak marked with an asterisk (*) at approximately 80° arises from the (911)-oriented low-background silicon wafer on which the NCs were deposited (Figure 3.3), rather than from the cubic NCs themselves. This contribution was appropriately modeled using the background signal of the bare silicon wafer. The inset provides a magnified view of the (200) reflection, whose significance is addressed in the main text. (b) Representative low-magnification HAADF-STEM image. (c) Size distribution histogram obtained from the analysis of over 300 individual particles from various HAADF-STEM images. The error bars represent two standard deviations (2σ). Reprinted with permission from ACS Nano 2024, 18, 38, 26233–26250. Copyright 2024 American Chemical Society.*

5.4.2 Homogeneous and Heterogeneous Material Shell Combinations Derived from α-$NaTmF_4$

The homogeneous combination of α-$NaREF_4$ with $NaYF_4$ is a commonly studied system. The PXRD pattern for α-$NaTmF_4$/$NaYF_4$ indicates the presence of two phases: cubic (99 wt %) and hexagonal (1 wt %). Given the very low concentration of the hexagonal phase, it is disregarded in the subsequent analysis. The Bragg peaks associated with the cubic phase are particularly sharper compared to those of the pure α-$NaTmF_4$ core NCs, suggesting a coherent growth of the NCs (Figure 5.3a). Pawley refinement reveals an increased lattice parameter (a = b = c = 5.5219 Å) relative to the starting core NCs (a = b = c = 5.4762 Å). The coherent domain size calculated with the WPPM approach also increases to 21.4 ± 1.6 nm (9.1 ± 2.4 nm for the core).

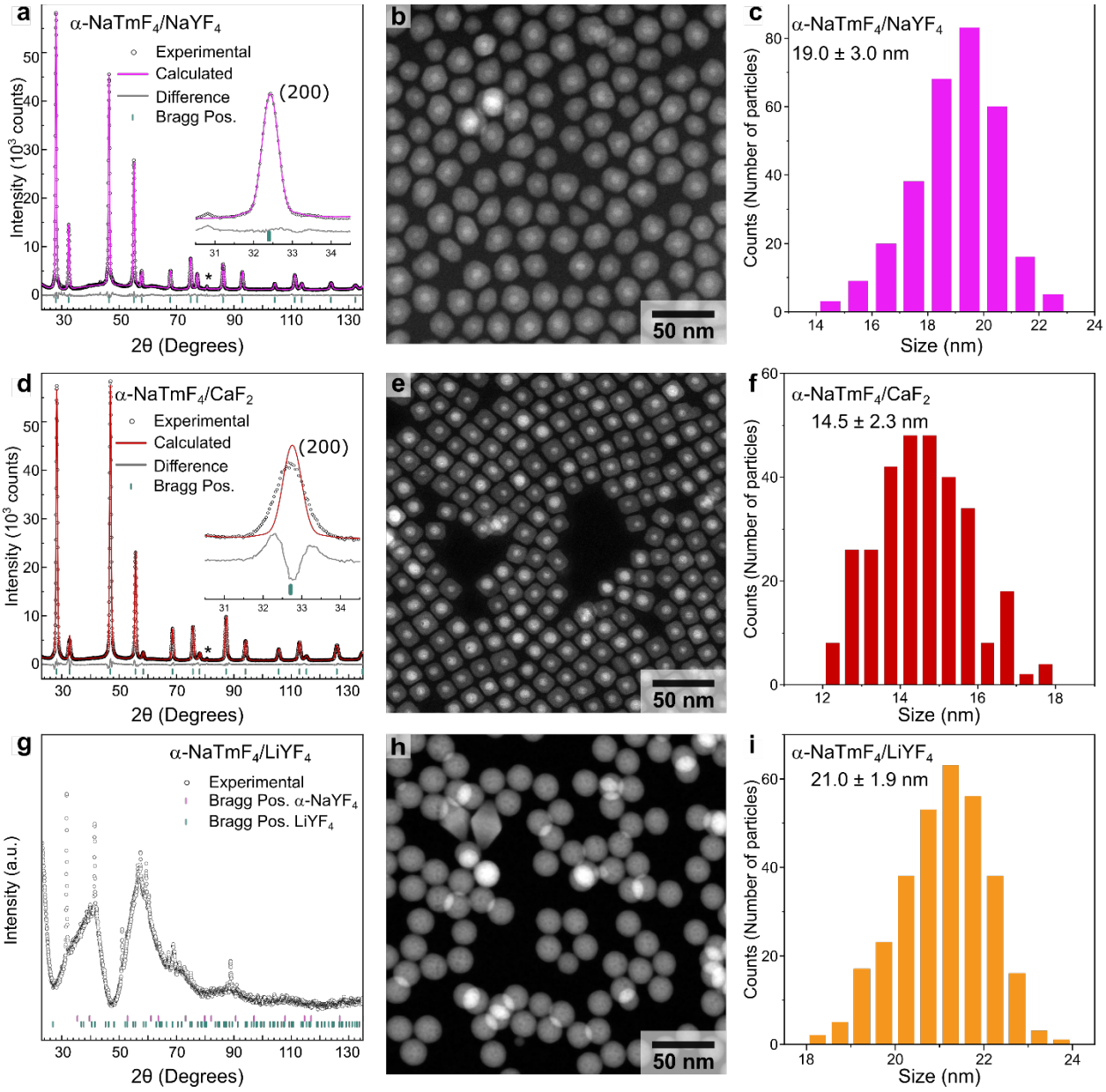


Figure 5.3 *Structural characterization of α-$NaTmF_4$ core NCs combined with different shell materials: cubic α-$NaYF_4$ (homogeneous combination – top row), cubic CaF_2 (heterogeneous combination – middle row), and tetragonal $LiYF_4$ (heterogeneous combination – bottom row). (a, d, g) Experimental PXRD patterns (black open symbols) and corresponding Pawley refinements (colored solid lines). Refinements are shown for the homogeneous ($NaYF_4$) and the first heterogeneous (CaF_2) combinations. The difference between experimental and calculated PXRD patterns is plotted in gray, and green vertical bars indicate Bragg peak positions. The peak marked with an asterisk (*) near 80° originates from the (911)-oriented low-background silicon wafer used as a substrate for drop-casting the NCs (Figure 3.3), rather than from the cubic NCs themselves. (Insets in a and d) Magnified views of the (200) reflection, the significance of which is discussed in the main text. (b, e, h) Representative low-magnification HAADF-STEM images. (c, f, i) Size distribution histograms obtained by analyzing at least 300 individual particles from multiple HAADF-STEM images. The error bars correspond to two standard deviations (2σ). Reprinted with permission from ACS Nano 2024, 18, 38, 26233–26250. Copyright 2024 American Chemical Society.*

HAADF-STEM imaging shows isotropic particles with a subtle contrast between the inner and outer regions. The overall size distribution histogram yields a mean size of 19.0 ± 3.0 nm, consistent with PXRD measurements. Despite the limited contrast, it was possible to obtain a “core only” histogram from the core-shell NCs (Figure 5.4, left), which is shifted toward smaller sizes, in comparison to the initial histogram obtained for the core NCs.

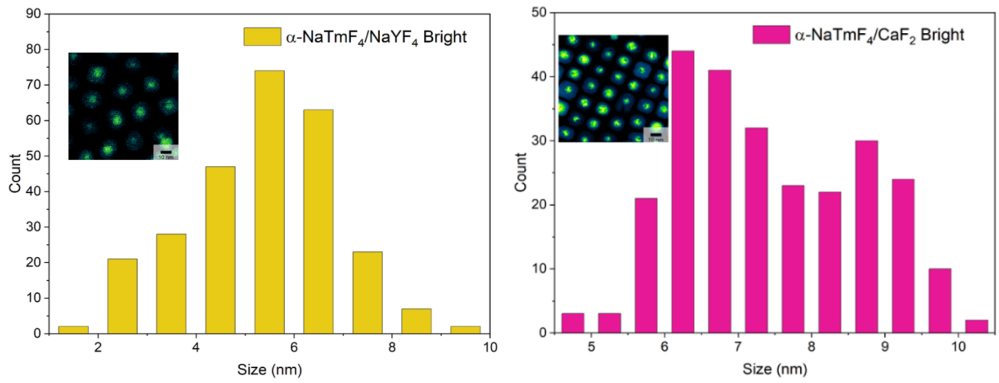


Figure 5.4 *Size distribution of the core region in α-NaTmF₄/NaYF₄ (left), α-NaTmF₄/CaF₂ (right) NCs. Size histogram showing the distribution of the core dimensions in α-NaTmF₄/CaF₂ NCs. A contrast-enhancing filter was applied to the HAADF-STEM images to improve visualization of the core–shell interface and allow accurate measurement of the core region. The inset presents an example of the filtered image used to define and measure the core dimensions for the histogram analysis.*

Moving to the heterostructured α-$NaTmF_4/CaF_2$, the PXRD pattern (Figure 5.3d, open symbols) shows a single cubic phase, without secondary phases. Despite the larger ionic radius of Ca^{2+} ($rCa^{2+}_{(VIII)} = 112\,pm$) compared to Y^{3+} ($rY^{3+}_{(VIII)} = 102\,pm$), Pawley refinement (Figure 5.3d, solid line) confirms that the lattice parameter (a = b = c = 5.4706 Å) remains nearly unchanged compared to the starting core NCs; while the calculation of the coherent domain size, using an isotropic model on the WPPM approach, increases to 16.4 ± 5.0 nm. Unlike the core NCs and homogeneous material combination, the Pawley refinement struggles to accurately model specific Bragg reflections such as (200) [Figure 5.3d, inset], (222), (420), and (600); which will be discussed later at the “*X-ray Diffraction Analysis of Core–Shell Phase Composition*” subsection. HAADF-STEM imaging reveals the formation of monodisperse cubes featuring rounded corners (Figure 5.3e), along with a distinct contrast between the inner and outer sections of the particles. The size distribution histogram (Figure 5.3f) indicates an average size of 14.5 ± 2.3 nm, consistent with the crystallite size determined via PXRD. The notable contrast difference

between the inner and outer particle regions facilitates the extraction of a precise size distribution histogram focusing solely on the brighter "core" region (Figure 5.4, right), which closely matches the size distribution histogram of the original core NCs (Figure 5.2c).

The PXRD pattern of the second heterogeneous combination, α-$NaTmF_4$ with $LiYF_4$, displays unusual characteristics, including the combination of extremely broad and relatively sharp peaks (Figure 5.3g). The broad peaks likely originate from the original α-$NaTmF_4$ cubic phase, which has been fragmented into very small crystallites within the tetragonal phase; meanwhile the sharper peaks confirm the formation of the tetragonal phase $LiYF_4$. The corresponding overview HAADF-STEM image corroborates the fragmentation of the initial core domain, showing a consistent contrast across the particles (Figure 5.3h), which are mostly spherical and have a mean size of 21.0 ± 1.9 nm (Figure 5.3i). Based on the PXRD and HAADF-STEM results, it is safe to assume that this sample is a full alloy; hence, further structural characterization of the heterogeneous material combination α-$NaTmF_4$/$LiYF_4$ was not conducted.

5.4.3 Homogeneous and Heterogeneous Material Shell Combinations Derived from α-$NaTmF_4$: Chemical organization

EDXS chemical mapping offers a straightforward approach to initially assess cation distribution within homogeneous and heterogeneous material combinations. Tm^{3+} EDXS chemical maps are particularly valuable, as Tm^{3+} should ideally be exclusive to the core in both material types; therefore, modifications in Tm^{3+} distribution can be readily identified through EDXS chemical map analysis. The EDXS maps reveal a distinct contrast in Tm^{3+} distribution between homo- (Figure 5.5a,b) and heterostructured (Figure 5.5i,j) NCs, with the homostructure exhibiting an intermixed interface. Subtle but clear differences are also observed in the Y^{3+} and Ca^{2+} EDXS maps of shell elements. In the heterogeneous combination, dark voids align with the localized Tm^{3+} distribution; this effect is minimal in the homogeneous combination's Y^{3+} distribution. Superimposing core- and shell-confined elements EDXS maps hint at alloy formation in the homogeneous combination (Figure 5.5d). Conversely, the heterogeneous combination likely forms particles with a distinct core–shell structure (Figure 5.5l).

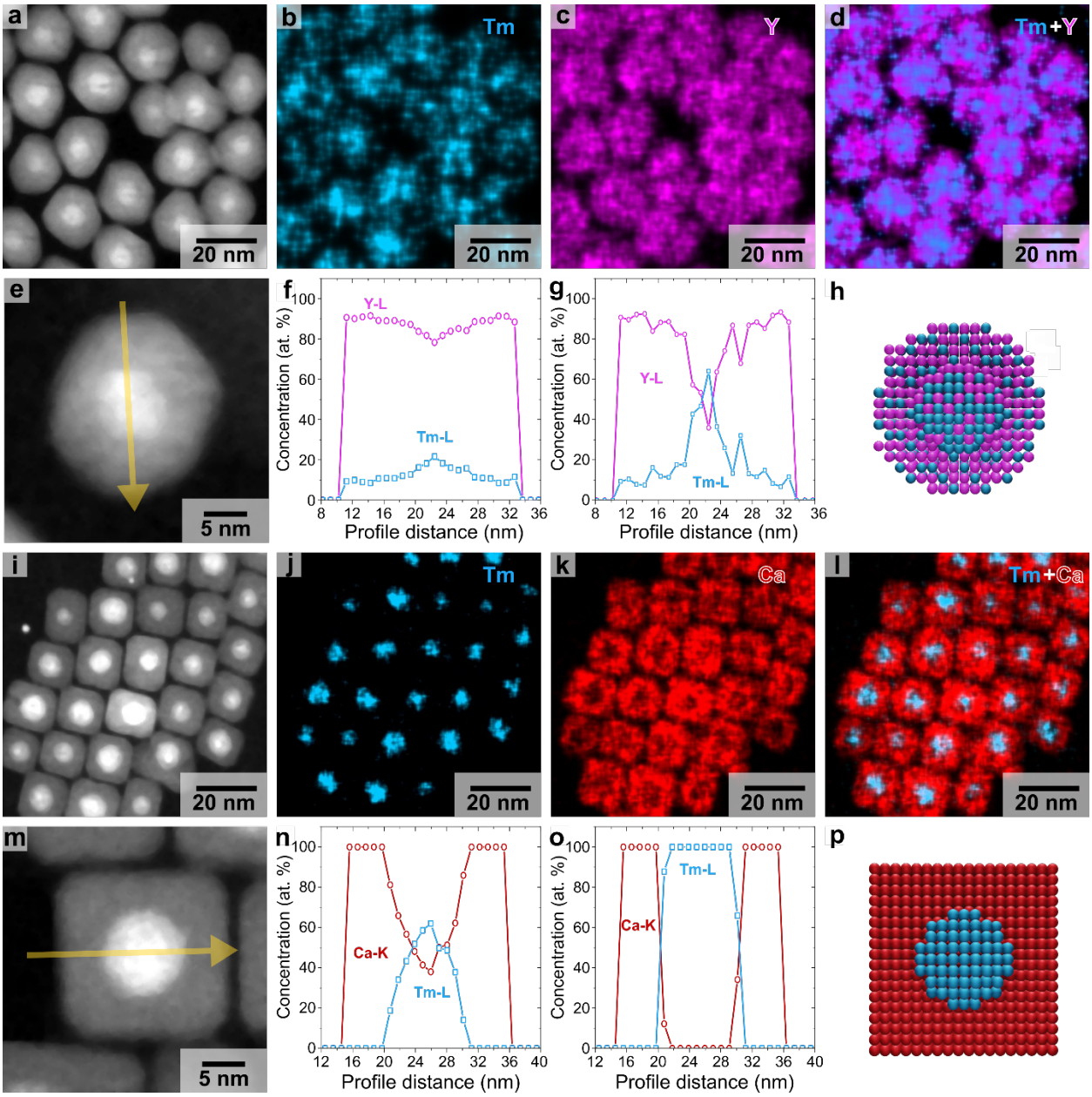


Figure 5.5 *Chemical analysis of α-$NaTmF_4$ core NCs combined with cubic α-$NaYF_4$ (homogeneous combination – first and second rows) and cubic CaF_2 (heterogeneous combination – third and fourth rows). (a, i) HAADF-STEM images of the regions selected for EDXS spectroscopy mapping. (b–d, j–l) Corresponding elemental maps of Tm (Tm-Lα line), Y (Y-L line), and Ca (Ca-Kα line), along with their overlay images for the homogeneous (b–d) and heterogeneous (j–l) combinations. (e, m) HAADF-STEM images of individual particles used for EDXS line-scan analysis (indicated by yellow arrows). (f, n) Normalized raw elemental profiles obtained from line-scan analysis. (g, o) Calculated elemental profiles using the subshell approach for the homogeneous (e–g) and heterogeneous (m–o) combinations. (h, p) Schematic representations showing the most probable cation distributions for the homogeneous and heterogeneous material combinations. Tm, Y, and Ca are represented in blue, magenta, and red, respectively. Reprinted with permission from ACS Nano 2024, 18, 38, 26233–26250. Copyright 2024 American Chemical Society.*

Chemical mapping results can be enhanced through EDXS line scans, which yield chemical concentration profiles along a line through the particle center, using 0.25 and 1 nm probe and step sizes, respectively. While limited to a single line, this provides chemical information with approximately 1 nm local precision. It is crucial to recognize that line scan EDXS spectra quantification results in "overlapped" chemical concentration profiles of the core and the shell, averaged along the electron beam's path. Thus, raw chemical concentration profiles require mathematical processing to derive localized chemical composition, correcting for the outermost "subshell" domain contribution (not the same shell as for the structures).[46,124]

Consequently, quasi-spherical/elliptical core and shell geometries were applied to the homogeneous material combination, while quasi-spherical core and cubic shell geometry were used for the heterogeneous material combination. While these geometries are idealizations, they provide reasonable approximations of actual shapes. To account for deviations from ideal geometries and particle orientation relative to the electron beam, a minimum of ten particles were analyzed per material combination.

The normalized raw chemical profiles of Tm^{3+} and Y^{3+}, acquired for the homogeneous material combination, reveal the presence of Tm^{3+} extending beyond the core region's spatial boundaries, detected up to the particle edges (Figure 5.5f). This observation aligns perfectly with the EDXS map of Tm^{3+} (Figure 5.5b).

Application of the subshell approach to the raw normalized concentration profiles of Tm^{3+} and Y^{3+} reveals a fully alloyed NCs (Figure 5.5g,h). Particularly, neither pure core nor pure shell domains are detected in the homogeneous material combination. This contrasts sharply with the Tm^{3+} and Ca^{2+} chemical profiles for the heterogeneous material combination, which are consistent with the formation of a core−shell structure featuring pure Tm-core and Ca-shell regions (Figure 5.5m). This finding supports the qualitative results obtained from EDXS mapping (Figure 5.5n).

5.5 $LiTmF_4$ Core Based Material Combinations

5.5.1 Starting $LiTmF_4$ Core NCs Characterizations

PXRD analysis of $LiTmF_4$ core NCs confirms the characteristic tetragonal structure, without any evidence of additional phases. The experimental PXRD pattern (Figure 5.6a, open symbol) aligns with a Pawley refinement (Figure 5.6a, solid line) utilizing a single tetragonal phase ($I4_1/a$). The synthesized $LiTmF_4$ core NCs exhibit lattice parameters of a = b = 5.14971 Å and c = 10.6507 Å. The Pawley refinement, employing an elliptical anisotropic model with the double Voigt approach,[147] yields anisotropic crystallite sizes of 14.6 ± 1.8 nm and 19.4 ± 2.1 nm for the short and long axes, respectively. These measurements correlate with the particle size distribution derived from HAADF-STEM images, with mean sizes of 14.7 ± 2.5 nm and 20.0 ± 2.9 nm for the short and long axes (Figure 5.6c), respectively. These synthesized $LiTmF_4$ NCs are used as the initial seeds for preparing material combinations with α-$NaYF_4$, CaF_2, and $LiYF_4$.

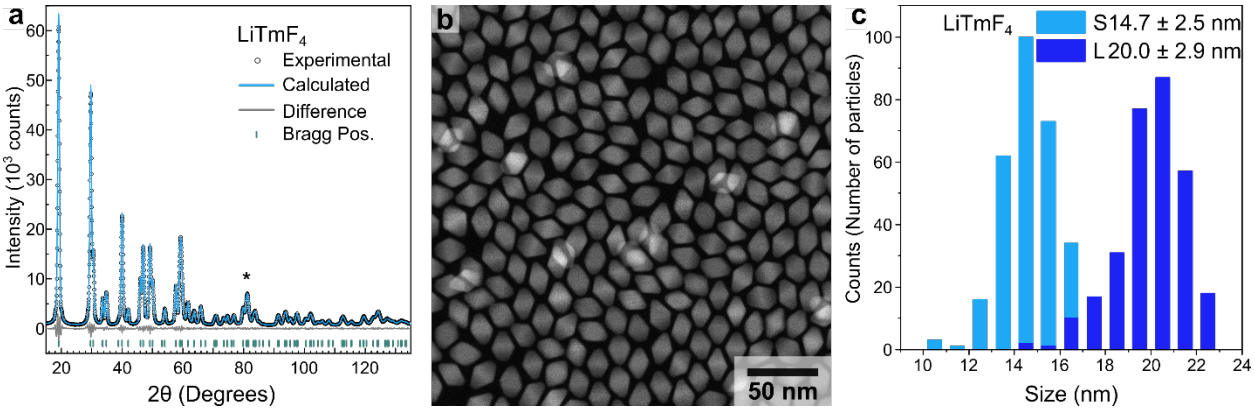


Figure 5.6 *Structural characterization of $LiTmF_4$ core NCs used as seeds for homogeneous and heterogeneous material combinations. (a) Experimental PXRD pattern (black open symbols) and corresponding Pawley refinement (colored solid line). The peak marked with an asterisk (*) near 80° originates from the (911)-oriented low-background silicon wafer used as a substrate for drop-casting the NCs (Figure 3.3), rather than from the cubic NCs themselves. The difference between the experimental and calculated patterns is shown in gray, with Bragg peak positions indicated by green vertical bars. (b) Representative low-magnification HAADF-STEM image. (c) Size distribution histograms for both the short (S) and long (L) axes, reflecting the anisotropic shape of the particles. At least 300 individual NCs from various HAADF-STEM images were analyzed. The error bars represent two standard deviations (2σ). Reprinted with permission from ACS Nano 2024, 18, 38, 26233–26250. Copyright 2024 American Chemical Society.*

5.5.2 Homogeneous and Heterogeneous Material Shell Combinations Derived from $LiTmF_4$

The PXRD pattern of the first heterogeneous material combination with $NaYF_4$ reveals a distinct $Fm\bar{3}m$ cubic phase (Figure 5.7a, open symbols), completely overshadowing the initial tetragonal phase ($I4_1/a$). Pawley refinement of this pattern yields a lattice parameter of 5.52321 Å for the cubic phase (a = b = c). This PXRD analysis indicates a complete disruption of the starting core NCs' structural integrity. This conclusion is supported by HAADF-STEM imaging, which shows a consistent contrast across the particles, and irregular shape NCs indicate the destruction of the original core NCs. Due to this alloying indication, further structural investigation of the first heterogeneous material combination $LiTmF_4/NaYF_4$ was considered unnecessary.

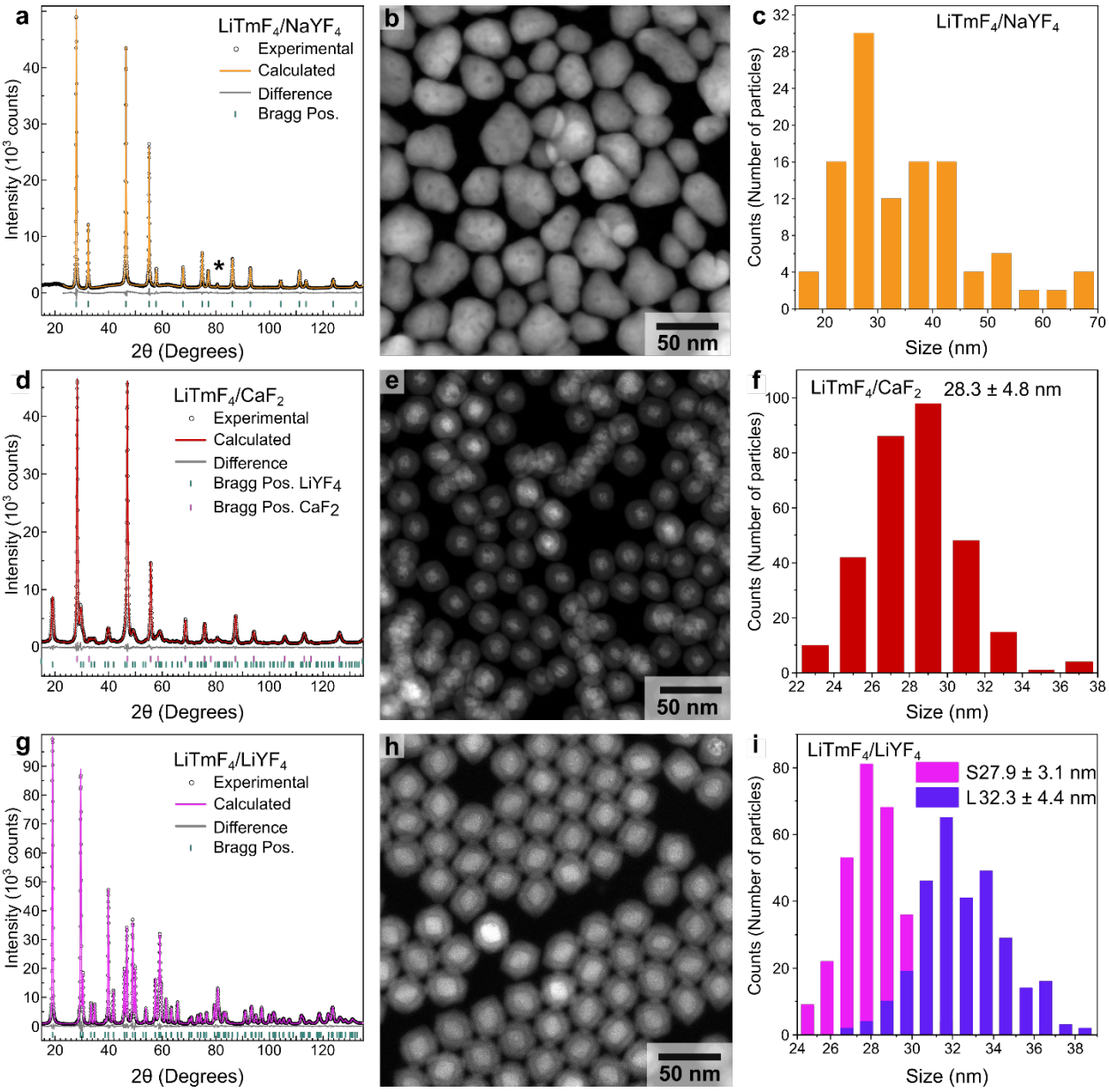


Figure 5.7 *Structural characterization of $LiTmF_4$ core NCs combined with various shell materials: cubic α-$NaYF_4$ (heterogeneous combination – top row), cubic CaF_2 (heterogeneous combination – middle row), and tetragonal $LiYF_4$ (homogeneous combination – bottom row). (a, d, g) Experimental PXRD patterns (black open symbols) and corresponding Pawley refinements (colored solid lines). The difference between experimental and calculated patterns is shown in gray, with Bragg peak positions indicated by green vertical bars. For the $LiTmF_4/CaF_2$ heterogeneous combination, Bragg positions for both the tetragonal (green) and cubic (pink) phases are shown. The peak marked with an asterisk (*) near 80° originates from the (911)-oriented low-background silicon wafer used for drop-casting the NCs (Figure 3.3), not from the NCs themselves. (b, e, h) Representative low-magnification HAADF-STEM images. (c, f, i) Size distribution histograms derived from the analysis of at least 300 individual particles from multiple HAADF-STEM images. The histograms reflect anisotropic shapes when present. Error bars represent two standard deviations (2σ). Reprinted with permission from ACS Nano 2024, 18, 38, 26233–26250. Copyright 2024 American Chemical Society.*

In contrast, the PXRD pattern of the second heterogeneous combination of $LiTmF_4/CaF_2$ shows the coexistence of the tetragonal phase and a new cubic phase ($Fm\bar{3}m$, a = b = c = 5.4648 Å, Figure 5.7d open symbols). Pawley refinement (Figure 5.7d, solid line) indicates slight modifications in the lattice parameters of the tetragonal phase (a = b = 5.1704 Å, c = 10.641 Å) compared to the starting core NCs. HAADF-STEM reveals the formation of isotropic NCs with a clear contrast difference between the core and shell regions (Figure 5.7e). The size distribution histogram (Figure 5.7f) indicates larger particles, with a mean size of 28.3 ± 4.0 nm. The distinct contrast between the inner and outer regions facilitates the extraction of a size distribution histogram (Figure 5.8) specifically for the bright "core" region. This bright “core” region, exhibit a slightly anisotropic shape, similar to the starting $LiTmF_4$ core NCs. Nevertheless, both short and long axes are slightly shorter than those of the starting core NCs, suggesting some modifications of the starting core after the shell growth.

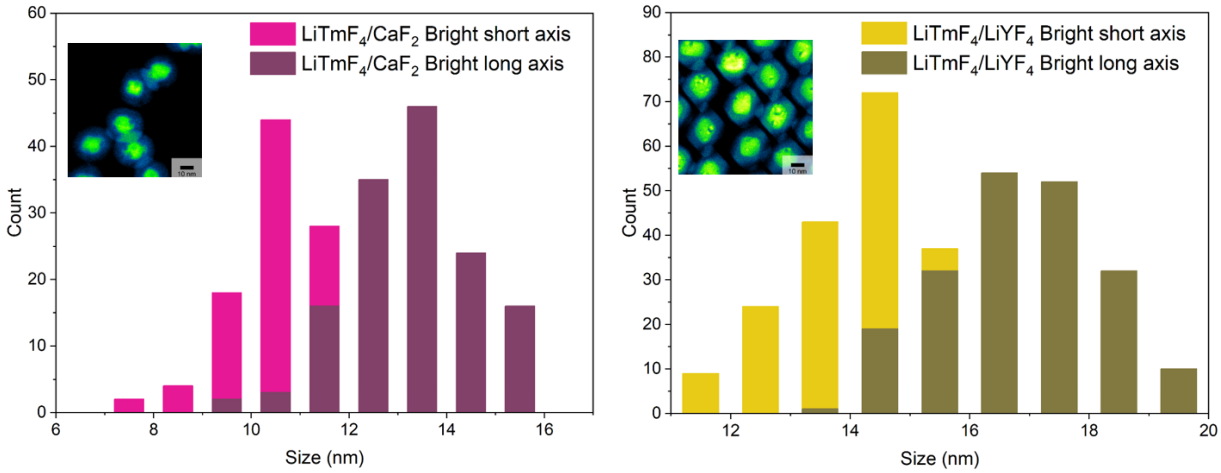


Figure 5.8 *Size distribution analysis of the core region in $LiTmF_4/CaF_2$ NCs. Histograms showing the measured short and long axes of the brightest (core) region in $LiTmF_4/CaF_2$ (left) and $LiTmF_4/LiYF_4$ (right) NCs. A contrast-enhancing filter was applied to the core–shell HAADF-STEM images to improve the distinction between core and shell regions. The inset displays an example of the filtered image used to identify the core region and determine its dimensions for statistical analysis.*

The PXRD pattern of the homogeneous combination $LiTmF_4/LiYF_4$ reveals a single tetragonal phase ($I4_1/a$), without secondary phases (Figure 5.7g). The Bragg peaks (Figure 5.7g, open symbols) of this tetragonal phase are particularly sharper than those

of the initial $LiTmF_4$ core NCs. Pawley refinement (Figure 5.7g, solid line) indicates an increase in the c lattice parameter (c = 10.7105 Å), but similar a and b parameters (5.1638 Å), with respect to the core. Furthermore, the calculated size of the coherent domains increases in comparison to the starting core NCs, reaching 29.6 ± 2.5 nm. HAADF-STEM imaging reveals slightly anisotropic particles, exhibiting a discernible contrast difference between their core and shell regions (Figure 5.7h). The extracted size distribution histogram (Figure 5.7i) aligns reasonably well with PXRD measurements, indicating mean sizes of 27.9 ± 3.1 nm and 32.3 ± 4.4 nm for the short and long axes, respectively. The contrast difference between the inner and outer regions facilitates the accurate extraction of a size distribution histogram specifically for the brighter "core" region (Figure 5.8). While the size of the short axis (14.3 ± 2.5 nm) corresponds well with that of the starting core NCs, the long axis appears shorter in comparison (16.9 ± 2.6 nm, Figure 5.2c).

5.5.3 Homogeneous and Heterogeneous Material Shell Combinations Derived from $LiTmF_4$: Chemical organization

EDXS chemical mapping demonstrates that Tm^{3+} is primarily localized within the expected core region, with evidence of ion migration into the shell region in both heterogeneous (Figure 5.9a,b) and homogeneous (Figure 5.9i,j) material combinations with $LiTmF_4$ core NCs. Tm^{3+} distribution seems contained in the homogeneous combination better, than compared to its heterogeneous counterpart. A contrasting observation with material combinations utilizing α-$NaTmF_4$ core NCs (Figure 5.5). Despite the high concentration of Tm^{3+} in the core region of the heterogeneous material combination, a secondary Tm^{3+} distribution of much lower intensity is also observed in the shell domain. While a similar phenomenon is observed in homogeneous material combination, in the heterogeneous material combination Tm^{3+} does not reach the outermost regions of the particles.

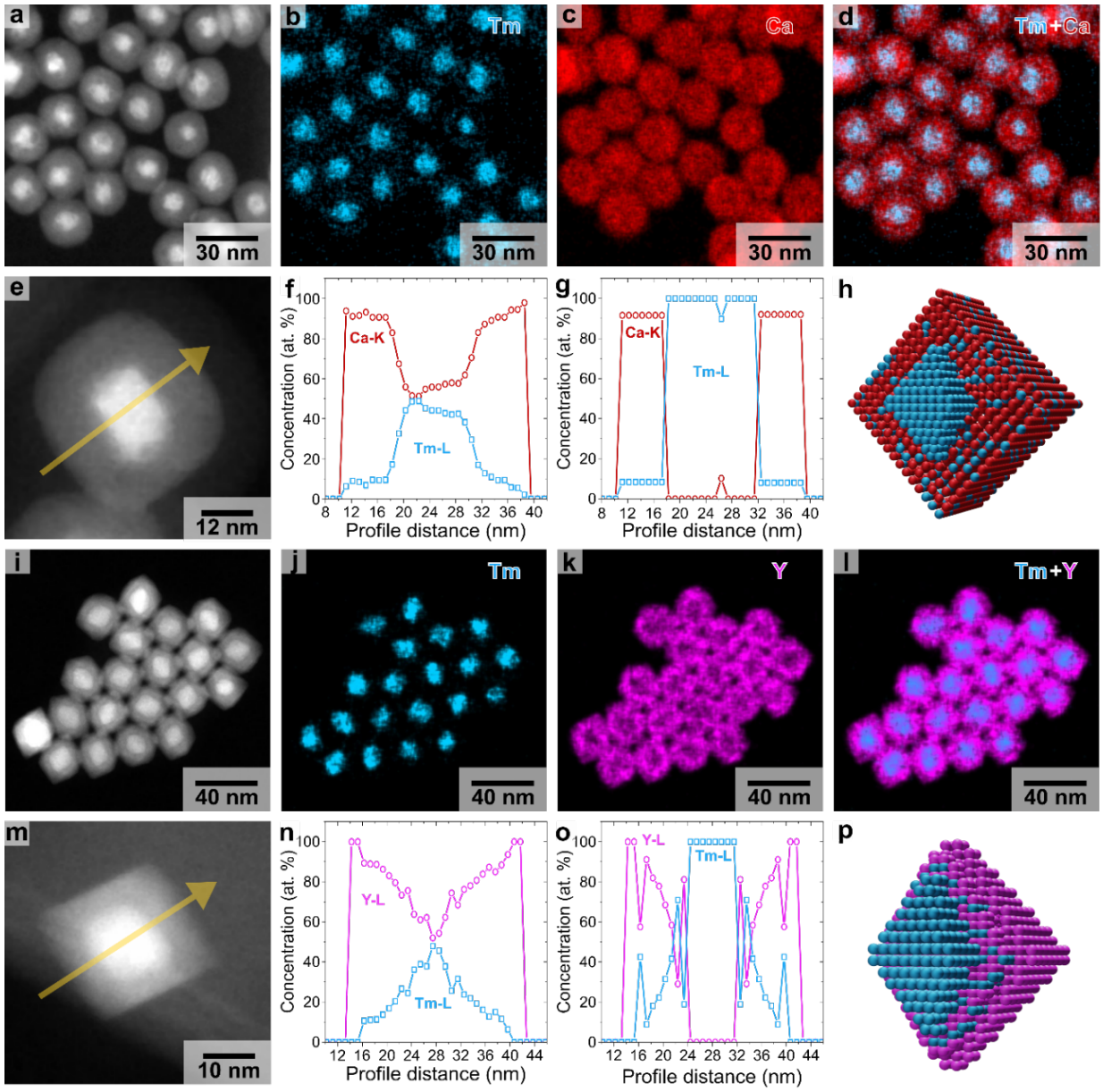


Figure 5.9 *Chemical analysis of $LiTmF_4$ core NCs combined with cubic CaF_2 (heterogeneous combination – first and second rows) and tetragonal $LiYF_4$ (homogeneous combination – third and fourth rows). (a, i) HAADF-STEM images of the regions selected for EDXS mapping. (b–d, j–l) Elemental maps of Tm (Tm-Lα line), Ca (Ca-Kα line), and Y (Y-Lα line), along with overlay images for the heterogeneous (b–d) and homogeneous (j–l) combinations. (e, m) HAADF-STEM images of single particles selected for EDXS line-scan analysis (yellow arrows). (f, n) Normalized raw elemental profiles obtained from the line scans. (g, o) Calculated elemental profiles based on the subshell approach. (h, p) Schematic representations of the most probable qualitative cation distributions for the heterogeneous and homogeneous material combinations. Tm, Y, and Ca are represented in blue, magenta, and red, respectively. Reprinted with permission from ACS Nano 2024, 18, 38, 26233–26250. Copyright 2024 American Chemical Society.*

EDXS mapping reveals dark voids in the innermost regions of the particles for both Ca^{2+} and Y^{3+} shell elements (Figure 5.9d,l), coinciding with the primary spatial distribution of Tm^{3+} from the core NCs. The superposition of EDXS maps for core and shell elements indicates core–shell structures in both heterogeneous and homogeneous combinations. However, unlike the homogeneous combination, which exhibits a thin, pure Y^{3+} region at the outermost edges, the heterogeneous combination lacks a distinct pure shell domain.

Normalized raw chemical profiles of Tm^{3+} in a single homostructured NC show its presence beyond the initial core NC boundaries, but without reaching the edges (Figure 5.9m). Applying a subshell approach with bipyramidal geometry reveals a true core–shell structure based on the EDXS profiles of Tm^{3+} and Y^{3+} (Figure 5.9o,p). Despite the presence of pure core and shell domains, an interfacial layer exists, suggesting that $LiTmF_4$ and $LiYF_4$ coexist with a nonhomogeneous alloy presenting concentration gradients between these domains. The concentration profile of Tm^{3+} appears "spiky" (Figure 5.9o), most likely due to fluctuations in the intermixing regions and deviations from the idealized model used in subshell analysis. It is worth noting that Tm^{3+} concentrations in the outermost regions of the core domain have larger errors due to thickness effects at the bipyramid tips.

The normalized raw chemical profile of Tm^{3+} (Figure 5.9e), derived from a single heterostructured NC, indicates the presence of Tm^{3+} extending beyond the core region's spatial boundaries reaching the particle's outermost edges (Figure 5.9f). Applying a subshell approach, utilizing idealized bipyramidal core and cubic shell geometries, to the raw EDXS chemical profiles of Tm^{3+} and Ca^{2+} demonstrates the formation of a core–shell structure (Figure 5.9g,h). However, unlike its homogeneous counterpart, a consistent concentration of Tm^{3+} is found throughout the entire shell domain (ca. 8% at.%), indicating the formation of a homogeneous Tm-doped shell, even though a pure core region is observed. The presence of Tm^{3+} in the shell region, as detected by EDXS line-scan analysis, supports the EDXS chemical map interpretation and is further corroborated by additional EDXS line scans and Rietveld refinement of the corresponding PXRD pattern. Indeed, refinement of the Ca site's SOF suggests a substitution of Ca (Wyckoff position 4a) by Tm^{3+} of up to 7 at. %. The doping of the CaF_2 shell by Tm^{3+} is also confirmed

through analysis of the 2-dimensional FT pattern derived from HRTEM images of the outermost shell region.

5.6 X-ray Diffraction Analysis of Core–Shell Phase Composition

In previous sections, evidence for the chemical organization (alloyed or core–shell structures) in material combinations with cubic α-$NaTmF_4$ or tetragonal $LiTmF_4$ core NCs relied on EDXS spectroscopy. However, a detailed inspection of the PXRD patterns of α-$NaTmF_4/CaF_2$ can reveal interesting, yet easily overlooked, features. Despite peak broadening due to small coherently diffracting domains, particular features of the PXRD patterns of NCs remain valuable for extracting structural information.

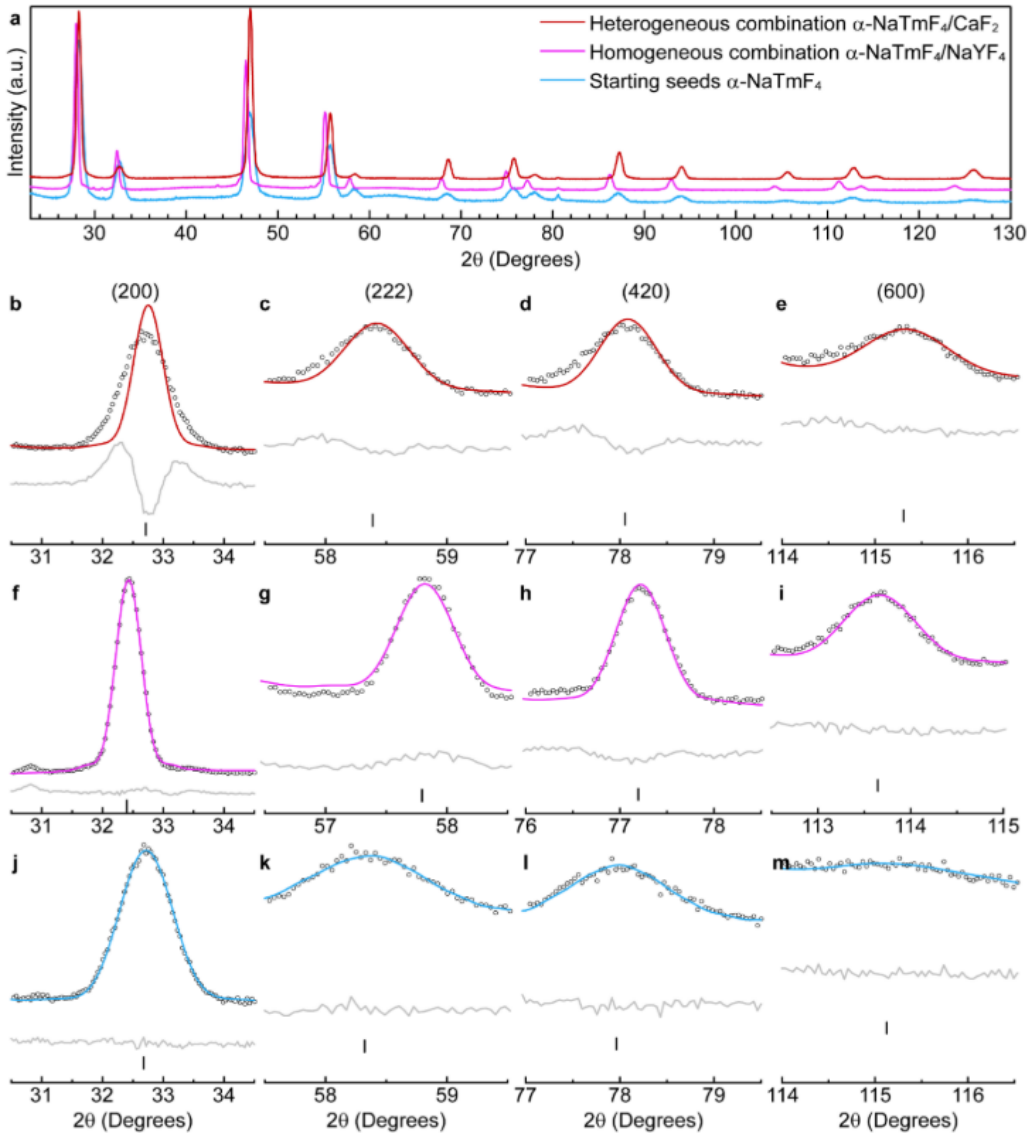


Figure 5.10 *Comparison of PXRD data for homogeneous and heterogeneous material combinations based on cubic α-NaTmF₄ core NCs. (a) Experimental PXRD patterns of α-NaTmF₄ core NCs (blue solid line), homogeneous α-NaTmF₄/NaYF₄ NCs (magenta solid line), and heterogeneous α-NaTmF₄/CaF₂ NCs (red solid line). (b–m) Experimental (black open symbols) and calculated (colored solid lines) profiles of selected Bragg reflections: (200), (222), (420), and (600). Peak profiles are presented for α-NaTmF₄ core NCs (bottom row), homogeneous α-NaTmF₄/NaYF₄ NCs (middle row), and heterogeneous α-NaTmF₄/CaF₂ NCs (top row), allowing direct comparison of structural changes across the different material combinations. Reprinted with permission from ACS Nano 2024, 18, 38, 26233–26250. Copyright 2024 American Chemical Society.*

Compared to the starting cubic seeds of α-$NaTmF_4$, the homogeneous combination (α-$NaTmF_4$/$NaYF_4$) exhibits a shift of all Bragg peaks toward lower two theta angles, while

the heterogeneous combination's peaks remain almost unchanged (Figure 5.10a). This suggests differences in the atomic scale organization between the two combinations.

Given that the materials used for both combinations are isostructural polymorphs ($Fm\bar{3}m$) with nearly identical lattice parameters, equivalent atomic-scale organizations should yield similar PXRD patterns for both combinations. The influence of the material combination on the atomic-scale structure is particularly evident, as the profiles of specific reflections, i.e. (200), (222), (420), and (600). These reflections are successfully modeled for the core (Figure 5.10, first row) and homostructured (Figure 5.10, second row) NCs, but not for the heterostructured (Figure 5.10 third row) NCs. These characteristics serve as distinct X-ray diffraction markers for distinguishing between alloying and phase segregation.

To validate this hypothesis, Debye's scattering equation was employed to simulate the theoretical diffraction pattern of various atomistic models for a single NC.[148,149] For an individual isotropic NC of CaF_2 with a size of 21.8 nm, the theoretical diffraction pattern indicates that the intensities of the (200), (222), (420) and (600) reflections are equal to or nearly zero (Figure 5.11). Conversely, when Ca^{2+} is substituted by Tm^{3+} in the model of the single NC, the intensities of the same reflections are distinctly non-zero (Figure 5.11). Consequently, given that the non-zero intensity of specific Bragg peaks of the cubic crystal structure is entirely governed by the presence of Tm^{3+} atoms, these Bragg peaks can be utilized to classify whether the underlying atomic-scale structure aligns with alloying or phase segregation.

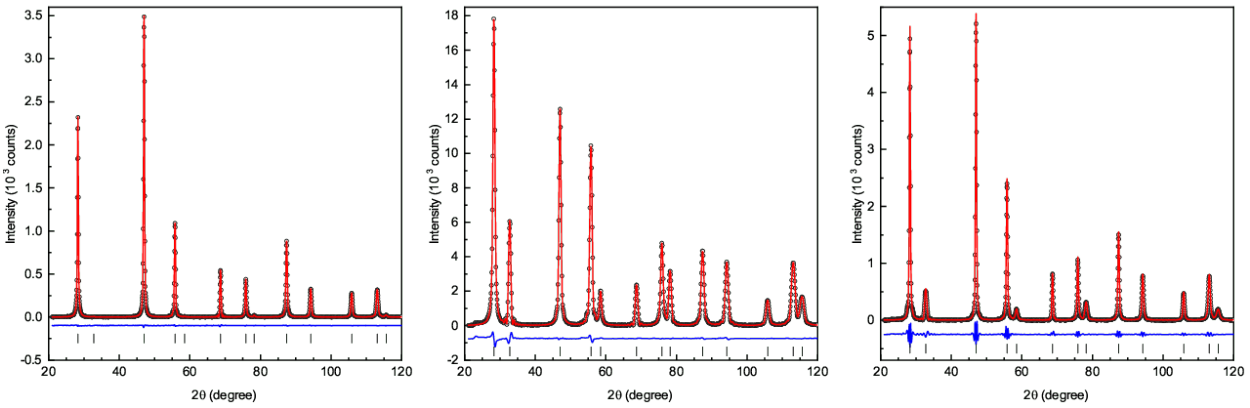


Figure 5.11 *Theoretical PXRD pattern obtained using the Debye's scattering equation with the fluorite crystal structure ($Fm\bar{3}m$). Wyckoff positions 4a and 8c are fully occupied by calcium and fluorine (left graph), thulium and fluorine (medium graph), respectively. Note that the intensity of reflections (200) and (222) is equal to zero while the intensity of reflections (420) and (600) are very weak. Additionally, theoretical PXRD pattern obtained using the Debye's scattering for α-$NaTmF_4/CaF_2$ with perfect coherence between the core and shell domains.*

The (200) reflection is particularly noteworthy due to its location at a low two-theta angle (ca. 32.5º), high relative intensity, and lack of peak overlap compared to the other reflections mentioned. As stated earlier in the chapter, the Pawley refinement of the experimental PXRD pattern for the cubic heterogeneous combination (α-$NaTmF_4/CaF_2$) fails to accurately model the line profile of the (200), (222), (420) and (600) reflections, even though it is suited to all other reflections. Given that the observation of the reflection in the PXRD pattern is exclusively related to the presence of Tm^{3+} within the diffracting domain, the discrepancy between the calculated and experimental line profiles can now be explained. Specifically, the size of the coherently diffracting domain within which Tm^{3+} is confined is appreciably smaller than the overall crystallite size. Thus, the experimental PXRD pattern of the heterostructured NCs reflects not only the size of the Tm^{3+} domain but also the size of the entire coherently diffracting domain, which includes both the Tm^{3+} and Ca^{2+} regions. Simulations indicated that the overall theoretical calculation of the diffraction pattern could not be understood as a convolution of separate core and shell contributions. Instead, simulations with perfect coherence between the core and shell domains can explain the observed diffractogram (Figure 5.11). Interestingly, the results obtained by advanced PXRD data analysis can be independently validated by analyzing HRTEM data.

In the direct space, the HRTEM image of a single α-$NaTmF_4/CaF_2$ NC confirms the structural coherence of the entire NC (Figure 5.12). As anticipated, a cubic crystal structure can index all reflections (highlighted in green and pink) of the FT pattern from a central region of the NC (Figure 5.12a,d). Analogous to PXRD, simulations indicate that the structure factor $|F_{(hkl)}|$ of certain reflections is near or equal to zero for pure CaF_2 (marked in green), but not when Tm^{3+} substitutes Ca^{2+} from 5% or higher. Observing all reflections in Figure 5.12d is expected because the FT pattern of the central region is a composite of the core and shell domain FT patterns. Conversely, the FT pattern of the outermost 3−4 nm shell region lacks specific reflections, particularly the (200), aligning with the formation of pure CaF_2 (Figure 5.12b,e). This observation validates the conclusion drawn from analyzing the peak broadening seen in specific Bragg reflections on the PXRD pattern of α-$NaTmF_4/CaF_2$ NCs.

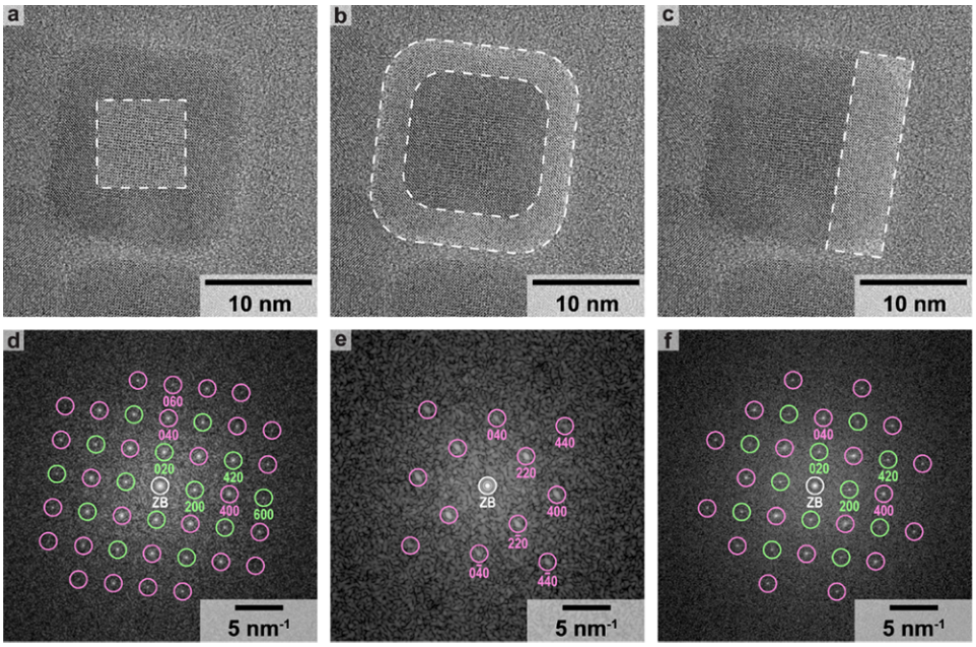


Figure 5.12 *High-resolution transmission electron microscopy (HRTEM) analysis of the heterogeneous α-$NaTmF_4/CaF_2$ material combination. (a–c) HRTEM images of different regions of the same NC, showing the inner core (a), the outermost shell region (~3–4 nm, b), and a thicker shell region (~5 nm, c). (d–f) Corresponding 2-dimensional Fourier transforms (FTs) of the areas highlighted with dashed boxes in the HRTEM images, along with indexed reflections. All FTs can be indexed to a cubic crystal structure (space group $Fm\bar{3}m$) along the [001] zone axis. To improve legibility, only a selection of reflection indices is shown; remaining reflections can be deduced from symmetry and the indexed references. The zero-order beam (ZB) is marked with a white circle. Reflections indicated by pink or green circles correspond to the cubic phase. Green-circled reflections have structure factors $|F_{(hkl)}|$ that are theoretically close to or equal to zero in pure CaF_2 and are therefore not expected to appear. Reprinted with permission from ACS Nano 2024, 18, 38, 26233–26250. Copyright 2024 American Chemical Society.*

Demonstrating the method's sensitivity, a thicker shell region's FT pattern (5 – 6 nm) was also obtained. As with the central region, the low intensity reflections appear (Figure 5.12c,f). This was expected because the analyzed region exceeds the pure CaF_2 shell thickness, thus, the corresponding FT pattern combines the pure CaF_2 shell and α-$NaTmF_4$ core domain FT patterns. Applying the same approach to HRTEM data of the heterogeneous combination $LiTmF_4/CaF_2$ (Figure 5.13) confirms Tm inclusion in the CaF_2 shell's crystal structure, consistent with EDXS and Rietveld refinement results.

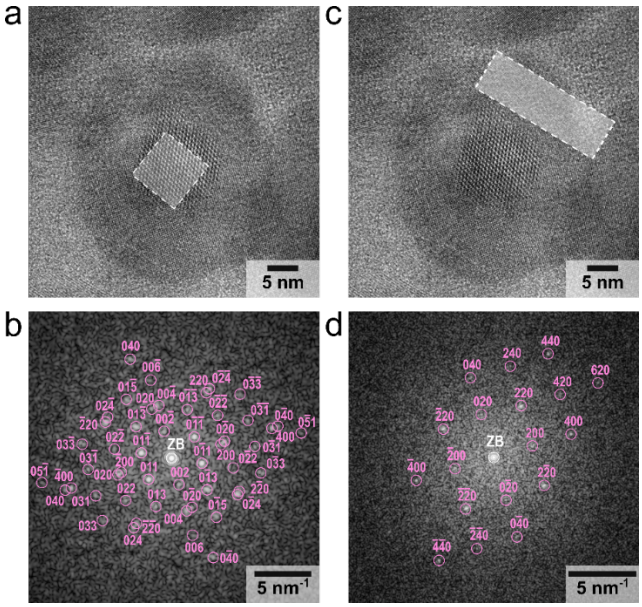


Figure 5.13 *High-resolution transmission electron microscopy (HRTEM) analysis of the $LiTmF_4/CaF_2$ heterogeneous material combination. (a, c) HRTEM overview images of the same $LiTmF_4/CaF_2$ NC, showing different regions for analysis (core and shell). (b, d) 2-dimensional Fourier transforms (FTs) of the areas marked with dashed boxes in the HRTEM images, with corresponding indexation. The FT from the core region (b) reveals reflections characteristic of both the tetragonal ($I4_1/a$) and cubic ($Fm\bar{3}m$) phases along the [001] zone axis. In contrast, the FT from the shell region (d) shows only reflections corresponding to the cubic ($Fm\bar{3}m$) phase in the same zone axis. For improved clarity, only a subset of reflection indices is shown; all others can be deduced based on symmetry and the indexed reflections. The zero-order beam (ZB) is marked with a white circle. Reprinted with permission from ACS Nano 2024, 18, 38, 26233–26250. Copyright 2024 American Chemical Society.*

It is important to note that it is possible to distinguishing between alloyed and core−shell structures via PXRD or HRTEM for some material combination types, as it requires the presence of unique features inherent to the pure materials' diffraction patterns. With the

homogeneous material combination, α-$NaTmF_4$/$NaYF_4$, neither PXRD nor HRTEM data can definitively differentiate between alloyed and core−shell structures because the zero-intensity of specific reflections is invalid when CaF_2 is replaced by α-$NaYF_4$. Therefore, only detailed EM characterization using EDXS spectroscopy can reveal the atomic scale organization. The same limitations apply to the homogeneous material combination $LiTmF_4$.

5.7 SWIR Emission of Tm^{3+} Based Material Combinations

The SWIR emission properties of different Tm^{3+}-based NCs were measured in the solid-state. Figure 5.14a illustrates a typical absorption spectrum for Tm^{3+} in the NIR-SWIR region. The absorption band centered at 800 nm is often favored as the optimal excitation wavelength for bioimaging, since it lies outside the water absorption region between 900−1050 nm (Figure 5.15). As a results, the excitation at 800 nm enabled deeper penetration in aqueous environments, this will be further explored in chapter 7. The widely recognized mechanism for Tm^{3+} emission above 1600 nm, depicted in Figure 5.14b, involves cross-relaxation between the $^3H_4$ and $^3F_4$ electronic energy levels of two Tm^{3+} ions.[150]

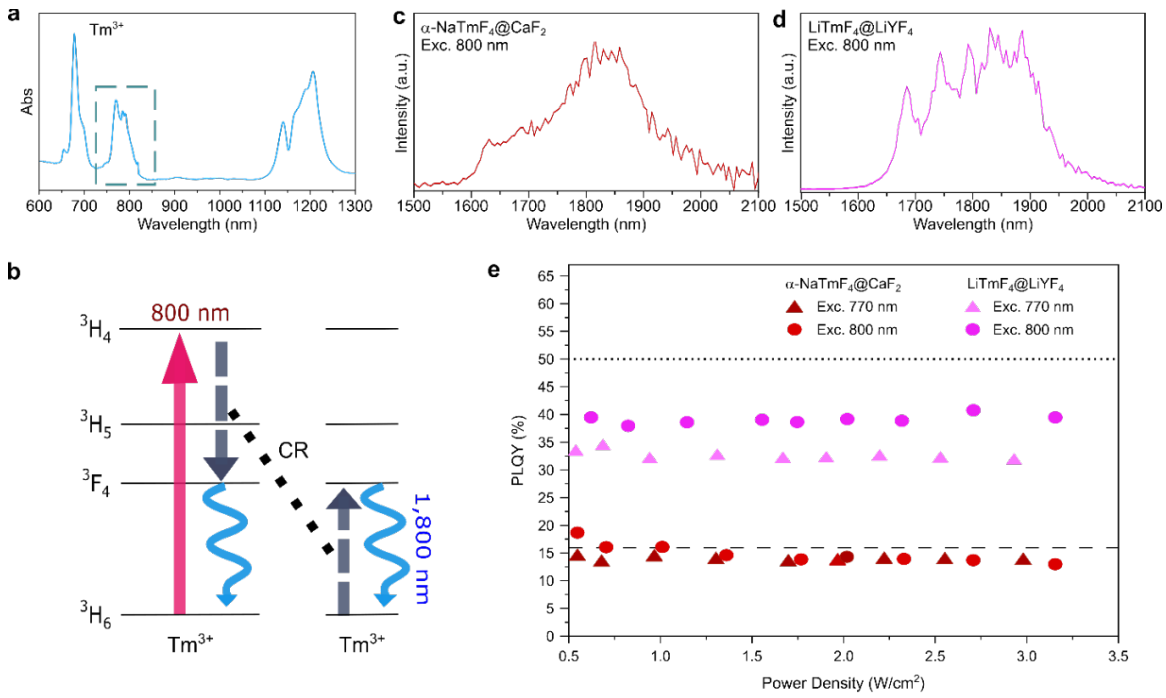


Figure 5.14 *Tm^{3+} downshifting optical properties in the far-end SWIR region for homogeneous and heterogeneous material combinations. (a) Typical absorption spectrum of Tm^{3+} ions. The shaded area indicates the wavelength range used for excitation of Tm^{3+}-based homo- and heterostructured NCs. (b) Schematic of the accepted downshifting mechanism for Tm^{3+} emission in the 1600–2100 nm range, involving cross-relaxation (CR) between neighboring Tm^{3+} ions. (c, d) Emission spectra of Tm^{3+} in the far-end SWIR region (λ_{em} = 1600–2100 nm) for the heterogeneous α-$NaTmF_4/CaF_2$ (c) and homogeneous $LiTmF_4/LiYF_4$ (d) material combinations. (e) Absolute power-dependent downshifting PLQY measurements from 0.5 to 3.5 W/cm^2 for the heterogeneous α-$NaTmF_4/CaF_2$ (light and dark red symbols) and the homogeneous $LiTmF_4/LiYF_4$ (light and dark pink symbols) NCs. The dashed line indicates the highest Tm^{3+} downshifting PLQY reported to date in the far-end SWIR region,[30] while the dotted line represents the maximum Er^{3+} downshifting PLQY in the 1400–1650 nm range, previously reported by the authors for a heterogeneous material combination.[94] Reprinted with permission from ACS Nano 2024, 18, 38, 26233–26250. Copyright 2024 American Chemical Society.*

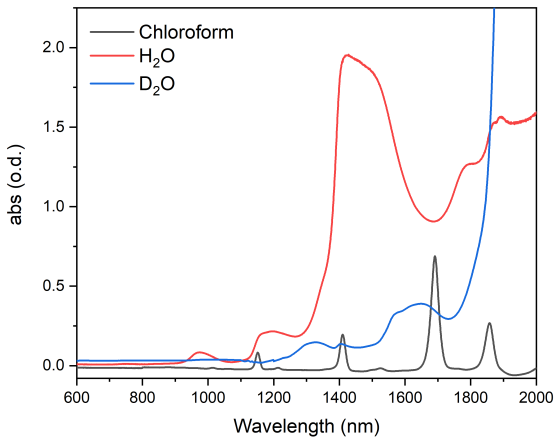


Figure 5.15 *NIR absorption spectra of solvents of interest (chloroform, H_2O and D_2O).*

As anticipated, no luminescence was detected in the starting core NCs of α-$NaTmF_4$ or $LiTmF_4$ due to extensive surface quenching as numerous energy migration pathways to surface quenching sites become accessible. Homogeneous α-$NaTmF_4$/$NaYF_4$, and heterogeneous α-$NaTmF_4$/$LiYF_4$, $LiTmF_4$/$NaYF_4$, and $LiTmF_4$/CaF_2 material combinations exhibited zero emission (Figure 5.16). The absence of Tm^{3+} emission in these material combinations can be attributed to the complete or partial redistribution of Tm^{3+} throughout the particle volume, lacking the pure protective inert shell. This ion migration of the optically active element introduces new avenues for energy leakage to surface quenchers.

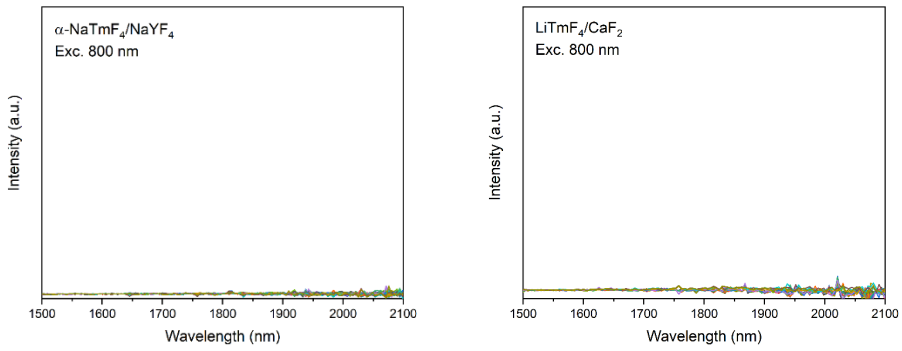


Figure 5.16 *Quenched emission behavior of α-$NaTmF_4$/$NaYF_4$ and $LiTmF_4$/CaF_2 NCs upon 800 nm excitation. The observed quenching is attributed to the optically inert shells ($NaYF_4$ or CaF_2, respectively), as the same α-$NaTmF_4$ or $LiTmF_4$ core seeds were used as in the emissive material combinations NCs. This indicates that the emission suppression arises from the shell material combination rather than from the active core.*

Among the six material combinations examined, only two displayed Tm^{3+} emission above 1600 nm, evidenced by the broad emission bands observed in both the cubic heterogeneous and tetragonal homogeneous combinations (Figure 5.14c,d). Power dependent absolute downshifting PLQY measurements were taken at 770 nm and 800 nm excitation wavelengths (Figure 5.14e). The cubic heterogeneous combination, which exhibits a core−shell structure with a sharp interface, showed a SWIR downshifting PLQY nearing 14%. This value is comparable to the highest PLQY values previously reported for Tm^{3+} emission above 1600 nm, (16%)[30] reported by Chang et al. and Yang et al. (14%).[106] Reducing the Tm^{3+} concentration in the initial α-$NaTmF_4$ core NCs to 50%

boosted the downshifting PLQY of the cubic heterogeneous material combination to 24% (Figure 5.17).

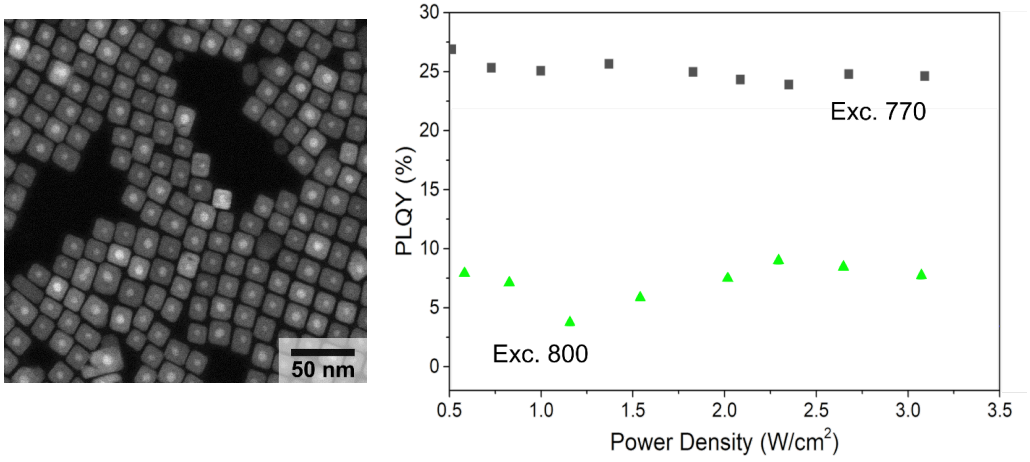


Figure 5.17 *Representative HAADF-STEM image and power-dependent PLQY of α-$NaTm_{0.5}Y_{0.5}F_4$/CaF_2 NCs. HAADF-STEM image of α-$NaTm_{0.5}Y_{0.5}F_4$/CaF_2 NCs (left). Power-dependent PLQY measured above 1600 nm emission under two excitation wavelengths: 770 nm and 800 nm (right). Reprinted with permission from ACS Nano 2024, 18, 38, 26233–26250. Copyright 2024 American Chemical Society.*

Given that the chemical composition of the cubic heterogeneous material combination was not deeply optimized, there is potential for further PLQY improvement. However, in the tetragonal homogeneous material combination ($LiTmF_4$/$LiYF_4$), the downshifting SWIR PLQY reached 39% (Figure 5.14e). To the best of the authors' knowledge, this is an unprecedented value for SWIR emission in the far SWIR region. This value, while slightly lower, is on par with the highest PLQY reported for Er^{3+} emission at 1550 nm (50%, Figure 5.14e).[94]

5.8 Discussion

Of the three material combinations utilizing identical optically active α-$NaTmF_4$ core NCs, Tm^{3+} emission above 1600 nm was observed in only one (α-$NaTmF_4$/CaF_2). Through EDXS chemical mapping, EDXS line scan analyses, and PXRD and HRTEM, it was found that different material combinations with the same cubic core NCs, synthesized under identical experimental conditions, resulted in markedly different chemical organizations.

Specifically, the extent of cation intermixing was heavily influenced by the type of shell material combined with the cubic core NCs. These variations directly impacted the SWIR emission performance of Tm^{3+}.

In cubic homogeneous material combinations involving isostructural crystalline phases capable of easily forming a solid solution, cation intermixing was extensive, leading to non-homogeneous alloy. It is worth highlighting that, the selected tetragonal shell material did not undergo separate nucleation, despite having dissimilar crystal structures. Instead, alloying was favored, and the initial cubic crystal structure was almost entirely converted to the tetragonal crystal structure. The hypothesis that the energetically favored tetragonal crystal structure drives the fragmentation and destruction of the starting core NCs can be dismissed, as the opposite effect was seen when growing a cubic shell on tetragonal core NCs.

The heterogeneous material combination between isostructural crystalline phases with limited miscibility (α-$NaTmF_4$ and CaF_2) was the only one that successfully formed a true core−shell structure, exhibiting no cation intermixing between the core and shell domains. Despite the lattice mismatch being similar between homogeneous and heterogeneous material combinations involving isostructural materials, crystallographic factors alone, such as crystal structure matching and lattice mismatch, are insufficient to predict the extent of intermixing. Since the material combinations were synthesized under identical experimental conditions (solvent, surfactant, precursors, synthesis methodology, heating rate, aging time, synthesis temperature), the interplay between crystallography and chemistry likely plays a significant role. Thus, the ease with which solid solutions form between the core and shell materials may significantly determine the stability of the starting core NCs upon contact with the shell precursor.

The results from the last three material combinations indicate that predicting the final chemical organization based solely on the type of material combination is currently impossible. Indeed, the same material combinations synthesized with tetragonal core NCs instead of cubic core NCs show dramatic differences in two out of three cases. Surprisingly, heterogeneous combinations involving different crystal structures lead to either the complete destruction of the starting core NCs or the formation of a core−shell

structure. Given that these combinations involve isostructural shell materials, it supports the hypothesis that shell precursors modify the stability of the starting core NCs. Moreover, the complete destruction of the starting tetragonal phase when combined with α-$NaYF_4$ suggests that the solid-state miscibility of the core and shell materials is a driving force. It is also important to note that while the heterogeneous $LiTmF_4/CaF_2$ material combination forms a core−shell structure similar to its isostructural counterpart, a key difference exists unlike the latter, where no Tm migrated into the CaF_2 shell, a small, constant Tm (~ 8 at.%) concentration was detected in the former, sufficient to quench the Tm SWIR emission.

Interestingly, the homogeneous combination with $LiTmF_4$ core NCs does not result in full alloying but in a core−shell structure with an alloyed interphase between the pure core and pure shell domains. The exceptionally high PLQY of 39% achieved with the homogeneous material combination can be attributed to two main factors: first, the lower site symmetry of the tetragonal crystal structure (compared to the higher site symmetry of the cubic crystal structure), as it is well-established that lower local symmetry weakens Laporte's selection rules, thereby promoting 4*f*−4*f* transitions.[151,152] The second factor is related to the interphase observed in the homogeneous tetragonal material combination, as it may also contribute to obtaining a more optimized interatomic distances between the optically active centers. For example, the best downshifting PLQY for the true core−shell structure with the cubic α-$NaTmF_4$ is obtained not with 100% Tm^{3+} but with a lower concentration (50%).

Despite investigating the same material combination as Chang et al., the absolute downshifting PLQY of Tm^{3+} reported here is significantly superior. This is possibly due to the water-free precursors used in this study (Figure 3.2), contrasting with the heavily hydrated metal precursors used by Chang et al. Water in the reactive medium introduces hydroxy groups (OH^-) that can integrate into the crystal structure of ternary alkali metal RE-based fluorides. Haase et al. have demonstrated the importance of maintaining an OH-free environment for efficient upconversion.[153]

Finally, Tm^{3+} SWIR downshifting luminescence is only detectable when a pure inert shell forms. The presence of Tm^{3+} in the outermost NC layer, regardless of concentration, fully

quenches SWIR emission. Protecting optically active core NCs from surface quenching sites, as demonstrated previously, and blocking energy migration pathways to these sites are critical. This is attributed to the importance of shielding optically active core NCs from surface quenching sites, as demonstrated two decades ago for RE-based luminescence.[154,155] Subsequently, the importance of blocking energy migration pathways to surface quenching sites has been demonstrated and utilized to tune and/or enhance the photoluminescence properties of RE-based NCs.[156–158] The inert shell approach remains the most effective strategy for optimizing RE-based NC performance. The results align with known quenching mechanisms and indicate that the growth of a pure inert protecting shell is not guaranteed and depends on the material combination.

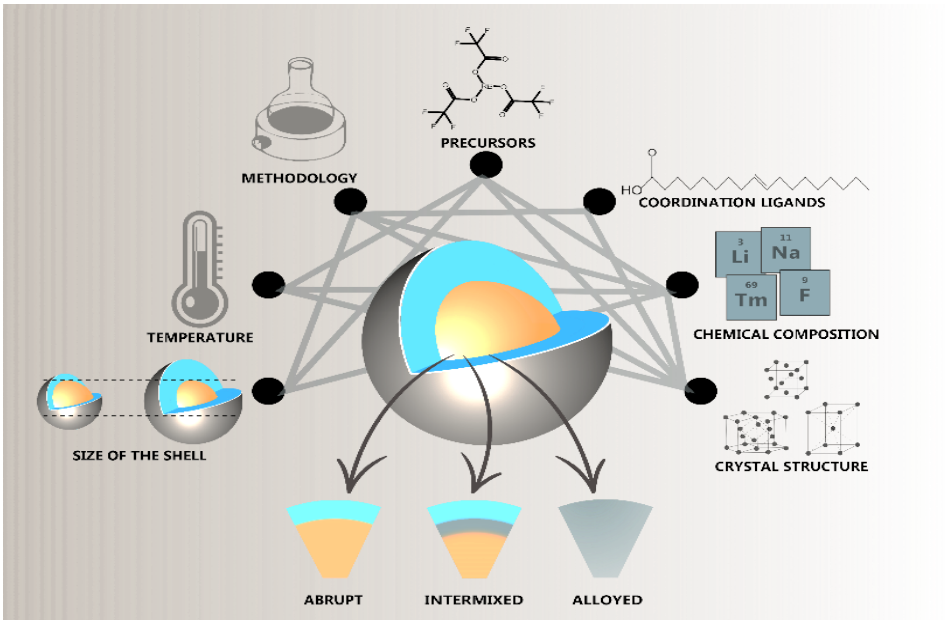
5.9 Summary

Despite extensive research spanning over two decades on RE-based core−shell NCs, the correlation between the atomic-scale organization of a chosen material combination and its photoluminescence properties remains underexplored. This study marks an initial investigation into the impact of various material combinations on the downshifting properties of synthesized homo- and heterostructured NCs. The findings, derived from static characterizations under a single set of experimental conditions, shed light on the diversity in the synthesis of RE-based core−shell NCs, challenging the "one-size-fits-all" approach. This diversity may be further amplified by altering experimental parameters, potentially leading to different outcomes even with the same material combination. Fortunately, EDXS spectroscopy can capture this diversity. It is now clear that, for suitable material combinations, EDXS spectroscopy, PXRD, and HRTEM can be effectively combined to extract precise information about the atomic-scale organization of core−shell NCs, facilitating the development of accurate atomistic 3D models of RE-based core−shell NCs. This study demonstrates a strong correlation between the SWIR optical performance of Tm^{3+} above 1600 nm and the actual atomic-scale organization of the final NCs. Different material combinations, synthesized under identical experimental conditions, can result in vastly different atomic-scale organizations, affecting Tm^{3+}'s downshifting performance in the far-end of the SWIR region, ranging from fully quenched

to highly efficient, with a PLQY value of 39%. The latter is 2.4−2.8 times higher than previously reported PLQY values. Moreover, the experimental results indicate that the formation of true core−shell structures with RE-based NCs is just one of many possibilities. Notably, among the six material combinations investigated under the same experimental conditions, only one resulted in a true core−shell structure. Unexpectedly, the results also suggest that achieving a true core−shell structure with an abrupt interface is not essential for maximizing optical performance, provided a pure protecting shell form. While the importance of a protecting outer shell in enhancing the PL performance of NCs, particularly RE-based NCs, is known, this study demonstrates that the formation of such a shell is not guaranteed and depends on the material combination. Consequently, only two out of the six material combinations examined under identical experimental conditions resulted in a pure protecting shell.

This work marks a substantial advance toward establishing guidelines for predicting the outcome of core−shell syntheses, based on atomic-scale organization, across diverse material combinations and experimental conditions. Achieving greater accuracy and predictive power will necessitate identifying and rationalizing the fundamental driving forces, molecular mechanisms, and dynamics governing the formation of RE-based core−shell NCs under various experimental conditions. This study lays the groundwork for a more comprehensive understanding, requiring collective effort to fully elucidate the broader picture. It is expected that the findings presented here will substantially impact the field of RE-based NCs, facilitating the optimization of their optical performance through a deeper understanding of their inherent structural and atomic-scale organization under varying experimental conditions. Specifically, in the context of *in vivo* optical imaging in the far-SWIR region, highly efficient NCs emitting in the 1650−2100 nm range can now be synthesized.

6. Effect of Intrinsic *vs.* Extrinsic Parameters on Cation Intermixing in RE Core–Shell Fluoride NCs



Contributions

The author was responsible for the synthesis of the NCs, performed the X-ray diffraction measurements, figures design, data analysis, and wrote the manuscript. Eduard Madirov and Dmitry Busko conducted and interpreted the optical characterization of the synthesized samples. Radian Popescu and Yolita M. Eggeler obtained the HAADF-STEM and chemical maps. Hana Mirmajidi, and Eva Hemmer provided NCs with the same chemical composition prepared by a different methodology. The overall project was supervised by Prof. Bryce S. Richards, who offered guidance. The conceptual framework for the study was developed by Dr. Damien Hudry, who also contributed critical input throughout the project.

6.1 Motivation

The previous chapters have demonstrated that it is possible to obtain highly efficient RE^{3+} fluoride NCs by avoiding or limiting intermixing. This was most clearly demonstrated for α-$NaREF_4/CaF_2$ heterostructure, where a sharp core–shell interface was obtained. In $LiTmF_4/LiYF_4$ NCs the interface is not perfectly abrupt, still, the optically active ions remain largely confined near the core region, and intermixing is limited, resulting in a sufficiently thick, undoped shell area, which makes it a very efficient material. Until this day it remains unclear to what extent the extrinsic synthesis parameters, such as reaction temperature, duration, and methodology, are responsible for limiting intermixing, or whether this behavior is primarily governed by intrinsic material properties.

By designing a controlled series of experiments and systematically mapping the variables involved in the synthesis of core–shell NCs, it may eventually be possible to unveil the true mechanism of core–shell formation. This understanding would enable precise control over interface structure and cation intermixing in core–shell NCs, a factor that is critical for the advancement of RE-doped fluoride NCs.

This chapter initiates the first conscious effort to correlate intrinsic and extrinsic parameters with the degree of intermixing in core–shell architectures. The study focuses on systems crystallizing in cubic (α-$NaTmF_4$), hexagonal (β-$NaGd_{0.5}Tm_{0.5}F_4$), and tetragonal ($LiTmF_4$) phases. Although a complete map of the intrinsic–extrinsic parameter space is beyond the scope of this work, the results presented here constitute a foundational step toward the construction of such a map.

6.2 Overview

RE^{3+} fluoride-based core–shell NCs have become an area of great interest as an effective method for creating highly efficient luminescent materials.[62,153] These core–shell nanostructures prevent nonradiative energy loss by reducing the effects of surface defects and quenching.[36,156,158,159] Core–shell nanostructures are more effective than other methods, such as using dye-based antennae[160] or doping with metallic cations.[161]

Core-multishell configurations have also been used to precisely tune optical properties by changing the optically active dopant ion(s) in each shell layer and optimizing shell thicknesses.[59,162,163]

The preceding chapters showed that heterogeneous core–shell NCs, such as α-$NaREF_4/CaF_2$; and homogeneous core–shell $LiTmF_4/LiYF_4$ have recently emerged as a highly effective material combinations for avoiding cation intermixing.[33,53,60–62,130,164,165] Furthermore, it was demonstrated that cation intermixing in RE^{3+} fluoride core–shell NCs is strongly dependent on the selected material combination.[62] Still, there are no clear observations whether intermixing is controlled by shell growth alone, or by the combined influence of intrinsic material properties and extrinsic synthesis conditions.

Therefore, it is crucial to systematically map the experimental landscape of parameters to identify the influence of synthesis conditions on intermixing. Given that the interplay between intrinsic (chemical composition of the materials, crystal structure, solubility limits, lattice mismatch, core size, decomposition temperature of precursors, etc.) and extrinsic parameters (synthesis methodology, temperature, concentration of precursor, type of precursor, solvents, synthesis time, etc.) have to be carefully selected when designing the synthesis of core–shell structures.[166–168] Until this day there is currently no reliable method to predict the interface pattern just by the synthesis parameters.

This chapter systematically examines that relationship by comparing core–shell NCs based on α-$NaTmF_4$, β-$NaGd_{0.5}Tm_{0.5}F_4$, and $LiTmF_4$ cores. Intrinsic parameters considered here include crystal structure, chemical composition, and precursor chemistry, while extrinsic parameters include shell precursor amount, and shell-growth temperature. Homogeneous and heterogeneous shells were grown under controlled conditions, and EDXS chemical mapping was used to evaluate the resulting Tm^{3+} distribution. By comparing the resulting interface architectures, from sharply confined core–shell structures to broadly intermixed systems, this chapter aims to identify which parameters most strongly determine cation redistribution during shell growth. The results provide a first parameter map for understanding how material choice and synthesis conditions jointly control interfacial organization in Tm^{3+}-doped fluoride core–shell NCs.

6.3 Results

Multiple 1.0 mmol batches of each core NCs (α-$NaTmF_4$, β-$NaGdTmF_4$, and $LiTmF_4$) were synthesized using the thermolysis method. The batches of each core NC were then combined and used as seeds for the growth of both homogeneous and heterogeneous shells. Tm^{3+} was selected as the optically active ion in the core because of its inherent self-sensitization, which allows for heavy doping while still generating efficient emission in the SWIR region from 1600 nm to 2000 nm. This simplifies the overall chemical composition and facilitates the mapping of the optically active ion distribution.

It is important to mention the difficulty in synthesizing pure β-$NaTmF_4$ NCs without any α-phase contamination. While heavier lanthanides, such as Tm^{3+}, generally favor a cubic structure over a hexagonal one,[169–171] the resulting NCs often consist of a combination of both phases and/or large nanorods. To achieve uniform and homogeneous β-$NaTmF_4$ NCs, 50% Gd^{3+} was incorporated into the crystal lattice, due to its well-known ability to stabilize the hexagonal structure.[172–174] In Chapter 5, section 5.5.3, it was shown that intermixing occurs in the $LiTmF_4/CaF_2$ heterogeneous core–shell, and was not investigated further in the chapter.

6.3.1 Structural Characterizations.

The mean core NCs sizes were determined to be 10.3 ± 1.8 nm for α–$NaTmF_4$ and 9.0 ± 2.2 nm for β-$NaGdTmF_4$, while $LiTmF_4$ cores exhibited a mean long-axis dimension of 28.9 ± 2.6 nm and a short-axis dimension of 18.8 ± 1.9 nm. Additional structural characterization, including HAADF-STEM and PXRD of the optically active cores used as seeds for shell growth are presented in Figure 6.1.

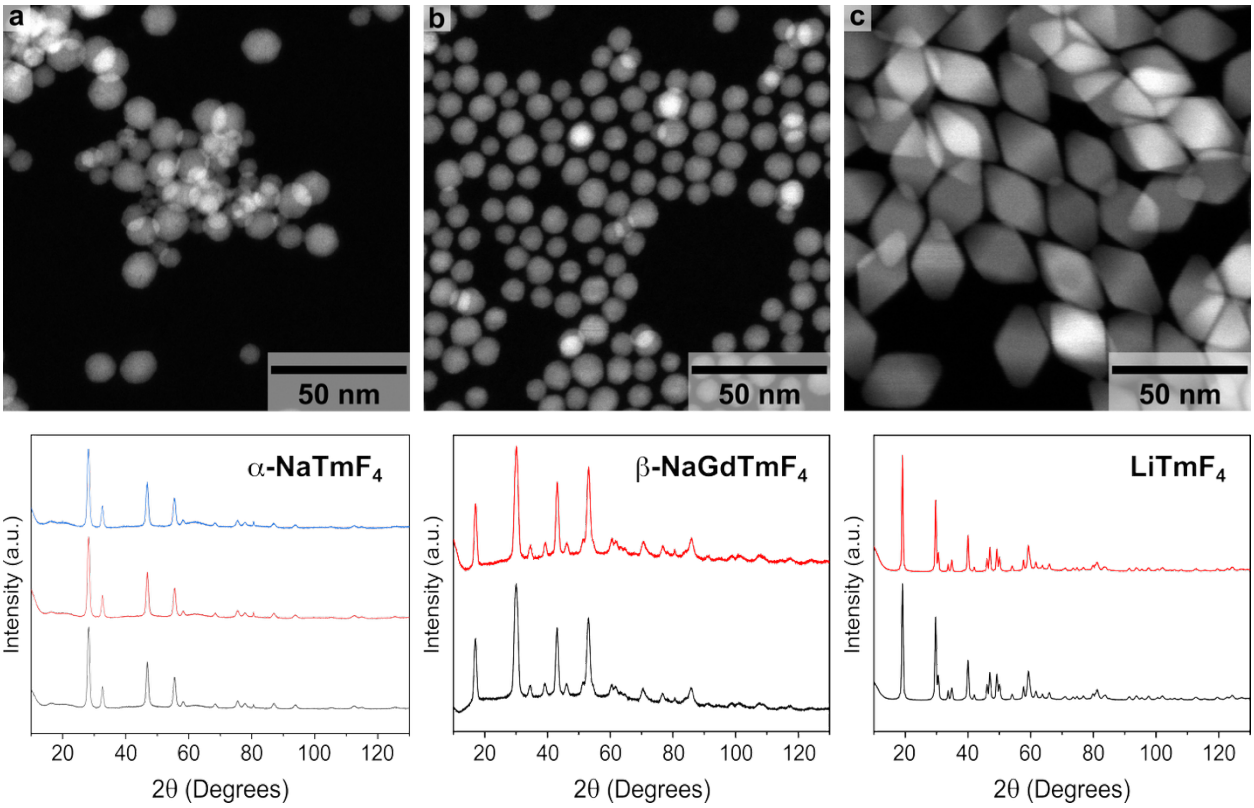


Figure 6.1 *Low-magnification HAADF-STEM images and PXRD analysis of optically active core NCs synthesized by different methods. Low-magnification HAADF-STEM images of (a) α-$NaTmF_4$, (b) β-$NaGdTmF_4$, and (c) $LiTmF_4$ NCs synthesized via thermal decomposition. Corresponding experimental PXRD patterns are shown for each optically active core material.*

Previous studies have shown a relationship between intermixing, shell thickness, and precursor selection in hexagonal β-$NaErF_4$:Yb/$NaYF_4$ NCs.[45,166] This study expands on this by maintaining constant shell precursors (trifluoroacetates only) while varying the crystal structure of the NCs used as seeds from (cubic, hexagonal, and tetragonal), as well as using homogeneous and heterogeneous shells. Furthermore, extrinsic parameters like synthesis methodology, aging temperature, and aging time were kept constant across all samples. Shell thickness was controlled by adjusting the shell precursor from 0.5, 1.0, and 2.0 mmol of the cation precursor. Intermixing was assessed by monitoring the spatial distribution of Tm^{3+} ions by EDXS chemical maps. Tm^{3+} ions are initially expected to remain within the core region, irrespective of the core's crystal structure, shell's chemical composition, and/or shell size.

6.3.2 The Influence of Varying Shell Thicknesses on Tm^{3+} Ion Distribution in α-$NaTmF_4$-based Core–shell NCs

Figures 6.2 and 6.3 presents representative HAADF-STEM images alongside corresponding EDXS chemical maps of α-$NaTmF_4$–based core–shell NCs with varying shell thicknesses illustrating the distribution of Y^{3+} and/or Ca^{2+} ions.

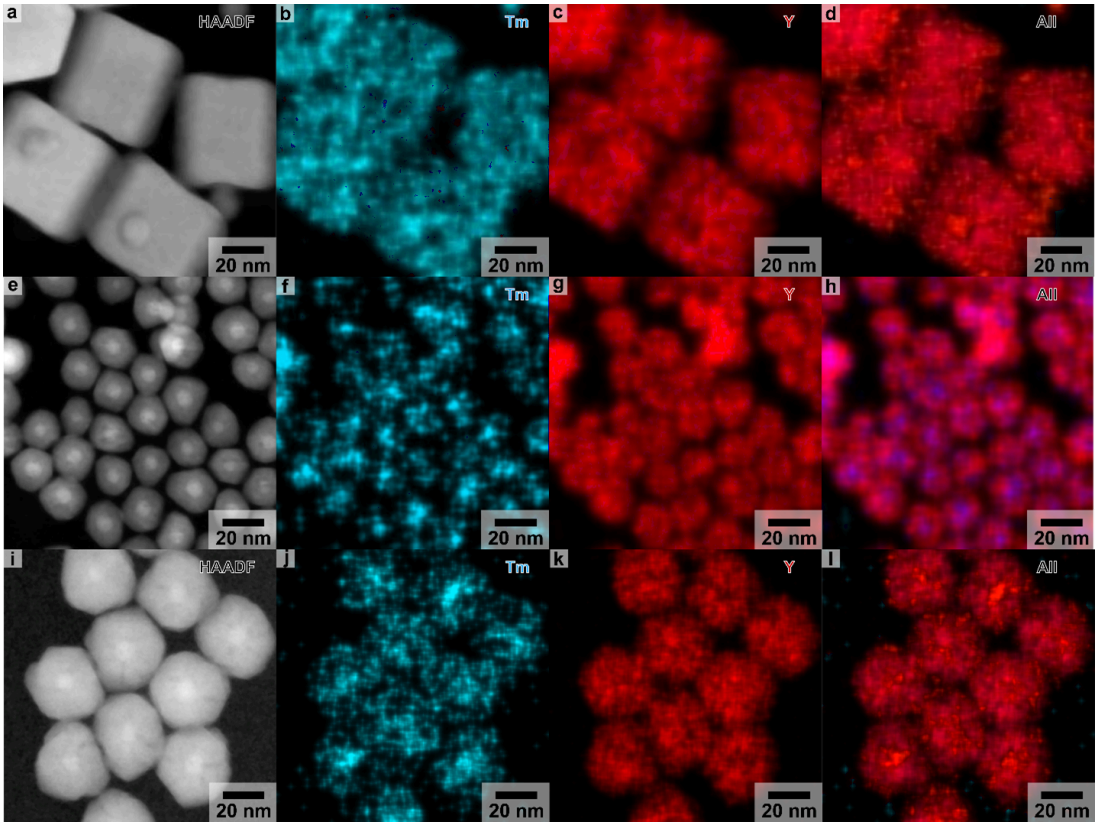


Figure 6.2 *High-magnification HAADF-STEM images of α-$NaTmF_4$/$NaYF_4$ NCs with different shell thicknesses, obtained by adjusting the amount of Na and Y precursors used during shell growth: 0.5 mmol (a), 1.0 mmol (e), and 2.0 mmol (i). Corresponding EDXS elemental maps show the distribution of Tm^{3+} (b, f, j) and Y^{3+} (c, g, k), along with the spatial overlap of both signals (d, h, l). All shell growths were carried out at an aging temperature of 300 °C*

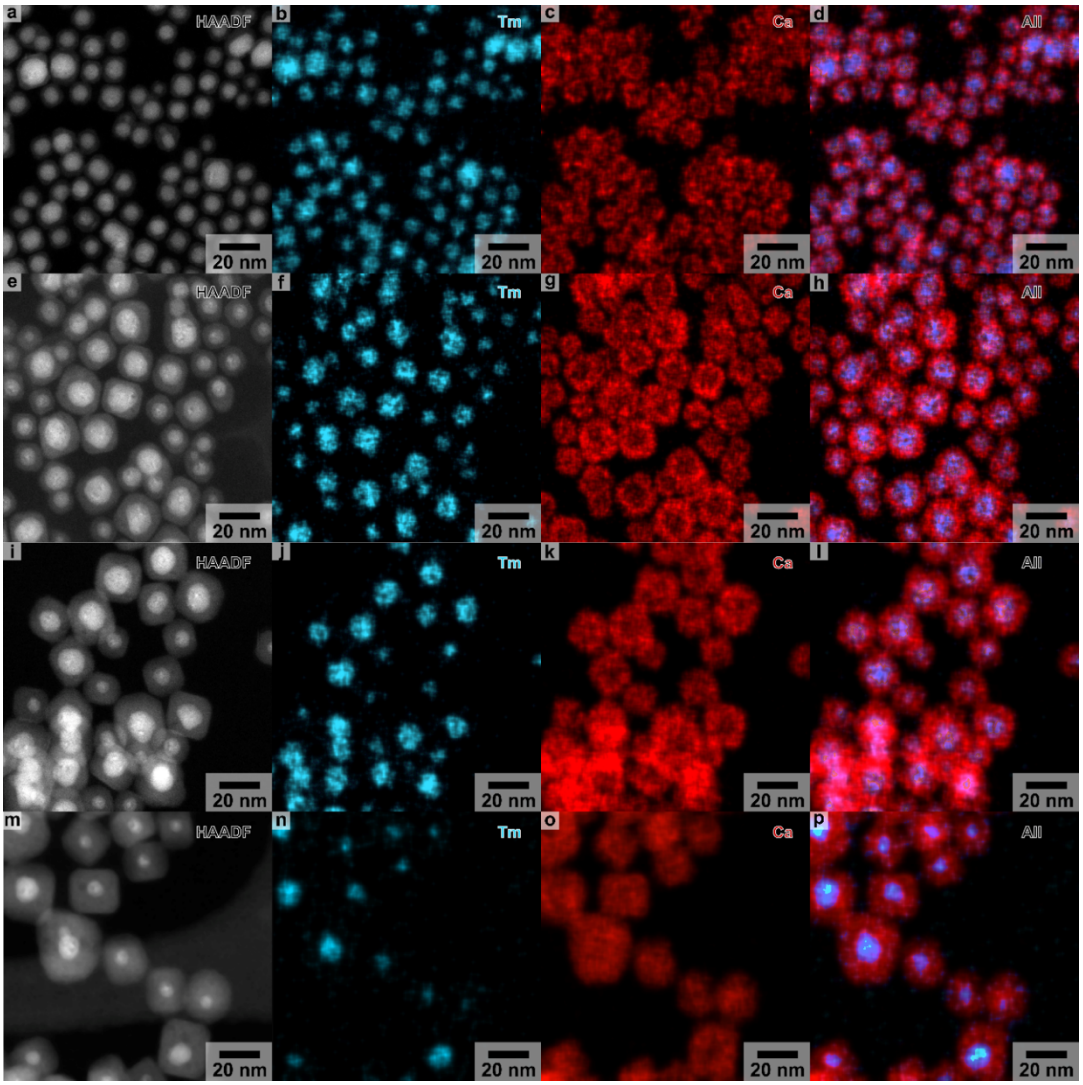


Figure 6.3 *High-magnification HAADF-STEM images of α-$NaTmF_4$/CaF_2 NCs with different shell thicknesses, obtained by adjusting the amount of CaF_2 precursor used during shell growth: 0.5 mmol (a), 1.0 mmol (e), 2.0 mmol (i), and 4.0 mmol (m). Corresponding EDXS elemental maps show the distribution of Tm^{3+} (b, f, j, n) and Ca^{2+} (c, g, k, o), along with the spatial overlap of both signals (d, h, l, p). All shell growths were carried out at an aging temperature of 300 °C.*

While PXRD patterns for the α-$NaTmF_4$-based homogeneous and heterogeneous NCs are shown in Figure 6.4

When a 0.5 mmol precursor concentration is used for the homogeneous $NaYF_4$ shell growth on α-$NaTmF_4$, the resulting NCs differ from the initial seeds. As shown in Figure 6.2a, the size and morphology change dramatically from an isotropic to an anisotropic rectangular shape; additionally, no Z-contrast due to the Tm^{3+} and Y^{3+} could be observed.

With this amount of shell precursor, the α-$NaTmF_4$ NCs appear to experience recrystallization rather than shell growth. This recrystallization causes the destruction of the original α-$NaTmF_4$ core (evident from the widespread Tm^{3+} signal), forming a type-III (alloyed) interface pattern. This destruction and recrystallization from cubic to hexagonal is evident in the PXRD patterns (Figure 6.4, left), which is dominated by the characteristic reflections of the hexagonal crystal structure. Previous studies have indicated that α-$NaREF_4$ NCs can experience a recrystallization process triggered by reheating at high temperatures, resulting in the formation of the β-phase.[175–177] Trying to grow a thin shell by using a low amount of shell precursors may have triggered a comparable effect, resulting in the growth of rectangular 25 nm β-$NaTm_{1-x}Y_xF_4$ NCs.

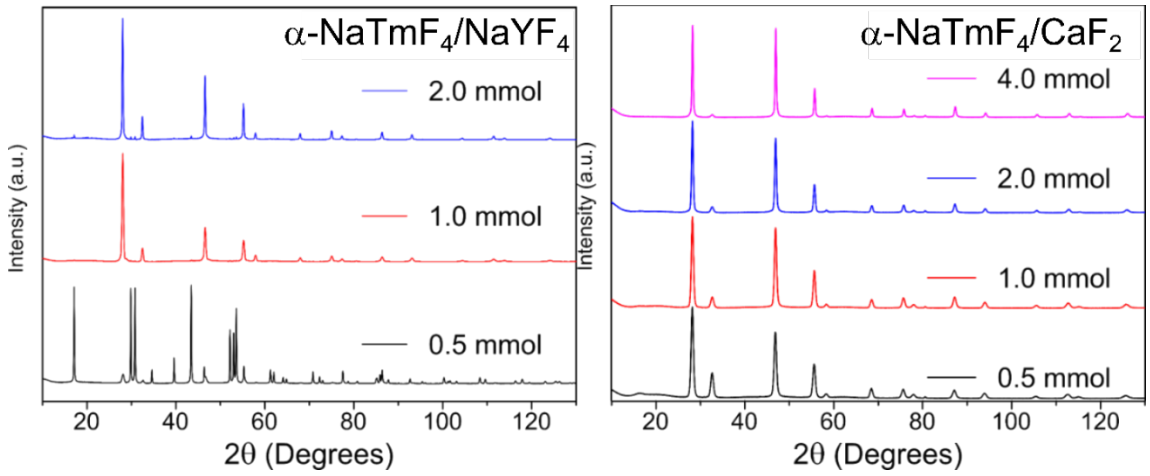


Figure 6.4 *PXRD analysis of α-$NaTmF_4$/$NaYF_4$, and α-$NaTmF_4$/CaF_2 NCs with varying shell thicknesses. Experimental PXRD patterns of α-$NaTmF_4$/$NaYF_4$ (left), and α-$NaTmF_4$/CaF_2 (right) NCs synthesized with different shell thicknesses. All samples were prepared under identical conditions, with a shell growth aging temperature of 300 °C.*

Increasing the shell precursor concentration, core–shell-like NCs are observed, keeping the isotropic morphology of the α-$NaTmF_4$ seeds. This homogeneous NCs showed a mean size of 23.7 nm using 1.0 mmol of shell precursors (Figure 6.2e) and increased to 37.2 nm when 2.0 mmol of shell precursors (Figure 6.2i) was used. Z-contrast can be observed at the core area, in both cases, with a more pronounced contrast observed in the 1.0 mmol NCs. The Tm^{3+} chemical maps for these NCs showed a large Tm^{3+}

distribution. With the large Tm^{3+} distribution it was impossible to determine the position of the core based on the signal from the chemical maps, suggesting the formation of a type-II or III interface (Figure 6.2b,f,j) in each case.

Conversely, when for the heterogeneous α-$NaTmF_4/CaF_2$, a clear Z-contrast is observed in the core area for all the shell sizes (Figures 6.3a,e,i,m). The measured mean sizes of the α-$NaTmF_4/CaF_2$ NCs were 10.8 nm, 12.1 nm, and 15.4 nm for 0.5 mmol, 1.0 mmol, and 2.0 mmol of shell precursors, respectively. PXRD patterns display only the characteristic reflections of the cubic structure, and no other phases or impurities were noticeable. The peaks become sharper as the precursor concentration increases, which is the result of the enlargement of the crystallite size by the epitaxial growth of the CaF_2 shell. Especial attention must be given to the (200) reflection intensity, which decreases by increasing the shell thickness. This (200) reflection will be discussed in more depth in the subsection "Diffraction data analysis from α-$NaTmF_4/CaF_2$ and β-$NaGdTmF_4/CaF_2$". Tm^{3+} chemical maps showed well-defined signal (Figures 6.3b,f,j,n) at the expected core location, during the whole range of the precursor's concentrations used. From the chemical maps a type-I interface pattern can be inferred and negligible intermixing.

6.3.3 The Effect of Varying Shell Thicknesses on Tm^{3+} Ion Distribution in β-$NaGdTmF_4$-based Core–shell NCs

Figures 6.5, 6.6, and 6.7 display HAADF-STEM images of β-$NaGdTmF_4/NaYF_4$ NCs with varying shell thicknesses. The average sizes were found to be 13.9 nm and 18.2 nm for NCs synthesized with precursor concentrations of 0.5 mmol and 1.0 mmol, respectively. Yet, a precursor concentration of 2.0 mmol led to highly polydisperse NCs with irregular shapes. The Z-contrast in HAADF-STEM images was distinguished between the 0.5 mmol and 1.0 mmol NCs but was not observed in the 2.0 mmol β-$NaGdTmF_4/NaYF_4$ NCs. The Tm^{3+} chemical maps for the 0.5 mmol NCs (Figure 6.5b) show what it might seem as a confined Tm^{3+} signal; nevertheless, the thin $NaYF_4$ shell makes it difficult to confirm a type-I interface pattern. For NCs synthesized with 1.0 mmol and 2.0 mmol of shell precursors, the Tm^{3+} signal was distributed everywhere in the NC, suggesting a type-III interface (Figure 6.6b and 6.7b).

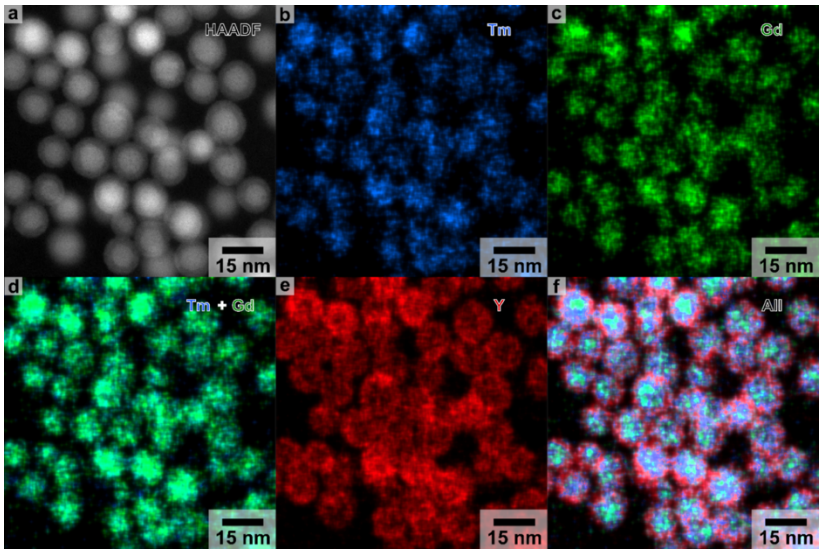


Figure 6.5 *(a) High-magnification HAADF-STEM image of β-NaGdTmF₄/NaYF₄ NCs with a thin NaYF₄ shell, synthesized using 0.5 mmol of precursors. (b–e) Corresponding EDXS chemical maps showing the spatial distribution of Tm^{3+} (b), Gd^{3+} (c), and Y^{3+} (e). (d) Overlap of the Tm^{3+} and Gd^{3+} signals. (f) Overlay of all three cation signals (Tm^{3+}, Gd^{3+}, and Y^{3+}). The shell growth was conducted at an aging temperature of 300 °C.*

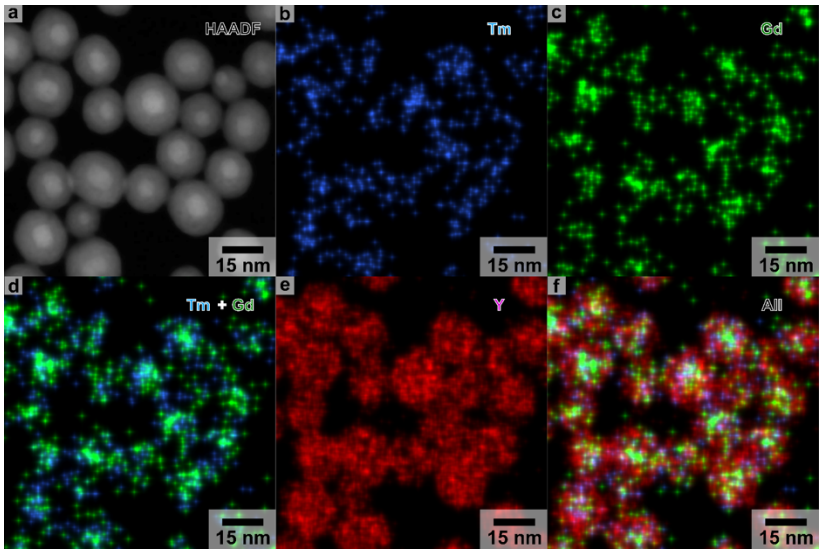


Figure 6.6 *(a) High-magnification HAADF-STEM image of β-NaGdTmF₄/NaYF₄ NCs with a NaYF₄ shell, synthesized using 1.0 mmol of precursors. (b–e) Corresponding EDXS chemical maps showing the spatial distribution of Tm^{3+} (b), Gd^{3+} (c), and Y^{3+} (e). (d) Overlap of the Tm^{3+} and Gd^{3+} signals. (f) Overlay of all three cation signals (Tm^{3+}, Gd^{3+}, and Y^{3+}). The shell growth was conducted at an aging temperature of 300 °C.*

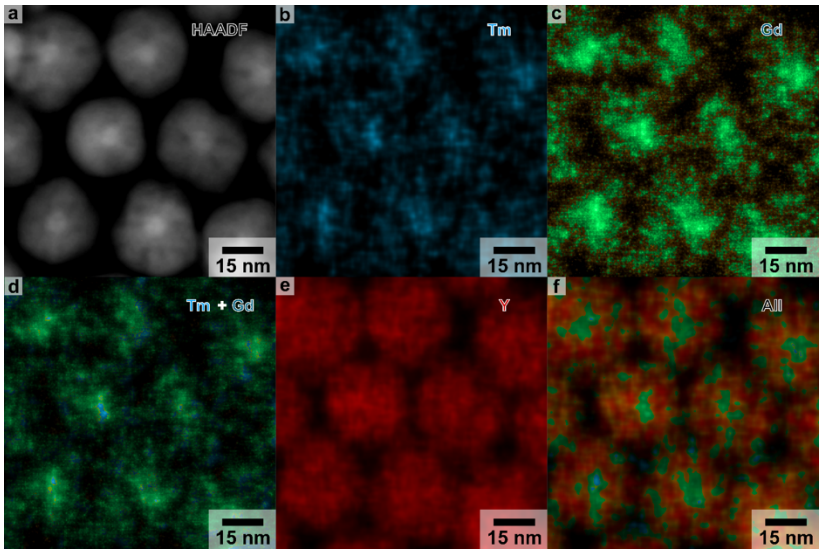


Figure 6.7 *(a) High-magnification HAADF-STEM image of β-NaGdTmF₄/NaYF₄ NCs with a thick NaYF₄ shell, synthesized using 2.0 mmol of precursors. (b–e) Corresponding EDXS chemical maps showing the spatial distribution of Tm^{3+} (b), Gd^{3+} (c), and Y^{3+} (e). (d) Overlap of the Tm^{3+} and Gd^{3+} signals. (f) Overlay of all three cation signals (Tm^{3+}, Gd^{3+}, and Y^{3+}). The shell growth was conducted at an aging temperature of 300 °C.*

Surprisingly, the average size of the β-$NaGdTmF_4/CaF_2$ NCs (Figure 6.8) remained nearly constant, regardless of the Ca^{2+} precursor amount, unlike other material combinations. Instead, the primary effect observed was the degree to which core seeds were successfully covered by the CaF_2 shell. Specifically, the mean size of the core-shell NCs at the lowest precursor amount was similar to the mean size when 1.0 mmol of precursors were used, and slightly lower than with 2.0 mmol of precursor amount (15.4 nm, 15.6 nm, and 18.4 nm, for 0.5 mmol, 1.0 mmol, and 2.0 mmol, respectively). Yet, a substantial amount of the core NCs stayed unshelled at 0.5 mmol (Figure 6.8a).

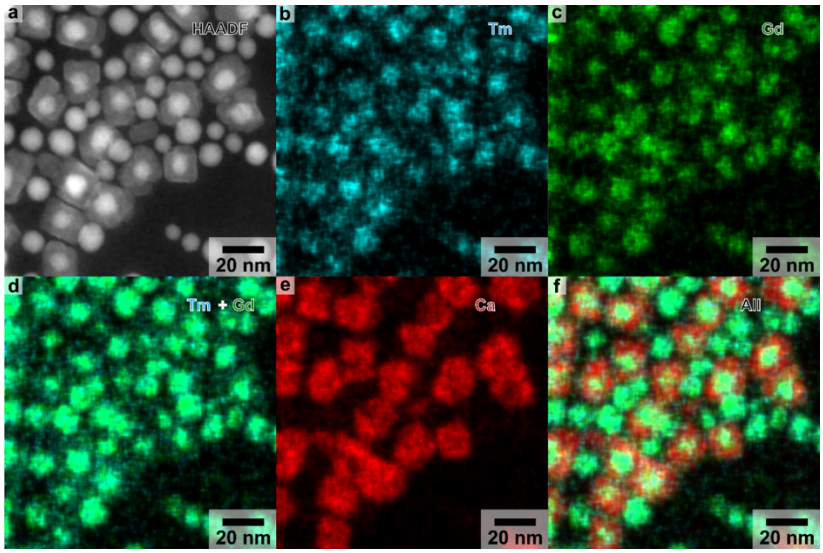


Figure 6.8 *(a) High-magnification HAADF-STEM image of β-$NaGdTmF_4$/$NaYF_4$ NCs with a CaF_2 shell, obtained using 0.5 mmol of precursors. (b–e) EDXS chemical maps showing the spatial distribution of Tm^{3+} (b), Gd^{3+} (c), and Y^{3+} (e). (d) Overlay of Tm^{3+} and Gd^{3+} signals. (f) Combined overlay of all three cationic species (Tm^{3+}, Gd^{3+}, and Y^{3+}). The shell growth was carried out at an aging temperature of 300 °C.*

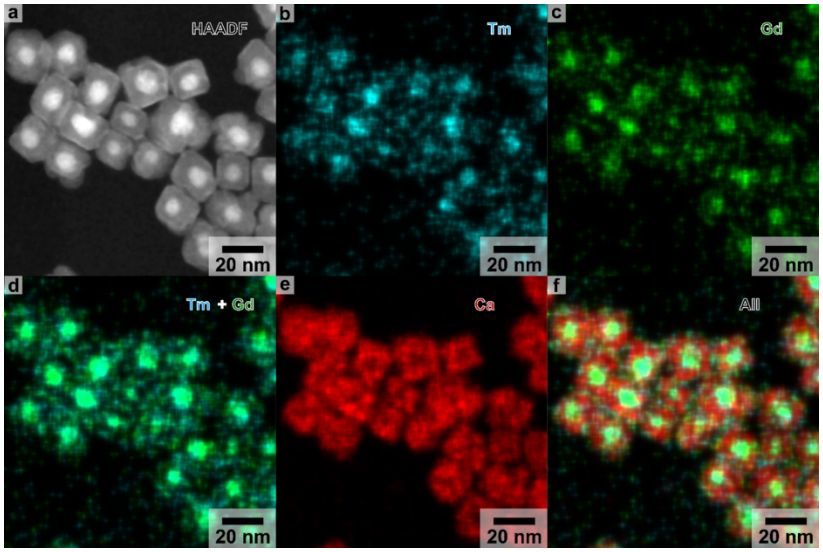


Figure 6.9 *High-magnification HAADF-STEM and EDXS analysis of β-$NaGdTmF_4$/$NaYF_4$ homostructures with a shell. (a) High-magnification HAADF-STEM image of β-$NaGdTmF_4$/$NaYF_4$ NCs with a thin $NaYF_4$ shell, obtained using 1.0 mmol of precursors. (b–e) EDXS chemical maps showing the spatial distribution of Tm^{3+} (b), Gd^{3+} (c), and Y^{3+} (e). (d) Overlay of Tm^{3+} and Gd^{3+} signals. (f) Combined overlay of all three cationic species (Tm^{3+}, Gd^{3+}, and Y^{3+}). The shell growth was carried out at an aging temperature of 300 °C.*

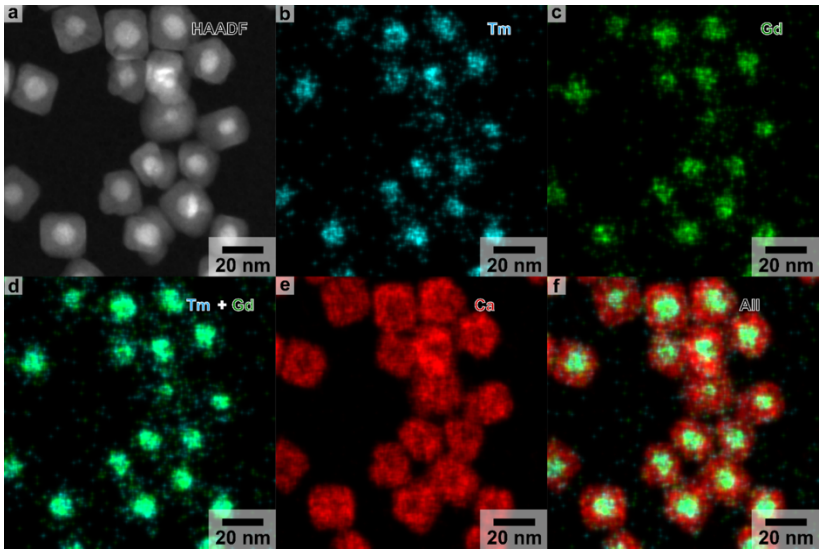


Figure 6.10 *High-magnification HAADF-STEM and EDXS analysis of β-$NaGdTmF_4$/$NaYF_4$ homostructures with a shell. (a) High-magnification HAADF-STEM image of β-$NaGdTmF_4$/$NaYF_4$ NCs with a thin $NaYF_4$ shell, obtained using 2.0 mmol of precursors. (b–e) EDXS chemical maps showing the spatial distribution of Tm^{3+} (b), Gd^{3+} (c), and Y^{3+} (e). (d) Overlay of Tm^{3+} and Gd^{3+} signals. (f) Combined overlay of all three cationic species (Tm^{3+}, Gd^{3+}, and Y^{3+}). The shell growth was carried out at an aging temperature of 300 °C.*

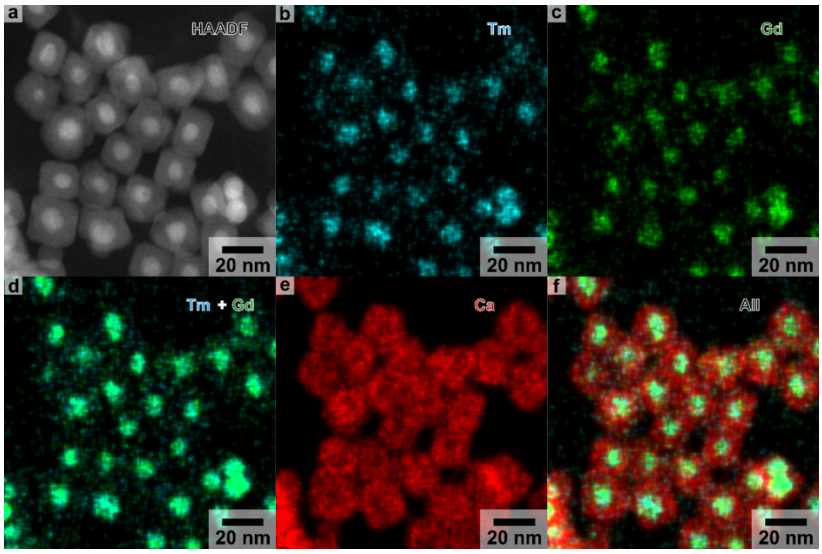


Figure 6.11 *High-magnification HAADF-STEM and EDXS analysis of β-$NaGdTmF_4$/$NaYF_4$ homostructures with a thick shell. (a) High-magnification HAADF-STEM image of β-$NaGdTmF_4$/$NaYF_4$ NCs with a thin $NaYF_4$ shell, obtained using 4.0 mmol of precursors. (b–e) EDXS chemical maps showing the spatial distribution of Tm^{3+} (b), Gd^{3+} (c), and Y^{3+} (e). (d) Overlay of Tm^{3+} and Gd^{3+} signals. (f) Combined overlay of all three cationic species (Tm^{3+}, Gd^{3+}, and Y^{3+}). The shell growth was carried out at an aging temperature of 300 °C.*

Interestingly, the Tm^{3+} chemical maps indicate some confinement of the signal, which may be attributed to a type-II (intermixed) interface. This observation aligns with previous studies that reported a degree of intermixing in heterogeneous core–shell NCs with different crystal structures and/or significant lattice mismatch. In the β-$NaGdTmF_4/CaF_2$ NCs the lattice mismatch is approximately 10% in the *a* and *b* unit cell parameters.[62,178] This intermixing is thought to be important for creating a transitional domain that facilitates the heterogeneous shell growth. The Tm^{3+} signal seems more confined with increasing shell precursor concentration (Figures 6.8b, 6.9b, 6.10b, and 6.11b). In fact, the Tm^{3+} signal at 2.0 mmol of β-$NaGdTmF_4/CaF_2$ is somewhat similar to the α-$NaTmF_4/CaF_2$ Tm^{3+} signal (Figures 6.3 and 6.11b).

The PXRD patterns of β-$NaGdTmF_4/NaYF_4$ NCs display the characteristic reflections of the hexagonal structure for the 0.5 mmol and 1.0 mmol (Figure 6.12). Nevertheless, the 2.0 mmol NC diffractogram show mainly the characteristic peaks of the cubic crystal structure.

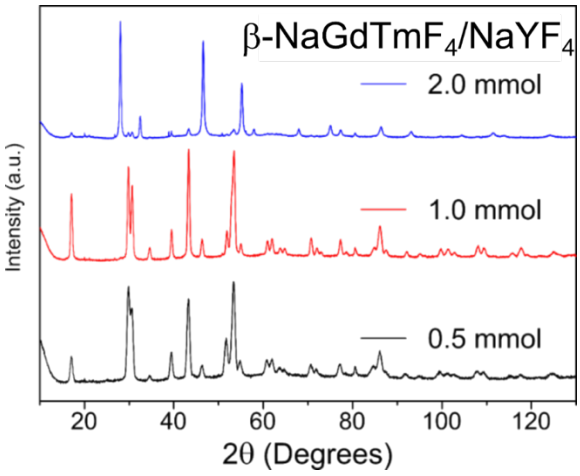


Figure 6.12 *PXRD analysis of β-$NaGdTmF_4/NaYF_4$ NCs with varying shell thicknesses. Experimental PXRD patterns of β-$NaGdTmF_4/NaYF_4$ NCs synthesized with different shell thicknesses. All samples were prepared under identical conditions, with a shell growth aging temperature of 300 °C.*

This recrystallization explains the significant change in the NCs morphology observed in Figure 6.7. Studies of $NaREF_4$ NCs recrystallization by adjusting the Y^{3+}/Gd^{3+} ratio have revealed that higher Y^{3+} concentrations helped stabilizing the cubic phase.[171,173,174] Specifically, research by Damasco et al.[173] has shown that approximately 10% Gd^{3+}

doping in $NaYF_4$ is needed to stabilize the hexagonal phase, but lower concentrations favoring the cubic structure. Similarly, Wang et al. reported that Gd^{3+} concentrations below 15% in $NaYF_4$ also result in the cubic phase.[174] These observations align with what is shown here, where a 2.0 mmol homogeneous shell reduces the Gd^{3+} content of the core–shell NCs from 50% to 16.6%, triggering the recrystallization to cubic phase. The slight 1 – 5% discrepancy can be due to the presence of Tm^{3+} ions, which may promote the recrystallization.[171]

6.3.4 Different Shell Thicknesses Effect on Tm^{3+} Ion Distribution on $LiTmF_4$-based Core–Shell NCs

The effect of different shell thicknesses on Tm^{3+} ion distribution in $LiTmF_4$-based core-shell NCs is examined via HAADF-STEM images of $LiTmF_4/LiYF_4$ NCs with different varied thicknesses, which are presented in Figure 6.13. These NCs exhibit the expected anisotropic rectangular bipyramidal morphology, displaying mean sizes of 42.5x32.6 nm, 55.9x39.6 nm, and 61.9x53.4 nm for the 0.5 mmol, 1.0 mmol, and 2.0 mmol shell precursor concentrations, respectively. HAADF-STEM images reveal a distinct Z-contrast that can be observed for all the NCs; in contrast, the 2.0 mmol precursor concentration (Figure 6.13i) results in a more rounded appearance of the bright core region compared to those obtained at lower concentrations.

In the case of the $LiTmF_4/LiYF_4$ NCs, the Tm^{3+} signal in the chemical maps seems to be primarily located within the core region (Figure 6.3b,f,j,n), irrespective of the shell thickness. Nevertheless, a subtle Tm^{3+} signal is detected in the shell area, which implies a type-II (intermixed) interface. Figure 6.14 displays the PXRD patterns of $LiTmF_4/LiYF_4$ NCs exhibit the characteristic reflections of the tetragonal structure, and no other impurities or secondary phases were identified for shell precursor concentrations of 0.5 mmol, 1.0 mmol, and 2.0 mmol. Because $LiYF_4$ is a homogeneous shell, lattice mismatch is not a concern. Heterogeneous $LiTmF_4/CaF_2$ NCs were not synthesized because it was already shown in chapter 5 (section 5.5.3, Figure 5.9a-g) demonstrated a good Z-contrast but also revealed that the Tm^{3+} signal extended to the shell's edge, resulting in complete luminescence quenching.

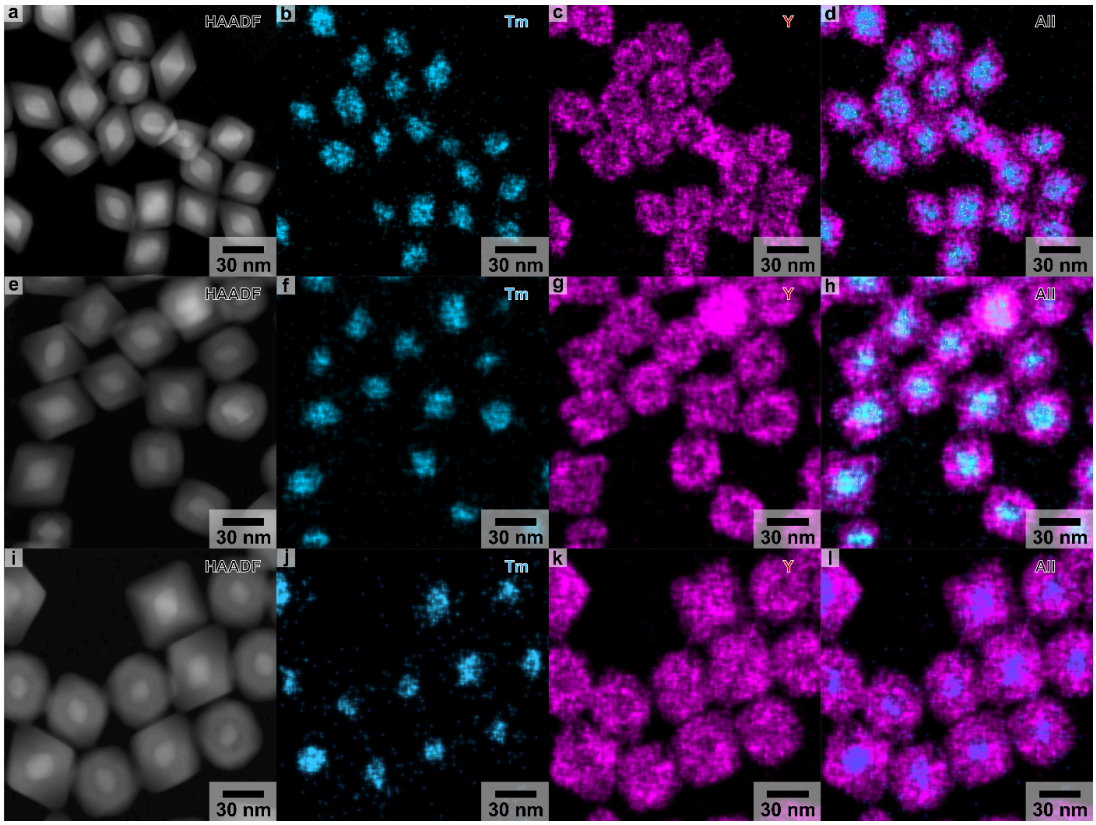


Figure 6.13 *High-magnification HAADF-STEM and EDXS analysis of $LiTmF_4/LiYF_4$ homostructures with varying shell thicknesses. HAADF-STEM images of $LiTmF_4/LiYF_4$ NCs synthesized with different shell thicknesses by varying the amount of $LiYF_4$ precursor: 0.5 mmol (a), 1.0 mmol (e), and 2.0 mmol (i). Corresponding EDXS chemical maps show the spatial distribution of Tm^{3+} (b, f, j) and Y^{3+} (c, g, k). (d, h, l) Overlay images showing the spatial overlap of Tm^{3+} and Y^{3+} signals for each shell thickness. Shell growth was performed at an aging temperature of 300 °C*

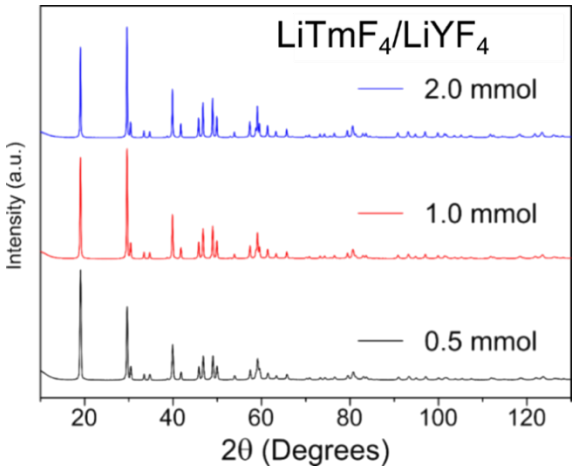


Figure 6.14 *PXRD analysis of $LiTmF_4/LiYF_4$ NCs with varying shell thicknesses. Experimental PXRD patterns of $LiTmF_4/LiYF_4$ NCs synthesized with different shell thicknesses. All samples were prepared under identical conditions, with a shell growth aging temperature of 300 °C.*

The $LiTmF_4/LiYF_4$ homostructures and α-$NaTmF_4/CaF_2$ heterostructures demonstrated a spatially restricted Tm^{3+} signal through all the parameters measures do far. This observation implies that the degree of intermixing can be reduced when the shell material is constrained to crystallizing in a singular crystal structure that corresponds to that of the core. For β-$NaGdTmF_4/CaF_2$ heterostructures, a certain level of intermixing was expected, as it is hypothesized that this intermixing facilitates a transitional zone between the disparate crystal structures. These results emphasize the importance of material pairings in dictating interface architecture, given that an identical core composition, synthesized under equivalent conditions, can yield varying interface patterns depending on the specific material combinations.

6.3.5 Diffraction Data Analysis from α-$NaTmF_4/CaF_2$ and β-$NaGdTmF_4/CaF_2$

A more thorough analysis of the diffraction patterns for heterogeneous combinations of α–$NaTmF_4/CaF_2$ and β-$NaGdTmF_4/CaF_2$ across all the shell thicknesses acquired offers more information into the identification of intermixing. Even though α-$NaTmF_4$ ($Fm\bar{3}m$, a = b = c = 5.476 Å, a = b = g = 90 °) and CaF_2 ($Fm\bar{3}m$, a = b = c = 5.470 Å, a = b = g = 90°) are isostructural polymorphs that possess almost identical lattice parameters and negligible lattice mismatch, there is a significant distinction in their respective diffraction patterns.

Previous research indicates that the (200) reflection observed at 32.7° can be used to detect the presence of RE ions within the CaF_2 crystal structure. Calculations using the Debye scattering equation show that pure CaF_2 has a (200) reflection with zero intensity.[148,149] However, when Tm^{3+} replaces some of the Ca^{2+} ions, the (200) reflection exhibits a non-zero intensity. Therefore, monitoring the intensity of this reflection can help differentiate between type-I and type-II/III interface architectures in NCs with a CaF_2 shell. Because the experimental PXRD pattern reflects the entire set of coherently diffracting domains, the intensity of the reflection is expected to decrease as CaF_2 content increases, which would be expected of a type-I (sharp) interface. This is a result of the combination of the zero-intensity reflection from CaF_2 and the non-zero contribution from α-$NaTmF_4$. Figure 6.15a demonstrates this expected behavior with increasing shell thickness for α-$NaTmF_4/CaF_2$ NCs. Nonetheless, β-$NaGdTmF_4$ ($P\bar{6}$, a = b = 6.004 Å, c = 3.594 Å, a =

b = 90 °, g = 120 °) and CaF_2 have distinct crystal structures, with a significant lattice mismatch of approximately 10% in the *a* and *b* unit cell parameters.

The PXRD pattern of the β-$NaGdTmF_4/CaF_2$ heterogeneous core–shell NCs shows that both cubic and hexagonal phases coexist. The reflection at 32.7° is absent in the β-$NaREF_4$ phase, and its intensity is zero for pure CaF_2. Therefore, this reflection should not appear in the diffraction pattern of β-$NaGdTmF_4/CaF_2$. Yet, its presence in all β-$NaGdTmF_4/CaF_2$ NCs diffraction patterns (Figure 6.15b) suggests that Gd^{3+}/Tm^{3+} ions are being incorporated into the cubic CaF_2 crystal lattice, confirming ion migration and intermixing in β-$NaGdTmF_4/CaF_2$ NCs across all shell thicknesses, which aligns with observations from the chemical maps (Figures 6.8b, 6.9b, 6.10b, and 6.11b).

Another key feature in the PXRD patterns of β–$NaGdTmF_4/CaF_2$ is that the intensity of the peaks associated with the hexagonal diffraction pattern decreases significantly with the addition of CaF_2. The hexagonal pattern disappears completely at a 4.0 mmol shell precursor amount (Figure 6.12). The phenomenon of hexagonal diffraction peaks disappearing during the formation of cubic heterogeneous core–shell NCs is not new, and has been reported several times before.[178–181] A common explanation attributes the loss of hexagonal diffraction to a larger volume of cubic phase material relative to the hexagonal phase. However, this explanation is insufficient considering that the CaF_2 shell's volume is roughly double that of the hexagonal core and the atomic scattering factors for Gd^{3+}/Tm^{3+} are greater than Ca^{2+}. Instead, the substantial reduction and eventual disappearance of characteristic hexagonal reflections in the PXRD patterns is likely due to a Ca^{2+}-induced phase transition, especially given the established intermixing in β–$NaGdTmF_4/CaF_2$ NCs. This transition is triggered by the incorporation of Ca^{2+} into the hexagonal β–$NaGdTmF_4$ lattice, transforming the hexagonal core into a cubic $NaGd_{0.5-x}Tm_{0.5-y}F_4:Ca_{x+y}$ structure. Because the Gd^{3+} content is essential for stabilizing the hexagonal crystal structure, the introduction of Ca^{2+}, which favors the cubic structure, effectively dilutes the Gd^{3+} concentration, thus promoting this phase transition.

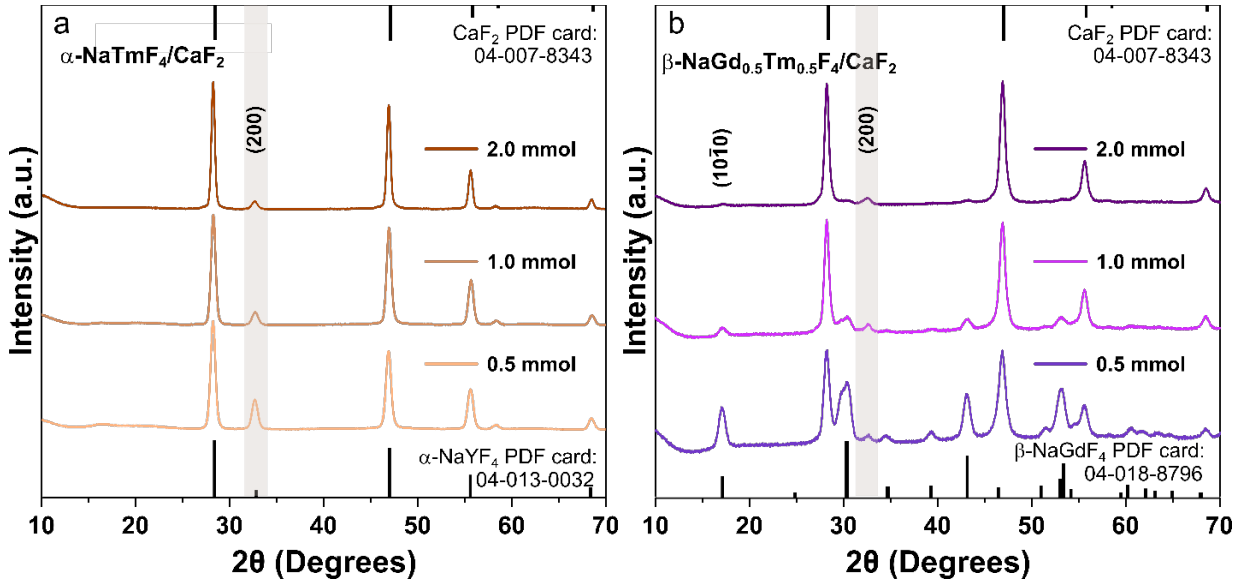


Figure 6.15 *(a, b) Experimental PXRD patterns of α-$NaTmF_4/CaF_2$ (a) and β-$NaGdTmF_4/CaF_2$ (b) heterogeneous NCs prepared with different shell thicknesses. The diffraction patterns were indexed using reference data from the PDF-4+ database for α-$NaYF_4$ (PDF 04-013-0032), β-$NaGdF_4$ (PDF 04-018-8796), and CaF_2 (PDF 04-007-8343). The shaded region highlights the (200) Bragg reflection of the cubic phase, which is sensitive to the presence of RE^{3+} ions within the lattice. In pure CaF_2, this reflection is absent (intensity = 0), as indicated in the reference pattern. In α-$NaTmF_4/CaF_2$, the (200) reflection intensity progressively decreases with increasing CaF_2 shell thickness, indicating reduced RE occupancy in the shell. In contrast, the emergence of the (200) reflection in β-$NaGdTmF_4/CaF_2$ diffraction patterns suggests the migration of Tm^{3+} ions from the core into the CaF_2 shell.*

When the Ca^{2+} precursor concentrations are lower (0.5 mmol and 1.0 mmol), the reflections from the hexagonal crystal structure likely come from cores without shells, where a phase transition was not started. This hexagonal to cubic phase transition from β-$NaGdTmF_4/CaF_2$ could also explain why the Tm^{3+} signal seemed more contained in the EDXS chemical maps of β-$NaGdTmF_4/CaF_2$ as the shell precursor amount increased (Figure 6.8b, 6.9b, 6.10b, and 6.11b). The reasons why CaF_2 can grow in β-$NaGdTmF_4$, creating an intermixed shell instead of separate nucleation, are still not clear. Nevertheless, the structural changes in β-$NaGdTmF_4/CaF_2$ heterostructures demonstrate how important it is to consider the interaction between composition, structure, and crystallinity when designing core–shell NCs.

To further investigate the phase transition, high-resolution transmission electron microscopy (HRTEM) images of β-$NaGdTmF_4$ (Figure 6.16) and β-$NaGdTmF_4/CaF_2$ (0.5

mmol, and 4.0 mmol shell precursors) NCs were obtained (Figure 6.17). Figure 6.16 shows a single β-$NaGdTmF_4$ NC in direct space (left side), along with its corresponding Fourier transform (FT) pattern (Figure 6.16, right side). The FT pattern can be indexed to a hexagonal crystal structure ($P\bar{6}$), consistent with observations from the PXRD patterns.

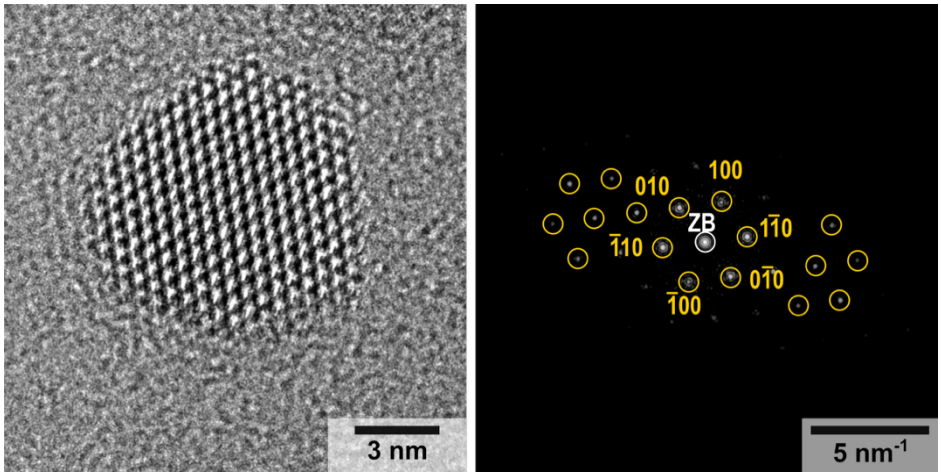


Figure 6.16 *HRTEM images of a β-$NaGdTmF_4$ NCs used as seeds. The white-highlighted areas in each image indicate the regions from which the 2-dimensional Fourier transforms (FTs) were obtained. The FT patterns correspond to the hexagonal (**$P\bar{6}$**) symmetry indexed along the [001] zone axis. The zero-order beam (ZB) is marked with a white circle.*

Although there were a lot of unshelled cores when using 0.5 mmol of Ca precursors, it is interesting to note that for the core–shell NCs the FT patterns taken from the center of the particle showed the superposition of the hexagonal and the cubic lattice structures (Figure 6.17b). Meanwhile, the FT patterns of the same NC acquired on the edge of the particle (shell region) showed only the reflections from the cubic structure (Figure 6.17d).

At 4.0 mmol of Ca shell precursors the FT patterns obtained from the central region of a β-$NaGdTmF_4$/CaF_2 heterogeneous NCs do not show any signs of the hexagonal crystal structure; instead, they align perfectly with the cubic crystal structure (Figure 6.17f,h). Even with the presence of a CaF_2 shell surrounding the core, there should be a superposition of FT patterns from both cubic and hexagonal structures if the β-$NaGdTmF_4$ was not destroyed, as seen when 0.5 mmol of shell precursors were used.

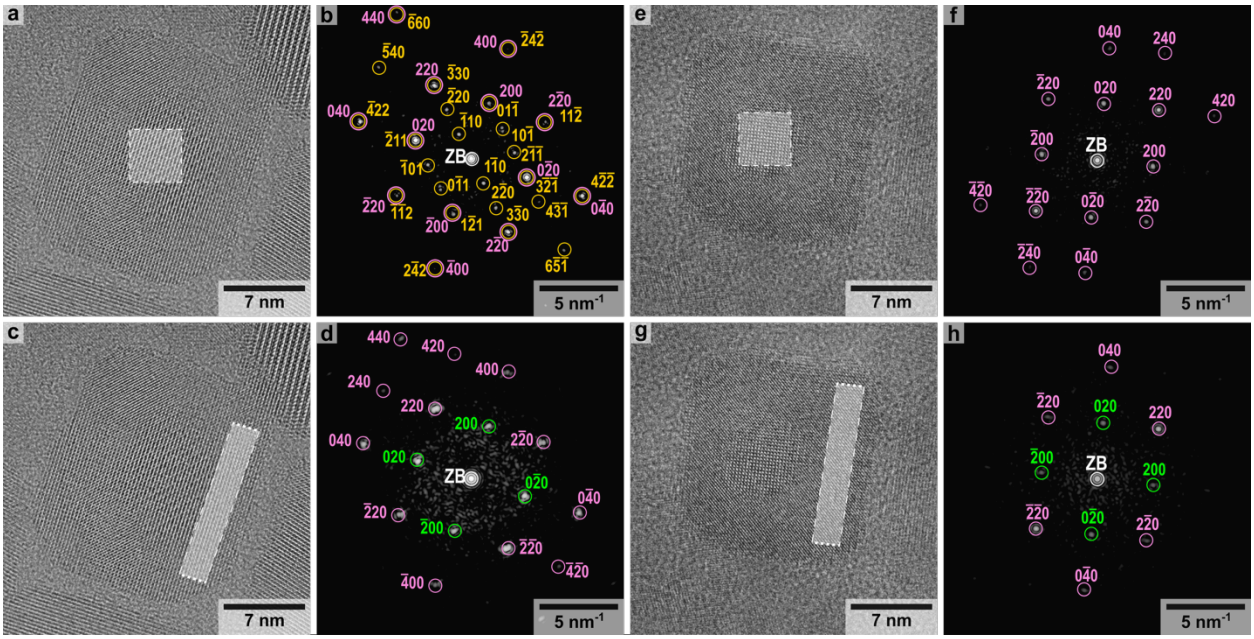


Figure 6.17 *(a, c) HRTEM images of a β-NaGdTmF₄/CaF₂ NC synthesized using 0.5 mmol of CaF₂ precursor, showing the core (a) and shell (c) regions. (e, g) HRTEM images of a NC synthesized using 4.0 mmol of CaF₂ precursor, also showing the core (e) and shell (g) regions. The white-highlighted areas in each image indicate the regions from which the 2-dimensional Fourier transforms (FTs) were obtained. The FT patterns corresponding to the 0.5 mmol sample reveal a superposition of hexagonal ($P\bar{6}$) symmetry for the core and cubic ($Fm\bar{3}m$) symmetry for the shell, both indexed along the [001] zone axis. In contrast, the FT patterns of the 4.0 mmol sample match the cubic ($Fm\bar{3}m$) crystal structure in the [001]- zone axis for both core and shell regions, indicating extensive intermixing. The zero-order beam (ZB) is marked with a white circle. Reflections indicated by green circles correspond to structure factors $|F_{(hkl)}|$ that are theoretically zero for pure CaF₂ and thus should be absent. Their presence indicates the incorporation of Gd^{3+}/Tm^{3+} ions into the CaF₂ shell.*

Additionally, the zero-intensity reflections for CaF_2 were found in the FT patterns, indicating the presence of Gd^{3+}/Tm^{3+} in the CaF_2 crystal lattice. These observations provide additional support for the intermixing suggested by the chemical maps in Figures 6.8b, 6.9b, 6.10b, and 6.11b. A similar effect is observed as with the homogeneous $NaYF_4$ shell, where increasing the amount of shell precursor triggered the destruction of the hexagonal crystal structure and favored the cubic structure. Even though some of the β-$NaGdTmF_4/CaF_2$ NCs recrystallized from hexagonal to cubic structure, for simplicity in the rest of the chapter, all the NCs where β-$NaGdTmF_4$ NCs were used as seeds will continue to be labeled as "β-".

6.3.6 Effect of Shell Growth Temperature on Intermixing

Since core–shell NCs are often synthesized using a fixed set of experimental parameters, the observation of intermixing is limited by a narrow window of these parameters. Modifying the shell growth temperature, particularly by reducing it below the core's synthesis temperature, could potentially reduce intermixing, favoring a type-I (sharp) interface more than at higher temperatures as the core should be more stable at temperatures lower than the temperature at which it was synthesized. Moreover, if ion migration greatly contributes to intermixing, lower temperatures could diminish the intermixing in these NCs.

To investigate this, the amount of shell precursor was kept constant at 1.0 mmol, while the shell growth temperature was lowered from 300 °C to 280 °C and 260 °C. Heterogeneous core–shell NCs were not synthesized at lower temperatures due to existing literature and the current findings indicating negligible intermixing in α-$NaTmF_4/CaF_2$ core–shell NCs at 300 °C; and that β-$NaGdTmF_4/CaF_2$ core–shell NCs undergo recrystallization suggesting that the synthesis temperature is not a driving force for intermixing in these core–shell NCs.

HAADF-STEM images of α-$NaTmF_4/NaYF_4$, β-$NaGdTmF_4/NaYF_4$, and $LiTmF_4/LiYF_4$ NCs synthesized at 260 °C and 280 °C (Figure 6.18, 6.19, 6.20, 6.21, and 6.22) reveal a clear Z-contrast across all samples, with no recrystallization observed, as each NC maintained the morphology of its respective seeds. Separate nucleation was observed at 260 °C for α-$NaTmF_4/NaYF_4$ and β-$NaGdTmF_4/NaYF_4$, but not at higher temperatures. Additionally, α-$NaTmF_4/NaYF_4$ NCs synthesized at 260 °C showed a less defined shell morphology. Though, α-$NaTmF_4/NaYF_4$ core–shell-like NCs were observed with mean sizes of 19.7 nm and 23.0 nm for the 260 °C and 280 °C synthesis temperatures, respectively. These values are similar to the 23.7 nm mean size of the α-$NaTmF_4/NaYF_4$ NCs prepared at 300 °C.

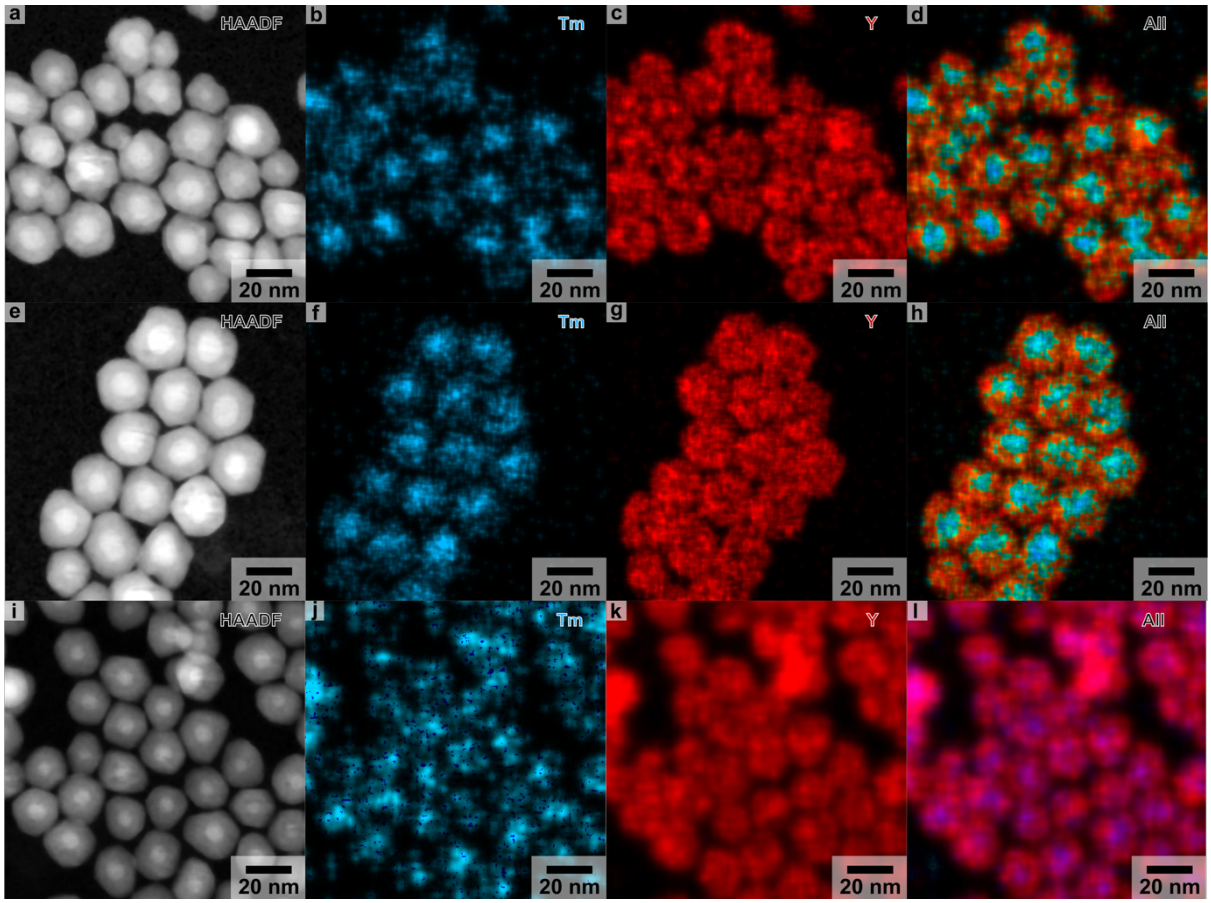


Figure 6.18 *HAADF-STEM images of α-$NaTmF_4/NaYF_4$ NCs synthesized using 1.0 mmol of precursors at aging temperatures of 260 °C (a-d), 280 °C (e-h), and 300 °C (i-l). Corresponding EDXS elemental maps show the spatial distribution of Tm^{3+} (b, f, j) and Y^{3+} (c, g, k). (d, h, l) Overlay images indicating the spatial overlap of Tm^{3+} and Y^{3+} signals at each temperature.*

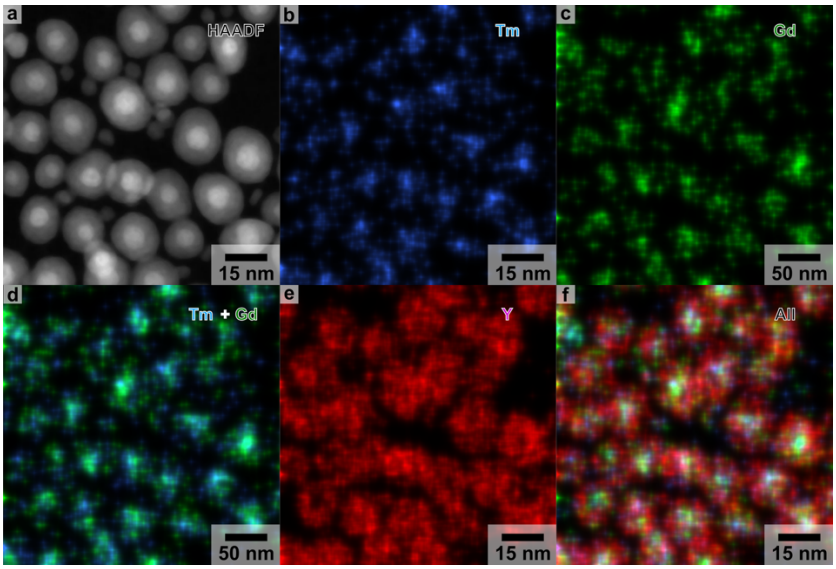


Figure 6.19 *HAADF-STEM images of β-$NaGdTmF_4$/$NaYF_4$ NCs synthesized using 1.0 mmol of precursors at aging temperatures of 260 °C. Corresponding EDXS elemental maps show the spatial distribution of Tm^{3+} (b), Gd^{3+} (c), Tm^{3+} and Gd^{3+} overlay (d) and Y^{3+} (e). (f) Overlay images indicating the spatial overlap of Tm^{3+} Gd^{3+}, and Y^{3+} signals at each temperature.*

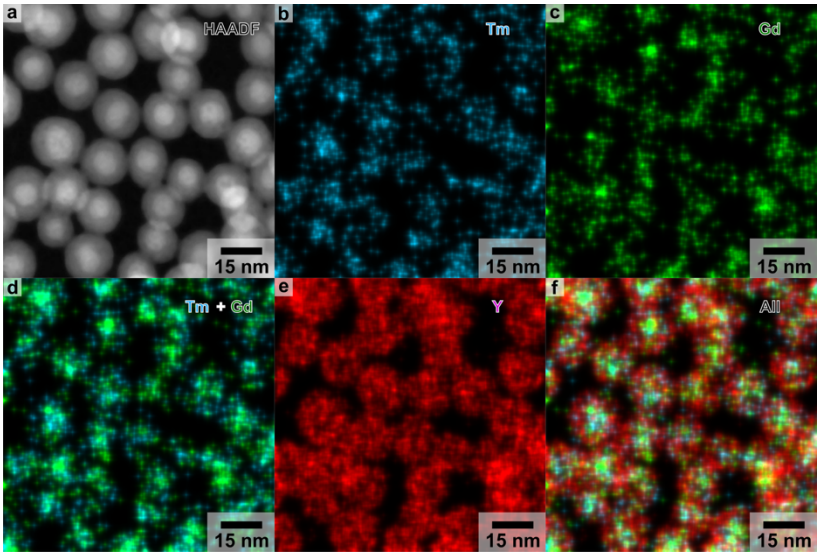


Figure 6.20 *HAADF-STEM images of β-$NaGdTmF_4$/$NaYF_4$ NCs synthesized using 1.0 mmol of precursors at aging temperatures of 280 °C. Corresponding EDXS elemental maps show the spatial distribution of Tm^{3+} (b), Gd^{3+} (c), Tm^{3+} and Gd^{3+} overlay (d) and Y^{3+} (e). (f) Overlay images indicating the spatial overlap of Tm^{3+} Gd^{3+}, and Y^{3+} signals at each temperature.*

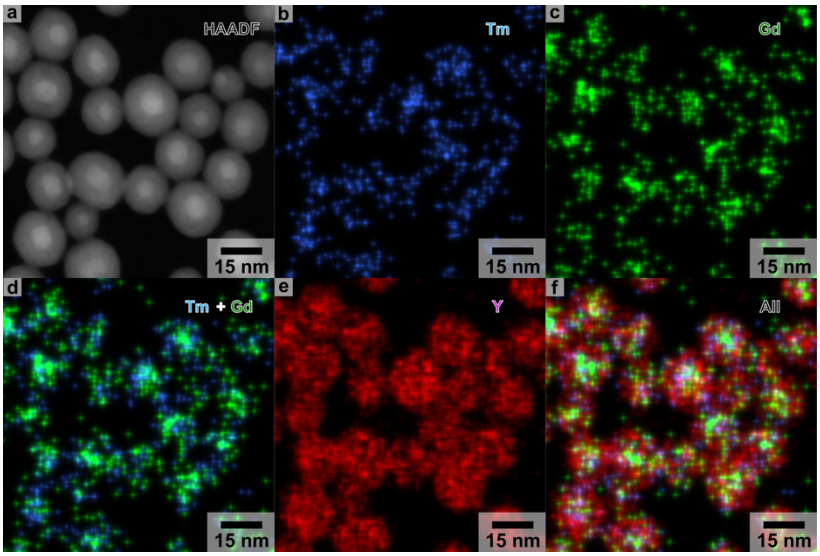


Figure 6.21 *HAADF-STEM images of β-NaGdTmF$_4$/NaYF$_4$ NCs synthesized using 1.0 mmol of precursors at aging temperatures of 300 °C. Corresponding EDXS elemental maps show the spatial distribution of Tm^{3+} (b), Gd^{3+} (c), Tm^{3+} and Gd^{3+} overlay (d) and Y^{3+} (e). (f) Overlay images indicating the spatial overlap of Tm^{3+} Gd^{3+}, and Y^{3+} signals at each temperature.*

The distribution of Tm^{3+} within the chemical maps of α-NaTmF$_4$/NaYF$_4$ NCs synthesized at 260 °C and 280 °C mirrors that of those synthesized at 300 °C, displaying a dispersed signal consistent with a type-III (alloyed) interface. For all homogeneous core–shell with α-NaTmF4, a dispersed Tm^{3+} signal distribution was observed, irrespective of the shell thickness or the synthesis temperature.

For the β-NaGdTmF$_4$/NaYF$_4$ NCs, the HAADF-STEM images reveal similar mean sizes of 15.5 nm and 15.6 nm for the NCs synthesized at 260 °C and 280 °C, respectively. These mean sizes are also comparable to the 18.2 nm size of the β-NaGdTmF$_4$/NaYF$_4$ NCs synthesized at 300 °C. Consistent with the overall NaREF$_4$/NaREF$_4$ series presented in this study, the Tm^{3+} chemical maps showed a dispersed signal. Although the Tm^{3+} signal appears most confined at 260 °C among the series, no significant difference was observed in the Tm^{3+} signal distribution at 280 °C and 300 °C, indicating a type-III (alloyed) interface in all cases.

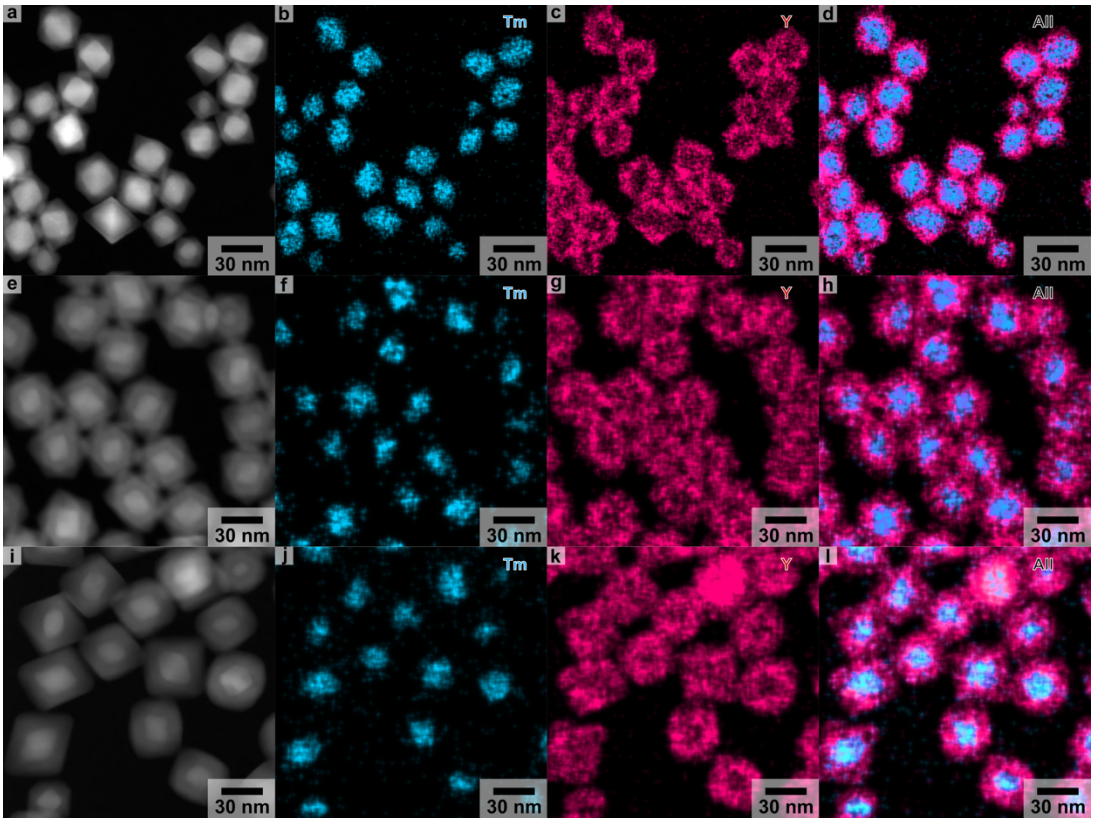


Figure 6.22 *HAADF-STEM images of $LiTmF_4/LiYF_4$ NCs synthesized using 1.0 mmol of precursors at aging temperatures of 260 °C (a-d), 280 °C (e-h), and 300 °C (i-l). Corresponding EDXS elemental maps show the spatial distribution of Tm^{3+} (b, f, j) and Y^{3+} (c, g, k). (d, h, l) Overlay images indicating the spatial overlap of Tm^{3+} and Y^{3+} signals at each temperature.*

For the $LiTmF_4/LiYF_4$ NCs, the shell formed at 260 °C was exceptionally thin in one direction which could be a potential energy loss area due to minimal coverage to the core NCs. At this temperature, the NCs measured 34.0x28.4 nm, but the size increased drastically at 280 °C, to 50.6x39.9 nm, approaching that of NCs synthesized at 300 °C. The distribution of Tm^{3+} in NCs synthesized at 280 °C was very similar to that of NCs synthesized at 300 °C, showing a concentrated region and a slight dispersion of the signal, indicative of a type-II (intermixed) interface. A hypothesis for the dispersed Tm^{3+} signal found in all $LiTmF_4$-based NCs could potentially arise from the partial dissolution of the $LiTmF_4$ seeds' bipyramidal tips. The increased surface curvature of these sharp tips raises their surface energy, making them more susceptible to dissolution and, consequently, the release of small quantities of Tm^{3+} ions into the shell growth solution.

Nevertheless, further investigation into the core–shell growth mechanism is required to verify this hypothesis.

It was hypothesized that lowering the aging temperature would be a key strategy to reduce or prevent intermixing. Still, comparative analysis of Tm^{3+} ion distribution among NCs synthesized at 260 °C, 280 °C, and 300 °C revealed no significant differences for α-$NaTmF_4$ and β-$NaGdTmF_4$ homogeneous core–shell NCs, which consistently exhibited a broad Tm^{3+} distribution. Conversely, $LiTmF_4$ homogeneous core–shell NCs maintained a confined Tm^{3+} signal with some dispersion around the core region. These results indicate that decreasing the temperature, even below the core formation temperature, did not consistently prevent or reduce the extent of intermixing in the fluoride-based core-shell NCs studied. Other factors, such as the competition between crystallographic phases, had a more pronounced influence on the degree of intermixing than the synthesis temperature. PXRD patterns of the NCs with the shells grown at different temperatures are shown in Figures 6.23.

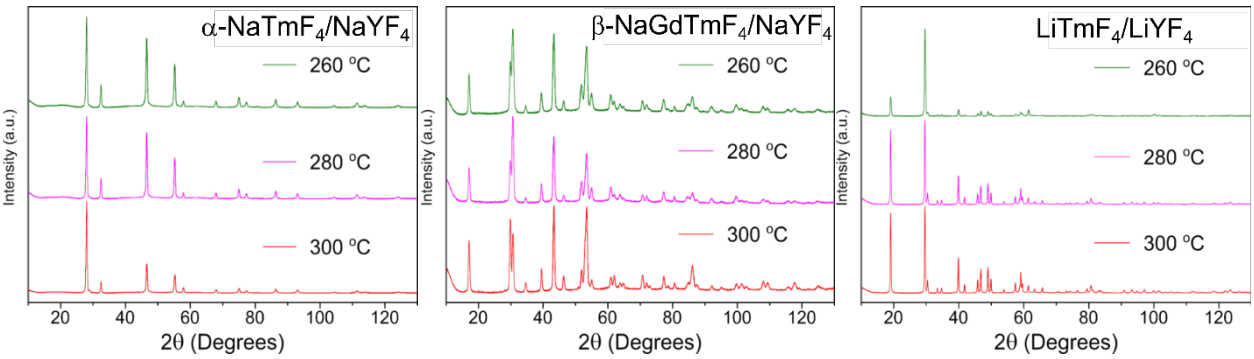


Figure 6.23 *Experimental PXRD patterns of α-$NaTmF_4$/$NaYF_4$, β-$NaGdTmF_4$/$NaYF_4$, and $LiTmF_4$/$LiYF_4$ NCs synthesized at 260 °C, 280 °C, and 300 °C. All samples were prepared under identical conditions, with a shell precursor concentration of 1.0 mmol.*

6.3.7 Optical Characterization

The high concentration of Tm^{3+} ions within a $NaREF_4$ host provides a favorable environment for the 1800 nm emission of Tm, as the established mechanism for this emission relies on a cross-relaxation process that becomes more efficient when multiple Tm^{3+} ions are in close proximity.[30,150] Figure 6.24 illustrates the SWIR downshifting

emission spectra of Tm^{3+} under 800 nm excitation for α-$NaTmF_4$/$NaYF_4$, α-$NaTmF_4$/CaF_2, β-$NaGdTmF_4$/$NaYF_4$, β-$NaGdTmF_4$/CaF_2, and $LiTmF_4$/$LiYF_4$. As expected, NCs with thin shells, like $LiTmF_4$/$LiYF_4$ NCs synthesized at 260 °C, or those without a pure shell, such as $NaREF_4$/$NaREF_4$ NCs, provided little to no protection against surface quenching, and showed the lowest emissions. The emission intensity increased when the pure shell thickness reached approximately 3 nm, indicating improved passivation, but then decreased with larger pure shell thickness. An exception to this trend was observed for β-$NaGdTmF_4$/CaF_2 NCs, where Ca^{2+} induced recrystallization from hexagonal to cubic.

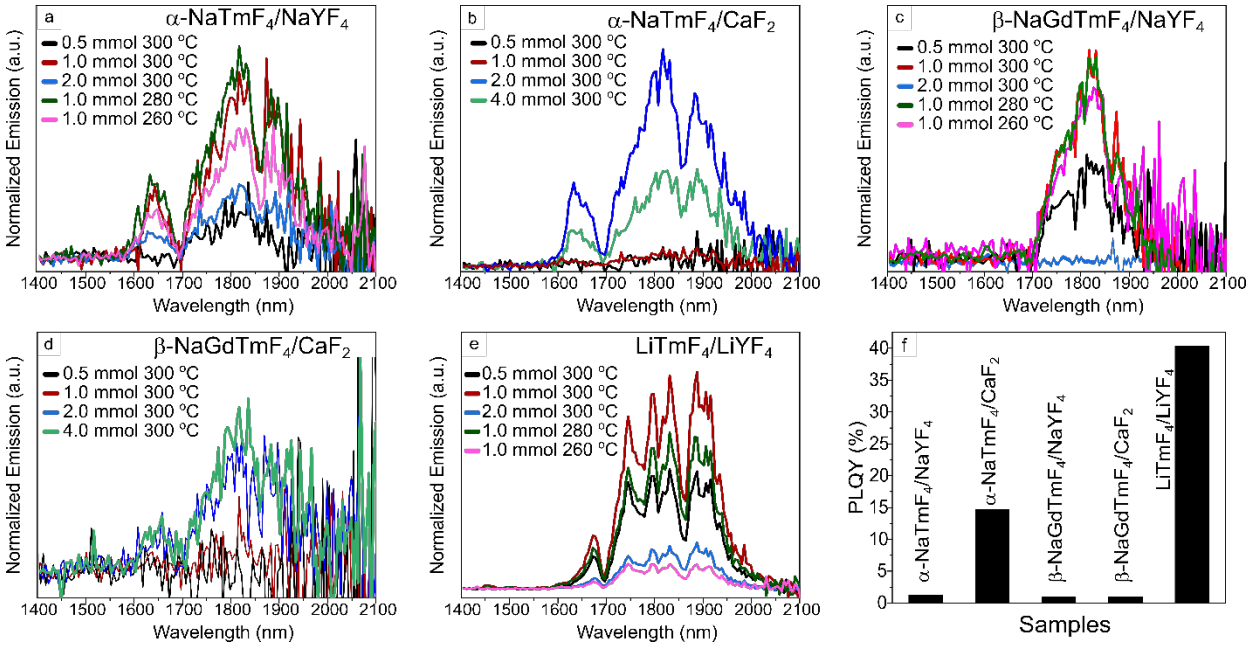


Figure 6.24 *(a–e) SWIR emission spectra (1400 nm < λ_{em} < 2100 nm) of the core–shell homo- and heterostructured NCs developed in this study, measured in chloroform under 800 nm excitation at a power density of approximately 3.5 W/cm². Solid lines represent emission from NCs with varying shell thicknesses, while translucent lines correspond to NCs synthesized at different aging temperatures. The emission spectra are normalized to their corresponding absorption values at the excitation wavelength. (f) PLQY values of the best-performing core–shell NCs from each homo- and heterostructured combination.*

The decrease of the downshifting emission intensity derived from increasing the shell thickness was noted by Fischer et al. This phenomenon was called "surface quenching-assisted downshifting" in their report,[36] and it was hypothesized that a certain

degree of surface quenching might enhance downshifting emission by preventing the population of higher energy levels.

Slight improvements in emission were observed for α-$NaTmF_4$ and β-$NaGdTmF_4$ homogeneous core–shell NCs synthesized at lower aging temperatures compared to those synthesized at 300 °C within their respective core–shell NC sets. The lower reaction temperature may have slightly reduced Tm^{3+} migration, which provided slightly better protection from quenchers. However, the efficiency of the α-$NaTmF_4$ and β-$NaGdTmF_4$ homogeneous core–shell NCs remained substantially lower than that of the α-$NaTmF_4/CaF_2$ heterogeneous core–shell NCs, as shown in the PLQY bar chart. Still, the homogeneous shell could not fully exploit fully the cores' emission potential due to intermixing. Overall, the highest emission intensities and PLQY were observed in NCs exhibiting minimal intermixing, reaching 14% for α–$NaTmF_4/CaF_2$ and 39% for $LiTmF_4/LiYF_4$. In contrast, NCs with a homogeneous shell displaying intermixing exhibited considerably lower PLQY, often below 2%, emphasizing the need to understand and control shell growth mechanisms to optimize optical properties. Further PLQY improvements could potentially be achieved even with intermixed NCs, as the Tm^{3+} ion concentration used was not optimized, since this work primarily focused on the distribution of Tm^{3+} ions rather than maximizing PLQY.

6.4 Summary

In summary, the successful synthesis of core–shell $NaREF_4$ or $LiTmF_4$ NCs relies on carefully managing both inherent material properties and external reaction conditions. Intermixing was observed under all synthesis conditions where lattice recrystallization was possible, as evidenced by the Tm^{3+} ion distribution in the chemical maps. Conversely, core–shell NCs with only one stable crystalline phase, such as α-$NaTmF_4/CaF_2$ (type-I interface) and $LiTmF_4/LiYF_4$ (type-II interface), consistently maintained the spatial confinement of Tm^{3+} ions and exhibited a pure shell region, thus mitigating intermixing. Our data also suggests that ion migration resulting from intermixing can destabilize the

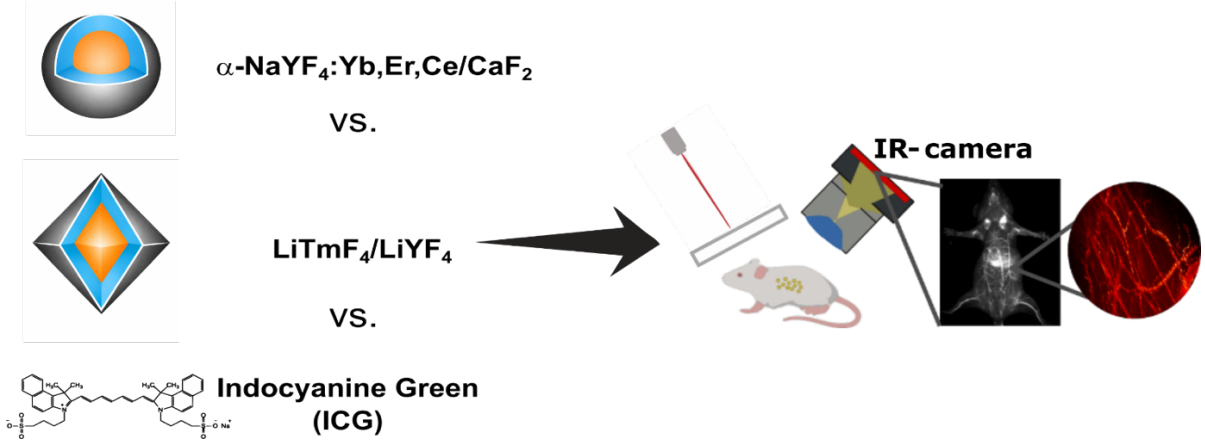
hexagonal phase in β-$NaGdTmF_4$ systems, leading to recrystallization into the cubic phase when thick shells of heterogeneous CaF_2 are grown.

While altering synthesis conditions, like using lower aging temperatures, was initially expected to reduce intermixing, these adjustments proved ineffective when competition between crystallographic phases was possible. This indicates that cation migration in these fluoride-based core–shell NCs is not significantly influenced by temperature under these conditions.

NCs with minimal intermixing demonstrated the highest SWIR emission intensity and PLQY, whereas those with significant intermixing exhibited low PLQY values. These results underscore the critical importance of controlling shell growth mechanisms to preserve the intended atomic-scale architecture and enhance optical properties. Future research should prioritize developing strategies to control crystallographic phase transitions and intermixing during synthesis.

Accurately mapping the individual and combined effects of all synthesis parameters on interface architecture and intermixing is a significant challenge that could take years to accomplish manually. While this study offers an initial understanding of how select intrinsic and extrinsic parameters vary, a truly comprehensive and accurate mapping will require advanced synthesis facilities with automated workflows. Overcoming these challenges and gaining a deeper understanding of these processes is essential for the rational design of next-generation RE-based luminescent NCs with enhanced performance.

7. Comparison of SWIR Fluorescence Performance: Nanocrystal Emitters *vs*. Indocyanine Green



The content of this chapter has been partially published in separate works and includes unpublished results.

***Arteaga Cardona, F.**, Jain, N., Popescu, R. et al. Preventing cation intermixing enables 50% quantum yield in sub-15 nm short-wave infrared-emitting rare-earth based core–shell nanocrystals. Nat Commun 14, 4462 (2023). https://doi.org/10.1038/s41467-023-40031-4.*

***Arteaga Cardona, F.**; Madirov, E.; Popescu, R.; Wang, D.; Busko, D.; Ectors, D.; Kübel, C.; Eggeler, Y. M.; Arús, B. A.; Chmyrov, A.; Bruns, O. T.; Richards, B. S.; Hudry, D. Dramatic Impact of Materials Combinations on the Chemical Organization of Core–shell Nanocrystals: Boosting the Tm^{3+} Emission above 1600 Nm. ACS Nano 2024. https://doi.org/10.1021/acsnano.4c07932.*

Contributions

The author prepared the samples, performed the XRD measurements, designed the figures, and analyzed the results. Bernardo A. Arús, Andriy Chmyrov, and Oliver T. Bruns provided the set-up and equipment and helped with the acquisition and analysis of the SWIR images. Damien Hudry and Bryce S. Richards conceived the initial idea, provided guidance during the project, contributed intellectual input.

7.1 Motivation

NCs exhibiting negligible cation intermixing have been successfully prepared and reported in this thesis; these NCs represent some of the most efficient SWIR-emitting materials reported to date, with record PLQY values at emission wavelengths centered around 1500 nm (α-$NaYF_4$:$Yb_{0.42}Er_{0.05}Ce_{0.03}$/$CaF_2$; PLQY ~50%; results available in Chapter 4)[61] and 1800 nm ($LiTmF_4$/$LiYF_4$; PLQY ~39%; results available in Chapter 5).[62] Given their outstanding optical performance, it is relevant to benchmark these NCs against indocyanine green (ICG; PLQY ~0.9%),[123] which is the most widely used SWIR emitting fluorophore in biomedical imaging and is approved for clinical use by the U.S. Food and Drug Administration.[182]

Beyond a direct performance comparison, this chapter aims to examine how imaging outcomes differ across distinct regions of the near- and short-wave infrared spectrum. Imaging at 1500 nm and 1800 nm is expected to be influenced not only by the intrinsic brightness of the fluorophores but also by wavelength-dependent effects such as tissue scattering, water absorption, and background attenuation. Evaluating these factors provides a more comprehensive understanding of the advantages and limitations associated with each material composition and spectral window.

To maintain focus on imaging performance, a full structural and optical characterization of the NCs is not repeated in this chapter; detailed analyses are provided in Chapters 4 and 5.

7.2 Overview

The SWIR imaging context and its advantages over conventional NIR-I fluorescence have been established in Section 2.5. Briefly, SWIR wavelengths (1000–2000 nm) reduce tissue scattering and autofluorescence, enabling greater penetration depth and improved signal-to-noise ratio relative to visible or NIR-I imaging. This chapter uses these properties as the basis for benchmarking the best-performing NCs developed in this thesis against ICG.

Among inorganic fluorophores, InAs and PbS quantum dots offer attractive SWIR properties (as reviewed in Section 2.5.2), but raise toxicity concerns that limit their clinical translation.[123] Most of the elements needed for the synthesis of QDs like Pb, Cd, As have well-documented toxicity claims.[115] Still some of these functionalities demonstrate the potential of InAs QDs to serve as versatile platforms for high-speed, high-resolution functional imaging.[183]

RE-doped NCs present an alternative to the QDs with discrete, narrow emission lines and long lifetimes, suitable for multiplexed imaging applications.[184] RE^{3+}-based NCs can be doped with specific lanthanides like Tm^{3+} and Er^{3+} to tune emission into different spectral regions of the SWIR, with lifetimes allowing time-domain imaging.[29] Furthermore, the toxicity concerns regarding RE-based NCs are less than for QDs, making them extremely attractive materials for SWIR imaging.

7.3 Results

7.3.1 Intralipid Phantom Test

The imaging performance of the 1500 nm and 1800 nm emitting NCs was first investigated using a 1% intralipid solution phantom in water. This well-established scattering model allows to determine the maximum signal penetration thickness that each NCs can achieve, while being irradiated with a 50 mW/cm^2 (or as close as possible depending on the laser limitations).[110] For this test the NCs were transferred to water using poly-acrylic acid (PAA).[98] The excitation wavelength was set as 980 nm for α-$NaYF_4$:Yb,Er,Ce/CaF_2 and 785 nm for $LiTmF_4$/$LiYF_4$, and ICG. To follow the attenuation of the signal, the images were taken after increasing the thickness of the intralipids each millimeter.

Figure 7.1 shows that the signal starts to exhibit increased noise for the $LiTmF_4$/$LiYF_4$ NCs at 8.0 mm of intralipid thickness, although the signal becomes increasingly faint, it remains detectable up to 10.0 mm. Meanwhile, for the α-$NaYF_4$:Yb,Er,Ce/CaF_2 NCs, the signal start to become noisy at a smaller thickness of 6.0 mm, and at 10.0 mm the signal is completely lost. The excitation at 785 nm is more favorable than the excitation at

980 nm, as water presents an absorption peak at that wavelength (Figure 5.15), which attenuates a significant fraction of the excitation wavelength and leads to an earlier loss of detectable signal, even when the PLQY of those NCs is the highest.

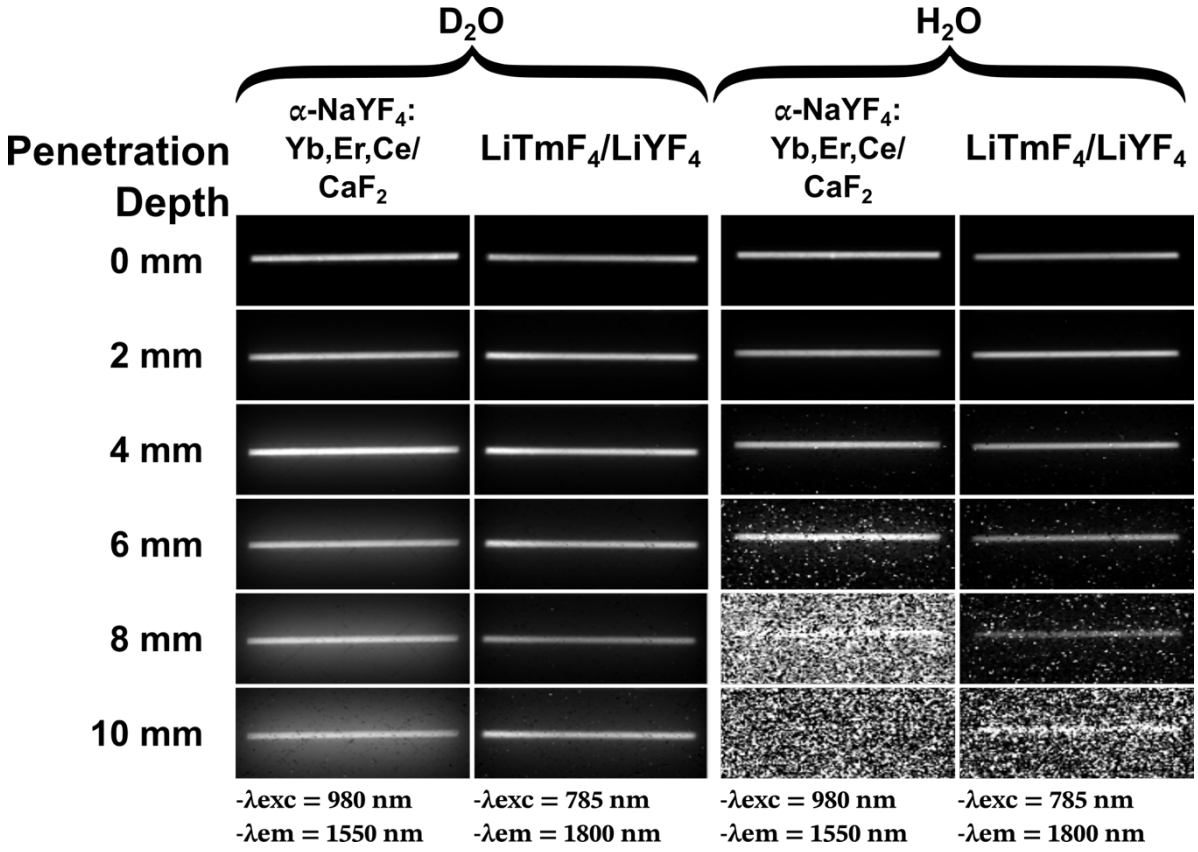


Figure 7.1 *Emission images of $LiTmF_4/LiYF_4$ and α-$NaYF_4$:Yb,Er,Ce/CaF_2 under varying intralipid thicknesses in D_2O and H_2O. Emission from capillary tubes filled with α-$NaYF_4$:Yb,Er,Ce/CaF_2 and $LiTmF_4/LiYF_4$, NCs excited at 980 nm for α-$NaYF_4$:Yb,Er,Ce/CaF_2 or 785 nm for $LiTmF_4/LiYF_4$, recorded within the 1400-1900 nm range. The measurements were performed through different thicknesses of a 1 vol % intralipid solution in either D_2O or H_2O. The excitation laser power density was adjusted to approximately 50 mW/cm^2, or as closely as possible within the limitations of the laser system.*

The effect of water absorption at 980 nm can be mitigated by dispersing the intralipids in D_2O instead of H_2O.[62] Under this condition, the fluorescence signal from both NCs is clearly detectable during all the measured thicknesses. Beyond improving signal visibility, the use of D_2O also enables a clearer assessment of the scattering effects as a function of intralipid thickness. While the 1800 nm emission shows negligible scattering during all the measured thicknesses; the 1500 nm emission began to exhibit scattering that became increasingly noticeable with increasing thickness (Figure 7.1). This behavior is consistent

with the wavelength-dependent scattering coefficient $\lambda^{-\alpha}$, where α is a tissue dependent constant.[114]

7.3.2 Brightness Test

A comparison of fluorescence brightness was then performed between the SWIR-emitting NCs and ICG. The emission peak of ICG is between 800-850 nm depending on the chemical environment where ICG is,[185] but the emission tail extends into most of the SWIR region. For this comparison ICG and the NCs were diluted in fetal bovine serum (FBS) to get a final concentration of 40 mg/mL, and 1300, 1500, and 1650 long pass (LP) filters were used to cut the contribution of ICG signal at lower wavelengths. The NCs were transferred into water using the same PAA method as for the intralipid tests, but and additional PEG chain was crosslinked with the PAA attached to the NCs. PEG can increase the blood-lifetime circulation of the NCs, which is crucial to acquire high-quality fluorescence images in practice.[186] The comparison between ICG, α-$NaYF_4$:Yb,Er,Ce/CaF_2 and $LiTmF_4$/$LiYF_4$ NCs is shown in Figure 7.2.

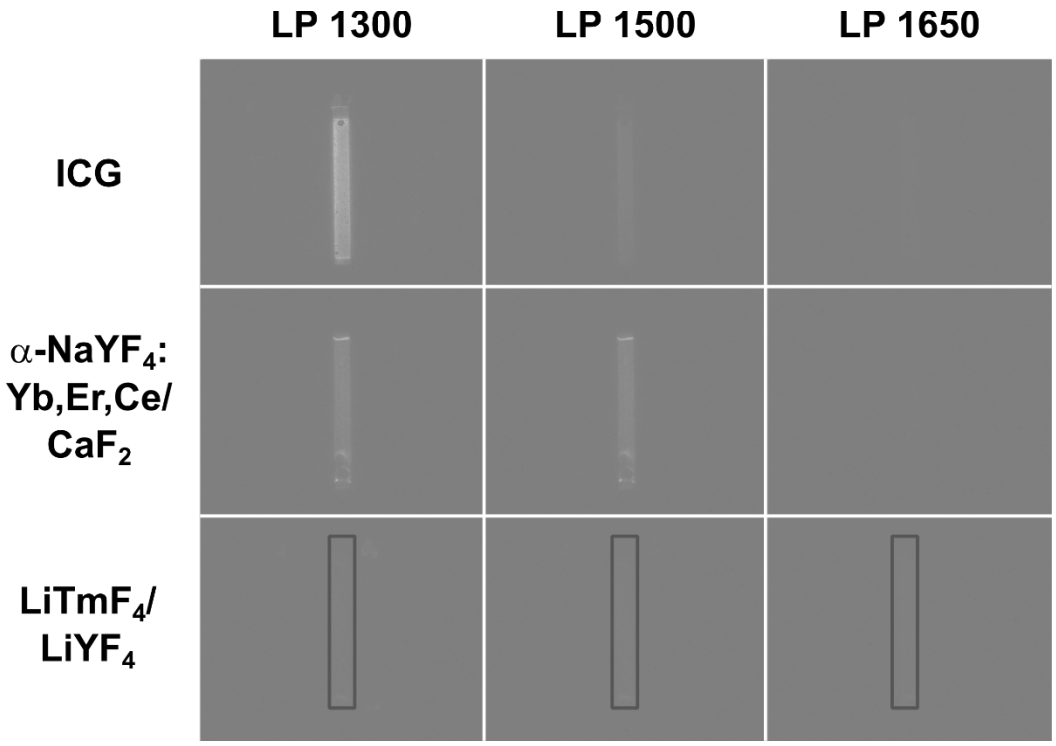


Figure 7.2 *Comparison of SWIR fluorescence brightness between ICG and RE-based core–shell NCs dispersed in water with fetal bovine serum (FBS). Long-pass filters at 1300, 1500, and 1650 nm were used to suppress the shorter-wavelength contribution of the ICG emission. The NCs were transferred into water using a polyacrylic acid (PAA) ligand exchange, followed by crosslinking with polyethylene glycol (PEG). All samples were measured at a power density of 100 mW/cm^2. An excitation wavelength of 800 nm was used for ICG and the LiTmF$_4$/LiYF$_4$ NCs, while the α-NaYF$_4$:Yb,Er,Ce/CaF$_2$ NCs were excited at 980 nm.*

The images reveal that ICG with a LP filter of 1300 exhibits the highest overall brightest. However, this brightness is severely reduced when the 1500 LP filter is used and becomes almost undetectable with the 1650 LP filter. This decrease in brightness is consistent since the emission peak of ICG is at shorter wavelengths and it is just the tail of the emission what it is being used.[187] In contrast, the brightness of α-NaYF$_4$:Yb,Er,Ce/CaF$_2$ NCs remains apparently unaltered switching the LP filter from 1300 to a 1500, and with the 1650 LP the signal is also not visible. Finally, the LiTmF$_4$/LiYF$_4$ NCs brightness were almost not visible at almost any LP filter; therefore, a rectangle was included as a visual aid to indicate the location of the sample tube. It is unclear why the LiTmF$_4$/LiYF$_4$ NCs didn't show a clear emission. One aspect could be the detection limits of the camera used, whose sensitivity extends until 1.9 μm. A second contributing factor, for the almost undetectable signal, could be a reduced effective mass

fraction of the optically active $LiTmF_4/LiYF_4$ NCs. Compared to α-$NaYF_4$:Yb,Er,Ce/CaF_2 NCs, $LiTmF_4/LiYF_4$ NCs are larger, which may lead to a higher surface coverage by PAA ligand. This increases the overall particle mass, while leaving the effective mass unchanged, thereby reducing the effective emitter concentration. Finally, Tm^{3+} has a lower absorption cross-section than Yb^{3+} by 2 orders of magnitude, which can also play an important role.

7.3.3 Fluorescent SWIR Imaging

Although the emission and brightness from $LiTmF_4/LiYF_4$ NCs was close to the detection limit under the applied imaging conditions, the heterogeneous α-$NaYF_4$:Yb,Er,Ce/CaF_2 system combines sufficient brightness with favorable SWIR contrast for *in vivo* imaging. Building on this, fluorescence angiography was performed to demonstrate the biological contrast achievable with these NCs. A blood pool agent was created using α-$NaYF_4$:Yb,Er,Ce/CaF_2 NCs in micelles. *In vivo* macroscopic SWIR fluorescence imaging facilitated high-contrast visualization of the fine mouse vasculature following intravenous injection of the micelles at the tail vein (Figure 7.3). A timelapse shows signal acquisition from the moment of injection (t = 0 s) to 75 s post-injection. Between 0 to 5 s after the injection there is no detectable signal, but at 10 s post-injection the signal becomes bright enough to outline the vascular structure of the mouse, and kidneys, yielding a high-contrast visualization of the mouse anatomy.

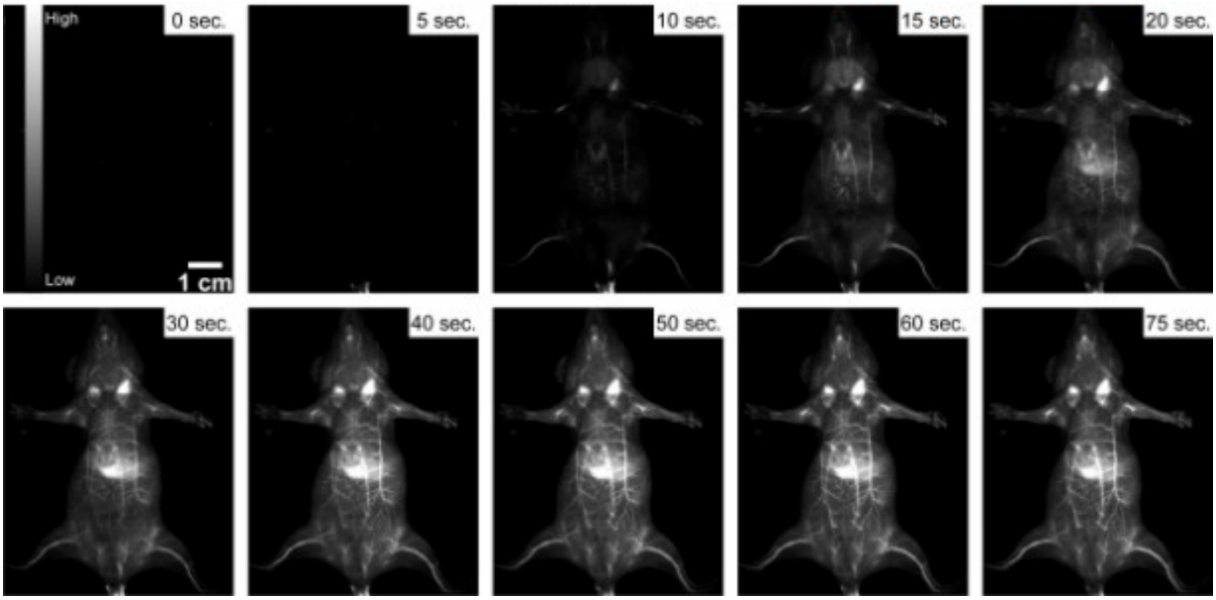


Figure 7.3 *In vivo SWIR fluorescence imaging following intravenous injection of α-$NaYF_4$:Yb,Er,Ce/CaF_2 micelles in a mouse model. Micelles were administered via tail vein injection, and SWIR fluorescence imaging was performed under diffuse 968 nm excitation (mean power density: 99.6 mW/cm²). Emission was collected using an InGaAs detector equipped with a 1450 nm long-pass filter. Single-frame images at various time points post-injection are shown at the same scale to illustrate biodistribution and temporal dynamics.*

7.4 Discussion

The results presented in this chapter demonstrate that the intrinsic efficiency or PLQY of a material is not the sole parameter to consider when designing contrast agents for *in vivo* fluorescence imaging. Instead, imaging performance is governed by a combination of factors of comparable importance, including excitation and emission wavelengths, absorption cross-section, and chemical composition. In particular, excitation in the 785-800 nm range, as used for $LiTmF_4/LiYF_4$ NCs and ICG proven more favorable than the excitation at 980 nm used for α-$NaYF_4$:Yb,Er,Ce/CaF_2 NCs, as it avoided the water absorption peak and enabled deeper signal penetration. Similarly, emission at longer wavelengths was shown to appreciably reduce scattering, with the Tm^{3+} emission starting at ~1650 nm shown negligible scattering even at intralipid thicknesses of up to 10 mm.[105]

Despite this advantage, the use of $LiTmF_4/LiYF_4$ NCs is ultimately limited by the intrinsically low absorption cross-section of Tm^{3+} ions. Published papers have reported absorption cross-sections for Tm^{3+} in the range of 10^{-22} cm^2,[30] whereas for Yb^{3+} the

reported values are around 10^{-20} cm^2,[26] approximately two orders of magnitude higher, allowing for more photons absorption and brighter SWIR emission. In comparison, ICG possesses a larger absorption cross-section on the order of 10^{-16} cm^2.[188] Although the NCs exhibited PLQY values up to two orders of magnitude higher than the PLQY value of ICG, the latter compensates through an absorption cross-section that is 4 - 6 orders of magnitude larger, allowing the absorption of significantly more excitation photons under identical irradiation conditions.

Excitation power cannot be increased arbitrarily, as in vivo imaging is constrained by skin exposure safety limits.[189] These safety limits place an upper limit on the usable excitation power density, making efficient photon absorption a critical requirement for practical biomedical applications.

Finally, the total injected mass represents an additional and often under considered parameter in the design of fluorescent probes for *in vivo* use. While ICG has a relatively high molecular weight (774.96 g/mol), its entire molecular structure actively participates in the absorption and emission processes. In contrast, NCs-based probes contain a high amount of mass that doesn't actively contribute to the emission process, including inert shell materials and surface ligands required for colloidal stability and biocompatibility. These components increase the overall mass that will be injected, thereby introducing a significant dead mass that hinders the use in real-world applications, where minimizing the injected material is a critical consideration.

7.5 Summary

This chapter evaluated the imaging performance of SWIR-emitting NCs in comparison with ICG. Through intralipid phantom studies, brightness comparison and *in vivo* fluorescence angiography, it was shown that PLQY alone is not a sufficient metric for predicting imaging performance in biological environments.

Longer emission wavelengths were found to substantially reduce scattering losses, with Tm^{3+}-based NCs emitting around 1800 nm exhibiting minimal scattering even at large penetration depths. Nevertheless, this advantage was offset by the intrinsically low

absorption cross-section of Tm^{3+} ions, which ultimately limited the detectable signal under realistic excitation conditions. Moreover, excitation in the 785-800 nm range proved more favorable than excitation at 980 nm due to reduced water absorption, highlighting the importance of selecting materials with excitation wavelengths that minimize tissue and solvent attenuation.

The comparison with ICG further highlighted the critical role of absorption cross-section in practical imaging scenarios. Despite its relatively low PLQY and emission peak outside the SWIR region, ICG benefits from an exceptionally large absorption cross-section, enabling strong signal generation under similar irradiation conditions. The data demonstrate that high intrinsic efficiency cannot be directly compensated for poor absorption when excitation power is restricted by safety considerations.

Finally, this chapter emphasized the importance of considering the total injected mass of fluorescent probes. While the full molecular structure of ICG contributes directly to fluorescence generation, NCs-based probes inherently contain substantial non-emissive components, including inert shells and surface ligands required for stability and biocompatibility. This additional dead mass represents a significant limitation for translation into real-world biomedical applications.

Overall, the results presented here highlight that optimal design of SWIR fluorescent probes for *in vivo* imaging requires a careful balance between emission wavelength, absorption efficiency, excitation conditions, and material composition. These insights provide practical design guidelines for the development of next-generation SWIR contrast agents and contextualize the performance of NC-based probes relative to established clinical fluorophores.

8. Conclusions and Outlook

8.1 Conclusions

This thesis establishes cation intermixing as a decisive and widespread phenomenon in RE-based fluoride core–shell NCs, one whose suppression enables significant gains in SWIR emission efficiency. While core–shell architectures have long been considered an effective strategy to enhance PLQY, the assumption that the core remains chemically and structurally intact during shell growth has rarely been critically examined. The results presented in this work demonstrate that this assumption is not generally valid and that cation redistribution across the core–shell interface is a common and decisive phenomenon.

By systematically studying different material combinations, crystal structures, and synthetic parameters, this work establishes relationships between interfacial organization, ion distribution, and optical performance. The findings show that achieving higher PLQY values does not solely depend on the presence of a shell, but rather on the shell's ability to spatially confine the optically active ions and suppress their migration toward the surface.

In the first part of the thesis, the intermixing behavior in homogeneous and heterogeneous core–shell NCs was investigated using α-$NaYF_4$:Yb,Er(Ce) cores. It was demonstrated that conventional homogeneous shells such as α-$NaYF_4$ lead to significant cation intermixing, causing the optically active ions to migrate toward the shell region. In contrast, the use of a heterogeneous CaF_2 shell enabled the formation of a chemically segregated core–shell structure with minimal intermixing. This heterostructure yielded a PLQY of ~50% in sub-15 nm NCs emitting in the SWIR range, representing one of the highest reported efficiencies for NCs of this size.

The second part of the thesis expanded the study to different material systems based on α-$NaTmF_4$ and $LiTmF_4$ cores combined with various shell materials. The results revealed that only specific material combinations lead to well-defined core–shell architectures, like α-$NaREF_4/CaF_2$ and $LiTmF_4/LiYF_4$. In particular, $LiTmF_4/LiYF_4$ NCs exhibited effective

spatial confinement of the activator ions and achieved a PLQY of ~39% above 1600 nm, even in the presence of moderate intermixing. This evidence indicates that while sharp interfaces are advantageous, the presence of a sufficiently thick and chemically pure shell is often the dominant factor in achieving high emission efficiency.

The influence of intrinsic and extrinsic parameters on intermixing and optical performance was systematically analyzed in the third part of the thesis. Intrinsic factors such as crystal structure and material composition were found to strongly affect the tendency toward intermixing, while extrinsic parameters-including shell thickness, growth temperature, and synthesis methodology-provided effective means of controlling ion distribution. Persistent intermixing was observed in several α/β-$NaREF_4$ homogeneous systems, whereas α-$NaREF_4/CaF_2$ and $LiTmF_4/LiYF_4$ demonstrated strong spatial confinement through all the tested synthesis parameters, as long as there are no ultrasmall core NCs (< 2 nm). These results establish a clear correlation between material selection, growth conditions, interfacial organization, and energy conversion efficiency.

In the final part of the thesis, α-$NaYF_4$:Yb,Er,Ce/CaF_2 (PLQY ~50%, λ_{em} 1500 nm) and $LiTmF_4/LiYF_4$ (PLQY ~39%, λ_{em} 1800 nm) NCs were compared against the clinical standard ICG for real application fluorescence SWIR imaging via *in vitro* and *in vivo* tests.

Overall, this thesis provides a comprehensive framework for understanding some parameters influencing cation intermixing in RE-based core–shell fluoride NCs. The results challenge the long-standing assumption of a chemically inert core during shell growth and demonstrate that interfacial ion redistribution is a key parameter governing optical performance. By identifying both intrinsic and extrinsic factors that influence intermixing, this work offers practical design principles for the development of highly efficient SWIR-emitting nanoprobes. The results establish control of cation intermixing as a central design principle for RE-based core–shell NCs. By establishing the link between interfacial chemistry and optical performance, this work contributes to the rational development of next-generation SWIR nanomaterials for advanced optical and biomedical technologies.

8.2 Outlook

The insights gained in this thesis open several promising directions for future research. First, a systematic mapping of additional heterogeneous material combinations could reveal new core–shell systems with improved structural stability and optical performance. Such studies may lead to the identification of previously unexplored host–shell pairs optimized for specific emission wavelengths or excitation regimes.

Second, further investigation into the kinetics and mechanisms of ion migration during shell growth could provide deeper understanding of interfacial processes at the nanoscale. Advanced *in situ* characterization techniques or time-resolved studies may help clarify the dynamics of intermixing and enable predictive control over the final ion distribution.

Third, optimization of additional extrinsic parameters not investigated here, such as precursor chemistry, core size, and other methodologies (like hot injection), could enable more precise control over interfacial organization. This may allow the fabrication of complex multi-shell or gradient structures designed to tailor energy transfer pathways and maximize emission efficiency.

Finally, the high-efficiency SWIR NCs developed in this work hold strong potential for practical biomedical applications, as the absorption and emission ranges improves penetration depths while minimizing scattering, and tissue autofluorescence. Future studies may focus on long-term biocompatibility, targeted functionalization, develop proper imaging acquisition protocols and integration into imaging platforms, paving the way toward clinical translation.

References

(1) Ozawa, T.; Yoshimura, H.; Kim, S. B. Advances in Fluorescence and Bioluminescence Imaging. *Anal. Chem.* **2013**, *85* (2), 590–609. https://doi.org/10.1021/ac3031724.

(2) Li, H.; Wang, X.; Li, X.; Zeng, S.; Chen, G. Clearable Shortwave-Infrared-Emitting NaErF4 Nanoparticles for Noninvasive Dynamic Vascular Imaging. *Chem. Mater.* **2020**, *32* (8), 3365–3375. https://doi.org/10.1021/acs.chemmater.9b04784.

(3) Hong, Z.; Chen, Z.; Chen, Q.; Yang, H. Advancing X-Ray Luminescence for Imaging, Biosensing, and Theragnostics. *Acc. Chem. Res.* **2023**, *56* (1), 37–51. https://doi.org/10.1021/acs.accounts.2c00517.

(4) Sun, Y.; Yu, M.; Liang, S.; Zhang, Y.; Li, C.; Mou, T.; Yang, W.; Zhang, X.; Li, B.; Huang, C.; Li, F. Fluorine-18 Labeled Rare-Earth Nanoparticles for Positron Emission Tomography (PET) Imaging of Sentinel Lymph Node. *Biomaterials* **2011**, *32* (11), 2999–3007. https://doi.org/https://doi.org/10.1016/j.biomaterials.2011.01.011.

(5) Jacques, S. L. Optical Properties of Biological Tissues: A Review. *Phys. Med. Biol.* **2013**, *58* (11), R37. https://doi.org/10.1088/0031-9155/58/11/R37.

(6) Khabir, Z.; Guller, A. E.; Rozova, V. S.; Liang, L.; Lai, Y.-J.; Goldys, E. M.; Hu, H.; Vickery, K.; Zvyagin, A. V. Tracing Upconversion Nanoparticle Penetration in Human Skin. *Colloids Surfaces B Biointerfaces* **2019**, *184*, 110480. https://doi.org/https://doi.org/10.1016/j.colsurfb.2019.110480.

(7) Wang, R.; Li, X.; Zhou, L.; Zhang, F. Epitaxial Seeded Growth of Rare-Earth Nanocrystals with Efficient 800 Nm Near-Infrared to 1525 Nm Short-Wavelength Infrared Downconversion Photoluminescence for In Vivo Bioimaging. *Angew. Chemie Int. Ed.* **2014**, *53* (45), 12086–12090. https://doi.org/https://doi.org/10.1002/anie.201407420.

(8) Piwoński, H.; Nozue, S.; Habuchi, S. The Pursuit of Shortwave Infrared-Emitting Nanoparticles with Bright Fluorescence through Molecular Design and Excited-State Engineering of Molecular Aggregates. *ACS Nanosci. Au* **2022**, *2* (4), 253–283. https://doi.org/10.1021/acsnanoscienceau.1c00038.

(9) Yu, H.; Ai, L.; Lu, S. Second Near-Infrared Fluorophores: Rational Design, Optical Enhancement Strategies, and Recent Advances in Imaging-Guided Biomedical Applications. *Chem* **2026**, *12* (3). https://doi.org/10.1016/j.chempr.2025.102867.

(10) Zhao, Y.; Pilvar, A.; Tank, A.; Peterson, H.; Jiang, J.; Aster, J. C.; Dumas, J. P.; Pierce, M. C.; Roblyer, D. Shortwave-Infrared Meso-Patterned Imaging Enables Label-Free Mapping of Tissue Water and Lipid Content. *Nat. Commun.* **2020**, *11* (1), 5355. https://doi.org/10.1038/s41467-020-19128-7.

(11) Wang, F.; Qu, L.; Ren, F.; Baghdasaryan, A.; Jiang, Y.; Hsu, R.; Liang, P.; Li, J.; Zhu, G.; Ma, Z.; Dai, H. High-Precision Tumor Resection down to Few-Cell Level Guided by NIR-IIb Molecular Fluorescence Imaging. *Proc. Natl. Acad. Sci.* **2022**, *119* (15), e2123111119. https://doi.org/10.1073/pnas.2123111119.

(12) Hu, Z.; Fang, C.; Li, B.; Zhang, Z.; Cao, C.; Cai, M.; Su, S.; Sun, X.; Shi, X.; Li, C.; Zhou, T.; Zhang, Y.; Chi, C.; He, P.; Xia, X.; Chen, Y.; Gambhir, S. S.; Cheng, Z.; Tian, J. First-in-Human Liver-Tumour Surgery Guided by Multispectral Fluorescence Imaging in the Visible and near-Infrared-I/II Windows. *Nat. Biomed. Eng.* **2020**, *4* (3), 259–271. https://doi.org/10.1038/s41551-019-0494-0.

(13) Wang, F.; Ren, F.; Ma, Z.; Qu, L.; Gourgues, R.; Xu, C.; Baghdasaryan, A.; Li, J.; Zadeh, I. E.; Los, J. W. N.; Fognini, A.; Qin-Dregely, J.; Dai, H. In Vivo Non-Invasive Confocal Fluorescence Imaging beyond 1,700 Nm Using Superconducting Nanowire Single-Photon Detectors. *Nat. Nanotechnol.* **2022**, *17* (6), 653–660. https://doi.org/10.1038/s41565-022-01130-3.

(14) Sarkar, S.; Le, P.; Geng, J.; Liu, Y.; Han, Z.; Zahid, M. U.; Nall, D.; Youn, Y.; Selvin, P. R.; Smith, A. M. Short-Wave Infrared Quantum Dots with Compact Sizes as Molecular Probes for Fluorescence Microscopy. *J. Am. Chem. Soc.* **2020**, *142* (7), 3449–3462. https://doi.org/10.1021/jacs.9b11567.

(15) Guo, Z.; Park, S.; Yoon, J.; Shin, I. Recent Progress in the Development of Near-Infrared Fluorescent Probes for Bioimaging Applications. *Chem. Soc. Rev.* **2014**, *43* (1), 16–29. https://doi.org/10.1039/C3CS60271K.

(16) Hong, G.; Lee, J. C.; Robinson, J. T.; Raaz, U.; Xie, L.; Huang, N. F.; Cooke, J. P.; Dai, H. Multifunctional in Vivo Vascular Imaging Using Near-Infrared II Fluorescence. *Nat. Med.* **2012**, *18* (12), 1841–1846. https://doi.org/10.1038/nm.2995.

(17) Jiang, T.; Amadei, C. A.; Gou, N.; Lin, Y.; Lan, J.; Vecitis, C. D.; Gu, A. Z. Toxicity of Single-Walled Carbon Nanotubes (SWCNTs): Effect of Lengths, Functional Groups and Electronic Structures Revealed by a Quantitative Toxicogenomics Assay. *Environ. Sci. Nano* **2020**, *7* (5), 1348–1364. https://doi.org/10.1039/D0EN00230E.

(18) Priyadarshi, A.; Masala, O.; Harris, J.; Gresty, N. C.; Pickett, N. L. Progress in the Development of Quantum Dots for SWIR Image Sensing Applications. In *Proc.SPIE*; 2025; Vol. 13469, p 1346908. https://doi.org/10.1117/12.3063195.

(19) Bruns, O. T.; Bischof, T. S.; Harris, D. K.; Franke, D.; Shi, Y.; Riedemann, L.; Bartelt, A.; Jaworski, F. B.; Carr, J. A.; Rowlands, C. J.; Wilson, M. W. B.; Chen, O.; Wei, H.; Hwang, G. W.; Montana, D. M.; Coropceanu, I.; Achorn, O. B.; Kloepper, J.; Heeren, J.; So, P. T. C.; Fukumura, D.; Jensen, K. F.; Jain, R. K.; Bawendi, M. G. Next-Generation in Vivo Optical Imaging with Short-Wave Infrared Quantum Dots. *Nat. Biomed. Eng.* **2017**, *1* (4), 56. https://doi.org/10.1038/s41551-017-0056.

(20) Skripka, A.; Mendez-Gonzalez, D.; Marin, R.; Ximendes, E.; del Rosal, B.; Jaque, D.; Rodríguez-Sevilla, P. Near Infrared Bioimaging and Biosensing with Semiconductor and Rare-Earth Nanoparticles: Recent Developments in Multifunctional Nanomaterials. *Nanoscale Adv.* **2021**, *3* (22), 6310–6329. https://doi.org/10.1039/D1NA00502B.

(21) Lei, Z.; Ling, X.; Mei, Q.; Fu, S.; Zhang, J.; Zhang, Y. An Excitation Navigating Energy Migration of Lanthanide Ions in Upconversion Nanoparticles. *Adv. Mater.* **2020**, *32* (9), 1906225. https://doi.org/https://doi.org/10.1002/adma.201906225.

(22) Zhang, K. Y.; Yu, Q.; Wei, H.; Liu, S.; Zhao, Q.; Huang, W. Long-Lived Emissive Probes for Time-Resolved Photoluminescence Bioimaging and Biosensing. *Chem. Rev.* **2018**, *118* (4), 1770–1839. https://doi.org/10.1021/acs.chemrev.7b00425.

(23) Lichtman, J. W.; Conchello, J.-A. Fluorescence Microscopy. *Nat. Methods* **2005**, *2* (12), 910–919. https://doi.org/10.1038/nmeth817.

(24) Wang, Z.; Thang, D. C.; Han, Q.; Zhao, X.; Xie, X.; Wang, Z.; Lin, J.; Xing, B. Near-Infrared Photocontrolled Therapeutic Release via Upconversion Nanocomposites. *J. Control. Release* **2020**, *324*, 104–123. https://doi.org/https://doi.org/10.1016/j.jconrel.2020.05.011.

(25) Marin, R.; Jaque, D.; Benayas, A. Switching to the Brighter Lane: Pathways to Boost the Absorption of Lanthanide-Doped Nanoparticles. *Nanoscale Horizons* **2021**. https://doi.org/10.1039/D0NH00627K.

(26) Zhao, M.; Sik, A.; Zhang, H.; Zhang, F. Tailored NIR-II Lanthanide Luminescent Nanocrystals for Improved Biomedical Application. *Adv. Opt. Mater.* **2023**, *11* (11), 2202039. https://doi.org/https://doi.org/10.1002/adom.202202039.

(27) Suyver, J. F.; Grimm, J.; van Veen, M. K.; Biner, D.; Krämer, K. W.; Güdel, H. U. Upconversion Spectroscopy and Properties of NaYF4 Doped with Er3+, Tm3+ and/or Yb3+. *J. Lumin.* **2006**, *117* (1), 1–12. https://doi.org/https://doi.org/10.1016/j.jlumin.2005.03.011.

(28) Shi, R.; Mudring, A.-V. Phonon-Mediated Nonradiative Relaxation in Ln3+-Doped Luminescent Nanocrystals. *ACS Mater. Lett.* **2022**, *4* (10), 1882–1903. https://doi.org/10.1021/acsmaterialslett.2c00595.

(29) Zhong, Y.; Ma, Z.; Zhu, S.; Yue, J.; Zhang, M.; Antaris, A. L.; Yuan, J.; Cui, R.; Wan, H.; Zhou, Y.; Wang, W.; Huang, N. F.; Luo, J.; Hu, Z.; Dai, H. Boosting the Down-Shifting Luminescence of Rare-Earth Nanocrystals for Biological Imaging beyond 1500 Nm. *Nat. Commun.* **2017**, *8* (1), 737. https://doi.org/10.1038/s41467-017-00917-6.

(30) Chang, Y.; Chen, H.; Xie, X.; Wan, Y.; Li, Q.; Wu, F.; Yang, R.; Wang, W.; Kong, X. Bright Tm3+-Based Downshifting Luminescence Nanoprobe Operating around 1800 Nm for NIR-IIb and c Bioimaging. *Nat. Commun.* **2023**, *14* (1), 1079. https://doi.org/10.1038/s41467-023-36813-5.

(31) Wang, L.; Li, X.; Li, Z.; Chu, W.; Li, R.; Lin, K.; Qian, H.; Wang, Y.; Wu, C.; Li, J.; Tu, D.; Zhang, Q.; Song, L.; Jiang, J.; Chen, X.; Luo, Y.; Xie, Y.; Xiong, Y. A New Cubic Phase for a NaYF4 Host Matrix Offering High Upconversion Luminescence Efficiency. *Adv. Mater.* **2015**, *27* (37), 5528–5533. https://doi.org/https://doi.org/10.1002/adma.201502748.

(32) Tan, M.; Monks, M.-J.; Huang, D.; Meng, Y.; Chen, X.; Zhou, Y.; Lim, S.-F.; Würth, C.; Resch-Genger, U.; Chen, G. Efficient Sub-15 Nm Cubic-Phase Core/Shell Upconversion Nanoparticles as Reporters for Ensemble and Single Particle Studies. *Nanoscale* **2020**, *12* (19), 10592–10599. https://doi.org/10.1039/D0NR02172E.

(33) Wang, Y.-F.; Sun, L.-D.; Xiao, J.-W.; Feng, W.; Zhou, J.-C.; Shen, J.; Yan, C.-H. Rare-Earth Nanoparticles with Enhanced Upconversion Emission and Suppressed Rare-Earth-Ion Leakage. *Chem. – A Eur. J.* **2012**, *18* (18), 5558–5564. https://doi.org/https://doi.org/10.1002/chem.201103485.

(34) Zhai, C.; Liu, G.; Xie, X.; Gao, J.; Ma, Y. Sharp Interface and Highly Efficient Upconversion Luminescence of CaF2@NaYbF4:Er@CaF2 Sandwich-Structured Nanoparticles. *Chem. Mater.* **2025**, *37* (4), 1468–1477. https://doi.org/10.1021/acs.chemmater.4c02781.

(35) Sun, L.-D.; Wang, Y.-F.; Yan, C.-H. Paradigms and Challenges for Bioapplication of Rare Earth Upconversion Luminescent Nanoparticles: Small Size and Tunable Emission/Excitation Spectra. *Acc. Chem. Res.* **2014**, *47* (4), 1001–1009. https://doi.org/10.1021/ar400218t.

(36) Fischer, S.; Bronstein, N. D.; Swabeck, J. K.; Chan, E. M.; Alivisatos, A. P. Precise Tuning of Surface Quenching for Luminescence Enhancement in Core–Shell Lanthanide-Doped Nanocrystals. *Nano Lett.* **2016**, *16* (11), 7241–7247. https://doi.org/10.1021/acs.nanolett.6b03683.

(37) Beeby, A.; M. Clarkson, I.; S. Dickins, R.; Faulkner, S.; Parker, D.; Royle, L.; S. de Sousa, A.; A. Gareth Williams, J.; Woods, M. Non-Radiative Deactivation of the Excited States of Europium, Terbium and Ytterbium Complexes by Proximate Energy-Matched OH, NH and CH Oscillators: An Improved Luminescence Method for Establishing Solution Hydration States. *J. Chem. Soc. Perkin Trans. 2* **1999**, No. 3, 493–504. https://doi.org/10.1039/A808692C.

(38) Zhang, Y.; Wen, R.; Hu, J.; Guan, D.; Qiu, X.; Zhang, Y.; Kohane, D. S.; Liu, Q. Enhancement of Single Upconversion Nanoparticle Imaging by Topologically Segregated Core-Shell Structure with Inward Energy Migration. *Nat. Commun.* **2022**, *13* (1), 5927. https://doi.org/10.1038/s41467-022-33660-8.

(39) Fan, Y.; Liu, L.; Zhang, F. Exploiting Lanthanide-Doped Upconversion Nanoparticles with Core/Shell Structures. *Nano Today* **2019**, *25*, 68–84. https://doi.org/https://doi.org/10.1016/j.nantod.2019.02.009.

(40) Johnson, N. J. J.; He, S.; Diao, S.; Chan, E. M.; Dai, H.; Almutairi, A. Direct Evidence for Coupled Surface and Concentration Quenching Dynamics in Lanthanide-Doped Nanocrystals. *J. Am. Chem. Soc.* **2017**, *139* (8), 3275–3282. https://doi.org/10.1021/jacs.7b00223.

(41) Mai, H.; Zhang, Y.; Sun, L.; Yan, C. Highly Efficient Multicolor Up-Conversion Emissions and Their

Mechanisms of Monodisperse NaYF 4 : Yb , Er Core and Core / Shell-Structured Nanocrystals. **2007**, 13721–13729.

(42) Chen, G.; Ohulchanskyy, T. Y.; Liu, S.; Law, W.-C.; Wu, F.; Swihart, M. T.; Ågren, H.; Prasad, P. N. Core/Shell NaGdF4:Nd3+/NaGdF4 Nanocrystals with Efficient Near-Infrared to Near-Infrared Downconversion Photoluminescence for Bioimaging Applications. *ACS Nano* **2012**, *6* (4), 2969–2977. https://doi.org/10.1021/nn2042362.

(43) Hudry, D.; Busko, D.; Popescu, R.; Gerthsen, D.; Abeykoon, A. M. M.; Kübel, C.; Bergfeldt, T.; Richards, B. S. Direct Evidence of Significant Cation Intermixing in Upconverting Core@Shell Nanocrystals: Toward a New Crystallochemical Model. *Chem. Mater.* **2017**, *29* (21), 9238–9246. https://doi.org/10.1021/acs.chemmater.7b03118.

(44) Hudry, D.; Busko, D.; Popescu, R.; Gerthsen, D.; Howard, I. A.; Richards, B. S. An Enhanced Energy Migration Strategy in Upconverting Nanocrystals: Color-Tuning with High Quantum Yield. *J. Mater. Chem. C* **2019**, *7* (24), 7371–7377. https://doi.org/10.1039/C9TC01567A.

(45) Hudry, D.; De Backer, A.; Popescu, R.; Busko, D.; Howard, I. A.; Bals, S.; Zhang, Y.; Pedrazo-Tardajos, A.; Van Aert, S.; Gerthsen, D.; Altantzis, T.; Richards, B. S. Interface Pattern Engineering in Core-Shell Upconverting Nanocrystals: Shedding Light on Critical Parameters and Consequences for the Photoluminescence Properties. *Small* **2021**, *17* (47), 2104441. https://doi.org/https://doi.org/10.1002/smll.202104441.

(46) Hudry, D.; Howard, I. A.; Popescu, R.; Gerthsen, D.; Richards, B. S. Structure–Property Relationships in Lanthanide-Doped Upconverting Nanocrystals: Recent Advances in Understanding Core–Shell Structures. *Adv. Mater.* **2019**, *31* (26), 1900623. https://doi.org/10.1002/adma.201900623.

(47) Johnson, N. J. J.; van Veggel, F. C. J. M. Sodium Lanthanide Fluoride Core-Shell Nanocrystals: A General Perspective on Epitaxial Shell Growth. *Nano Res.* **2013**, *6* (8), 547–561. https://doi.org/10.1007/s12274-013-0333-7.

(48) Shi, R.; Brites, C. D. S.; Carlos, L. D. Understanding the Shell Passivation in Ln3+-Doped Luminescent Nanocrystals. *Small Struct.* **2022**, *3* (3), 2100194. https://doi.org/https://doi.org/10.1002/sstr.202100194.

(49) Xu, W.; Zhang, S.; Wei, A.; Deng, D.; Zhou, S.; Xu, S.; Lei, L. Advancing Multi-Optical Performances in Lanthanide-Doped Fluoride Core@Shell Nanoarchitectures by Minimizing Cation Intermixing. *Adv. Funct. Mater.* **2025**, *35* (8), 2415815. https://doi.org/https://doi.org/10.1002/adfm.202415815.

(50) Bastian, P. U.; Robel, N.; Schmidt, P.; Schrumpf, T.; Günter, C.; Roddatis, V.; Kumke, M. U. Resonance Energy Transfer to Track the Motion of Lanthanide Ions;What Drives the Intermixing in Core-Shell Upconverting Nanoparticles? *Biosensors*. 2021. https://doi.org/10.3390/bios11120515.

(51) Yang, D.; Zheng, W.; Huang, P.; Zhang, M.; Zhang, W.; Shao, Z.; Zhang, W.; Yi, X.; Chen, X. A Sandwiched Luminescent Heterostructure Based on Lanthanide-Doped Gd2O2S@NaYF4 Core/Shell Nanocrystals. *Aggregate* **2023**, *4* (6), e387. https://doi.org/https://doi.org/10.1002/agt2.387.

(52) An, Z.; Huang, J.; Yan, L.; He, L.; Zhou, B. Multichannel Control of PersL/Upconversion/Down-Shifting Luminescence in a Single Core–Shell Nanoparticle for Information Encryption. *J. Phys. Chem. Lett.* **2022**, *13* (39), 9007–9013. https://doi.org/10.1021/acs.jpclett.2c02396.

(53) Prorok, K.; Bednarkiewicz, A.; Cichy, B.; Gnach, A.; Misiak, M.; Sobczyk, M.; Strek, W. The Impact of Shell Host (NaYF4/CaF2) and Shell Deposition Methods on the up-Conversion Enhancement in Tb3+, Yb3+ Codoped Colloidal α-NaYF4 Core–Shell Nanoparticles. *Nanoscale* **2014**, *6* (3), 1855–1864. https://doi.org/10.1039/C3NR05412H.

(54) Su, Y.; Liu, X.; Lei, P.; Xu, X.; Dong, L.; Guo, X.; Yan, X.; Wang, P.; Song, S.; Feng, J.; Zhang, H.

Core–Shell–Shell Heterostructures of α-NaLuF4:Yb/Er@NaLuF4:Yb@MF2 (M = Ca, Sr, Ba) with Remarkably Enhanced Upconversion Luminescence. *Dalt. Trans.* **2016**, *45* (27), 11129–11136. https://doi.org/10.1039/C6DT01005A.

(55) Shen, J.; Chen, G.; Ohulchanskyy, T. Y.; Kesseli, S. J.; Buchholz, S.; Li, Z.; Prasad, P. N.; Han, G. Tunable Near Infrared to Ultraviolet Upconversion Luminescence Enhancement in (α-NaYF4:Yb,Tm)/CaF2 Core/Shell Nanoparticles for In Situ Real-Time Recorded Biocompatible Photoactivation. *Small* **2013**, *9* (19), 3213–3217. https://doi.org/https://doi.org/10.1002/smll.201300234.

(56) Wu, R.; Zhou, J.; Lei, L.; Zhang, S.; Xiao, Z.; Zhang, J.; Xu, S. α-NaYF4:Yb3+-Tm3+@CaF2 Nanocrystals for NIR-to-NIR Temperature Sensing. *Chem. Phys. Lett.* **2017**, *667*, 206–210. https://doi.org/https://doi.org/10.1016/j.cplett.2016.10.040.

(57) Dong, H.; Sun, L.-D.; Wang, Y.-F.; Ke, J.; Si, R.; Xiao, J.-W.; Lyu, G.-M.; Shi, S.; Yan, C.-H. Efficient Tailoring of Upconversion Selectivity by Engineering Local Structure of Lanthanides in NaxREF3+x Nanocrystals. *J. Am. Chem. Soc.* **2015**, *137* (20), 6569–6576. https://doi.org/10.1021/jacs.5b01718.

(58) Chen, G.; Shen, J.; Ohulchanskyy, T. Y.; Patel, N. J.; Kutikov, A.; Li, Z.; Song, J.; Pandey, R. K.; Ågren, H.; Prasad, P. N.; Han, G. (α-NaYbF4:Tm3+)/CaF2 Core/Shell Nanoparticles with Efficient Near-Infrared to Near-Infrared Upconversion for High-Contrast Deep Tissue Bioimaging. *ACS Nano* **2012**, *6* (9), 8280–8287. https://doi.org/10.1021/nn302972r.

(59) Li, Y.; Gu, Y.; Yuan, W.; Cao, T.; Li, K.; Yang, S.; Zhou, Z.; Li, F. Core–Shell–Shell NaYbF4:Tm@CaF2@NaDyF4 Nanocomposites for Upconversion/T2-Weighted MRI/Computed Tomography Lymphatic Imaging. *ACS Appl. Mater. Interfaces* **2016**, *8* (30), 19208–19216. https://doi.org/10.1021/acsami.6b02856.

(60) Chen, G.; Shen, J.; Ohulchanskyy, T. Y.; Patel, N. J.; Kutikov, A.; Li, Z.; Song, J.; Pandey, R. K.; Ågren, H.; Prasad, P. N.; Han, G. (α-NaYbF4:Tm3+)/CaF2 Core/Shell Nanoparticles with Efficient Near-Infrared to Near-Infrared Upconversion for High-Contrast Deep Tissue Bioimaging. *ACS Nano* **2012**, *6* (9), 8280–8287. https://doi.org/10.1021/nn302972r.

(61) Arteaga Cardona, F.; Jain, N.; Popescu, R.; Busko, D.; Madirov, E.; Arús, B. A.; Gerthsen, D.; De Backer, A.; Bals, S.; Bruns, O. T.; Chmyrov, A.; Van Aert, S.; Richards, B. S.; Hudry, D. Preventing Cation Intermixing Enables 50% Quantum Yield in Sub-15 Nm Short-Wave Infrared-Emitting Rare-Earth Based Core-Shell Nanocrystals. *Nat. Commun.* **2023**, *14* (1), 4462. https://doi.org/10.1038/s41467-023-40031-4.

(62) Arteaga Cardona, F.; Madirov, E.; Popescu, R.; Wang, D.; Busko, D.; Ectors, D.; Kübel, C.; Eggeler, Y. M.; Arús, B. A.; Chmyrov, A.; Bruns, O. T.; Richards, B. S.; Hudry, D. Dramatic Impact of Materials Combinations on the Chemical Organization of Core-Shell Nanocrystals: Boosting the Tm3+ Emission above 1600 Nm. *ACS Nano* **2024**. https://doi.org/10.1021/acsnano.4c07932.

(63) Voncken, J. H. L. The Rare Earth Elements—A Special Group of Metals BT - The Rare Earth Elements: An Introduction; Voncken, J. H. L., Ed.; Springer International Publishing: Cham, 2016; pp 1–13. https://doi.org/10.1007/978-3-319-26809-5_1.

(64) Bünzli, J.-C. G.; Eliseeva, S. V. Basics of Lanthanide Photophysics BT - Lanthanide Luminescence: Photophysical, Analytical and Biological Aspects; Hänninen, P., Härmä, H., Eds.; Springer Berlin Heidelberg: Berlin, Heidelberg, 2011; pp 1–45. https://doi.org/10.1007/4243_2010_3.

(65) Bünzli, J.-C. G.; Piguet, C. Taking Advantage of Luminescent Lanthanide Ions. *Chem. Soc. Rev.* **2005**, *34* (12), 1048–1077. https://doi.org/10.1039/B406082M.

(66) de Bettencourt-Dias, A. Introduction to Lanthanide Ion Luminescence. In *Luminescence of Lanthanide Ions in Coordination Compounds and Nanomaterials*; 2014; pp 1–48. https://doi.org/https://doi.org/10.1002/9781118682760.ch01.

(67) Balabhadra, S.; Reid, M. F.; Golovko, V.; Wells, J.-P. R. A Comparison of the Yb3+ Absorption and Upconversion Excitation Spectra for Both the Cubic and Hexagonal Phases of NaYF4:Yb3+/Er3+ Nanoparticles. *Opt. Mater. (Amst).* **2020**, *107*, 110050. https://doi.org/https://doi.org/10.1016/j.optmat.2020.110050.

(68) Peijzel, P. S.; Meijerink, A.; Wegh, R. T.; Reid, M. F.; Burdick, G. W. A Complete 4fn Energy Level Diagram for All Trivalent Lanthanide Ions. *J. Solid State Chem.* **2005**, *178* (2), 448–453. https://doi.org/https://doi.org/10.1016/j.jssc.2004.07.046.

(69) Tan, M.; del Rosal, B.; Zhang, Y.; Martín Rodríguez, E.; Hu, J.; Zhou, Z.; Fan, R.; Ortgies, D. H.; Fernández, N.; Chaves-Coira, I.; Núñez, Á.; Jaque, D.; Chen, G. Rare-Earth-Doped Fluoride Nanoparticles with Engineered Long Luminescence Lifetime for Time-Gated in Vivo Optical Imaging in the Second Biological Window. *Nanoscale* **2018**, *10* (37), 17771–17780. https://doi.org/10.1039/C8NR02382D.

(70) Zhong, Y.; Ma, Z.; Wang, F.; Wang, X.; Yang, Y.; Liu, Y.; Zhao, X.; Li, J.; Du, H.; Zhang, M.; Cui, Q.; Zhu, S.; Sun, Q.; Wan, H.; Tian, Y.; Liu, Q.; Wang, W.; Garcia, K. C.; Dai, H. In Vivo Molecular Imaging for Immunotherapy Using Ultra-Bright near-Infrared-IIb Rare-Earth Nanoparticles. *Nat. Biotechnol.* **2019**, *37* (11), 1322–1331. https://doi.org/10.1038/s41587-019-0262-4.

(71) Cao, J.; Zhu, B.; Zheng, K.; He, S.; Meng, L.; Song, J.; Yang, H. Recent Progress in NIR-II Contrast Agent for Biological Imaging. *Front. Bioeng. Biotechnol.* **2020**, *Volume 7-2019*.

(72) Mi, C.; Guan, M.; Zhang, X.; Yang, L.; Wu, S.; Yang, Z.; Guo, Z.; Liao, J.; Zhou, J.; Lin, F.; Ma, E.; Jin, D.; Yuan, X. High Spatial and Temporal Resolution NIR-IIb Gastrointestinal Imaging in Mice. *Nano Lett.* **2022**, *22* (7), 2793–2800. https://doi.org/10.1021/acs.nanolett.1c04909.

(73) Liu, S.; An, Z.; Huang, J.; Zhou, B. Enabling Efficient NIR-II Luminescence in Lithium-Sublattice Core—Shell Nanocrystals towards Stark Sublevel Based Nanothermometry. *Nano Res.* **2023**, *16* (1), 1626–1633. https://doi.org/10.1007/s12274-022-5121-9.

(74) Hu, Y.; Liang, X.; Wang, Y.; Liu, E.; Hu, X.; Fan, J. Enhancement of the Red Upconversion Luminescence in NaYF4:Yb3+, Er3+ Nanoparticles by the Transition Metal Ions Doping. *Ceram. Int.* **2015**, *41* (10, Part B), 14545–14553. https://doi.org/https://doi.org/10.1016/j.ceramint.2015.07.171.

(75) Yoshimoto, K.; Masuno, A.; Ueda, M.; Inoue, H.; Yamamoto, H.; Kawashima, T. Low Phonon Energies and Wideband Optical Windows of La2O3-Ga2O3 Glasses Prepared Using an Aerodynamic Levitation Technique. *Sci. Rep.* **2017**, *7* (1), 45600. https://doi.org/10.1038/srep45600.

(76) Exarhos, G. J.; Miller, P. J.; Risen Jr., W. M. Interionic Vibrations and Glass Transitions in Ionic Oxide Metaphosphate Glasses. *J. Chem. Phys.* **1974**, *60* (11), 4145–4155. https://doi.org/10.1063/1.1680881.

(77) Mathews, M. D.; Ambekar, B. R.; Tyagi, A. K.; Köhler, J. High Temperature X-Ray Diffraction Studies on Sodium Yttrium Fluoride. *J. Alloys Compd.* **2004**, *377* (1), 162–166. https://doi.org/https://doi.org/10.1016/j.jallcom.2003.12.043.

(78) Dong, C.; Korinek, A.; Blasiak, B.; Tomanek, B.; van Veggel, F. C. J. M. Cation Exchange: A Facile Method To Make NaYF4:Yb,Tm-NaGdF4 Core–Shell Nanoparticles with a Thin, Tunable, and Uniform Shell. *Chem. Mater.* **2012**, *24* (7), 1297–1305. https://doi.org/10.1021/cm2036844.

(79) Chun-Hua Yan, Chao Zhang, L.-D. S. Synthesis of Rare Earth Nanomaterials. In *Rare Earth Nanotechnology*; Jenny Stanford Publishing., 2012; p 42. https://doi.org/https://doi.org/10.1201/b12310.

(80) Boyer, J.-C.; Vetrone, F.; Cuccia, L. A.; Capobianco, J. A. Synthesis of Colloidal Upconverting NaYF4 Nanocrystals Doped with Er3+, Yb3+ and Tm3+, Yb3+ via Thermal Decomposition of Lanthanide Trifluoroacetate Precursors. *J. Am. Chem. Soc.* **2006**, *128* (23), 7444–7445.

https://doi.org/10.1021/ja061848b.

(81) Qi, X.; Lee, C.; Ursprung, B.; Skripka, A.; Schuck, P. J.; Chan, E. M.; Cohen, B. E. Short-Wave Infrared Upconverting Nanoparticles. *J. Am. Chem. Soc.* **2024**, *146* (43), 29292–29296. https://doi.org/10.1021/jacs.4c11181.

(82) De Roo, J. Chemical Considerations for Colloidal Nanocrystal Synthesis. *Chem. Mater.* **2022**, *34* (13), 5766–5779. https://doi.org/10.1021/acs.chemmater.2c01058.

(83) Liang, X.; Wang, X.; Zhuang, J.; Peng, Q.; Li, Y. Synthesis of NaYF4 Nanocrystals with Predictable Phase and Shape. *Adv. Funct. Mater.* **2007**, *17* (15), 2757–2765. https://doi.org/https://doi.org/10.1002/adfm.200600807.

(84) Feng, Y.; Li, Z.; Li, Q.; Yuan, J.; Tu, L.; Ning, L.; Zhang, H. Internal OH− Induced Cascade Quenching of Upconversion Luminescence in NaYF4:Yb/Er Nanocrystals. *Light Sci. Appl.* **2021**, *10* (1), 105. https://doi.org/10.1038/s41377-021-00550-5.

(85) Li, R.; Fang, X.; Ren, J.; Chen, B.; Yuan, X.; Pan, X.; Zhang, P.; Zhang, L.; Tu, D.; Fang, Z.; Chen, X.; Ju, Q. The Effect of Surface-Capping Oleic Acid on the Optical Properties of Lanthanide-Doped Nanocrystals. *Nanoscale* **2021**, *13* (29), 12494–12504. https://doi.org/10.1039/D0NR08488C.

(86) Mai, H.-X.; Zhang, Y.-W.; Si, R.; Yan, Z.-G.; Sun, L.; You, L.-P.; Yan, C.-H. High-Quality Sodium Rare-Earth Fluoride Nanocrystals: Controlled Synthesis and Optical Properties. *J. Am. Chem. Soc.* **2006**, *128* (19), 6426–6436. https://doi.org/10.1021/ja060212h.

(87) Huang, K.; Li, Z.; Li, Y.; Yu, N.; Gao, X.; Huang, L.; Lim, S. F.; Han, G. Three-Dimensional Colloidal Controlled Growth of Core–Shell Heterostructured Persistent Luminescence Nanocrystals. *Nano Lett.* **2021**, *21* (12), 4903–4910. https://doi.org/10.1021/acs.nanolett.0c04940.

(88) Boyer, J.-C.; van Veggel, F. C. J. M. Absolute Quantum Yield Measurements of Colloidal NaYF4: Er3+, Yb3+ Upconverting Nanoparticles. *Nanoscale* **2010**, *2* (8), 1417–1419. https://doi.org/10.1039/C0NR00253D.

(89) Eaton, D. F. Reference Materials for Fluorescence Measurement. **1988**, *60* (7), 1107–1114. https://doi.org/doi:10.1351/pac198860071107.

(90) Madirov, E.; Busko, D.; Cardona, F. A.; Hudry, D.; Kuznetsov, S. V; Konyushkin, V. A.; Nakladov, A. N.; Alexandrov, A. A.; Howard, I. A.; Richards, B. S.; Turshatov, A. Comparison of Quantum Yield of Upconversion Nanocrystals Determined by Absolute and Relative Methods. *Adv. Photonics Res.* **2023**, *4* (2), 2200187. https://doi.org/https://doi.org/10.1002/adpr.202200187.

(91) Faulkner, D. O.; McDowell, J. J.; Price, A. J.; Perovic, D. D.; Kherani, N. P.; Ozin, G. A. Measurement of Absolute Photoluminescence Quantum Yields Using Integrating Spheres – Which Way to Go? *Laser Photon. Rev.* **2012**, *6* (6), 802–806. https://doi.org/https://doi.org/10.1002/lpor.201200077.

(92) de Mello, J. C.; Wittmann, H. F.; Friend, R. H. An Improved Experimental Determination of External Photoluminescence Quantum Efficiency. *Adv. Mater.* **1997**, *9* (3), 230–232. https://doi.org/https://doi.org/10.1002/adma.19970090308.

(93) Joseph, R. E.; Jiménez, C.; Hudry, D.; Gao, G.; Busko, D.; Biner, D.; Turshatov, A.; Krämer, K.; Richards, B. S.; Howard, I. A. Critical Power Density: A Metric To Compare the Excitation Power Density Dependence of Photon Upconversion in Different Inorganic Host Materials. *J. Phys. Chem. A* **2019**, *123* (31), 6799–6811. https://doi.org/10.1021/acs.jpca.9b03851.

(94) Arteaga Cardona, F.; Jain, N.; Popescu, R.; Busko, D.; Madirov, E.; Arús, B. A.; Gerthsen, D.; De Backer, A.; Bals, S.; Bruns, O. T.; Chmyrov, A.; Van Aert, S.; Richards, B. S.; Hudry, D. Preventing Cation Intermixing Enables 50% Quantum Yield in Sub-15 Nm Short-Wave Infrared-Emitting Rare-Earth Based Core-Shell Nanocrystals. *Nat. Commun.* **2023**, *14* (1), 7–11. https://doi.org/10.1038/s41467-023-40031-4.

(95) Lei, X.; Li, R.; Tu, D.; Shang, X.; Liu, Y.; You, W.; Sun, C.; Zhang, F.; Chen, X. Intense Near-Infrared-II Luminescence from NaCeF4:Er/Yb Nanoprobes for in Vitro Bioassay and in Vivo Bioimaging. *Chem. Sci.* **2018**, *9* (20), 4682–4688. https://doi.org/10.1039/C8SC00927A.

(96) Wang, X.; Hu, H.; Zhang, H.; Li, C.; An, B.; Dai, J. Single Ultrasmall Mn2+-Doped NaNdF4 Nanocrystals as Multimodal Nanoprobes for Magnetic Resonance and Second near-Infrared Fluorescence Imaging. *Nano Res.* **2018**, *11* (2), 1069–1081. https://doi.org/10.1007/s12274-017-1727-8.

(97) Yu, Z.; Shi, J.; Li, J.; Li, P.; Zhang, H. Luminescence Enhancement of CaF2:Nd3+ Nanoparticles in the Second near-Infrared Window for in Vivo Imaging through Y3+ Doping. *J. Mater. Chem. B* **2018**, *6* (8), 1238–1243. https://doi.org/10.1039/C7TB03052E.

(98) Li, Y.; Zeng, S.; Hao, J. Non-Invasive Optical Guided Tumor Metastasis/Vessel Imaging by Using Lanthanide Nanoprobe with Enhanced Down-Shifting Emission beyond 1500 Nm. *ACS Nano* **2019**, *13* (1), 248–259. https://doi.org/10.1021/acsnano.8b05431.

(99) Shao, W.; Chen, G.; Kuzmin, A.; Kutscher, H. L.; Pliss, A.; Ohulchanskyy, T. Y.; Prasad, P. N. Tunable Narrow Band Emissions from Dye-Sensitized Core/Shell/Shell Nanocrystals in the Second Near-Infrared Biological Window. *J. Am. Chem. Soc.* **2016**, *138* (50), 16192–16195. https://doi.org/10.1021/jacs.6b08973.

(100) Wang, X.; Yakovliev, A.; Ohulchanskyy, T. Y.; Wu, L.; Zeng, S.; Han, X.; Qu, J.; Chen, G. Efficient Erbium-Sensitized Core/Shell Nanocrystals for Short Wave Infrared Bioimaging. *Adv. Opt. Mater.* **2018**, *6* (20), 1800690. https://doi.org/https://doi.org/10.1002/adom.201800690.

(101) He, S.; Chen, S.; Li, D.; Wu, Y.; Zhang, X.; Liu, J.; Song, J.; Liu, L.; Qu, J.; Cheng, Z. High Affinity to Skeleton Rare Earth Doped Nanoparticles for Near-Infrared II Imaging. *Nano Lett.* **2019**, *19* (5), 2985–2992. https://doi.org/10.1021/acs.nanolett.9b00140.

(102) Wang, W.; Feng, Z.; Li, B.; Chang, Y.; Li, X.; Yan, X.; Chen, R.; Yu, X.; Zhao, H.; Lu, G.; Kong, X.; Qian, J.; Liu, X. Er3+ Self-Sensitized Nanoprobes with Enhanced 1525 Nm Downshifting Emission for NIR-IIb in Vivo Bio-Imaging. *J. Mater. Chem. B* **2021**, *9* (12), 2899–2908. https://doi.org/10.1039/D0TB02728F.

(103) Naczynski, D. J.; Tan, M. C.; Zevon, M.; Wall, B.; Kohl, J.; Kulesa, A.; Chen, S.; Roth, C. M.; Riman, R. E.; Moghe, P. V. Rare-Earth-Doped Biological Composites as in Vivo Shortwave Infrared Reporters. *Nat. Commun.* **2013**, *4* (1), 2199. https://doi.org/10.1038/ncomms3199.

(104) Hu, Q.; Kong, N.; Chai, Y.; Xing, Z.; Wu, Y.; Zhang, J.; Li, F.; Zhu, X. A Lanthanide Nanocomposite with Cross-Relaxation Enhanced near-Infrared Emissions as a Ratiometric Nanothermometer. *Nanoscale Horizons* **2022**, *7* (10), 1177–1185. https://doi.org/10.1039/D2NH00283C.

(105) Chen, Z.-H.; Wang, X.; Yang, M.; Ming, J.; Yun, B.; Zhang, L.; Wang, X.; Yu, P.; Xu, J.; Zhang, H.; Zhang, F. An Extended NIR-II Superior Imaging Window from 1500 to 1900 Nm for High-Resolution In Vivo Multiplexed Imaging Based on Lanthanide Nanocrystals. *Angew. Chemie Int. Ed.* **2023**, *62* (49), e202311883. https://doi.org/https://doi.org/10.1002/anie.202311883.

(106) Yang, Y.; Chen, Y.; Pei, P.; Fan, Y.; Wang, S.; Zhang, H.; Zhao, D.; Qian, B.-Z.; Zhang, F. Fluorescence-Amplified Nanocrystals in the Second near-Infrared Window for in Vivo Real-Time Dynamic Multiplexed Imaging. *Nat. Nanotechnol.* **2023**. https://doi.org/10.1038/s41565-023-01422-2.

(107) Bruns, O. T.; Bischof, T. S.; Harris, D. K.; Franke, D.; Shi, Y.; Riedemann, L.; Bartelt, A.; Jaworski, F. B.; Carr, J. A.; Rowlands, C. J.; Wilson, M. W. B.; Chen, O.; Wei, H.; Hwang, G. W.; Montana, D. M.; Coropceanu, I.; Achorn, O. B.; Kloepper, J.; Heeren, J.; So, P. T. C.; Fukumura, D.; Jensen, K. F.; Jain, R. K.; Bawendi, M. G. Next-Generation in Vivo Optical Imaging with Short-Wave Infrared Quantum Dots. *Nat. Biomed. Eng.* **2017**, *1* (4), 56. https://doi.org/10.1038/s41551-017-0056.

(108) Hong, G.; Antaris, A. L.; Dai, H. Near-Infrared Fluorophores for Biomedical Imaging. *Nat. Biomed. Eng.* **2017**, *1* (1), 10. https://doi.org/10.1038/s41551-016-0010.

(109) Kono, T.; Yamada, J. In Vivo Measurement of Optical Properties of Human Skin for 450–800 Nm and 950–1600 Nm Wavelengths. *Int. J. Thermophys.* **2019**, *40* (5), 51. https://doi.org/10.1007/s10765-019-2515-3.

(110) Carr, J. A.; Aellen, M.; Franke, D.; So, P. T. C.; Bruns, O. T.; Bawendi, M. G. Absorption by Water Increases Fluorescence Image Contrast of Biological Tissue in the Shortwave Infrared. *Proc. Natl. Acad. Sci.* **2018**, *115* (37), 9080–9085. https://doi.org/10.1073/pnas.1803210115.

(111) Wang, F.; Zhong, Y.; Bruns, O.; Liang, Y.; Dai, H. In Vivo NIR-II Fluorescence Imaging for Biology and Medicine. *Nat. Photonics* **2024**, *18* (6), 535–547. https://doi.org/10.1038/s41566-024-01391-5.

(112) Soo Choi, H.; Liu, W.; Misra, P.; Tanaka, E.; Zimmer, J. P.; Itty Ipe, B.; Bawendi, M. G.; Frangioni, J. V. Renal Clearance of Quantum Dots. *Nat. Biotechnol.* **2007**, *25* (10), 1165–1170. https://doi.org/10.1038/nbt1340.

(113) Feng, R.; Li, G.; Ko, C.-N.; Zhang, Z.; Wan, J.-B.; Zhang, Q.-W. Long-Lived Second Near-Infrared Luminescent Probes: An Emerging Role in Time-Resolved Luminescence Bioimaging and Biosensing. *Small Struct.* **2023**, *4* (2), 2200131. https://doi.org/https://doi.org/10.1002/sstr.202200131.

(114) Diao, S.; Blackburn, J. L.; Hong, G.; Antaris, A. L.; Chang, J.; Wu, J. Z.; Zhang, B.; Cheng, K.; Kuo, C. J.; Dai, H. Fluorescence Imaging In Vivo at Wavelengths beyond 1500 Nm. *Angew. Chemie Int. Ed.* **2015**, *54* (49), 14758–14762. https://doi.org/https://doi.org/10.1002/anie.201507473.

(115) Liu, P.; Zhao, R.; Li, H.; Zhu, T.; Li, Y.; Wang, H.; Zhang, X.-D. Near-Infrared-II Deep Tissue Fluorescence Microscopy and Application. *Nano Res.* **2023**, *16* (1), 692–714. https://doi.org/10.1007/s12274-022-4836-y.

(116) Li, C.; Guan, X.; Zhang, X.; Zhou, D.; Son, S.; Xu, Y.; Deng, M.; Guo, Z.; Sun, Y.; Kim, J. S. NIR-II Bioimaging of Small Molecule Fluorophores: From Basic Research to Clinical Applications. *Biosens. Bioelectron.* **2022**, *216*, 114620. https://doi.org/https://doi.org/10.1016/j.bios.2022.114620.

(117) Pitruzzello, G. Seeing into Deep Tissue. *Nat. Photonics* **2023**, *17* (5), 376–377. https://doi.org/10.1038/s41566-023-01200-5.

(118) Huang, B.; Hu, J.; Li, H.; Luo, M.-Y.; Chen, S.; Zhang, M.; Sun, Z.-J.; Cui, R. Near-Infrared IIb Emitting Nanoprobe for High-Resolution Real-Time Imaging-Guided Photothermal Therapy Triggering Enhanced Anti-Tumor Immunity. *ACS Appl. Bio Mater.* **2020**, *3* (3), 1636–1645. https://doi.org/10.1021/acsabm.9b01202.

(119) Jia, Q.; Li, Z.; Bai, M.; Yan, H.; Zhang, R.; Ji, Y.; Feng, Y.; Yang, Z.; Wang, Z.; Li, J. Estimating Dynamic Vascular Perfusion Based on Er-Based Lanthanide Nanoprobes with Enhanced down-Conversion Emission beyond 1500 Nm. *Theranostics* **2021**, *11* (20), 9859–9872. https://doi.org/10.7150/thno.65771.

(120) Feng, Z.; Tang, T.; Wu, T.; Yu, X.; Zhang, Y.; Wang, M.; Zheng, J.; Ying, Y.; Chen, S.; Zhou, J.; Fan, X.; Zhang, D.; Li, S.; Zhang, M.; Qian, J. Perfecting and Extending the Near-Infrared Imaging Window. *Light Sci. Appl.* **2021**, *10* (1), 197. https://doi.org/10.1038/s41377-021-00628-0.

(121) Ren, F.; Huang, H.; Yang, H.; Xia, B.; Ma, Z.; Zhang, Y.; Wu, F.; Li, C.; He, T.; Wang, Q. Tailoring Near-Infrared-IIb Fluorescence of Thulium(III) by Nanocrystal Structure Engineering. *Nano Lett.* **2023**, *23* (21), 10058–10065. https://doi.org/10.1021/acs.nanolett.3c03543.

(122) Zhang, M.; Yue, J.; Cui, R.; Ma, Z.; Wan, H.; Wang, F.; Zhu, S.; Zhou, Y.; Kuang, Y.; Zhong, Y.; Pang, D.-W.; Dai, H. Bright Quantum Dots Emitting at ~1,600 Nm in the NIR-IIb Window for Deep

Tissue Fluorescence Imaging. *Proc. Natl. Acad. Sci.* **2018**, *115* (26), 6590–6595. https://doi.org/10.1073/pnas.1806153115.

(123) Schmidt, E. L.; Ou, Z.; Ximendes, E.; Cui, H.; Keck, C. H. C.; Jaque, D.; Hong, G. Near-Infrared II Fluorescence Imaging. *Nat. Rev. Methods Prim.* **2024**, *4* (1), 23. https://doi.org/10.1038/s43586-024-00301-x.

(124) Kind, C.; Popescu, R.; Schneider, R.; Müller, E.; Gerthsen, D.; Feldmann, C. Advanced Bimetallic In–Cu/Ag/Au Nanostructures via Microemulsion-Based Reaction. *RSC Adv.* **2012**, *2* (25), 9473–9487. https://doi.org/10.1039/C2RA21659K.

(125) Liang, W.; He, S.; Wu, S. Fluorescence Imaging in Second Near-Infrared Window: Developments, Challenges, and Opportunities. *Adv. NanoBiomed Res.* **2022**, *2* (11), 2200087. https://doi.org/https://doi.org/10.1002/anbr.202200087.

(126) Saleh, M. I.; Panas, I. D.; Frenzel, F.; Würth, C.; Rühle, B.; Slominskii, Y. L.; Demchenko, A.; Resch-Genger, U. Sensitization of Upconverting Nanoparticles with a NIR-Emissive Cyanine Dye Using a Micellar Encapsulation Approach. *Methods Appl. Fluoresc.* **2019**, *7* (1), 14003. https://doi.org/10.1088/2050-6120/aafe1f.

(127) Chen, G.; Shao, W.; Valiev, R. R.; Ohulchanskyy, T. Y.; He, G. S.; Ågren, H.; Prasad, P. N. Efficient Broadband Upconversion of Near-Infrared Light in Dye-Sensitized Core/Shell Nanocrystals. *Adv. Opt. Mater.* **2016**, *4* (11), 1760–1766. https://doi.org/https://doi.org/10.1002/adom.201600556.

(128) Chen, Y.; D'Amario, C.; Gee, A.; Duong, H. T. T.; Shimoni, O.; Valenzuela, S. M. Dispersion Stability and Biocompatibility of Four Ligand-Exchanged NaYF4: Yb, Er Upconversion Nanoparticles. *Acta Biomater.* **2020**, *102*, 384–393. https://doi.org/https://doi.org/10.1016/j.actbio.2019.11.048.

(129) Xu, J.; Yang, D.; Han, W.; Dong, S.; Jia, T.; He, F.; Bi, H.; Gai, S.; Li, L.; Yang, P. A Novel Strategy for Markedly Enhancing the Red Upconversion Emission in Er3+/Tm3+ Cooperated Nanoparticles. *J. Mater. Chem. C* **2018**, *6* (28), 7533–7540. https://doi.org/10.1039/C8TC02370K.

(130) Shen, B.; Cheng, S.; Gu, Y.; Ni, D.; Gao, Y.; Su, Q.; Feng, W.; Li, F. Revisiting the Optimized Doping Ratio in Core/Shell Nanostructured Upconversion Particles. *Nanoscale* **2017**, *9* (5), 1964–1971. https://doi.org/10.1039/C6NR07687D.

(131) Chen, B.; Wang, F. Combating Concentration Quenching in Upconversion Nanoparticles. *Acc. Chem. Res.* **2020**, *53* (2), 358–367. https://doi.org/10.1021/acs.accounts.9b00453.

(132) Wen, S.; Li, D.; Liu, Y.; Chen, C.; Wang, F.; Zhou, J.; Bao, G.; Zhang, L.; Jin, D. Power-Dependent Optimal Concentrations of Tm3+ and Yb3+ in Upconversion Nanoparticles. *J. Phys. Chem. Lett.* **2022**, *13* (23), 5316–5323. https://doi.org/10.1021/acs.jpclett.2c01186.

(133) Dühnen, S.; Haase, M. Study on the Intermixing of Core and Shell in NaEuF4/NaGdF4 Core/Shell Nanocrystals. *Chem. Mater.* **2015**, *27* (24), 8375–8386. https://doi.org/10.1021/acs.chemmater.5b03846.

(134) Bastian, P. U.; Nacak, S.; Roddatis, V.; Kumke, M. U. Tracking the Motion of Lanthanide Ions within Core–Shell–Shell NaYF4 Nanocrystals via Resonance Energy Transfer. *J. Phys. Chem. C* **2020**, *124* (20), 11229–11238. https://doi.org/10.1021/acs.jpcc.0c02588.

(135) Scardi, P.; Azanza Ricardo, C. L.; Perez-Demydenko, C.; Coelho, A. A. Whole Powder Pattern Modelling Macros for TOPAS. *J. Appl. Crystallogr.* **2018**, *51* (6), 1752–1765. https://doi.org/10.1107/S160057671801289X.

(136) Scardi, P. Diffraction Line Profiles in the Rietveld Method. *Cryst. Growth Des.* **2020**, *20* (10), 6903–6916. https://doi.org/10.1021/acs.cgd.0c00956.

(137) Lazic, I.; Bosch, E. G. T.; Lazar, S.; Wirix, M.; Yücelen, E. Integrated Differential Phase Contrast (IDPC)–Direct Phase Imaging in STEM for Thin Samples. *Microsc. Microanal.* **2016**, *22* (S3), 36–37. https://doi.org/10.1017/S1431927616001033.

(138) De Backer, A.; van den Bos, K. H. W.; Van den Broek, W.; Sijbers, J.; Van Aert, S. StatSTEM: An Efficient Approach for Accurate and Precise Model-Based Quantification of Atomic Resolution Electron Microscopy Images. *Ultramicroscopy* **2016**, *171*, 104–116. https://doi.org/https://doi.org/10.1016/j.ultramic.2016.08.018.

(139) Van Aert, S.; Verbeeck, J.; Erni, R.; Bals, S.; Luysberg, M.; Dyck, D. Van; Tendeloo, G. Van. Quantitative Atomic Resolution Mapping Using High-Angle Annular Dark Field Scanning Transmission Electron Microscopy. *Ultramicroscopy* **2009**, *109* (10), 1236–1244. https://doi.org/https://doi.org/10.1016/j.ultramic.2009.05.010.

(140) Du, P.; An, R.; Liang, Y.; Lei, P.; Zhang, H. Emerging NIR-II Luminescent Bioprobes Based on Lanthanide-Doped Nanoparticles: From Design towards Diverse Bioapplications. *Coord. Chem. Rev.* **2022**, *471*, 214745. https://doi.org/https://doi.org/10.1016/j.ccr.2022.214745.

(141) Meng, J.; Cui, Y.; Wang, Y. Rare Earth-Doped Nanocrystals for Bioimaging in the near-Infrared Region. *J. Mater. Chem. B* **2022**, *10* (42), 8596–8615. https://doi.org/10.1039/D2TB01731H.

(142) Ge, X.; Wei, R.; Sun, L. Lanthanide Nanoparticles with Efficient Near-Infrared-II Emission for Biological Applications. *J. Mater. Chem. B* **2020**, *8* (45), 10257–10270. https://doi.org/10.1039/D0TB01745K.

(143) Volk, A. A.; Epps, R. W.; Yonemoto, D. T.; Masters, B. S.; Castellano, F. N.; Reyes, K. G.; Abolhasani, M. AlphaFlow: Autonomous Discovery and Optimization of Multi-Step Chemistry Using a Self-Driven Fluidic Lab Guided by Reinforcement Learning. *Nat. Commun.* **2023**, *14* (1), 1403. https://doi.org/10.1038/s41467-023-37139-y.

(144) Yang, B.; Cang, J.; Li, Z.; Chen, J. Nanocrystals as Performance-Boosting Materials for Solar Cells. *Nanoscale Adv.* **2024**, *6* (5), 1331–1360. https://doi.org/10.1039/D3NA01063E.

(145) Zhang, C.; Yin, Q.; Ge, S.; Qi, J.; Han, Q.; Gao, W.; Wang, Y.; Zhang, M.; Dong, J. Optical Anti-Counterfeiting and Information Storage Based on Rare-Earth-Doped Luminescent Materials. *Mater. Res. Bull.* **2024**, *176*, 112801. https://doi.org/https://doi.org/10.1016/j.materresbull.2024.112801.

(146) Shannon, R. D. Revised Effective Ionic Radii and Systematic Studies of Interatomic Distances in Halides and Chalcogenides. *Acta Crystallogr. Sect. A* **1976**, *32* (5), 751–767. https://doi.org/10.1107/S0567739476001551.

(147) Ectors, D.; Goetz-Neunhoeffer, F.; Neubauer, J. A Generalized Geometric Approach to Anisotropic Peak Broadening Due to Domain Morphology. *J. Appl. Crystallogr.* **2015**, *48* (1), 189–194. https://doi.org/10.1107/S1600576714026557.

(148) *Debyer*. https://debyer.readthedocs.io/en/latest/#direct-space-patterns.

(149) Gelisio, L.; Scardi, P. 100 Years of Debye's Scattering Equation. *Acta Crystallogr. Sect. A* **2016**, *72* (6), 608–620.

(150) Ganem, J.; Crawford, J.; Schmidt, P.; Jenkins, N. W.; Bowman, S. R. Thulium Cross-Relaxation in a Low Phonon Energy Crystalline Host. *Phys. Rev. B* **2002**, *66* (24), 245101. https://doi.org/10.1103/PhysRevB.66.245101.

(151) Wisser, M. D.; Chea, M.; Lin, Y.; Wu, D. M.; Mao, W. L.; Salleo, A.; Dionne, J. A. Strain-Induced Modification of Optical Selection Rules in Lanthanide-Based Upconverting Nanoparticles. *Nano Lett.* **2015**, *15* (3), 1891–1897. https://doi.org/10.1021/nl504738k.

(152) Liang, L.; Feng, Z.; Zhang, Q.; Cong, T. Do; Wang, Y.; Qin, X.; Yi, Z.; Ang, M. J. Y.; Zhou, L.;

Feng, H.; Xing, B.; Gu, M.; Li, X.; Liu, X. Continuous-Wave near-Infrared Stimulated-Emission Depletion Microscopy Using Downshifting Lanthanide Nanoparticles. *Nat. Nanotechnol.* **2021**, *16* (9), 975–980. https://doi.org/10.1038/s41565-021-00927-y.

(153) Würth, C.; Grauel, B.; Pons, M.; Frenzel, F.; Rissiek, P.; Rücker, K.; Haase, M.; Resch-Genger, U. Yb- and Er Concentration Dependence of the Upconversion Luminescence of Highly Doped NaYF4:Yb,Er/NaYF4:Lu Core/Shell Nanocrystals Prepared by a Water-Free Synthesis. *Nano Res.* **2022**, *15* (10), 9639–9646. https://doi.org/10.1007/s12274-022-4570-5.

(154) Yi, G.-S.; Chow, G.-M. Water-Soluble NaYF4:Yb,Er(Tm)/NaYF4/Polymer Core/Shell/Shell Nanoparticles with Significant Enhancement of Upconversion Fluorescence. *Chem. Mater.* **2007**, *19* (3), 341–343. https://doi.org/10.1021/cm062447y.

(155) Kömpe, K.; Borchert, H.; Storz, J.; Lobo, A.; Adam, S.; Möller, T.; Haase, M. Green-Emitting CePO4:Tb/LaPO4 Core–Shell Nanoparticles with 70 % Photoluminescence Quantum Yield. *Angew. Chemie Int. Ed.* **2003**, *42* (44), 5513–5516. https://doi.org/https://doi.org/10.1002/anie.200351943.

(156) Su, Q.; Han, S.; Xie, X.; Zhu, H.; Chen, H.; Chen, C.-K.; Liu, R.-S.; Chen, X.; Wang, F.; Liu, X. The Effect of Surface Coating on Energy Migration-Mediated Upconversion. *J. Am. Chem. Soc.* **2012**, *134* (51), 20849–20857. https://doi.org/10.1021/ja3111048.

(157) Wang, F.; Deng, R.; Wang, J.; Wang, Q.; Han, Y.; Zhu, H.; Chen, X.; Liu, X. Tuning Upconversion through Energy Migration in Core–Shell Nanoparticles. *Nat. Mater.* **2011**, *10* (12), 968–973. https://doi.org/10.1038/nmat3149.

(158) Wang, F.; Wang, J.; Liu, X. Direct Evidence of a Surface Quenching Effect on Size-Dependent Luminescence of Upconversion Nanoparticles. *Angew. Chemie Int. Ed.* **2010**, *49* (41), 7456–7460. https://doi.org/https://doi.org/10.1002/anie.201003959.

(159) Rabouw, F. T.; Prins, P. T.; Villanueva-Delgado, P.; Castelijns, M.; Geitenbeek, R. G.; Meijerink, A. Quenching Pathways in NaYF4:Er3+,Yb3+ Upconversion Nanocrystals. *ACS Nano* **2018**, *12* (5), 4812–4823. https://doi.org/10.1021/acsnano.8b01545.

(160) Meng, X.; Xie, Y.; Shen, T.; Wang, J.; Ning, K.; Wang, J.; Cao, C. Rare Earth Fluoride with Dye-Sensitized Upconversion Luminescence under Dual-Excitation Wavelength. *Inorg. Chem. Commun.* **2024**, *167*, 112672. https://doi.org/https://doi.org/10.1016/j.inoche.2024.112672.

(161) Wang, L.; Han, S.; Li, C.; Tu, D.; Chen, X. Lanthanide-Doped Inorganic Nanoprobes for Luminescent Assays of Biomarkers. *Accounts Mater. Res.* **2023**, *4* (2), 193–204. https://doi.org/10.1021/accountsmr.2c00233.

(162) Liu, S.; Yan, L.; Huang, J.; Zhang, Q.; Zhou, B. Controlling Upconversion in Emerging Multilayer Core–Shell Nanostructures: From Fundamentals to Frontier Applications. *Chem. Soc. Rev.* **2022**, *51* (5), 1729–1765. https://doi.org/10.1039/D1CS00753J.

(163) Huang, J.; Tao, L.; Wei, H.; Huang, H.; Zhang, Q.; Zhou, B. Full-Color Tuning in Multi-Layer Core-Shell Nanoparticles from Single-Wavelength Excitation. *Nat. Commun.* **2025**, *16* (1), 2378. https://doi.org/10.1038/s41467-025-57622-y.

(164) Xue, M.; Zhu, X.; Qiu, X.; Gu, Y.; Feng, W.; Li, F. Highly Enhanced Cooperative Upconversion Luminescence through Energy Transfer Optimization and Quenching Protection. *ACS Appl. Mater. Interfaces* **2016**, *8* (28), 17894–17901. https://doi.org/10.1021/acsami.6b05609.

(165) Cai, Z.; Qin, Y.; Guo, X.; Tang, H.; Wang, M.; Zhao, X.; Xia, D.; Hu, Y.; Zhan, Q.; Wei, W. High-Efficiency and Water-Quenching-Resistant Tb3+-Based Nanoparticles for Single-Particle Imaging. **2021**, *10* (7), 1845–1852. https://doi.org/doi:10.1515/nanoph-2021-0010.

(166) Halimi, I.; Rodrigues, E. M.; Maurizio, S. L.; Sun, H.-Q. T.; Grewal, M.; Boase, E. M.; Liu, N.; Marin, R.; Hemmer, E. Pick Your Precursor! Tailoring the Size and Crystal Phase of Microwave-

Synthesized Sub-10 Nm Upconverting Nanoparticles. *J. Mater. Chem. C* **2019**, *7* (48), 15364–15374. https://doi.org/10.1039/C9TC04817K.

(167) Hemmer, E. (Invited) Lanthanide-Based Nanoparticles Via Rapid Microwave-Assisted Synthesis and Their Application from Biomedicine to Printing. *ECS Meet. Abstr.* **2022**, *MA2022-01* (20), 1097. https://doi.org/10.1149/MA2022-01201097mtgabs.

(168) Ding, M.; Lu, C.; Cao, L.; Ni, Y.; Xu, Z. Controllable Synthesis, Formation Mechanism and Upconversion Luminescence of β-NaYF4 : Yb3+/Er3+ Microcrystals by Hydrothermal Process. *CrystEngComm* **2013**, *15* (41), 8366–8373. https://doi.org/10.1039/C3CE41427B.

(169) Grzechnik, A.; Friese, K. Crystal Structures and Stability of NaLnF4 (Ln = La, Ce, Pr, Nd, Sm and Gd) Studied with Synchrotron Single-Crystal and Powder Diffraction. *Dalt. Trans.* **2012**, *41* (34), 10258–10266. https://doi.org/10.1039/C2DT30650F.

(170) Ghosh, P.; Sharma, R. K.; Chouryal, Y. N.; Mudring, A.-V. Size of the Rare-Earth Ions: A Key Factor in Phase Tuning and Morphology Control of Binary and Ternary Rare-Earth Fluoride Materials. *RSC Adv.* **2017**, *7* (53), 33467–33476. https://doi.org/10.1039/C7RA06741K.

(171) Ren, J.; Jia, G.; Guo, Y.; Wang, A.; Xu, S. Unraveling Morphology and Phase Control of NaLnF4 Upconverting Nanocrystals. *J. Phys. Chem. C* **2016**, *120* (2), 1342–1351. https://doi.org/10.1021/acs.jpcc.5b11048.

(172) Zhang, J.; Mi, C.; Wu, H.; Huang, H.; Mao, C.; Xu, S. Synthesis of NaYF(4):Yb/Er/Gd up-Conversion Luminescent Nanoparticles and Luminescence Resonance Energy Transfer-Based Protein Detection. *Anal. Biochem.* **2012**, *421* (2), 673–679. https://doi.org/10.1016/j.ab.2011.11.008.

(173) Damasco, J. A.; Chen, G.; Shao, W.; Ågren, H.; Huang, H.; Song, W.; Lovell, J. F.; Prasad, P. N. Size-Tunable and Monodisperse Tm3+/Gd3+-Doped Hexagonal NaYbF4 Nanoparticles with Engineered Efficient near Infrared-to-near Infrared Upconversion for in Vivo Imaging. *ACS Appl. Mater. Interfaces* **2014**, *6* (16), 13884–13893. https://doi.org/10.1021/am503288d.

(174) Wang, F.; Han, Y.; Lim, C. S.; Lu, Y.; Wang, J.; Xu, J.; Chen, H.; Zhang, C.; Hong, M.; Liu, X. Simultaneous Phase and Size Control of Upconversion Nanocrystals through Lanthanide Doping. *Nature* **2010**, *463* (7284), 1061–1065. https://doi.org/10.1038/nature08777.

(175) Rastogi, C. K.; Lu, E.; Tam, J.; Pichaandi, J. M.; Howe, J.; Winnik, M. A. Influence of the Sodium Precursor on the Cubic-to-Hexagonal Phase Transformation and Controlled Preparation of Uniform NaNdF4 Nanoparticles. *Langmuir* **2021**. https://doi.org/10.1021/acs.langmuir.0c03346.

(176) Lu, E.; Pichaandi, J.; Rastogi, C. K.; Arnett, L. P.; Winnik, M. A. Influence of Cubic-to-Hexagonal-Phase Transformation on the Uniformity of NaLnF4 (Ho, Tb, Eu, Sm) Nanoparticles. *Chem. Mater.* **2019**, *31* (23), 9742–9749. https://doi.org/10.1021/acs.chemmater.9b03421.

(177) Saha, S.; Pala, R. G. S.; Sivakumar, S. Catalyzing Cubic-to-Hexagonal Phase Transition in NaYF4 via Ligand Enhanced Surface Ordering. *Cryst. Growth Des.* **2018**, *18* (9), 5080–5088. https://doi.org/10.1021/acs.cgd.8b00535.

(178) Dong, H.; Sun, L.-D.; Li, L.-D.; Si, R.; Liu, R.; Yan, C.-H. Selective Cation Exchange Enabled Growth of Lanthanide Core/Shell Nanoparticles with Dissimilar Structure. *J. Am. Chem. Soc.* **2017**, *139* (51), 18492–18495. https://doi.org/10.1021/jacs.7b11836.

(179) Zou, Q.; Marcelot, C.; Ratel-Ramond, N.; Yi, X.; Roblin, P.; Frenzel, F.; Resch-Genger, U.; Eftekhari, A.; Bouchet, A.; Coudret, C.; Verelst, M.; Chen, X.; Mauricot, R.; Roux, C. Heterogeneous Oxysulfide@Fluoride Core/Shell Nanocrystals for Upconversion-Based Nanothermometry. *ACS Nano* **2022**, *16* (8), 12107–12117. https://doi.org/10.1021/acsnano.2c02423.

(180) Shao, Q.; Yang, C.; Chen, X.; Zhang, H.; Feng, G.; Zhou, S. Core-Mediated Synthesis, Growth

Mechanism and near-Infrared Luminescence Enhancement of α-NaGdF4@β-NaLuF4:Nd3+ Core–Shell Nanocrystals. *CrystEngComm* **2020**, *22* (8), 1359–1367. https://doi.org/10.1039/C9CE01748H.

(181) Ren, Y.; Winter, H.; Rosch, J. G.; Jung, K.; Duross, A. N.; Landry, M. R.; Pratx, G.; Sun, C. PEGylated β-NaGdF4/Tb@CaF2 Core/Shell Nanophosphors for Enhanced Radioluminescence and Folate Receptor Targeting. *ACS Appl. Nano Mater.* **2019**, *2* (6), 3718–3727. https://doi.org/10.1021/acsanm.9b00629.

(182) U.S. Food and Drug Administration. Indocyanine Green for Injection, USP. https://www.accessdata.fda.gov/drugsatfda_docs/label/2006/011525s017lbl.pdf.

(183) Zhou, J.; Yang, Y.; Zhang, C. Toward Biocompatible Semiconductor Quantum Dots: From Biosynthesis and Bioconjugation to Biomedical Application. *Chem. Rev.* **2015**, *115* (21), 11669–11717. https://doi.org/10.1021/acs.chemrev.5b00049.

(184) Ma, B. L.; Zhai, X.; Du, G.; Zhou, J. Orthogonal Shortwave Infrared Emission Based on Rare Earth Nanoparticles for Interference-Free Logical Codes and Bio-Imaging. *Chem. Sci.* **2019**, *10* (11), 3281–3288. https://doi.org/10.1039/C8SC05044A.

(185) Bhavane, R.; Starosolski, Z.; Stupin, I.; Ghaghada, K. B.; Annapragada, A. NIR-II Fluorescence Imaging Using Indocyanine Green Nanoparticles. *Sci. Rep.* **2018**, *8* (1), 14455. https://doi.org/10.1038/s41598-018-32754-y.

(186) Fan, W.; Peng, H.; Yu, Z.; Wang, L.; He, H.; Ma, Y.; Qi, J.; Lu, Y.; Wu, W. The Long-Circulating Effect of Pegylated Nanoparticles Revisited via Simultaneous Monitoring of Both the Drug Payloads and Nanocarriers. *Acta Pharm. Sin. B* **2022**, *12* (5), 2479–2493. https://doi.org/https://doi.org/10.1016/j.apsb.2021.11.016.

(187) Yuan, B.; Chen, N.; Zhu, Q. Emission and Absorption Properties of Indocyanine Green in Intralipid Solution. *J. Biomed. Opt.* **2004**, *9* (3), 497–503. https://doi.org/10.1117/1.1695411.

(188) Desmettre, T.; Devoisselle, J. M.; Mordon, S. Fluorescence Properties and Metabolic Features of Indocyanine Green (ICG) as Related to Angiography. *Surv. Ophthalmol.* **2000**, *45* (1), 15–27. https://doi.org/10.1016/s0039-6257(00)00123-5.

(189) Guidelines on Limits of Exposure to Laser Radiation of Wavelengths between 180 Nm and 1,000 Microm. International Commission on Non-Ionizing Radiation Protection. *Health Phys.* **1996**, *71* (5), 804–819.